NORTHWESTERN UNIVERSITY

Interfacial Electrochemistry and Surface Modification of Thin-Film $LiMn_2O_4$ Cathodes in Lithium Ion Batteries

A DISSERTATION SUBMITTED TO THE GRADUATE SCHOOL
IN PARTIAL FULFILLMENT OF THE REQUIREMENTS

for the degree

DOCTOR OF PHILOSOPHY

Field of Materials Science and Engineering

By

Xiankai Yu

EVANSTON, ILLINOIS

September 2019

ABSTRACT

Interfacial Electrochemistry and Surface Modification of Thin-Film $LiMn_2O_4$ Cathodes in Lithium Ion Batteries

Xiankai Yu

Materials Science and Engineering, Northwestern University

This dissertation presents a comprehensive study of thin-film $LiMn_2O_4$ (LMO) cathodes applied in lithium ion batteries (LIBs). The primary aim was to establish fundamental understanding of the relationship between interfacial LMO chemistry/electrochemistry and its detrimental drawback, i.e. fast capacity fade over long term cycling, and then develop effective mitigation methods. Taking advantage of multiple advanced materials characterization techniques including *in situ* synchrotron X-ray scattering, high resolution scanning transmission electron microscopy (STEM), electron energy loss spectroscopy (EELS), X-ray photoelectron spectroscopy (XPS) depth profile, four main research topics are covered here: 1) characterization of the surface chemistry of hetero-epitaxial LMO thin films, 2) studying cathode electrolyte interphase in terms of chemical composition and manganese distribution, 3) exploring ultrahigh power density LMO thin film cathodes, and 4) determining the effect of protective surface coatings on LMO cycling stability.

LMO || $La_{0.5}Sr_{0.5}CoO_3$ (LSCO) || $SrTiO_3$ 111 (STO) hetero-epitaxial thin films fabricated by pulsed laser deposition (PLD) were electrochemically cycled in cells with Li counter electrodes while doing *in situ* synchrotron X-ray scattering characterization. Since surface roughness limits the resolution of the low-angle x-ray scattering, surface roughness was studied. Roughness resulted from LMO 3D island nucleation due to relatively large lattice mismatch between LMO

and LSCO, and induced dislocation generation discerned in high resolution STEM images. Low angle synchrotron X-ray scattering indicated rapid formation of cathode electrolyte interphase (CEI) morphology that gradually became stable after the first cycle.

A new synthesis method for thin-films cathodes was developed with the structure LMO || Au-Pd || stainless steel (SS). Chemical compositions of the CEI layer on the cathodes were examined by XPS depth profiling. The observation that considerable manganese was present in the CEI provides a new mechanism for loss of LMO capacity. A novel fabrication route based on multilayer sputtering deposition was developed for constructing high-quality LMO thin-film cathodes on well-engineered Pt || Ti || Al_2O_3 substrates with excellent electrochemical performance. Ultrahigh rate capability was achieved on a 25 nm thin-film LMO cathode exhibiting a high capacity retention of 85% at 80C (equivalent to 45 s of full charge). That remarkable performance was primarily attributed to the relatively short Li-ion diffusion length in the 25 nm thick LMO layers, the absence of a rate-limiting phase separation process, and the good electrical contact between the LMO and Pt layers.

The effect of thin LSCO layers on 25 nm thin-film LMO || Pt || Ti || Al_2O_3 cathodes on LMO cycling stability was studied. 3-electrode EIS analysis observed increased CEI ohmic resistance and LMO surface charge transfer resistance with thicker LSCO coating applied, indicating the significance of accurately controlling and determining optimized coating thickness. A coating layer of 2 nm LSCO significantly improved LMO capacity retention over 500 cycles from 84% to 95%. It was found that the LSCO coating suppressed phase separation of LMO, resulting in higher cycling stability attributed to a more stable solid-solution phase. In addition, it was observed that the LSCO coating inhibited grain cracking and crystallinity loss, improving

LMO capacity retention. A Mn_3O_4-like defect tetragonal spinel was revealed by STEM-ABF in cycled LMO and the LSCO surface coating was believed to inhibit that phase transition which caused LMO structure distortion due to Mn migration and lattice oxygen loss. Formation of the Mn_3O_4-like phase was further verified by EELS analysis of manganese oxidation states. Quantification of the Mn L_3/L_2 white-line ratios showed that the Mn oxidation state of cycled LMO averaged +2.4, consistent with the Mn oxidation state in the newly formed Mn_3O_4-like spinel.

ACKNOWLEDGEMENTS

It would be impossible for me to complete my doctoral thesis work without the important help and support from many people around me. I would like to take this opportunity to sincerely express my tremendous gratitude to all of them.

First and foremost, I would like to take my deepest thank to my advisor Prof. Scott Barnett for his support and guidance throughout my graduate research life over the past five years at Northwestern University. He led me into my research world with great patience, incredible passion and amazing knowledge, and meanwhile gave me enough space and time to explore the unknown on my own. More importantly, his optimistic and sweet personality has always inspired me to positively face problems I encountered during research, especially when there was no one else in my research group to follow at the very beginning.

I would also like to thank Prof. Michal Bedzyk, Prof. Chris Wolverton and Dr. Tim Fister for serving on my thesis committee. Their suggestions in my thesis proposal provided me with new ideas and insights about subsequent research.

I am extremely thankful to my mentor Dr. Zhao Gao, who gave my lab tour and safety training. He taught me how to use lab instruments, synthesize battery materials and tape casting. He was always supportive and provided me useful suggestions when I met problems.

Additionally, this work could not be accomplished without my many collaborators. This work was supported as part of the Center for Electrochemical Energy Science, an Energy Frontier Research Center funded by the U.S. Department of Energy, Office of Science, Basic Energy Sciences. Research at the Advanced Photon was supported by DOE, Office of Science, BES. I

would like to show special acknowledgements to D. Bruce Buchholz who helped to fabricate all the thin films by PLD, Dr. Xiao Chen who helped finish the in situ synchrotron x-ray scattering and electrochemical tests work at Argonne National Laboratory, Prof. Qianqian Li, and Dr. Yao-bin Xu who helped with the excellent STEM work, Dr. Kan-sheng Chen and Prof. Lei Li who taught and helped me with the coin-type batteries assembly and electrochemical tests. My sincere thanks also go to Dr. Roberto Scipioni who taught me EIS fitting for LIBs and provided remarkable contribution to my thesis and publications.

I also greatly appreciate help from all other previous and present members in my research group. They helped me a lot with my research as well as my social life. It was a great pleasure to work with them all.

Finally, I would like to dedicate this dissertation to my dear parents and elder brother in China. It is their love, support, encouragement and criticism that help me conquer any obstacles in my work and life.

LIST OF ABBREVIATIONS

AFM	Atomic-Force Microscopy
CE	Coulombic Efficiency
CEI	Cathode Electrolyte Interphase
CTR	Crystal Truncation Rod
CV	Cyclic Voltammetry
DMC	Dimethyl Carbonate
EC	Ethylene Carbonate
EMC	Ethyl Methyl Carbonate
EELS	Electron Energy Loss Spectroscopy
EIS	Electrochemical Impedance Spectroscopy
GCPL	Galvanostatic Cycling with Potential Limitation
GIXRD	Grazing Incidence X-ray Diffraction
ICA	Incremental Capacity Analysis
ICP-MS	Inductively-Coupled Plasma-Mass Spectroscopy
LIB	Lithium Ion Battery
LMO	$LiMn_2O_4$, Lithium Manganese Oxide
PLD	Pulsed Laser Deposition
SEI	Solid Electrolyte Interphase
SRO	$SrRuO_3$, Strontium Ruthenate
STO	$SrTiO_3$, Strontium titanate
STEM	Scanning Transmission Electron Microscopy
TEM	Transmission Electron Microscopy
XRD	X-ray Diffraction
XRR	X-ray Reflectivity
XPS	X-ray Photoelectron Spectroscopy

TABLE OF CONTENTS

LIST OF FIGURES AND TABLES

Chapter 1: Introduction

Modern society is heavily dependent on fossil fuels, and the associated CO_2 emission is one of the primary causes of climate change.[1] One promising approach to reduce the use of fossil fuels is via electric vehicles, which has been facilitated over the last decade by lithium ion batteries (LIBs).[2, 3] LIBs also have applications for grid energy storage, which is becoming increasingly important for enabling increasing utilization of renewable energy generation.[4] Although LIBs have been extremely successful in applications for portable electronics, significant challenges remain for the transportation and grid storage applications because of the much higher power density and greater energy storage capacity requirements, and the associated high cost and mass of the battery packs. Thus, developing advanced battery technologies is becoming one of the most important topics in emerging electrochemistry, materials, and energy sciences.[1] Besides improvements in energy density, improved cycle life, stability, safety, and calendar life are urgently needed in next-generation LIBs.

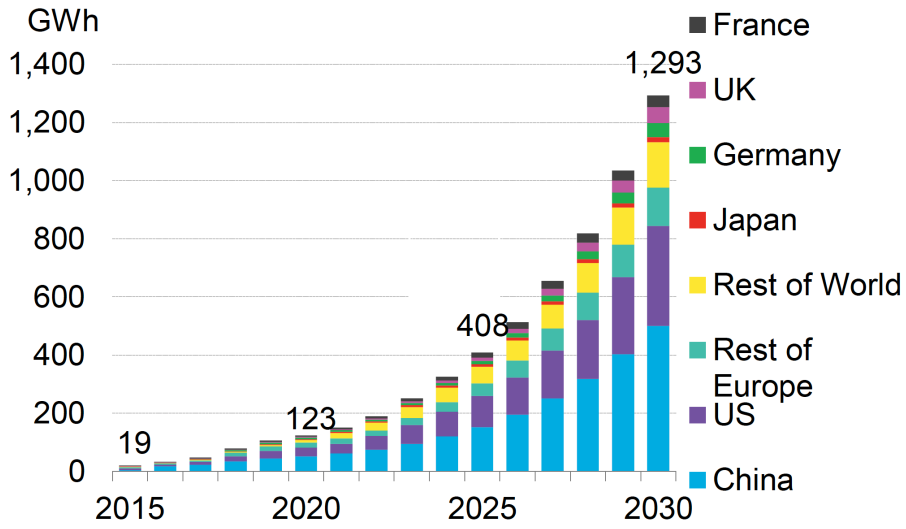

Figure 1.1 Forecasted demand for lithium ion batteries from EVs, 2010-30 (GWh) (Source: Bloomberg New Energy Finance).

Li-ion batteries have brought about tremendous revolution of sustainable transport that has transformed modern daily life due to their high energy and power densities, from maturity in portable electronic devices like laptops and mobile phones, to recent successful application in full electric vehicles (EVs) and hybrid electric vehicles (HEVs), to future electrification of Internet of Things (IoT) which extents conventional internet connectivity into smart microdevices such as sensors, wearable electronics and microelectromechanical systems (MEMSs).[5, 6] Bloomberg New Energy Finance forecasted tremendously increasing demand for lithium ion batteries for EVs in 2017 shown in **Figure 1.1**. By the year of 2030, the total demand for EV batteries is around 1300 GWh, from some 100 GWh in 2018. In addition, it is reported the global lithium ion battery market was valued at US$ 23 Billion in 2017 and is expected to grow at a CAGR of 15% during the forecast period 2018 – 2025, to account to US$ 71 Billion by 2025.[7] In fact, LIB is now almost an aggressively indispensable commodity from daily life to national safety defense. The key advantage of Li-ion batteries is their ability to store much more energy than other battery chemistries in terms of both gravimetric (Wh/kg) and volumetric energy density (Wh/L) indicated in **Figure 1.2.**[8, 9] Besides, a higher voltage output makes LIB better choice for many specialized applications than other secondary batteries.[9]

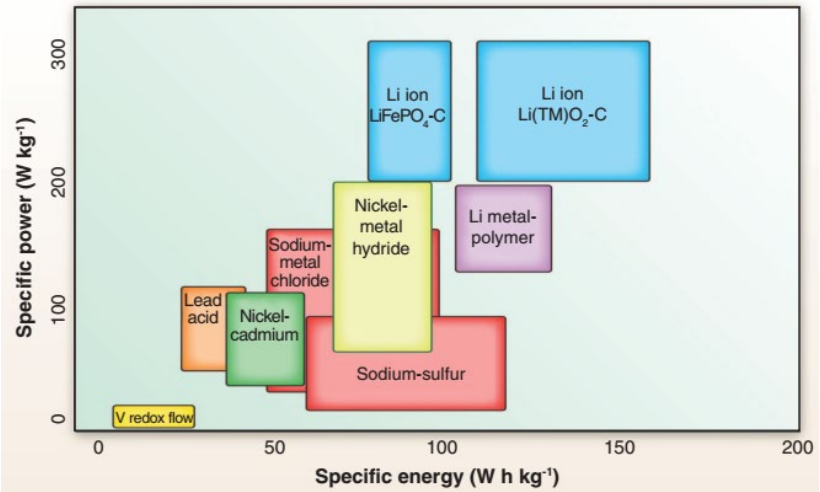

Figure 1.2 Gravimetric power and energy densities for different rechargeable batteries.[9]

Since its first commercialization by SONY in 1991, there have been continuous but slow improvements in LIB performance, such as in energy density, power density, cycling stability, safety and cycle life.[10] To mitigate the gap between the slow advancement and the urgent market demands for safer LIBs with much higher capacity, better rate capability and cyclability, it is necessary to examine issues and drawbacks of current LIBs especially addressing materials challenges while developing next generation LIBs. With dramatically reduced cost of present mature LIBs achieved by the buildup of many state-of-the-art battery factories like Tesla Gigafactory[8], the primary issue inhibiting the large-scale battery applications is the limited battery energy density. Although this can potentially be overcome through advanced battery technologies such as Li-metal solid state batteries and emerging new battery concepts and beyond Li-ion battery such as Li-O_2, Li-S, Na-ion, Mg-ion batteries, etc..[11-13], these approaches will still require major breakthroughs to become commercially viable.[14-16]

There are a number of opportunities for increasing energy density in conventional LIBs utilizing advanced cathodes. $LiCoO_2$ is so far the most successful cathode materials for the last

two decades. Other widely applied cathode materials include layered compounds $LiMO_2$ (M = Co, Ni, Mn, etc.), spinel compounds LiM_2O_4 (M = Mn, etc.), and olivine compounds $LiMPO_4$ (M = Fe, Mn, Ni, Co, etc.).[17] Higher energy density alternative include the high voltage binary $LiNi_{0.5}Mn_{1.5}O_4$, high nickel content ternary $LiNi_xMn_yCo_{1-x-y}O_2$ and $LiNi_xCo_yAl_{1-x-y}O_2$, and lithium-rich materials $Li[Li_xM_{1-x}]O_2$ and $xLi_2MnO_3 \cdot (1-x)LiMO_2$.[17, 18] Among them, $LiMn_2O_4$ (LMO) is a promising alternative that has been receiving intensive research interest, avoiding $LiCoO_2$ drawbacks of high cost, toxicity, structural instability, etc..[18, 19] However, one of the challenges concerning $LiMn_2O_4$ commercialization is fast capacity fading on cycling especially at elevated temperature.[20, 21] It is well established that interfacial chemistry primarily accounts for capacity fading, including manganese dissolution into electrolyte through a disproportionation reaction, detrimental electrolyte decomposition resulting formation of cathode electrolyte interphase (CEI), surface irreversible interphase transition, and cooperative Jahn-Teller distortion of LMO surface lattice structure.[22, 23]

To obtain more accurate observation of the complicated interfacial processes in $LiMn_2O_4$-based LIBs, researchers believe well-defined robust 2D interfaces with controlled nanostructure, morphology and chemical stability are required.[24, 25] In literature, precise and comprehensive characterizations were constrained due to complexity of LMO particle-based composite cathode. Particle shape, size, composite pack density and electrode components (solvent, binder and conductive additive) can significantly affect cell performance.[26, 27] Strategy of this thesis work was applying well-engineered LMO electrodes with a thin-film-based geometry which were more suitable for clarifying mechanisms of those aforementioned interfacial reactions. Unlike LMO particles, an LMO thin film can serve as a model cathode for fundamental studies of interfacial electrochemistry in LIBs, attributed to the following merits. First, thin film techniques such as

sputtering and pulsed laser deposition (PLD) provide rapid and effective routes to fabricate high-quality thin films (both LMO and ultrathin coatings) with desired properties such as thickness, surface morphology, uniformity and crystallinity.[28, 29] Second, much shortened Li^+ diffusion pathway in thin-film LMO facilitates unraveling surface coating mechanisms without influence from Li-ion transport kinetics in LMO. Besides, LMO thin films grown on conductive substrates such as Pt require no solvents, binders or additives for electrochemical tests, which reduces errors from sample variations and hence benefits precise characterizations. At last, a high quality thin-film geometry of LMO is ideally suited for interfacial studies by a range of advanced *in situ* and *ex situ* characterization tools such as synchrotron X-ray scattering and absorption spectroscopy, high-resolution scanning transmission electron microscopy (STEM), electron energy loss spectroscopy (EELS), X-ray photoelectron spectroscopy (XPS), atomic force microscopy (AFM), and etc..[30-33]

This thesis work contains two main aspects. First is to develop an improved understanding of performance degradation in LMO-based LIB cathodes, utilizing thin-film LMO-based batteries to probe electrode interfacial chemistry. The second aspect is to develop and study surface barrier layers as methods to improve LMO capacity retention, again using the thin film geometry in order to enable fundamental studies of interfacial phenomena. The thesis is organized as follows. A detailed literature review of LMO cathode material is covered in Chapter 2, followed by the experimental methods description in Chapter 3. The following four chapters cover four main topics and/or challenges that comprise the core of this thesis. Firstly, hetero-epitaxial LMO thin films as model cathodes are introduced to explore crystal structure evolution and LMO/electrolyte interface morphology change during cycling in Chapter 4. Secondly, investigations of the CEI layer on

LMO, and its role in capacity fade, is described in Chapter 5. Thirdly, the extremely high power density of thin-film LMO cathodes is explored and discussed in terms of LMO chemical kinetics and fast charge/discharge behaviors in Chapter 6. The effect on capacity retention of thin oxide barrier layers on thin-film LMO cathodes is finally studied using a variety of advanced characterization methods and discussed in Chapter 7.

Chapter 2: Background and Motivation

2.1 Lithium Ion Batteries

2.1.1 Principle and components

The genesis of rechargeable LIBs concept came from fundamental electrochemistry studies in 1970s by researchers like Thackeray and John Goodenough who first discovered layered and intercalation oxides for LIB cathode materials of good chemical stability and high voltage.[1, 34] The fact that Li is not only the most electropositive (–3.04 V vs. $H_2/2H^+$) but also the lightest element motivated the developing of LIBs, theoretically providing tremendously high specific capacity and energy density.[35] In 1991, Sony Corporation successfully commercialized the well-known $Li_xC_6/LiCoO_2$ Li-ion battery which had a typical rechargeable LIB structure of four basic components: graphite anode, lithium transition metal oxide cathode, micro-porous separator and Li^+ conducting organic electrolyte, as illustrated in **Figure 2.1**. This type of LIB with a high potential of ~3.7 V (3 times that of alkaline batteries) and gravimetric energy densities as high as 120–150 Wh/kg (2-3 times those of Ni–Cd batteries), is now found in most today's portable electronic devices.[35]

A LIB is also called a "rocking chair" battery because Li ion shuttles between anode and cathode through the electrolyte during charge and discharge processes. Take $Li_xC_6/LiPF_6$-EC&DMC/$LixCoO_2$ battery (configuration shown in **Figure 2.1**) for example, the redox process is as follows. The green battery is usually assembled in the discharge state, that is the cathode is $LiCoO_2$ and anode is just empty graphite. During charging, Li ions are extracted from the cathode host, migrate through the electrolyte and intercalate into graphite anode while electrons are generated from cathode and circulate through the external circuit to anode. In this process, the

$LiCoO_2$ cathode is oxidized losing x electrons becoming $Li_{1-x}CoO_2$ and the anode is reduced capturing x electrons forming Li_xC_6 and vice versa for the discharge process.[35]

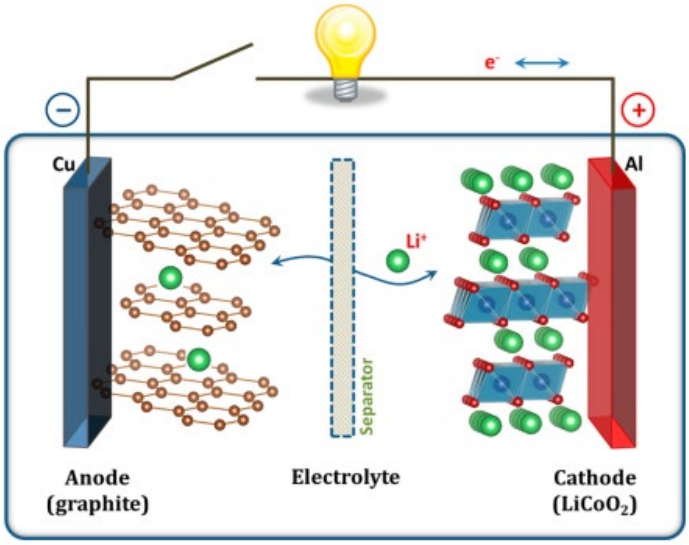

Figure 2.1 Schematic illustration of a typical commercialized LIBs (graphite/Li+ electrolyte/LiCoO2).[1]

The development of LIBs is heavily dependent on engineering advanced materials of both electrodes and electrolyte. In the battery community, there is an extensive agreement that safety issue concerning LIBs using flammable nonaqueous liquid electrolytes should be seriously addressed before massive automotive application of current LIBs.[11, 36] In solid state chemistry, a thermodynamically stable battery requires the chemical potentials of anode and cathode are within the chemical potential window of electrolyte. **Figure 2.2a** schematically illustrates relative chemical potential diagram in a typical LIB. The energy gap E_g of the lowest unoccupied molecular orbital (LUMO) and the highest occupied molecular orbital (HOMO) is the potential "window" of a liquid electrolyte. For solid electrolyte, E_g is between the bottom of the conduction band and top of the valence band of the electrolyte.[1] If the electrochemical potential $\mu_a(Li)$ of an

anode is above the LUMO, the electrolyte will be reduced unless an electron passivation solid-electrolyte interphase layer (SEI) is formed to prevent the reduction reaction; Similarly, if $\mu_c(Li)$ is below the HOMO, the electrolyte will be oxidized unless a passivation cathode-electrolyte interphase (CEI) layer blocks electron transfer at the interface.[37] Therefore, a thermodynamically stable LIB requires the electrode electrochemical potentials $\mu_a(Li)$ and $\mu_c(Li)$ are constrained within the potential window of the electrolyte. That is, the open circuit voltage of a LIB:

$$O_{CV} = \frac{\mu_a(Li) - \mu_c(Li)}{e} \leq E_g \tag{2.1}$$

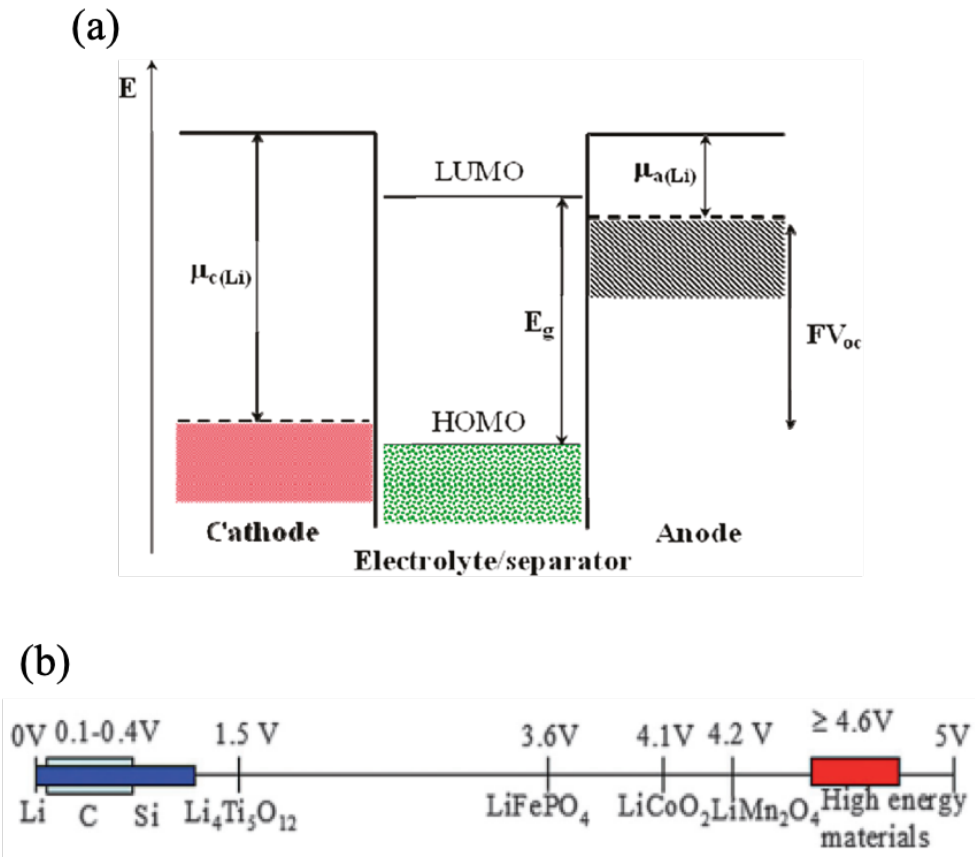

Figure 2.2 (a) Schematic energy diagram of a LIB at open circuit. μ_a(Li) and μ_c(Li) are the lithium chemical potential in the anode and cathode, respectively. E_g is the chemical potential window of the electrolyte.[37] (b) Relative working potential of several typical materials for LIBs.[18]

To date, graphite is the most widely-used anode material over the past decades. Graphite has low electrochemical potential (slightly above Li/Li^+ to avoid dendrite formation), good rate capability, low volume expansion during lithiation, high coulombic efficiency (CE), good electronic conductivity and is totally based on carbon which is inexpensive and abundant.[18] The stable layered structure of graphite facilitates lithium ion lithiation/delithiation process. But graphite anode is limited by its relatively small practical specific capacity (around 350 mAh/g, one Li-ion per six carbon atoms with a stoichiometry of LiC_6). Lithium metal as anode theoretically provides extremely large theoretical specific capacity (around 3860 mAh/g), which however suffers from severe safety issue caused by lithium dendrite or inhomogeneous lithium plating.[35] For current liquid organic electrolyte, such as the conventional electrolyte 1M LiPF6 in EC:DMC (1:1), the potential window E_g is about 1.3V – 4.7V vs. Li/Li^+.[38] Both graphite and lithium metal anodes are out of the electrolyte electrochemical potential window, resulting formation of a SEI layer which further reduces anode capacity.[34] Alloy anodes are another promising option due to their high specific capacity ranging from 783mAh/g for SnO_2 up to 4211mAh/g for silicon.[39] However, large volume expansion and structural instability are critical challenges for those materials.[39] Titanium-based materials are alternative anode materials to graphite because of small volume change, excellent cycling life and high working potential (above 1 V vs. Li/Li^+, typical example of $Li_4Ti_5O_{12}$ in **Figure 2.2b**) which mitigates SEI and dendrite safety issues.[40] Those materials, however, are restricted to low capacity (less than 330mAh/g) and electronic conductivity.[39] A potential-capacity diagram of current anode and cathode materials is summarized in **Figure 2.3**.[35]

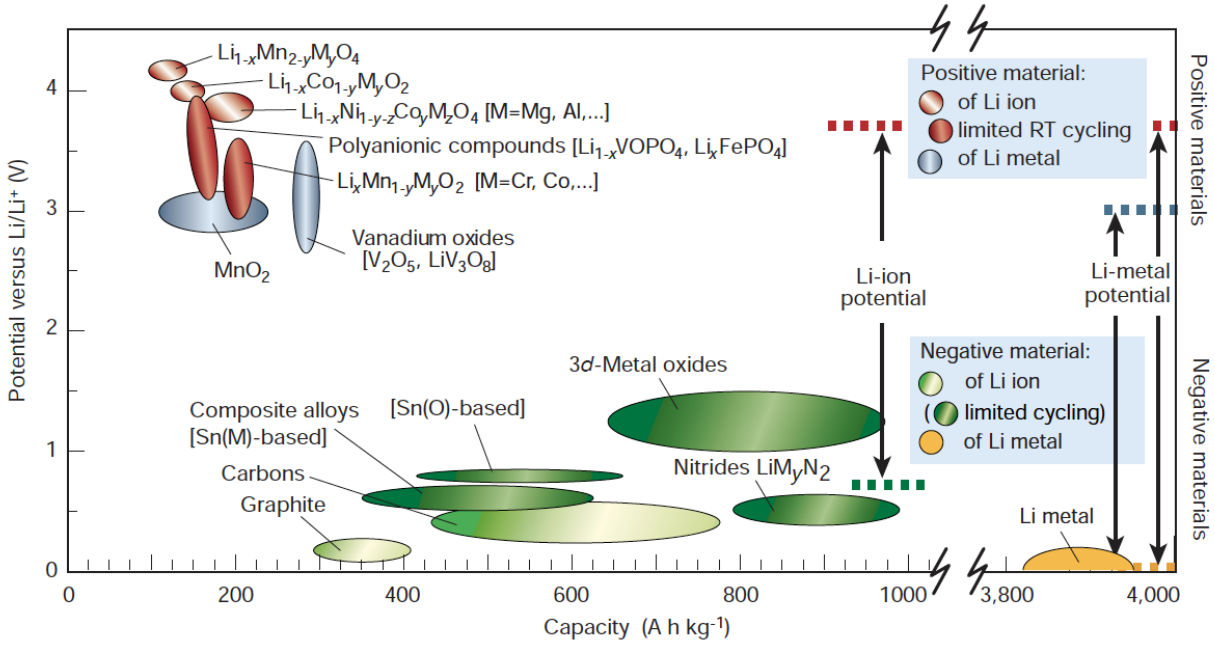

Figure 2.3 Voltage versus capacity for anode and cathode materials presently used or under development for the next generation of lithium batteries.[35]

In current design of LIBs, the cell voltage and capacity are mainly determined by the cathode materials. Therefore, developing advanced cathode materials of high capacity, rate capability and chemical stability, and long cycling life has become extremely important. Toward that end, massive amounts of efforts have been making by both industry and academia communities over recent decades.[39] In a traditional LIB cell, the high voltage arises from usage of intercalation reaction chemistry between the most electropositive lithium ion and the cathode of host materials. The conventional cathode materials which are primarily transition metal oxides can be categorized by intercalation structure into three types: layered compounds $LiMO_2$ (M = Co, Ni, Mn, etc.), spinel compounds LiM_2O_4 (M = Mn, etc.), and olivine compounds $LiMPO_4$ (M = Fe, Mn, Ni, Co, etc.).[41] Crystalline structures of those three kinds of compounds are illustrated in **Figure 2.4**. New intercalation materials such as silicates Li_2MSiO_4, tavorites $LiMPO_4F$ and borates

$LiMBO_3$, hybrid materials such as Li_5FeO_4, Li_6CoO4, and lithium-rich materials $Li[Li_xM_{1-x}]O_2$ and $xLi_2MnO_3 \cdot (1-x)LiMO_2$ also attract increasing research interests in recent years.[17, 19, 34] Recently, emerging developments of advanced cathodes of high energy density focus on high voltage binary $LiNi_{0.5}Mn_{1.5}O_4$, high nickel content ternary $LiNi_xMn_yCo_{1-x-y}O_2$ and $LiNi_xCo_yAl_{1-x-y}O_2$, and lithium-rich materials $Li[Li_xM_{1-x}]O_2$ and $xLi_2MnO_3 \cdot (1-x)LiMO_2$.[17, 18] Furthermore, anion and cation substitutions from the above intercalation materials are becoming a fashion on tuning chemical stability and rate capacity of the origin host materials.[42]

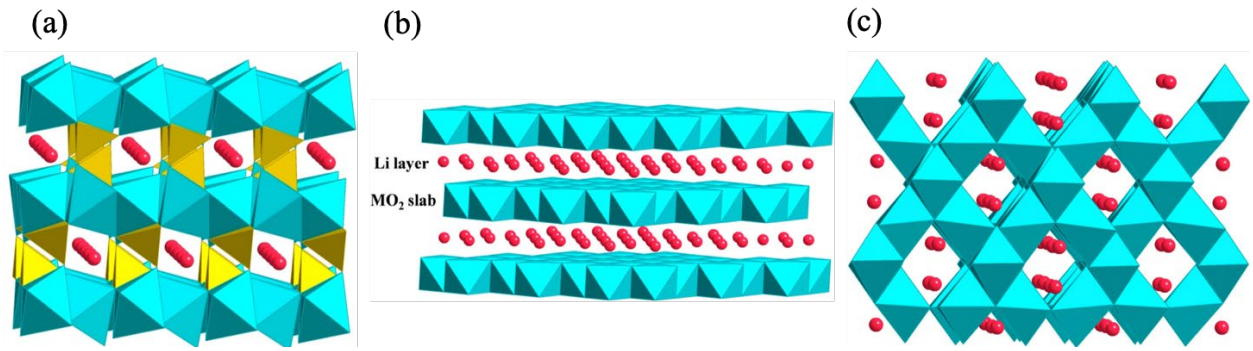

Figure 2.4 Crystal structures of 1D-type (a), 2D-type (b) and 3D-type (c) cathode materials.[17]

In summary, there are key requirements for a potential cathode material to be successfully used in LIBs, such as: 1) The material should contain a readily reducible/oxidizable ion such as transition metal; 2) The material should be able to react with lithium in a reversible manner; 3) The redox electrochemical reactions of the material occur at high voltage and with high free energy, which guarantees relatively high energy density and capacity; 4) The material should rapidly react with lithium demonstrating high power density. High power density of a cathode material accompany with fast charge/discharge capability is an especially essential factor for successful applications in EVs; 5) The material should be both thermodynamically and (electro)chemically stable upon abuse conditions; 6) The materials should be low cost and

environmentally benign.[43] There is always tradeoffs when choosing proper cathode materials with maximized satisfaction of key requirements aforementioned. Therefore, it is still far premature to decide the best cathode material for LIBs at present. In this thesis work, spinel-type $LiMn_2O_4$ is studied as cathode host materials due to its appealing advantages of low cost, no toxicity, good structural and chemical stability, and high rate capability compared to the conventional cathode materials such as $LiCoO_2$ and $LiFePO_4$.[42]

In a full LIB, current collectors are required to bridge external circuit with electrodes for electrochemical tests. Aluminum foil which is resistant to an oxidizing potential is used as the current collector at cathode side, while copper foil serves as anode current collector because it does not react with lithium ion at low potential.[44] To increase electron conductivity of the cathode, conductive additive such as carbon black is usually added with a binder such as polyvinylidene fluoride (PVDF) to physically hold the active materials and conductive additive together. A micro-porous thin film of Li^+ ions conducting polymer sheet (polyethylene or polypropylene) is usually used as the separator which allows electrolyte to penetrate and prevents internal short circuit and thus keeps the batteries safe under high temperature condition due to a high thermal stability.[45]

2.1.2 $LiMn_2O_4$ cathode and interfacial chemistry in LIBs

Lithium manganese oxide $LiMn_2O_4$ (LMO) is one of the most promising cathode materials with advantages of high abundance, low cost, no toxicity, good structural and chemical stability, proper Mn^{3+}/Mn^{4+} redox potential (4.1 V vs. Li/Li^+), and relatively higher rate capability compared to the conventional cathode material $LiCoO_2$ and $LiFePO_4$.[19] LMO obtains a cubic spinel crystal structure (general formula $A[B_2]O_4$) with lattice constant of a = 8.248Å and space group of $Fd\bar{3}m$.[1] The cubic close-packed array of oxygen (32e) accommodates Li and Mn^{3+}/Mn^{4+} cations at one eighth of tetrahedral (8a) and half of octahedral (16d) sites, respectively (shown in **Figure 2.5**a).[46]

Unlike layered materials, it is well known this cathode material remains a highly bonded $[B_2]O_4$ framework of spinel structure during lithiation and delithiation within proper voltage range.[47, 48] The interstitial space which can be treated as a three-dimensional network of face-sharing tetrahedral (8a) and empty octahedral (16c) sites in $[Mn_2]O_4$ framework offers 3D pathway for lithium ions reversibly transport within the host structure (**Figure 2.5**b).[49, 50]

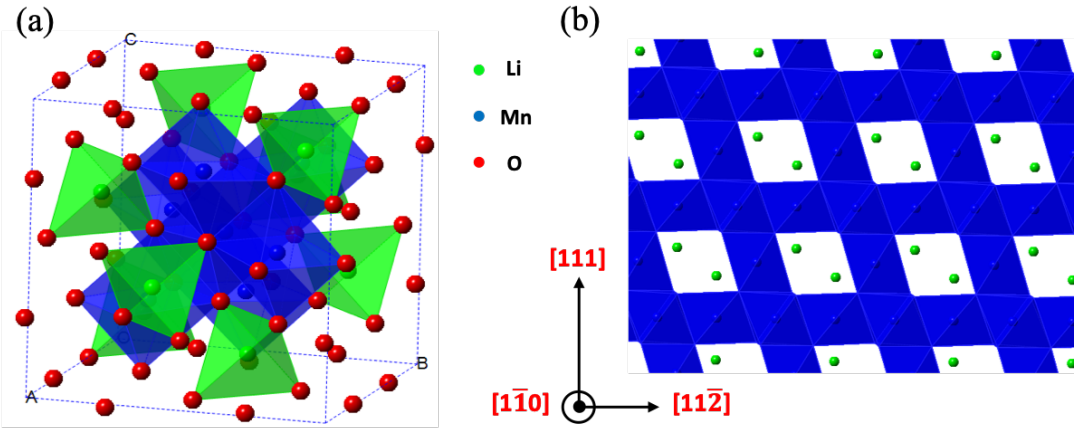

Figure 2.5 (a) Crystal structure of spinel $LiMn_2O_4$ with Li (green) occupying tetrahedral sites (8a) and Mn (blue) occupying octahedral sites (16d); (b) (110) lattice plane of the $[Mn_2]O_4$ framework consisting of MnO_6 octahedra with separate Li, O and Mn columns forming a diamond configuration.

In intercalation lithium ion batteries, both surface and interface chemistry and electrochemistry play key roles in determining rate capacity and cycling reversibility.[32] The interface kinetics includes electron transport between current collectors and electrodes, lithium ion intercalation and extraction at the interface between the electrolyte and electrodes, and lithium ion diffusion within the electrode materials.[51] Among those processes, interfacial resistance of lithium ion (de)intercalation mainly due to complex electrode surface morphology, interphase formation, surface structure distortion, space charge effect and grain boundary is believed by the majority to be a great emerging challenge, especially for the state-of-the-art all-solid-state LIBs.[52] Massive

efforts are dedicated to developing understanding of interfacial lithium ion transport impedance at both solid-liquid and solid-solid interfaces in the forms of bulk or thin film, polycrystal or single crystal.[53, 54] Another critical obstacle concerning $LiMn_2O_4$ commercialization is fast capacity fading (or poor cyclability) on cycling especially at elevated temperature.[55] It is well established interfacial (electro)chemistry accounts for capacity fading, which is directly associated with Mn^{3+} dissolution into electrolyte through a disproportionation reaction and hence manganese deposition onto anode[23], detrimental electrolyte decomposition resulting formation of solid electrolyte interface (SEI) layer[56], irreversible interphase transition[57], loss of crystallinity over long time cycling[58], and cooperative Jahn-Teller distortion of $Mn^{3+}O_6$ octahedra (high spin $3d^4$, $t_{2g}^3e_g^1$) at deep discharge state[21, 59]. Among them, manganese dissolution is considered to be a vital factor leading to LMO capacity fade since Mn dissolution not only results in direct loss of active cathode materials, but also increases cell resistances associated with manganese ions dissolution, migration and deposition (DMD) processes.[26, 60, 61] Those phenomena involve complicated interfacial reaction mechanisms which lead to extensive researches concentrated in understanding LMO capacity fading mechanisms and developing corresponding mitigative methods, facilitated by advancement of modern characterization tools such as X-ray photoelectron spectroscopy (XPS), in-situ synchrotron X-ray scattering and absorption spectroscopy, atomic force microscopy (AFM), high resolution scanning transmission electron microscopy (STEM), etc..[23, 24, 31, 33, 59]

2.2 Current Status, Challenges and Motivations of $LiMn_2O_4$ Cathodes

Focus and challenges of tons of researches on LMO cathode material is mainly on developing fundamental understanding of capacity fading mechanisms and engineering mitigation methods to improve LMO capacity retention over long time and high current rate cycling.[60] This

subchapter (section 2.2) summarizes current status of LMO researches including four research topics and/or challenges which are also core contributions of this thesis work, in an attempt to address the aforementioned challenges concerning LMO cathode.

2.2.1 Electrochemistry on unique $LiMn_2O_4$ lattice planes

Although LMO is a 3D-type cathode material with isotropic 3D channels for lithium ion migration during intercalation/deintercalation reactions, it has been found (electro)chemical reactions at LMO/liquid electrolyte interface involving Mn dissolution, CEI layer formation, interphase formation, LMO surface morphology and crystalline structure distortion, etc. are highly associated with various LMO lattice planes attached to the liquid electrolyte.[62-65] Various LMO particle shapes with various exposed crystalline planes (illustrated in **Figure 2.6**) and corresponding plane area ratios primarily determine Mn dissolution reaction rate.[5966] Research has shown that new phases (like Mn_3O_4, $LiMnO_2$, $Li_2Mn_2O_4$, etc.) irreversibly formed at LMO surface accounts for alternative capacity loss (Mn loss) apart from Mn dissolution by disproportionation reaction.[67, 68] **Figure 2.7** illustrates that due to those series of LMO interfacial (electro)electrochemical reactions including Mn dissolution, electrolyte oxidation and interphase formation, CEI layer morphology and thickness vary on different LMO lattice planes attached to the electrolyte. Besides, recent study suggests Mn dissolution is largely dependent on the lattice orientation of the LMO surface attached to the electrolyte and {110} surface aligned to Li diffusion channels are most vulnerable to Mn dissolution.[62, 65] Kim et al. concluded that LMO (111) surface with Li-rich layer is more resistant to Mn dissolution by DFT calculations.[63, 64] Under synthesis conditions that favor stability of undoped LMO powder, the thermodynamic equilibrium shape of the LMO particle is predicted to be a truncated octahedron with very similar surface energies of (001) to (111) planes. Higher Li chemical potentials and temperatures drastically favor formation

of LMO particles dominated by (001) lattice planes (shown in **Figure 2.8)**.[59] Therefore, they suggest excess lithium environment and too high synthesis temperature should be avoided to obtain high Mn dissolution resistant LMO particles.

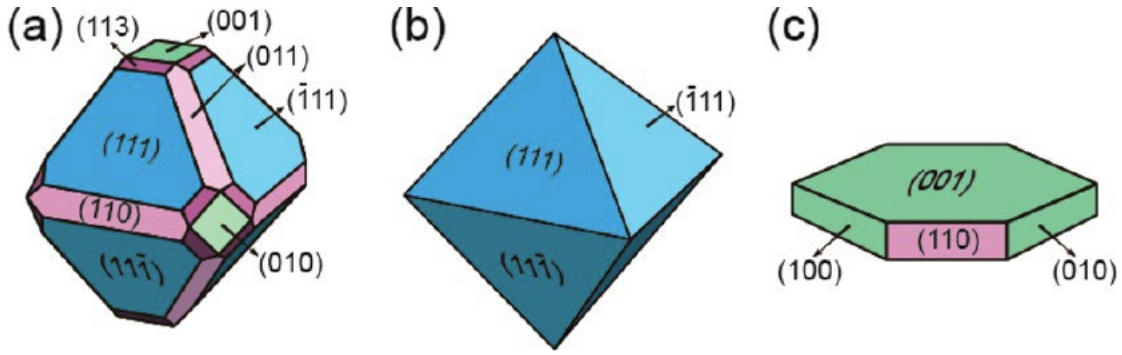

Figure 2.6 Schematic illustration of LiMn2O4 with various crystal shapes. (a) Truncated octahedron (OhT). (b) Bare octahedron (Oh). (c) platelet (PL). The surfaces with equivalent crystal orientations are presented in the same colors.[65]

To explore and verify those DFT calculation results summarized above, a model epitaxial LMO thin film on an electrically conductive buffer layer and holding a well-controlled lattice stack orientation with atomically flat surface is desired to examine Mn dissolution and surface crystalline structure and morphology evolution during reversible cycling via both in situ and ex situ methods such as synchrotron X-ray scattering, high resolution STEM, etc..[24, 59, 69-72] Chapter 4 covers this research topic by fabrication and atomic structure observation of a hetero-epitaxial LMO/LSCO/STO bilayer which was further assembled into a "transmission cell" for operando synchrotron X-ray scattering study of crystalline structure and LMO/electrolyte morphology change upon cycling.

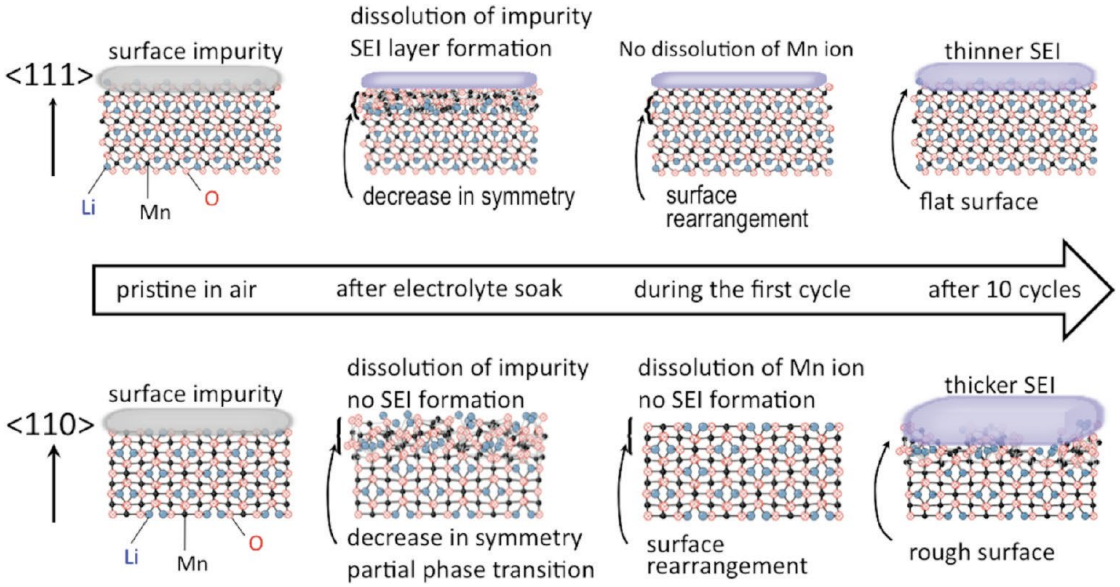

Figure 2.7 Schematic of surface reactions for (111) and (110) crystal planes of $LiMn_2O_4$ characterized by in situ XRD and XRR measurements and ex situ TEM observations.[62]

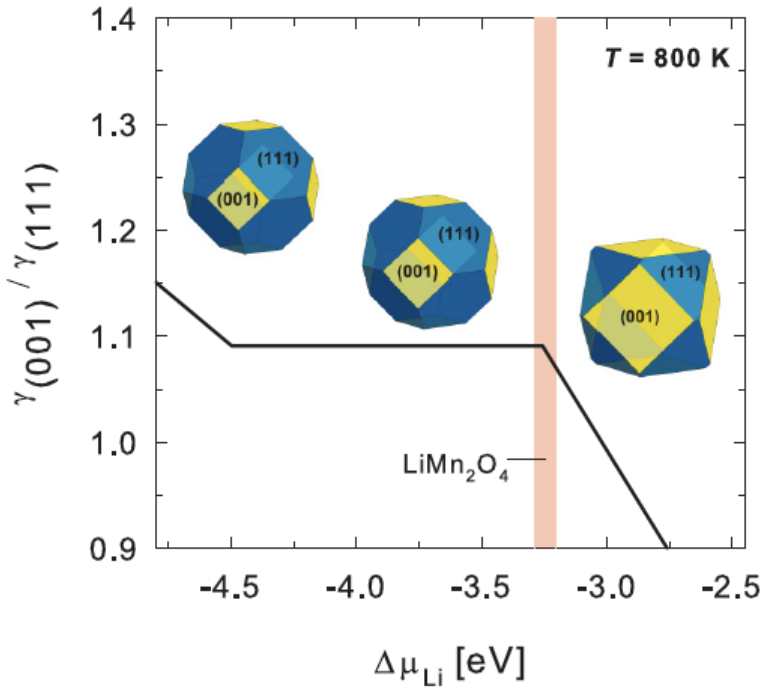

Figure 2.8 (Color online) The (001) to (111) surface energy ratio and the corresponding representative LMO particle shapes as a function of Li chemical potential at an oxygen chemical potential corresponding to T = 800Kand pO_2 of 0.2 atm. Shaded region shows the stability range of bulk LMO.[64]

2.2.2 Revisit cathode electrolyte interphase (CEI) on $LiMn_2O_4$ thin film surface

It is well known in battery community that electrically nonconductive solid electrolyte interphase (SEI) on graphite anode plays critical role in preventing continuous liquid electrolyte reductive decomposition while resulting in direct loss of lithium and hence capacity by formation of lithium salts in gradually growing SEI on the anode surface.[23, 73-75] The electrolyte decomposition reactions occur due to higher reduction potential of the electrolyte than chemical potential of anode materials.[18] Similarly, a passivation interphase layer or so-called cathode electrolyte interphase (CEI) is usually formed on cathode surface due to oxidative decomposition of the electrolyte solvent (such as ethylene carbonate (EC), dimethyl carbonate (DMC), ethyl methyl carbonate (EMC), etc.) and side reactions of cathode materials surface.[76, 77] However, there is much less known about the nature of CEI layer, such as chemical compositions, formation mechanisms, functionalities, etc., properties of which vary with cathode surface, state of charge, temperature and electrolyte compositions, etc..[77] It has been point out there are differences between SEI and CEI formation reactions.[23, 78] Apart from electrolyte decomposition on cathode surface similar to SEI formation, CEI formation processes involve cathode materials reaction with electrolyte, such as Mn dissolution and surface interphase formation reactions of LMO cathode.[60] **Figure 2.9**a illustrates Mn dissolution reactions on LMO cathode surface, associated solvent-derived HF acid formation due to salt $LiPF_6$ dissociation with present of water.[78, 79] As for chemical compositions, photoelectron spectroscopy (PES) with conventional or synchrotron X-ray radiation or neutron radiation sources coupled with depth profiling capability haven been widely used to examine and identify species contents in CEI layer.[76, 78, 80, 81] A typical example using XPS to characterize chemical compositions of both SEI and CEI is summarized in **Figure 2.9**b and c.[70]

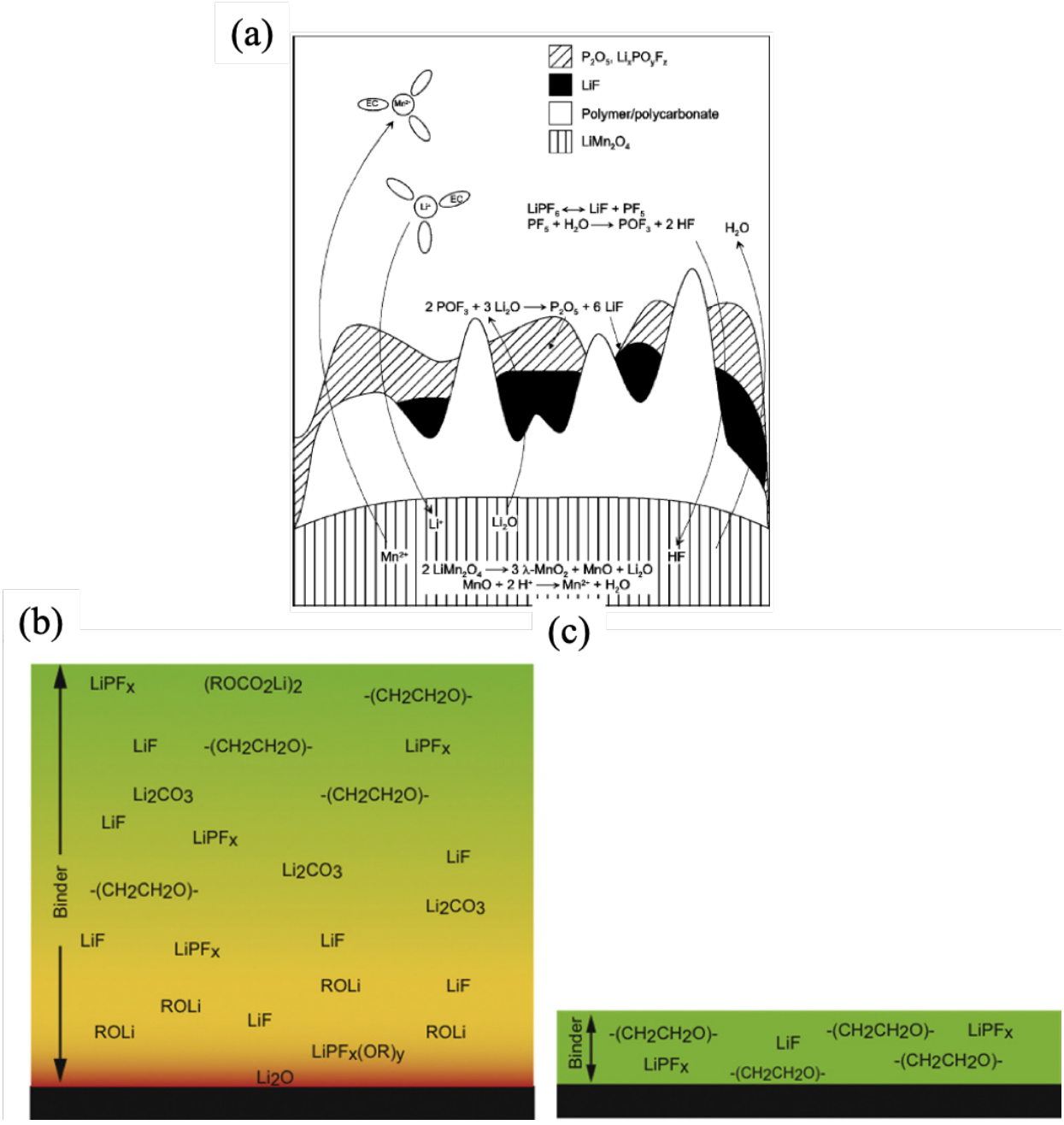

Figure 2.9 (a) A proposed model for the solid permeable interface surface layer formed on a $LiMn_2O_4$ electrode.[78] Schematic pictures of (b) the SEI on a lithiated graphite anode and (c) the CEI on a carbon coated delithiated lithium iron phosphate cathode, as seen in PES measurements.[76]

As elucidated in Chapter 2.1.2, one critical challenge of LMO cathode is severe capacity loss or poor cycalability upon cycling especailly at elevated temperature. Conventional widson

being that electrode-electrolyte interfacial (electro)chemistry, including so called manganess dissluiton, accounts for degradation of LMO.[60, 82] Since manganese dissolution reactions are directly associated with CEI layer formation on LMO cathode surface, it is enssential and necessary to develop deep understanding of CEI layer in order to illustrate LMO cathode capacity fading mechanisms. To that end, chaper 5 covers another topic of this thesis work in an attmept to revist and characterize chemical composition distrubutions in CEI layer on LMO thin film cathode.

2.2.3 Engineering of high power density $LiMn_2O_4$ thin film cathodes

Nowadays, there has been a rapidly increasing trend to pursuit the future of Internet of Things (IoT) which extents conventional internet connectivity into smart physical microdevices, such as sensors, wearable electronics, remote monitors, and microelectromechanical systems (MEMSs).[6] However, crucial challenges especially developing high power density sources at millimeter scale lay ahead of fabricating next generation embedded microelectronics of IoT.[83, 84] Lithium ion battery (LIB) is maturely developed power storage technology and has been applied in some microelectronics. However, microstructures of conventional bulk electrode materials impose restrictions on high rate capability.[85, 86] Downscaling the electrode materials has been intensively studied by synthesis of nanostructured particles with a variety of shapes, morphologies, crystallinities and porosities in efforts to shorten Li^+ and electron migration channels and hence improve high rate capability.[85, 87-93]

Thin films share similar characteristic length scale to nano particles and hence nanoscale effects are supposed to reveal.[85, 94] Therefore, all solid state thin-film batteries are believed to be promising candidates with readily higher power density than bulk lithium ion batteries (LIBs) due to much shortened Li^+ diffusion distance.[28, 29, 89, 95] Actually, according to the roadmap of LIB

development in **Figure 2.10**a, the trend in next decade moves forward to solid state LIBs which are believed to be safer and delivery higher energy density and power density. All solid state thin film batteries especially received numerous interests. Choice of cathode materials largely determines achievable power density of a LIB. Typical cathode materials for LIBs, such as $LiFePO_4$, $LiCoO_2$, $LiNi_xMn_yCo_{1-x-y}O_2$ and $LiMn_2O_4$, are categorized to be classical intercalation-type materials which suffer from kinetic issues of constrained solid-state diffusion of lithium ions during intercalation reactions.[96-98] As a result, most of current LIBs allow only up to moderate charging/discharging current rates. Still and all, lithium manganese oxide $LiMn_2O_4$ (LMO) has been received wide-spread interests due to its intrinsic characteristic of 3D Li+ diffusion pathways obtaining relatively higher rate capability than the others.[1, 5, 19, 26]

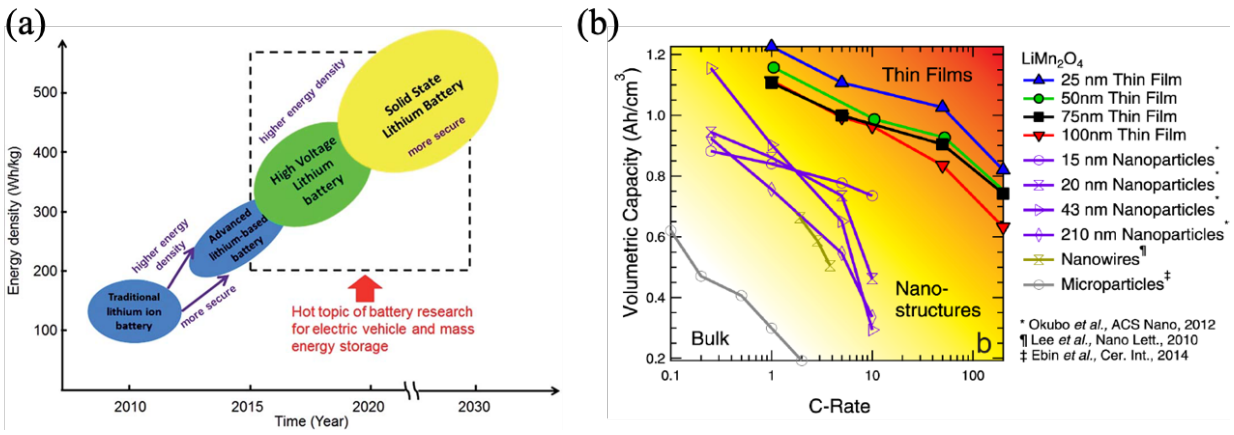

Figure 2.10 (a) Roadmap for the development of Li-based batteries.[99] (b) Volumetric (lithiation) capacity vs C-rate for LMO thin films with different thickness. All films show excellent rate performance retaining over 80% of their 1 C capacity while charging in 1.2 min (50 C).[89]

Since conventional bulk LMO cathodes consisting of microsized particles are unlikely to be charged/discharged at high rate due to poor electron conduction and long lithium ion diffusion pathways within both single microsized LMO particle and the cathode composite bulk pack, considerable efforts have been made to develop high power density LMO thin film cathodes.[27, 29,

[85, 89] For example, Put et al. explored high rate stability of LMO thin films cycled at various current rates within extended voltage window of 2 – 4.3 V.[89] They demonstrated superiorly high rate capability of LMO thin film cathodes comparing to nanosized and microsized LMO particle composite electrodes as shown in **Figure 2.10**b. Fehse et al. applied LMO thin film electrodes into pseudocapactive microbatteries achieving ultrafast dischargeable capability.[29] In addition, LMO thin films have been widely applied to study critical interfacial (electro)chemical issues in LMO-based LIBs, such as surface coating effects[57], manganese dissolution reactions and cathode electrolyte interphase (CEI) formation[57, 82], due to superior merits of LMO electrodes with thin-film geometry which obtain well-controlled reaction area, surface morpholgy and crystalline structure, and avoid complexities presented in bulk-type composite electrode such as additives, binders and solvents.[26, 27, 82, 100] Experimentally, both polycrystalline and epitaxial LMO thin films have been successfully fabricated using a variety of deposition techniques including pulsed laser deposition (PLD), radio-frequency (r.f.) magnetron sputtering, atomic layer deposition (ALD) and chemical solution deposition (CSD).[62, 69, 70, 101-104] Among those techniques, magnetron sputtering is widely adopted for multilayer depositions of metal and oxide thin films.[29, 100] To ensure high rate cycling of LMO electrodes, a well constructued current collecting back contact system is required. It is common to direct use electrically conductive substrates such as stainless steel (SS) and Pt foil as current collectors while another choice is to engineer a stack of successive thin film layers including barrier layer (Al_2O_3, SiO_2), adhesion layer (Ti, TiN) and conductive buffer layer (Pt, Au, ITO) on top of insulating substrates (Si, Al_2O_3, YSZ).[29, 100, 10557, 64]

In chapter 6, we report on fabrication of well-architected LMO thin-film-based cathode consisting of a multilayer stack LMO/Pt/Ti/Al_2O_3 substrate back screen printed with Au paste using magnetron sputtering. The prepared LMO thin film cathodes with various thickness were

electrochemically cycled at a series of current rates to explore their cycling stability and high rate capability. Chemical kinetics of those thin film cathodes are reported using both galvanostatic intermittent titration technique (GITT) and electrochemical impedance spectroscopy (EIS). Phase separation and stabilities of redox reactions at two potential plateaus of LMO cathodes were explored. At last, analysis of cell impedances during cycling was conducted via EIS measurement and fitting.

2.2.4 Surface modification of $LiMn_2O_4$ thin film cathode

Manganese dissolution has been considered to be a crucial chain-reaction factor leading to the capacity fade since increase of cell resistances on both electrodes and formations of SEI and CEI layers are inevitably associated with manganese ions dissolution, migration and re-deposition (DMD) processes.[21, 26, 60, 61] It's generally believed that principal causes of manganese dissolution are Mn^{3+} disproportionation reaction due to attack of HF acid at the interface between LMO and electrolyte[26, 61, 106, 107], irreversible loss of MnO to form more stable surface single-phase structures due to instability of the spinel LMO two-phase structure at high voltage[60, 61, 67, 106], and ready existence of Mn^{2+} prone to be dissolved at certain truncated LMO surfaces.[60, 63-65, 108-110] It has been always difficult to determine which single mechanism above remarkably dominants manganese dissolution reactions over the whole cycling life of LMO cathodes.[60]

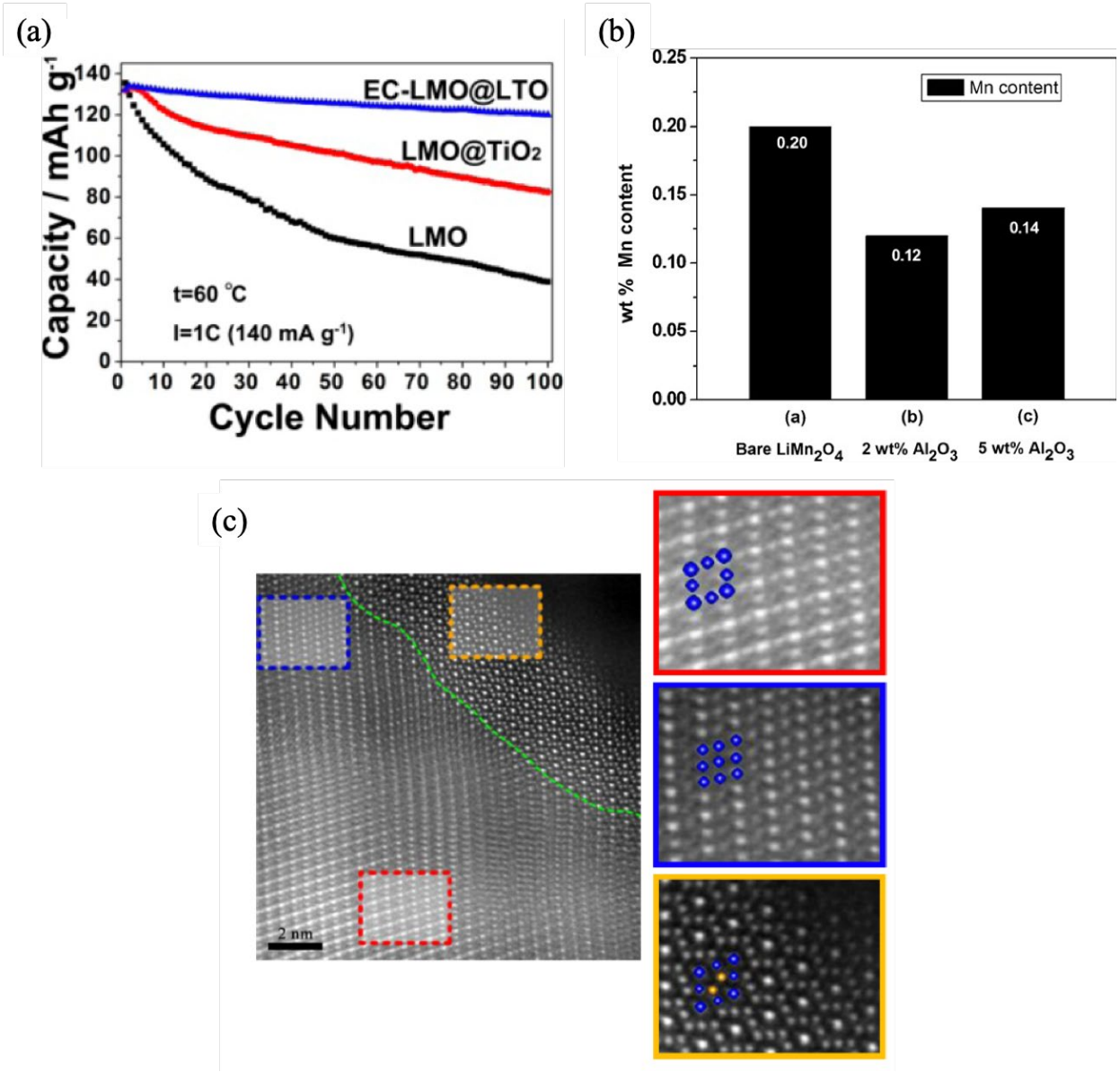

Figure 2.11 (a) Specific capacity of LMO cathodes w/o coatings of LTO or TiO_2.[111] (b) Contents of dissolved manganese of LMO cathodes w/o surface ALD coating Al_2O_3 after cycling.[112] (c) HAADF images taken along the [110] zone axis of the LMO spinel cathode charged to 4.3 V. Magnified views of selected regions are shown in the right panels, where the contrast corresponding to the Mn columns at 16d and 8a sites is indicated by blue and orange spheres, respectively. The boundary between the bulk and the surface regions is marked by the green dashed line.[68]

Successful prevention strategies such as cationic and anionic doping[106, 113-116], surface coating[21, 57, 117-119], morphology tailoring[65, 108], and use of electrolyte additives treatments[120-122],

have been applied to mitigate Mn dissolution. Among them, surface coating is treated as one of the most effective and economical approach without large sacrifice of LMO initial capacity, an inferior drawback of metal element doping.[57, 60] A variety of metal oxides such as Al_2O_3, ZnO, ZrO_2, TiO_2, Y_2O_3, $LiAlO_2$, $LiCoO_2$ have been coated on LMO particles to suppress Mn dissolution.[21, 118, 119, 123-125] **Figure 2.11**a demonstrates an example of using surface coating to remarkably improve LMO capacity retention while dissolved Mn contents were measured after cycling of LMO cathode with and without coating (shown in **Figure 2.11**b), indicating surface coating layer successfully alleviated Mn dissolution. Although LMO cathode capacity retention has been improved, there is yet not much detail on the fundamental mechanisms of manganese dissolution and how coating layers inhibit those aforementioned Mn ion-involved (electro)chemical reactions. For instance, there has been a controversy surrounded oxidation state of the dissolved manganese ions and those in the deposited manganese species on anode and cathode SEI (CEI) layers.[126-129] It is reported new interphases can be formed on LMO surface once charged to a high voltage shown in **Figure 2.11**c. It has been not clarified if surface coatings help to stabilize surface crystalline structure of LMO cathode during cycling. Besides, the suppression effects of coating layers can vary significantly with coating materials choice, coating layer thickness and coating routes.[21, 57, 118, 119] It is becoming great challenge to architect and further examine effective candidate coatings due to the complicated interfacial reactions among the coating layer, LMO electrode and electrolyte.[117, 130] With an aim to develop basic understanding of the manganese dissolution and address the crucial issues above, following criteria of a promising LMO coating layer should be stressed: 1) thin and uniform to cover entire LMO surface; 2) electrochemically stable on cycling and not react with LMO; 3) retain enough Li-ion conductivity; 4) rapid route to fabricate LMO cathode covered with various coatings.[118]

So far, LMO particles have been mostly used for coating study in literature.[21, 57, 117-119, 130] However, precise characterization is constrained due to complexity of LMO particle-based composite cathode. Particle shape, size, composite pack density and electrode components (solvent, binder and conductive additive) can significantly affect cell performance apart from coating layer.[26, 27] Unlike LMO particles, LMO thin films can serve as a more appropriate model cathode to comprehensively study manganese dissolution and coating effects in LIBs, due to superior merits of LMO electrodes with thin-film geometry which obtain well-controlled reaction area, surface morpholgy and crystalline structure, and avoid complexities presented in bulk-type composite electrode such as additives, binders and solvents.[26, 27, 82, 100] To develop fundamental understanding of surface coating effects, advanced characterization at the molecular level is highly desired for precisely examining the interfacial reaction processes in LIBs.[30]

In chapter 7, the perovskite oxide LSCO was chosen as a coating material due to its high electrical conductivity at room temperature and good electrochemical stability.[131, 132] Taking into consideration thickness and crystallinity of coatings, the promoted surface modification effects of LSCO on LMO thin film cathodes with a specific address of suppressing manganese dissolution processes were comprehensively examined via a series of electrochemical tests and various advanced characterization methods such as XPS, high-resolution STEM, EELS, EIS, etc.

Chapter 3: Experimental Methods and Instrumentation

3.1 Thin Film Deposition Technologies

As described in section 2.2.1, primary modern thin film deposition techniques includes pulsed laser deposition (PLD), chemical vapor deposition (CVD), thermal evaporation, radio-frequency (r.f.) magnetron sputtering, molecular beam epitaxy (MBE), atomic layer deposition (ALD) and chemical solution deposition (CSD). Herein, we use PLD to fabricate LMO thin films and magnetron sputtering to deposit current collecting layers and surface coating layers. In situ synchrotron X-Ray diffraction, thin film XRD and XRR, AFM, SEM, high resolution STEM, EELS and XPS are used to examine epitaxial properties of the thin films. Electrochemical tests are conducted in a specially designed "transmission geometry" cell for in situ synchrotron XRD measurements. For general electrochemical tests, a coin-type half cell with lithium metal as anode was used.

3.1.1 Pulsed laser deposition

Pulsed laser deposition (PLD) is a physical vapor deposition (PVD) technique which has been used to fabricate high quality films more than a decade. In PLD process, a high-power pulsed laser beam is focused inside a high vacuum chamber to strike, melt, evaporate and ionize material from the surface of a target that is to be deposited. When the laser pulse is absorbed by the target, energy is first converted to electronic excitation and then into thermal, chemical and mechanical energy resulting in evaporation, ablation, plasma formation and even exfoliation.[133] This process which can occur either in ultrahigh vacuum or in the presence of a background gas, such as oxygen which is commonly used for oxide films produces a transient, highly luminous plasma plume that expands rapidly away from the target surface.[134] The neutral plasma plume contains many energetic species including atoms, molecules, electrons, ions, clusters, particulates and molten

globules which migrate onto a substrate surface and then condense, nucleate and grow into thin films.[135] **Figure 3.1** illustrates a schematic view of the vacuum chamber of a PLD system and the PLD instrument used in this work.

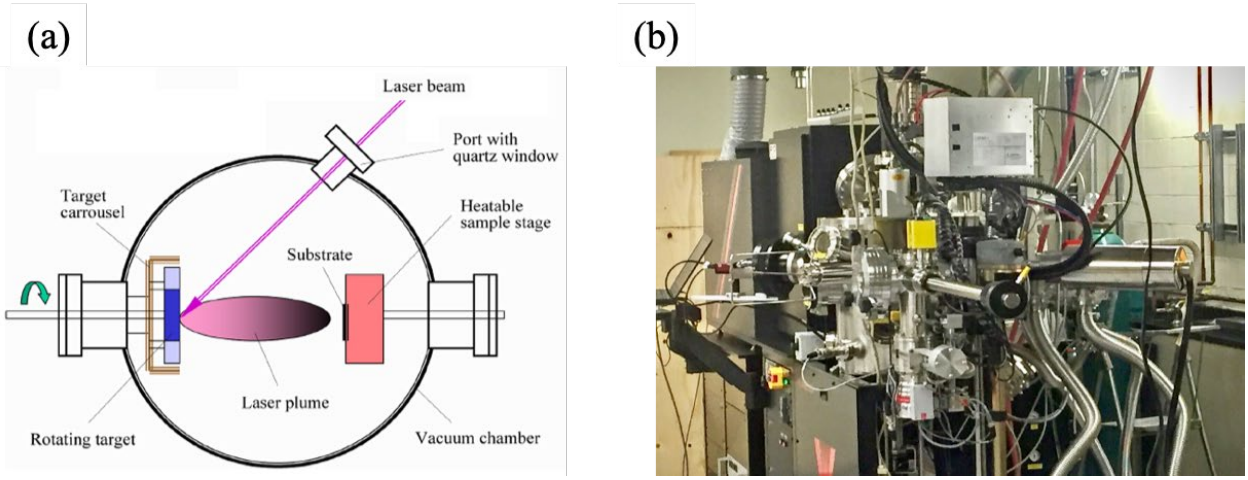

Figure 3.1 Schematic top view a PLD chamber[134] (a) and PLD instrument in Northwestern University Pulsed Laser Deposition Facility (b).

The detailed PLD processes are very complex mainly including the target material ablation by the laser irradiation, the plasma plume formation and nucleation and growth of the crystalline thin films on the substrate. Each of these steps is crucial for the crystallinity, uniformity and stoichiometry of the resulting thin films. In practice, couple of critical variables such as laser fluence, background gas pressure, substrate temperature and working distance are precisely controlled to manipulate desired properties of the films. Therefore, the optimization can sometimes cost a considerable amount of time and effort.

Unlike thermal evaporation which produces a vapor composition dependent on the vapor pressures of elements in the target material, the laser-induced expulsion in PLD produces a plume of material with stoichiometry nearly the same as the target. It is normally easier to obtain the desired film stoichiometry for multi-element materials using PLD than other deposition

technologies. Besides, a relatively high deposition rates, typically ~100 Å/min, can be achieved using PLD by controlling the laser fluence, while the film thickness is accurately tuned by simply turning the deposition duration. By housing several targets at the same time, it is convenient to conduct multilayer thin films deposition without breaking the vacuum to switch targets which usually can cause surface contamination.[134] Despite the aforementioned novel advantages of PLD technique, several drawbacks require of careful examination or circumvention to produce thin films of high quality. The plasma plume is highly forward directed, resulting in a narrow angular distribution of the ablated species and non-uniform thickness across the films. In addition, particulates of molten material as large as a few micrometers can fall onto the substrate due to sub-surface boiling, expulsion of the liquid layer by shock wave recoil pressure and exfoliation, which is detrimental to the properties of the film being deposited. Several simple methods can undermine effects of the above issues. For instance, rotating both the target and substrate can help to produce larger uniform films. Adoption of upward deposition is an effective way to prevent the large particulates from arriving to the substrates.[136]

3.1.2 Magnetron sputtering

Sputter deposition is a type of physical vapor deposition (PVD) method which involves ejecting material from a "target" that is a materials source onto a "substrate" such as a silicon wafer by using radio frequency (RF) or direct current (DC) glow plasma discharge.[137] Unlike PLD descried in section 3.1.1, plasma in sputtering deposition is created by impact ionization which involves inelastic collisions of accelerated electrons under applied high voltage with background gas molecules (usually inert gases such as argon, krypton and xenon, or nitrogen and oxygen for reaction sputtering deposition of nitrides and oxides). By inelastic collision, background gases receive energy and dissociate into energetic radicals, ions, molecules and electrons which quickly

form a neutral gas which is called glow discharge or plasma. Positively charged energetic ions from the plasma accelerated by potentials ranging from a few hundred to a few thousand electron volts collide with the negatively charged target material, and atoms from the target are ejected away as a vapor for subsequent deposition on a substrate. Magnetron sputtering uses a closed magnetic field to trap electrons, increasing the efficiency of the initial ionization process and creating the plasma at lower pressures, reducing both background gas incorporation in the growing film and energy losses in the sputtered atom through gas collisions.[138] The sputtering process is schematically illustrated in **Figure 3.2**a. All polycrystalline LMO thin films and corresponding current collecting layers (Pt/Ti) were fabricated using a sputter system in NUFAB facility center at Northwestern university (**Figure 3.2**b)

The sputtering targets are fabricated from materials that one subsequently wishes to deposit on the surface of the component facing the electrode. Conductive materials can be deposited using a direct current (DC) power supply and insulators can be deposited by using a radio frequency (RF) power supply. Charge build-up on insulating targets can be avoided with the use of RF sputtering where the sign of the anode-cathode bias is varied at a high rate of 13.56 MHz which is one of the frequencies in the RF spectrum that has been allocated to “industrial applications” as is by far the most common frequency used in the sputtering application.[138] RF sputtering works well to produce highly insulating oxide films but with the added expense of RF power supplies and impedance matching networks. Another type of sputter deposition is reactive sputtering. In reactive sputtering, the sputtered particles undergo a chemical reaction before coating the substrate. The deposited film is therefore different from the target material. The chemical reaction that the particles undergo is with a reactive gas introduced into the sputtering chamber such as oxygen or nitrogen; oxide and nitride films are often fabricated using reactive sputtering. The

composition of the film can be controlled by varying the relative pressures of the inert and reactive gases. Film stoichiometry is an important parameter for optimizing functional properties like the stress in SiN_x, electrical conductivity in TiN_x and the index of refraction of SiO_x.[137]

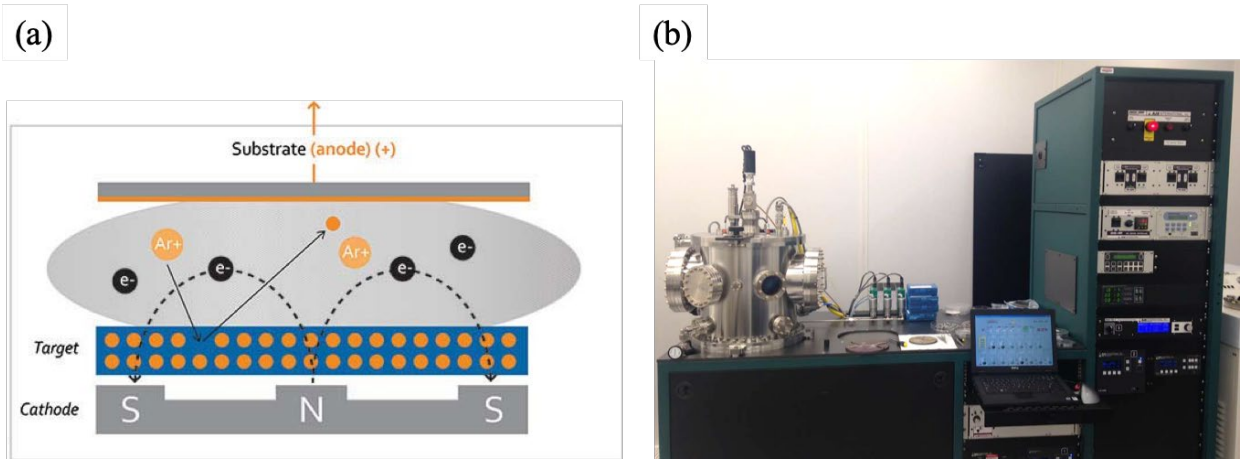

Figure 3.2 Schematic illustration of a magnetron sputtering system[139] (a) and a AJA Orion sputter instrument in NUFAB Cleanroom at Northwestern University (b).

3.2 Novel Strategies of Constructing High-Quality and Cyclable Thin-Film LMO Cathodes

Since LMO is nearly insulating, great challenges were encountered to well construct a functional current collecting system for achieving cyclable high performance thin-film LMO cathodes. Two viable stack configuration for fabricating cyclable thin-film LMO cathodes are illustrated in **Figure 3.3**a. In the first configuraton, LMO thin films have been deposited on electrically conductive substrates such as stainless steel (SS), Al, Ti and Pt foils which directly worked as current collectors.[57, 140-144] Alternatively, a stack of successive thin film layers including barrier layer (Al_2O_3, SiO_2), adhesion layer (Ti, TiN) and conductive buffer layer (Pt, Au, ITO) on top of insulating substrates (Si, Al_2O_3, YSZ) was also engineered for LMO deposition.[29, 100, 105, 145, 146] At the very beginning of this thesis work, 100 nm LMO thin films were sputtering deposited on polished bare SS substrates (#304 steel) which were heated at 650 ºC during deposition.

However, the LMO cathodes attained very tiny capacity due to elemental contaminations of Fe, Cr, Ni interdiffusing from the SS substrates which resulted in loss of cubic spinel LMO phase. Efforts were made by introducing a Au-Pd barrier layer (600 nm) between SS and LMO to prevent the vital interdiffusion issue. Nearly pure spinel LMO phase was only obtained if the deposition was conducted at room temperature and the LMO thin films were post annealed at a relatively low temperture (≤ 450 ºC). Those LMO thin films annealed at 450 ºC obtained poor crystallinity leading to small capacity (around half of the theoretical value for LMO, discussed in chapter 5). Rapid thermal annealing (RTA) at a higher temperature (700 ºC – 1000 ºC) was tried to get better LMO crystallinity but failed due to apparent elemental interdiffusion even the annealing period was less than 1 minute.

A series of potential current collecting systems summarized in the table of **Figure 3.3**b were tested to get high-quality and high performance thin-film LMO cathodes. It was found bare Ti foil could be directly used as a substate. However, LMO cathode even anneald at 750 ºC demonstrted very poor initial capacity. Au-Pd, TiN, $La_{0.5}Sr_{0.5}CoO_3$ (LSCO) and indium-doped tin oxide (ITO) were applied as conductinve barrier (or buffer) layers on SS, Ti and Si substrates. Thin-film LMO cathodes grown on those substrates could only poorly performed when the post-annealing temperature was not over 450 ºC. The best peformance was achieved for LMO deposited on Pt || Ti || SiO_2 || Si or Pt || Ti || Al_2O_3 functional substrates. The former substrate was not used due to more complex fabrication procedure with an extra barrier layer deposition of SiO_2. It was intersting that a thin layer of Ti worked better than TiN as a cohesive layer for Pt layer deposition on Si or Al_2O_3 substrates once the post-annealing temperature was relatively high, i.e. 750 ºC. Probable interpretatation was that TiN could be oxided and release gases which damage the Pt layer when the whole cathode was annealed at 750 ºC in air. For this thesis work, LMO || Au-Pd ||

SS (@ 450 ºC) and LMO || Pt || Ti || Al_2O_3 (@ 750 ºC) were used in chapter 5 and chapter 6 & 7, respectively.

(a)

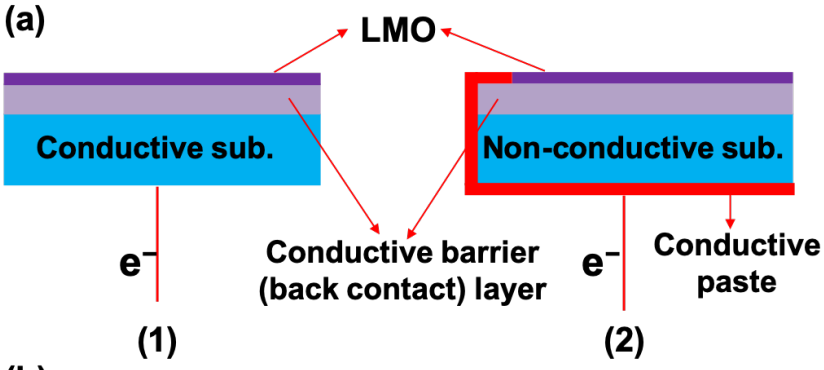

(b)

	Configuration	450 ºC	750 ºC
Substrates	SS	✗	✗
	Ti	✓	✓
	Mo	✗	✗
With conductive barrier layer	Au-Pd/SS	✓	✗
	Au-Pd/TiN/SS	✓	✗
	Au-Pd/TiN/Ti	✓	✗
	Au-Pd/TiN/Si	✓	✗
	Au-Pd/LSCO/SS	✓	✗
	Au-Pd/ITO/SS	✓	✗
	ITO/SS	✓	✗
	ITO/Al_2O_3	✓	✓
	Pt/TiN/Al_2O_3	✓	✗
	Pt/Ti/SiO_2/Si	✓	✓✓
	Pt/Ti/Al_2O_3	✓	✓✓

Figure 3.3 (a) Two feasible functional current collecting configurations of fabricating cyclable thin-film LMO cathodes. (b) A summary of a series of current collecting combinations explored in this thesis work in order to synthesize high-quality thin-film LMO cathodes with best electrochemical performance. All thin films were deposited at room temperature and post-annealed at 450 ºC and 750 ºC in air. "✓" stands for works and "✓✓" denotes much better, while "✗" indicates not works.

Another unexpected obstacle was to assemble thin-film-based coin cells which could normally work during electrochemical testing. Regular procedure adopted for assembling particle-based composite electrodes coin cells was applied to make the thin-film coin cells at first. **Figure 3.4** presents incremental capacity (IC) curves from a 25 nm thin-film LMO-based coin-type cell with lithium metal as anode. The cell was loaded enough amount of liquid electrolyte (200 μL 1 M $LiPF_6$ in 1:1EC/EMC) and pressed at a uniaxial pressure of 1500 psi for 10 seconds like what was usually done for particle composite electrodes. However, a poor capacity and huge overpotential were observed which turned out to be caused by huge Li-ion transfer resistance due to excessive liquid electrolyte and overlarge press pressure. Excess liquid electrolyte can be soaked in a particle composite electrode pack and high press pressure usually helps improve Li-ion conduction, which nevertheless is not suitable for thin-film electrodes. Over a number of trials, a successful assembling procedure was developed for CR2036 coin cells with thin-film LMO as cathodes (illustrated in **Figure 3.4**b):

1) Evacuate samples in loading chamber of Ar glovebox for 5 times
2) Place LMO thin film in center of a positive case
3) Add 1 drop of electrolyte onto LMO (~20 μL EC/EMC, looks like EMC worked better than DMC or DEC)
4) Place a polyolefin separator on top of LMO (16 mm dia. cutting by punch)
5) Add another drop of electrolyte (~20 μL)
6) Place a Li metal disk on top of the separator (13 mm dia. cutting by punch)
7) Place a SS spacer (15 mm dia.) and a spring on top of the Li metal disk
8) Seal the stack with a negative cap
9) Press the cell with an uniaxial pressure @ 600 psi without stay

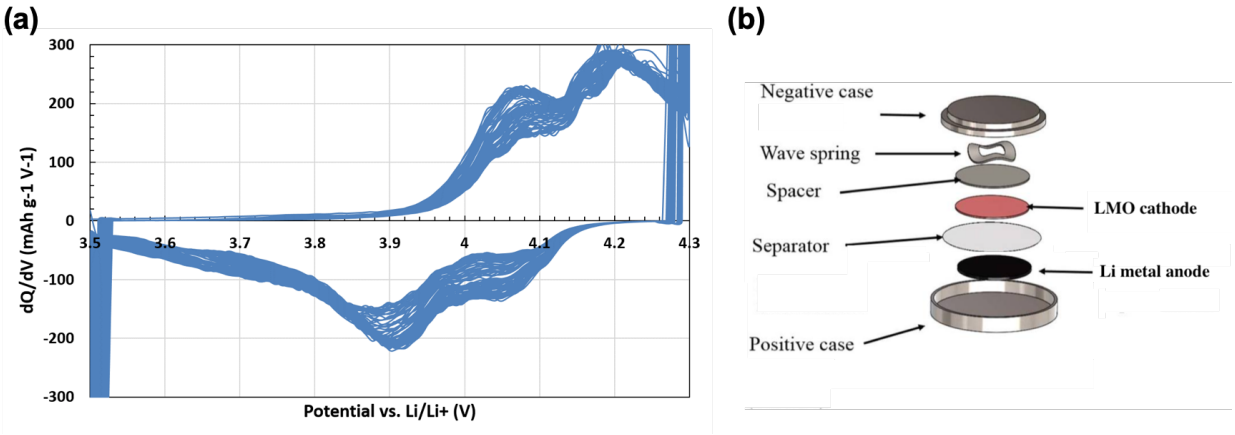

Figure 3.4 (a) Incremental capacity (IC) profiles from a 25 nm thin-film LMO-based coin-type half cell loaded with 200 µL electrolyte (1 M $LiPF_6$ in 1:1EC/EMC) and pressed at a uniaxial pressure of 1500 psi for 10 seconds. The cell was cycled between 3.5 – 4.3 V at 1C. (b) Stack of a CR2036 coin-type half cell with lithium metal as anode and thin-film LMO as cathode.

3.3 In situ Synchrotron X-ray Scattering and Electrochemical Tests

This cell used to assemble the full battery with thin film cathode is called a "transmission-geometry" cell (illustrated in **Figure 3.3**) because the x-rays pass through the circular opening in the cell. The thin film cathode is fully immersed in the 1:1 EC/DMC + 1 M $LiPF_6$ electrolyte (Novolyte), in analogy with a traditional beaker electrochemical cell. The electrolyte inlet and outlet (syringe + stopcock + Teflon tubing, not shown) are attached via PVDF compression fittings on the cell body's NPT fittings. The counter/reference electrode is a piece of lithium foil crimped to a copper wire and laid above the sample in the cell. The copper wire is epoxied to glass tubing (to seal from outside air) and attached using a compression fitting. The other NPT fittings are capped but could be used for additional electrodes or a bubbler. The working electrode has a primary O-ring seal at the sample using a custom miniature O-ring and secondary O-ring seals at the working clamp. We found that the working electrode seal is particularly important for samples with non-ideal conductivity and nanoscale thicknesses, where leakage currents can become comparable to redox processes. In this case, IR losses appeared to be minimal. The exposed area

of the electrode is 0.25 cm^2. All Kel-f and Teflon parts in contact with the electrolyte were soaked overnight in concentrated (97%) sulfuric acid + nochromix and then rinsed repeatedly with DI water until the pH of the effluent was above 6.5. The remaining parts were sonicated in methanol and rinsed with DI water. All parts are dried in a vacuum furnace for at least 12 hours before assembly. The cell is mostly assembled outside of the glovebox; the lithium metal, windows, and electrolyte are attached inside an Ar-filled glovebox (O2 < 1 ppm).[147]

All x-ray scattering measurements were taken at the Advanced Photon Source, sector 33BM-C, using a four circle Huber diffractometer and a Pilatus 100k area detector at 20.000 keV (λ = 0.6198 Å). The beam was sagittally focused on the sample using the Si 111 monochromator's second crystal located 30 m upstream. The beam was collimated before the sample to a 1.5x0.2 mm spot with an incident flux of $5x10^{10}$ photon/s. The scattered x-rays were collimated by a 10x1 mm slit to minimize exposure to the direct beam or nonspecular contributions from the multilayer Bragg peaks. In this configuration the beam was essentially parallel and spill-off corrections were proportional to 1/q. Samples were measured in a vertical specular geometry. Due to the small lateral dimensions of the sample and the narrow rocking curve of the surface reflection (0.020° FWHM), the height and orientation of the sample were measured and calibrated between each reflectivity scan. Using the area detector, we were able to integrate the background-subtracted reflectivity intensity in real-time (rather than relying on offset specular scans or rocking scans).[147] Cyclic voltammetry (CV) was carried out using a potentio/galvanostat (CHI760d, INC). The potential was swept from 3 V to 4.5 V at a fine interval 0.001 V/s. Galvanostatic charge-discharge measurements were performed after the CV measurement. A constant current at a rate of 0.64 C was applied for the charged or discharged conditions at 25 ºC without any holding time.

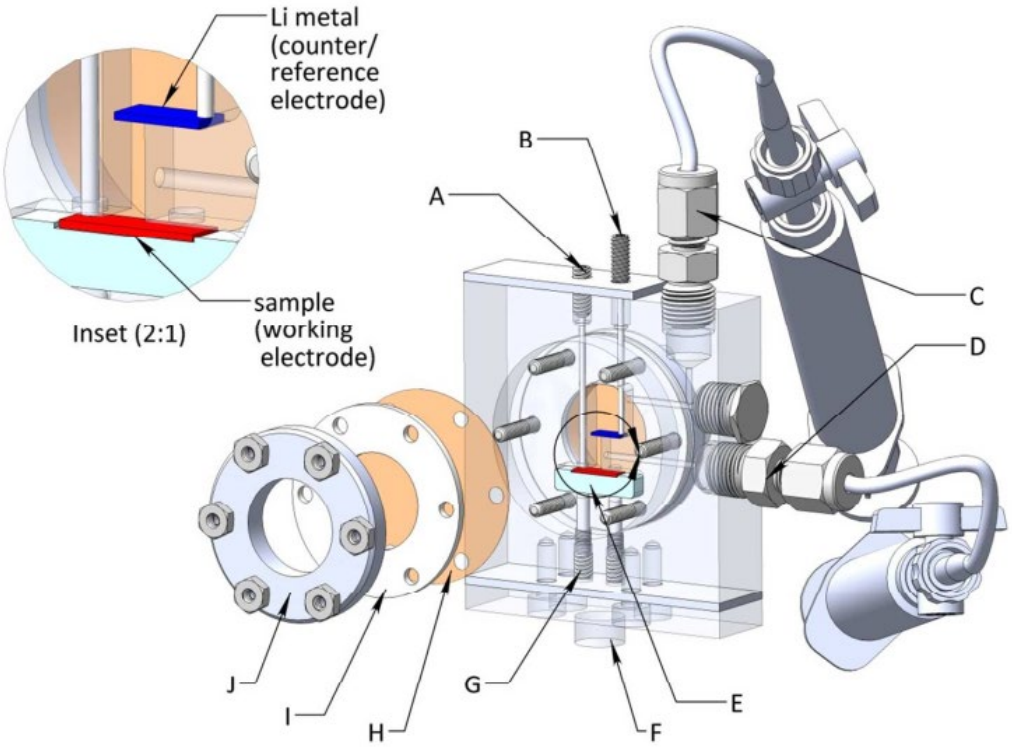

Figure 3.5 A fully assembled transmission cell used for in situ synchrotron XRD and XRR measurements during electrochemical test. The inset shows the 10x10x0.5mm thin film sample and the lithium metal counter electrode. Components in contact with solution are made of Kel-f or Teflon. The parts are: A, working electrode plunger (Teon-coated stainless steel pin); B, counter/reference electrode plunger; C, electrolyte outlet; D, electrolyte inlet; E, sample holder; F, goniometer adaptor; G, sample height adjuster; H, Window (75 µm-thick Kapton); I, window gasket; J, window clamp.[148]

3.4 Ex situ Thin Film X-ray Diffraction and Reflectometry

Ex situ thin film X-ray diffraction technique is a non-destructive method that provides information regarding symmetric property, interfacial crystal structure and preferred orientations of both out-of-plane and in-plane. Meanwhile, ex situ X-ray reflectivity at small incidence angle which is one of the best experimental techniques to determine surface and interface roughness, film thickness, and the density of the thin film samples in a nondestructive manner prior to and after the electrochemical reactions.[149, 150] **Figure 3.4** illustrates the schematic of Advanced Thin film X-ray system-Grazing incidence in-plane diffractometer (ATX-G, Rigaku) used in this

work.[151] A high intensity 18 kW copper x-ray rotating anode source (Cu Kα1) coupled with a multilayer mirror equips the system with selectable x-ray optical configurations which are suitable for measurements of single crystal and poly-crystalline ultrathin films. Besides, a high-precision 5-axis goniometer with several 4-crystal monochromators combining a multilayer mirror enables grazing incidence, in-plane diffraction measurement for single crystalline thin films. Specular XRD is performed by rotating the counter arm on the horizontal plane coupled with a high precision $2\theta/\omega$ goniometer. The in-plane diffraction or off-specular diffraction measurements are performed by rotating the counter arm upward along the sample surface by the $2\theta\chi$-axis at fixed $2\theta\omega$ value. In addition, a phi-scan on certain reflection plane at fixed $2\theta\chi$ value can be conducted to gain symmetric information of the thin films.

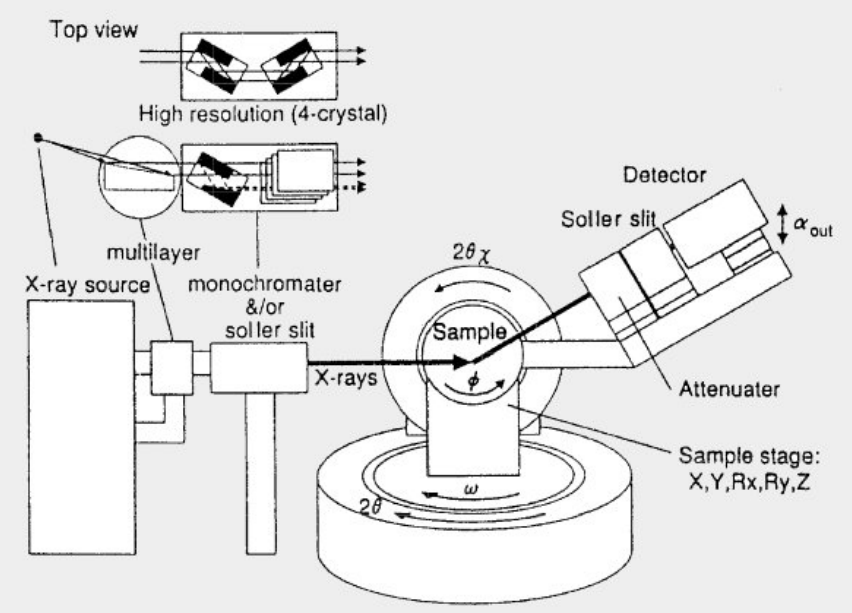

Figure 3.6 Schematic of the ATX-G setup (from Jerome B. Cohen X-Ray Diffraction Facility, Northwestern University).

Ex situ x-ray reflectivity measurements is performed by a specular $2\theta/\omega$ scan at a grazing incidence angle with well alignment of the sample and goniometers. The background scattering is

obtained by ridge scans at an offset of 3 times FWHM of R_y peak. For multilayer thin films, thickness, density and surface roughness of each layer are acquired by fitting the raw XRR data after correction of beam spill-off using a Motofit package[152] in Igor Pro software (WaveMetric, INC.). Below is a summary of calculating theoretical reflectivity steps in reference 73. The specular reflectivity is calculated using the Abeles formulation[153] as a function of the perpendicular momentum transfer, Q_z:

$$Q_z = \frac{4\pi}{\lambda} sin\theta \tag{3.1}$$

The specular reflectivity (R) defined as the ratio of reflected intensity over incident intensity of x-ray beam is calculated using the *Abeles* matrix method for stratified interface illustrated in **Figure 3.5**. The measured reflectivity depends on scattering length density (SLD) profile, ($\rho(z)$), which can be well approximated by a slab model in which layers of thickness (d_n), scattering length density (ρ_n) and roughness (σ_n, n+1) are sandwiched between the super- and sub-phases. ρ(z) is calculated using the erf error function:

$$\rho(z) = \sum_{i=0}^{N} \frac{\rho_i - \rho_{i+1}}{2}\left(1 + \mathrm{erf}\left(\frac{z - z_i}{\sqrt{2}\sigma_i}\right)\right) \tag{3.2}$$

The total reflection is from refracted beam at each of the layers with a wave vector k_n for layer n, which is expressed with respect to scattering length density ρ_n as:

$$k_n = \sqrt{k_0^2 - 4\pi(\rho_n - \rho_0)} \tag{3.3}$$

The Fresnel reflection coefficient between layer n and n+1 is:

$$r_{n,n+1} = \frac{k_n - k_{n-1}}{k_n + k_{n+1}} \exp\left(-2k_n k_{n+1}\sigma_{n,n+1}^2\right) \tag{3.4}$$

where an interface roughness $\sigma_{n,n+1}$ is used to account for the interfacial morphology. The reflectivity is calculated by the Abeles matrix:

$$\mathrm{R} = \left|\frac{M_{00}}{M_{10}}\right|^2, \qquad M = \prod_{0}^{n} c_n \tag{3.5}$$

where c_n is a 2x2 characteristic matrix:

$$c_n = \begin{bmatrix} \exp(\beta_n) & r_n \exp(\beta_n) \\ r_n \exp(-\beta_n) & \exp(-\beta_n) \end{bmatrix}, \qquad \beta_n = k_n d_n \tag{3.6}$$

By changing the parameters that describe each layer, a refinement procedure is applied to minimize the differences between the theoretical and measured reflectivity data by minimizing the χ^2 error value:

$$\chi^2 = \sum_{n=1}^{L} \frac{1}{L-P}\left(\frac{y_{n,obs} - y_{n,calc}}{y_{n,error}}\right)^2 \tag{3.7}$$

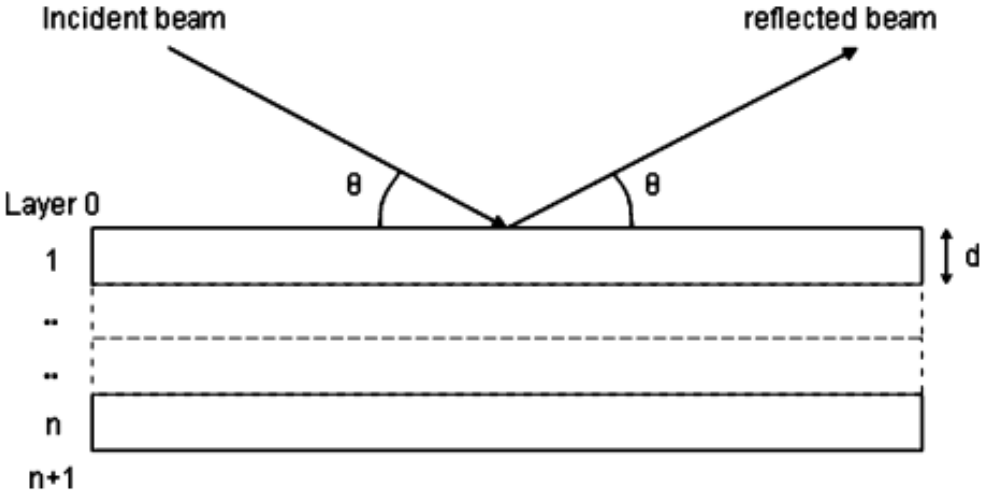

Figure 3.7 A slab model showing specular reflectivity from a stratified medium.[152]

3.5 AFM, SEM and High Resolution STEM

Atomic-force microscopy (AFM) is a very-high-resolution type of scanning probe microscopy (SPM), with demonstrated resolution on the order of a nanometer. AFM is usually used in three major aspects: force measurement, imaging, and manipulation. AFM imaging is a great tool for studying surface morphology of thin films. For imaging function, the reaction of the probe to the forces that the sample surface imposes on it can be used to form an image of the three-dimensional shape (topography) of a sample surface at an extremely high resolution. This is achieved by raster scanning the physical position of the sample with respect to the tip and recording the height of the probe that corresponds to a constant probe-sample interaction.[154] This process is schematically illustrated in left image of **Figure 3.6**a. The surface topography is commonly displayed as a pseudo color height plot. A Dimension FastScan® Atomic Force Microscope (**Figure 3.6**b) is used in this work to study surface morphology of the thin films. This AFM instrument delivers extreme imaging speed with atomic resolution and achieves AFM imaging without compromising highest resolution, application flexibility, or productivity. Besides, 20Hz Tapping Mode scan rates of this instrument provide excellent quality images, matching that typically seen at 1Hz and maintaining good quality even at scan rates >100Hz with a scanning area as large as 35 μm.

A scanning electron microscope (SEM) is also widely used for surface topography characterization. SEM is a type of electron microscope that produces images of a sample by scanning the surface with a focused beam of electrons. The electrons interact with atoms in the sample, producing various signals that contain information about the surface topography and composition of the sample. The electron beam is scanned in a raster scan pattern, and the position of the beam is combined with the intensity of the detected signal to produce an image. In the most

common SEM mode, secondary electrons emitted by atoms excited by the electron beam are detected using an Everhart-Thornley detector. The number of secondary electrons that can be detected, and thus the signal intensity, depends, among other things, on specimen topography. SEM can achieve resolution better than 1 nanometer. Specimens are observed in high vacuum in conventional SEM, or in low vacuum or wet conditions in variable pressure or environmental SEM, and at a wide range of cryogenic or elevated temperatures with specialized instruments.[155]

The signals used by a scanning electron microscope to produce an image result from interactions of the electron beam with atoms at various depths within the sample. Various types of signals are produced including secondary electrons (SE), reflected or back-scattered electrons (BSE), characteristic X-rays and light (cathodoluminescence) (CL), absorbed current (specimen current) and transmitted electrons. Secondary electron detectors are standard equipment in all SEMs, but it is rare for a single machine to have detectors for all other possible signals.[155] Apart form imaging function, SEM is also couple with elemental composition characterization functionality which is achieved by energy-dispersive X-ray spectroscopy (EDS). It relies on an interaction of some source of X-ray excitation and a sample. Its characterization capabilities are due in large part to the fundamental principle that each element has a unique atomic structure allowing a unique set of peaks on its electromagnetic emission spectrum.[156] When the primary electron beam is focused on the specimen, the incident beam may excite an electron in the inner shell, ejecting it from the shell while creating an electron hole where the electron was. An electron from an outer, higher-energy shell then fills the hole, and the difference in energy between the higher-energy shell and the lower energy shell may be released in the form of an X-ray. The number and energy of the X-rays emitted from a specimen can be measured by an energy-dispersive spectrometer. As the energies of the X-rays are characteristic of the difference in energy

between the two shells and of the atomic structure of the emitting element, EDS allows the elemental composition of the specimen to be measured.[156]

High resolution TEM (HRTEM) is a useful tool for imaging cross sectional crystal structure by examine the observed lattice planes. Scanning TEM (STEM) equipped with an annular dark-field (ADF) detector and electron energy-loss spectrometer (EELS) is a very powerful tool to obtain useful structural and chemical information with atomic resolution.[157] The image contrast is roughly proportional to the square of the atomic number, which enable enables direct observation and direct, robust interpretation of columns of both light and heavy atoms, such as Li, O and transition metal elements commonly seen in LIB materials.[32] Furthermore, state-of-the-art STEM coupled with a spherical aberration corrector can significantly be improved in spatial resolution. By using this advanced imaging technology, Li ions and even hydrogen atoms have been visualized successfully in real-space and real-time.[158] In addition, electron energy-loss spectroscopy (EELS) and energy-dispersive X-ray spectroscopy (EDS) can be performed in TEM to explore the elemental distribution, local chemical and electronic properties of materials with high spatial and high energy resolution.[32]

In this work, JEOL JEM-2100 (**Figure 3.6**c) which is an analytical scanning transmission atomic resolution electron microscope from Electron Probe Instrumentation Center (EPIC) in Northwestern University is used for study the interfacial structure and local chemical properties of the LMO/LSCO bilayer thin films. It has a high brightness Schottky FEG emitter operated at 200kV, with 0.1 nm lattice resolution in HRTEM mode and 0.2 nm spatial resolution in STEM and analytical mode. The HAADF STEM detector, Oxford EDS system and Gatan GIF system enable atomically Z-contrast imaging, EDS and EELS point analysis of sub-nanoscale resolution,

and automated line scans and maps. Besides, the Gatan double-tilt heating stage (up to 1100 degrees) and Low-Z(Be) double -tilt holder makes it possible for analytical x-ray microanalysis.

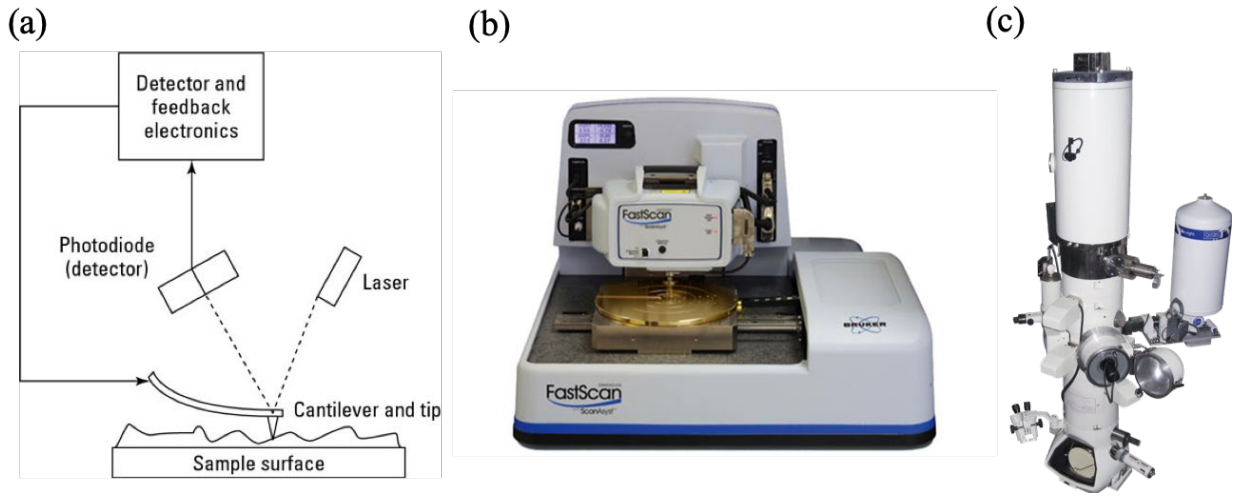

Figure 3.8 Schematic of an atomic force microscope (a) and pictures of a Bruker Dimension FastScan AFM device from Scanned Probe Imaging and Development (SPID) facility (b) and a JEOL JEM-2100 from Electron Probe Instrumentation Center (EPIC) (c) in Northwestern University.

3.6 X-ray Photoelectron Spectroscopy

X-ray photoelectron spectroscopy (XPS) is a surface-sensitive quantitative spectroscopic technique that measures the elemental composition at the parts per thousand range, empirical formula, chemical state and electronic state of the elements that exist within a material.[159] XPS spectra are obtained by irradiating a material with a beam of X-rays while simultaneously measuring the kinetic energy and number of electrons that escape from the top 1 to 10 nm of the material being analyzed. In order to eliminate loss of the ejected photoelectrons from specimen to electron counting detector due to undesired collision, XPS requires ultra-high vacuum (UHV) conditions. **Figure 3.7** shows basic components of a monochromatic XPS system. Because the energy of an X-ray with particular wavelength is known (for Al Kα X-rays, E_{photon} = 1486.7 eV), and because the emitted electrons' kinetic energies are measured, the electron binding energy of

each of the emitted electrons can be determined by using an equation that is based on the work of Ernest Rutherford (1914):

$$E_{binding} = E_{photon} - (E_{kinetic} + \phi) \quad (3.8)$$

where $E_{binding}$ is the binding energy (BE) of the electron, E_{photon} is the energy of the X-ray photons being used, $E_{kinetic}$ is the kinetic energy of the electron as measured by the instrument and ϕ is the work function dependent on both the spectrometer and the material. Each element produces a characteristic set of XPS peaks at characteristic binding energy values that directly identify each element that exists in or on the surface of the material being analyzed. These characteristic spectral peaks correspond to the electron configuration of the electrons within the atoms, e.g., 1s, 2s, 2p, 3s, etc. The number of detected electrons in each of the characteristic peaks is directly related to the amount of element within the XPS sampling volume.

Apart from surface elemental detection, XPS is also used to determine elemental compositions along depth of thin film samples through. This technique is called XPS depth profiling which applies plasma to sputter specimen surface layer by layer along depth direction after each XPS scan on newly formed specimen surface. Afterwards, an elemental composition distribution can be obtain by combining XPS data stack.[160]

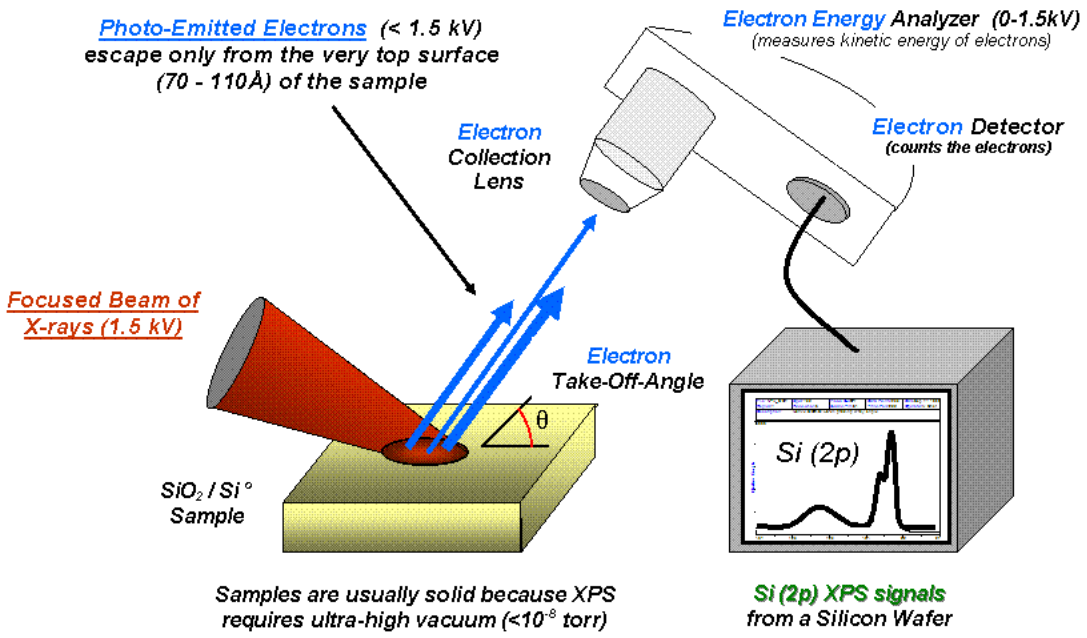

Figure 3.9 Basic components of a monochromatic XPS system.[159]

3.7 Cyclic Voltammetry and Galvanostatic Cycling

Cyclic voltammetry (CV) is a type of potentiodynamic electrochemical measurement. In a cyclic voltammetry experiment, the working electrode potential is ramped linearly versus time. Unlike in linear sweep voltammetry, after the set potential is reached in a CV experiment, the working electrode's potential is ramped in the opposite direction to return to the initial potential. The rate of voltage change over time during each of these phases is known as the experiment's scan rate (mV/s). Generally in LIB testing, the scan rate ranges from 10^{-2} – 10^{2} mV/s. These cycles of ramps in potential may be repeated as many times as needed. The current at the working electrode is plotted versus the applied voltage (that is, the working electrode's potential) to give the cyclic voltammogram trace. CV is generally used to study the electrochemical properties of an analyte in solution or of a molecule that is adsorbed onto the electrode. CV has become an important and widely used electroanalytical technique in many areas of chemistry. It is often used

to study a variety of redox processes, to determine the stability of reaction products, the presence of intermediates in redox reactions, electron transfer kinetics, and the reversibility of a reaction. CV can also be used to determine the electron stoichiometry of a system, the diffusion coefficient of an analyte, and the formal reduction potential of an analyte, which can be used as an identification tool. In addition, because concentration is proportional to current in a reversible, Nernstian system, the concentration of an unknown solution can be determined by generating a calibration curve of current vs. concentration.[161] CV testing conducted in chapter 4 was in a specially designed "transmission cell" using a potentio/galvanostat (CHI760d, INC) as described in section 3.2.

Galvanostatic cycling is another common electrochemical testing technique used to characterize cycling stability and rate capability of batteries and supercapacitors. In a galvanostatic cycling test, a battery is charged/discharged at a constant current within a preset voltage window. The current is usually expressed as a C-rate, calculated from the battery total capacity. The C-rate is a measure of the rate at which a battery is charged or discharged relatively to its maximum capacity. For example, a C-rate of 1 C means that the necessary current is applied or drained from the battery to completely charge or discharge it in one hour. C-rates multiples of 1 C are also exploited. Since the capacity is expressed in ampere hour, calculating the current necessary to charge or discharge a battery is straightforward. The direct data from galvanostatic cycling is cell voltage vs time which can be processed into cell voltage vs. capacity and total capacity vs. cycle number. It is helpful sometimes to take derivative of capacity in regard to cell voltage, resulting a plot illustrating important information of the electrode materials (electro)chemical properties, such as redox peak position, overpotentials, chemical kinetics, etc. Batteries studied in chapter 5, 6 and 7 were all assembled in an argon glovebox with oxygen and water contents less than 0.5 ppm

shown in **Figure 3.8**a. A CR2036 coin-type half cell was used to assemble the LMO thin film cathode and lithium metal anode as schematically illustrated in **Figure 3.8**b. An Arbin battery test system was used for galvanostatic cycling and a Bio-Logic battery test instrument was used to conduct coupled galvanostatic cycling and electrochemical impedance spectroscopy (EIS) measurements by establish corresponding program. The two instruments are shown in **Figure 3.8**c and d, respectively.

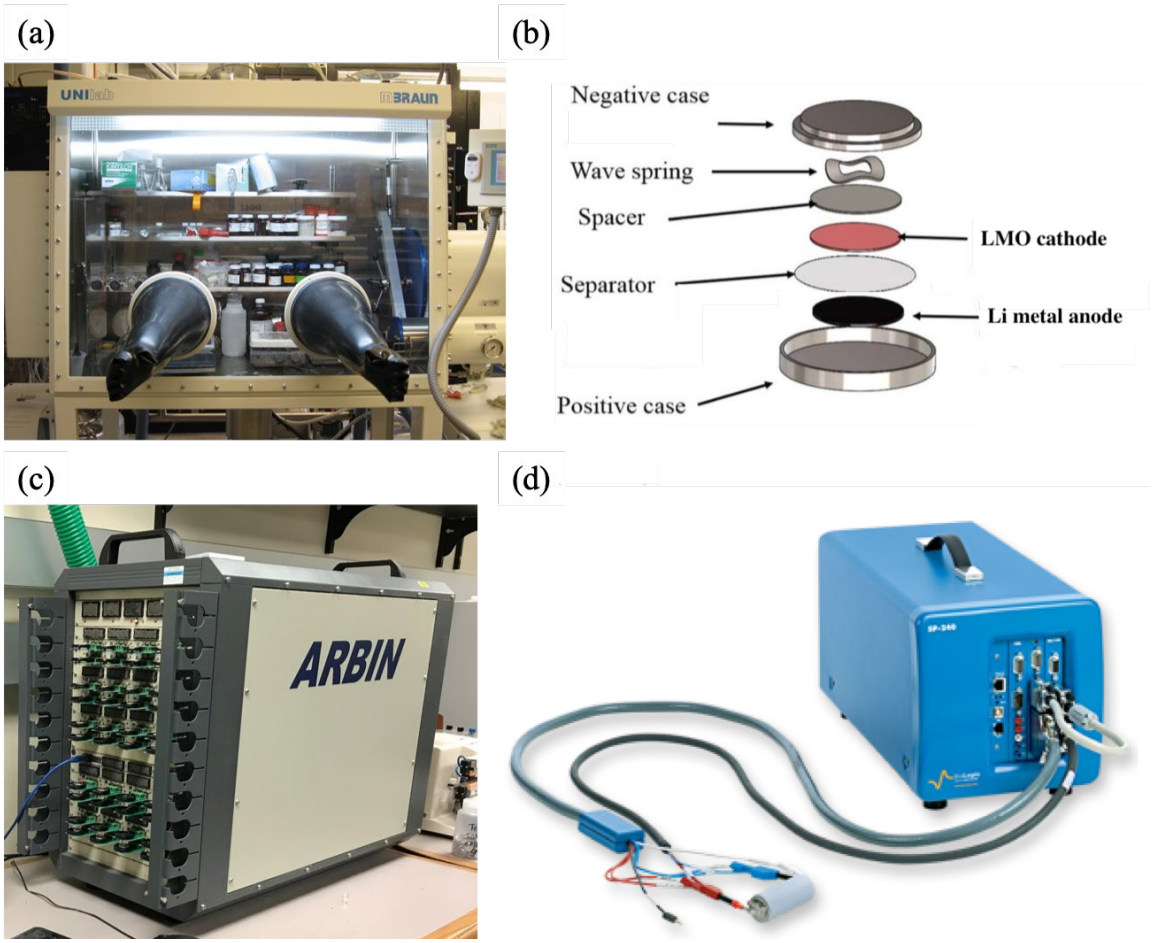

Figure 3.10 (a) A argon glovebox with oxygen and water contents < 0.5 ppm. It is used to assemble coin type batteries in the thesis work. (b) Components of a CR2036 coin-type half cell with lithium metal as anode and LMO thin film as cathode. (c) An Arbin battery testing system used for galvanostatic cycling. (d) An EC Lab Bio-Logic system with multiple programable battery testing functions including galvanostatic cycling, cyclic voltammetry and electrochemical impedance spectroscopy.

3.8 Electrochemical Impedance Spectroscopy

Electrochemical impedance spectroscopy (EIS) is one of the few characterization methods available that allows the kinetics of the electrochemical reactions occurring at electrodes to be probed under operating conditions. EIS is used in this thesis work to characterize and calculate interfacial resistances, Li^+ diffusivity and electrode surface charge transfer resistance in LMO thin film batteries. In its most basic embodiment, EIS is used to deconvolute the total cell resistance into ohmic resistance (ion transport through the electrolyte) and polarization resistance (reaction kinetics at the electrode). This is possible because the characteristic frequency for the chemical reactions at the electrodes occurs at a much lower frequency than electronic or atomic transport processes in the electrolyte bulk. In EIS, a small perturbing AC signal (5-20 mV) is usually applied onto the cell and the current response is measured as demonstrated in **Figure 3.9**.

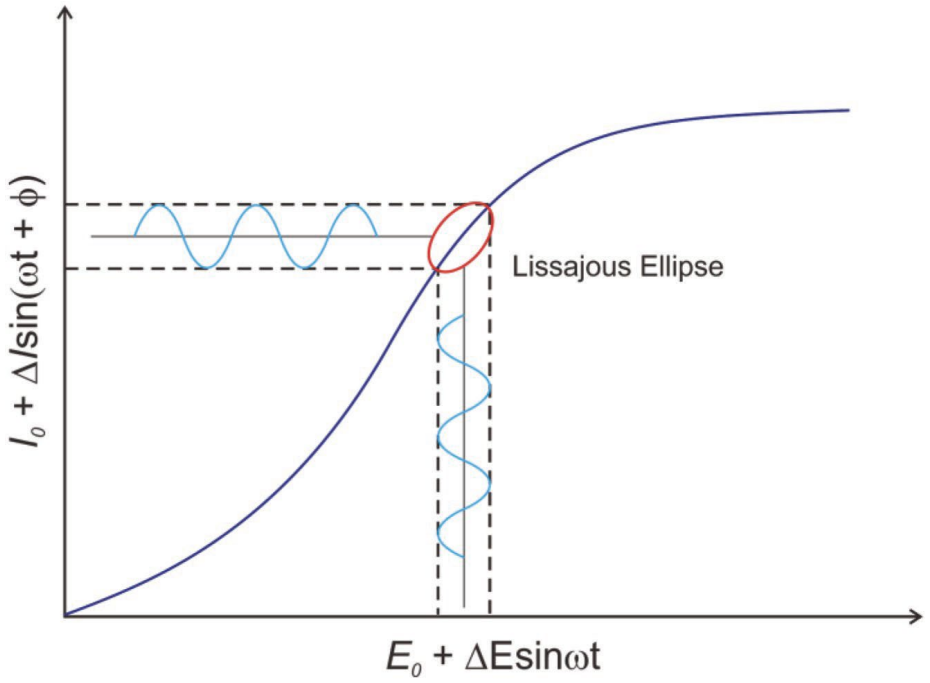

Figure 3.11 Schematic of EIS measurement where a small perturbing voltage signal is introduced around a potential E_0 and the current response around I_0 is measured. The relationship between the signals gives the system total impedance.[162]

The relation between the phase lag and the amplitude change gives the complex impedance. The voltage signal is then stepped through a range of frequencies from about 10^{-2} - 10^{5} Hz. The upper frequency is typically limited by inductance in the test setup (high-frequency cut-off) and the lower frequency is the DC limit where the imaginary portion of the impedance drops to zero and the real impedance matches the resistance in DC operation. Practically, the frequency may not go all the way to the DC limit because at very low frequencies, the collection time becomes unreasonably large. The EIS data is generally displayed as a Nyquist plot that plots the real versus the imaginary impedance, and a Bode plot that plots the imaginary impedance versus the frequency of the AC voltage signal. The EIS data can be analyzed and fitted mathematically suing an equivalent circuit model (ECM) to determine the processes that occur inside a battery cell and calculate interface resistances and electrode kinetics. An ECM exhibited in **Figure 3.10** was used in this thesis work to model a half cell consisting of LMO thin film cathode, liquid electrolyte, lithium metal cathode and stainless steel or Pt current collectors. Detailed description and interpretation of this ECM is coved in chapter 5.

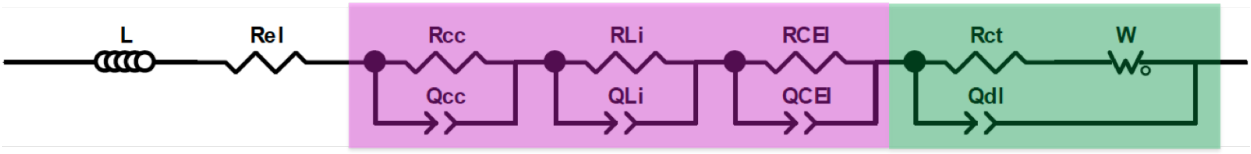

Figure 3.12 An equivalent circuit model applied to represent processes in a lithium ion battery and used to fit the EIS data.

Chapter 4: Pulsed Laser Deposition and Characterization of Hetero-epitaxial $LiMn_2O_4/La_{0.5}Sr_{0.5}CoO_3$ Bilayer Thin Films as Model Lithium Ion Battery Cathodes

4.1 Introduction

Lithium ion batteries (LIBs) are now widely used for sustainable transport, such as full electric vehicles (EVs) and hybrid electric vehicles (HEVs), and portable devices such as laptops and mobile phones, due to their high energy and power densities.[1, 5] Lithium manganese oxide $LiMn_2O_4$ (LMO) is a well-established LIB cathode material with the characteristics of low cost, low toxicity, good structural and chemical stability, a good Mn^{3+}/Mn^{4+} redox potential (4.1 V vs. Li/Li^+), and fast charging rates.[18, 19, 35] Despite these merits, one critical obstacle for LMO-based LIBs is its loss of capacity upon repeated electrochemical cycling, especially at elevated temperature.[20, 21] LMO capacity fading is attributed to Mn^{2+} dissolution into the electrolyte through a disproportionation reaction, detrimental electrolyte decomposition resulting in the formation of a solid electrolyte interface (SEI) layer, irreversible interphase formation, and cooperative Jahn-Teller distortion of $Mn^{3+}O_6$ octahedra (high spin $3d^4$, $t_{2g}^3e_g^1$) at a deep state of discharge.[22, 23, 59] These reactions remain poorly understood and accurate characterizations are limited due to the complex interface between LMO and the liquid electrolyte. For instance, many factors including surface morphology, surface impurity, surface reconstruction, crystal defects and grain boundaries significantly affect the (electro)chemical reactions at a polycrystalline LMO/electrolyte interface. Besides, complicated kinetics exist at the electrode surface, including electron transport between the current collector and electrode, lithium ion intercalation and extraction at the interface, and lithium ion diffusion within the electrodes.[52]

Advanced *in situ* characterization at the molecular level is important for precisely examining the interfacial reaction processes. Epitaxially grown LMO thin films are ideal for such fundamental studies.[24, 25, 69, 72, 89, 163-165] When well prepared, they can provide well-defined LMO surfaces with low defect densities, well-defined crystallographic orientation, and a small lattice strain. Unlike particle-based electrodes, the thin film geometry is well suited for interface study by a range of advanced *in situ* and *ex situ* characterization tools such as X-ray photoelectron spectroscopy (XPS), synchrotron X-ray scattering and absorption spectroscopy, atomic force microscopy (AFM), and high-resolution scanning transmission electron microscopy (STEM).[30, 31, 33, 62, 71] Epitaxial films grown on different orientation substrates allow one to probe interfacial effects on different-orientation LMO surfaces; for example, it would be possible to check DFT calculations indicating that the LMO (111) surface is more resistant to Mn dissolution than other orientations.[64, 65]

To date, epitaxial LMO thin films have been successfully grown on various substrates, such as $SrTiO_3$, MgO, Al_2O_3, Pt and Au, using a variety of deposition techniques including pulsed laser deposition (PLD), radio-frequency (r.f.) magnetron sputtering, atomic layer deposition (ALD) and chemical solution deposition (CSD).[62, 69, 70, 101-104] Most ceramic oxide substrates and LMO thin films have relatively poor electrical conductivity. Thus, to carry out electrochemical tests on epitaxial LMO films, a conducting back contact to the LMO electrode is required. Nb-doped $SrTiO_3$ (STO) substrates (0.5% Nb) are one option, providing a useful conductivity of 5×10^{-3} Ω cm at ambient temperature.[59, 69] However, Nb-doped STO can lose conductivity at oxidizing conditions, either during LMO film growth (typically with a background O_2 pressure), or upon electrochemical cycling at the elevated potentials associated with delithiation of cathode materials.

Alternatively, $SrRuO_3$, Pt, and Au have been grown as conductive back-contact buffer layers prior to the growth of LMO thin films.[5, 32, 62, 70, 166, 167] It is well known that noble metals like Pt and Au have poor wettability with oxide substrates, making them unsuitable for uniform epitaxial oxide film growth, especially at high temperature which is required to get LMO of high crystallinity.[168, 169]

Hirayama et al. were the first to examine interfacial structural change between liquid electrolytes and epitaxial LMO thin films grown on conductive Nb-doped STO substrates of different crystalline orientations using *in situ* and *ex situ* XRR and XRD measurements.[5, 59, 62] However, in situ observations of the interfacial reactions were extremely limited due to poor epitaxy and/or bad electrochemical reversibility of the LMO thin films. Gao et al. used EELS-STEM to analyze local LMO compositions and structure gradients as a function of the distance from the interface of epitaxial LMO thin films on Au.[32] So far, most current HRTEM studies have been focused on the interface between LMO and the substrate rather than the LMO/electrolyte interface. Therefore, model LMO thin films of high epitaxy and electrochemical reversibility are desired for comprehensive characterizations of electrode/electrolyte interfaces by in situ X-ray scattering and HRTEM. The same approach is also important for studying other electrode materials, including LMO with transition metal doping or surface coating.[170-172]

In this chapter, the structure and electrochemical reactivity of hetero-epitaxial bilayers of LMO/LSCO grown on single crystal STO (111) substrates using pulsed laser deposition (PLD) are demonstrated. The perovskite oxide LSCO was chosen as a conductive buffer layer based on its high metallic conductivity (~ 10^4 S/cm at room temperature) and its good lattice match with both STO (–1.7%) and spinel LMO (7.5%). The bilayer crystal structure, epitaxy and

surface/interface roughnesses were observed by synchrotron X-ray diffraction, X-ray reflectivity, AFM, and high resolution TEM. The reversibility and stability of these bilayers were probed by electrochemical cycling and *in situ* synchrotron X-ray scattering.

4.2 Experimental Details

Sample Preparation. A stoichiometric $LiMn_2O_4$ target (2 inch in diameter, MTI, 99.99% purity) was used as the PLD source material. The $La_{0.5}Sr_{0.5}CoO_3$ PLD target was prepared as follows. The LSCO powder was first synthesized using solid state reaction[173] from La_2O_3 (Sigma-Aldrich, ≥ 99.9%), $SrCO_3$ (Sigma-Aldrich, ≥ 99.9%) and $CoCO_3$ (Alfa Aesar, ≥ 99.5%). These powders were mixed through a roller ball mill for 48 h, followed by firing at 1100 ºC for 24 h in air. The heating rate was 120 ºC/h while the cooling rate was kept at 90 ºC/h. The resulting LSCO powder was then ball milled in ethanol for 72 h. The as-synthesized LSCO powder obtained X-ray diffraction peaks (upper line in **Figure 1**) that match well with standard $La_{0.5}Sr_{0.5}CoO_3$ (ICSD #184073), indicating successful synthesis of high-crystallinity LSCO powder. Bulk $La_{1-x}Sr_xCoO_3$ (x = 0.5) has a slightly rhombohedrally distorted crystal structure with a pseudo cubic lattice constant a_c = 3.837 Å (inset in **Figure 1**); the calculated lattice constant a_c was 3.835 Å from the 110 reflection.[174, 175] For PLD target fabrication, the prepared LSCO powder was first tape cast (Tape Casting Warehouse, INC.) onto a polyethylene (PET) carrier film. The tapes were then cut, stacked and hot laminated at 80 ºC for 30 min under a pressure of 5000 psi. Finally, the laminated stack was punched into a pellet with 1.2-inch diameter, and sintered at 1350 ºC for 24 h in air, yielding a 1-inch diameter 3 mm thick LSCO target with a density of around 90%.

The LMO and LSCO layers were grown on STO (111) substrates using a KrF excimer laser with a wavelength of 248 nm and a PLD apparatus (PLD/MBE 2300, PVD Products, Inc.). The

substrates were acetone washed and pre-annealed at 1000 ºC for 8 h in air. The LMO and LSCO deposition conditions are summarized in **Table 4.1**. Two bilayer thin films with different LSCO buffer layer thicknesses (5 nm and 10 nm) were grown in order to examine the effect of buffer layer thickness on the crystallographic perfection and surface morphology of LMO layer. After LSCO growth, PLD conditions were immediately switched for subsequent LMO growth. Avoiding air exposure between the two growth steps proved to be important, as initial experiments where the LSCO film were taken out of the vacuum chamber prior to LMO growth yielded films of poor quality. To get high electrical conductivity and good crystallinity of LSCO buffer layer, a large O_2 partial pressure (300 mTorr) and relatively high substrate temperature were applied.[176, 177] Additionally, a slow cooling rate of 5 ºC/min was chosen to avoid oxygen deficiency in LSCO buffer layers.[173, 178] Both LMO and LSCO single layers were also synthesized on STO (111) substrates as controls.

Table 4.1 PLD conditions for epitaxial LMO/LSCO/STO (111) bilayer thin films.

Target	Temperature (°C)	Working distance (mm)	Duration time (s)	Laser fluence (mJ/pulse)	Frequency (Hz)	O_2 partial pressure (mTorr)
LMO	650	75	150	200	5	30
LSCO	650	60	260	270	5	300

Sample Characterization. Inductively Coupled Plasma Mass Spectrometry (ICP-MS, Thermo Scientific™ iCAP Q) was used to determine the Li:Mn and La:Sr:Co ratios in the films. The surface morphology and roughness of all thin films were observed by Atomic Force Microscopy (AFM, Bruker Dimension FastScan®). Powder X-ray diffraction was done on Scintag

XDS2000 with Cu Kα (λ = 1.5406 Å) radiation. Epitaxy and crystal orientations were characterized by thin-film X-ray diffraction (ATX-G, Rigaku) with Cu Kα (λ = 1.5406 Å, incident slit = 0.2 mm) radiation. X-Ray reflectivity (ATX-G, Rigaku) measurements were conducted to calculate thickness and roughness of each layer by fitting the XRR data using a Motofit package in Igor Pro software (WaveMetric, INC.). Cross-sectional TEM samples of LMO/LSCO bilayers were prepared by a dual-beam focused ion beam (FIB, FEI Helios Nanolab 600) with a 1-μm-thick protective Pt layer on the sample surface. High resolution TEM (JEOL Co., JEM-2100F) observations were conducted at 200 kV with a field-emission gun electron source.

Electrochemical Test. Electrochemical measurements were performed using a specially designed spectroelectrochemical cell for *in operando* synchrotron X-ray scattering measurements in a "transmission" geometry.[147] The cells were assembled inside an argon glove box with lithium metal as the counter/reference electrodes, the LMO/LSCO bilayer thin films as the working electrode and 1:1 EC/DMC + 1 M $LiPF_6$ as the electrolyte. Cyclic voltammetry (CV) scans were performed using a Potentiostat/Galvanostat (CHI760d, INC) electrochemical analyzer. The potential was swept from 2.5 V to 4.3 V at intervals of 0.5 mV/s. *In situ* synchrotron X-ray scattering measurements were performed during the cycling process at Advanced Photon Source (APS) sector 33BM-C in Argonne National Laboratory (ANL), using a four-circle Huber diffractometer and a Pilatus 100k area detector with X-ray photon energy of 20.000 keV (λ = 0.6198 Å) and an incident flux of $\sim 10^{10}$ photons/s. The X-ray beam (with cross section of 2 × 0.2 mm^2 and divergence of 40 μrad = 0.0005 $Å^{-1}$ along 2θ direction) illuminated a 2 mm × 3 mm area on the sample.

4.3 Results and Discussion

Growth results for LSCO and LMO single layers on STO substrates are described first, followed by a discussion of results for LMO/LSCO bi-layers.

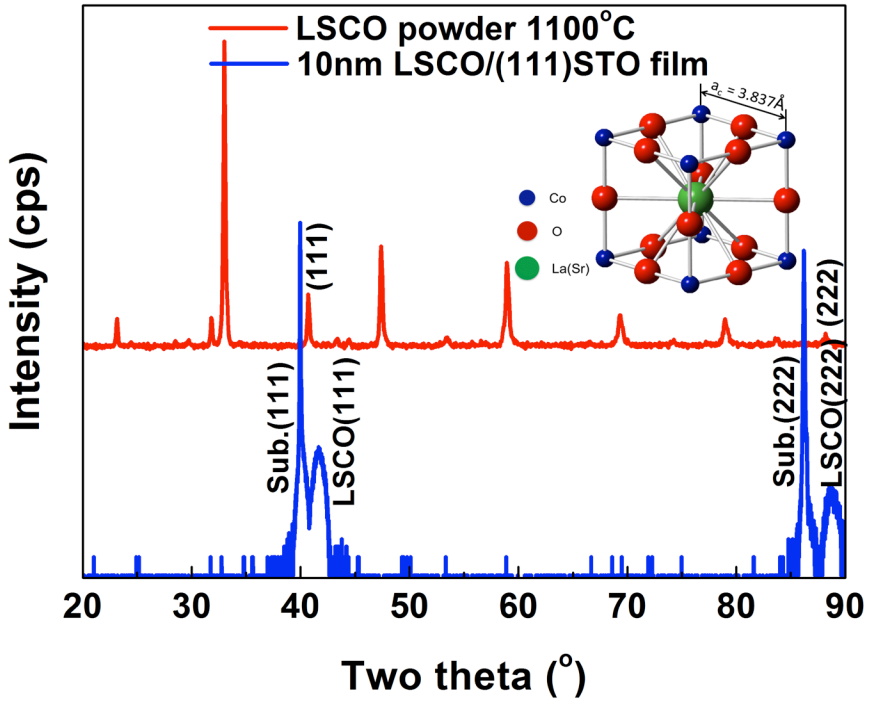

Figure 4.1 XRD pattern of as-synthesized $La_{0.5}Sr_{0.5}CoO_3$ powder (red line) and specular thin film XRD pattern from 10 nm LSCO thin film grown on STO (111) (blue line).

LSCO layers on STO (111). ICP-MS was used to check the composition of LSCO films and the ratio of La, Sr and Co is about 0.47:0.49:1, indicating a chemical formula of $La_{0.47}Sr_{0.49}CoO_{3-\delta}$ for the LSCO films. The specular XRD pattern from the 10-nm-thick LSCO film is demonstrated in **Figure 4.1** (lower line). The pattern shows diffraction lines of the (111) and (222) planes from both the LSCO film and STO (111) substrate, indicating that the LSCO film had a [111] out-of-plane crystal orientation. Comparison with the LSCO powder pattern (**Figure 4.1** upper line) shows a shift of the film peaks to larger 2θ angle, due to coherency strain caused by the negative lattice misfit (–1.7%) between LSCO and the substrate STO. The XRD in-plane scan

and phi-scan at the LSCO $(1\bar{1}0)$ reflection are shown in **Figure 4.2**a-b. The in-plane scan reveals LSCO lattice planes normal to the thin film surface while phi-scan is an azimuthal scan at a fixed in-plane momentum transfer $Q_{//}$ corresponding to the $(1\bar{1}0)$ Bragg reflection of the LSCO film. Only $(1\bar{1}0)$ and $(2\bar{2}0)$ reflection peaks from both LSCO and STO appear and overlap. These results reveal that the LSCO film had a preferred $[1\bar{1}0]$ in-plane crystalline orientation with a sixfold symmetry indicated by the peak separation of 60°, matching that of STO and demonstrating a "cube-on-cube" epitaxial relationship between LSCO and STO: LSCO {111} // STO {111}, $[1\bar{1}0]$ LSCO // $[1\bar{1}0]$ STO. A specular ω-rocking curve (RC) scan on peak LSCO (111) shown in **Figure 4.2**a inset reveals a full width at half maximum (FWHM) value of 0.07°, which is close to values reported in literature for epitaxial LSCO thin films.[179] The specular ω-RC scan was conducted at a fixed specular momentum transfer $Q_{\perp}$ value corresponding to the (111) Bragg reflection of the LSCO film. These results reveal a strained and epitaxial LSCO film was synthesized with little defects and slight structural misorientations. Epitaxial LSCO thin films have been grown on various substrates using PLD; the present results are in good agreement with literature reports for LSCO on STO.[173, 180] A low angle XRR profile of the obtained LSCO film shown in **Figure 4.2**c reveals several interference fringes. The spectrum is plotted as a function of scattering vector $Q_z = 4\pi \sin\theta/\lambda$, where λ is the X-ray wavelength (1.5406 Å) and θ is the incident angle. The inset shows a fitting electron density profile of the LSCO film. The fit matches the data well for an LSCO film thickness of 98.3 Å, with interface and surface roughnesses of 5.1 Å and 6.2 Å, respectively. Surface morphology was examined by AFM with a 3D image and a line section profile (**Figure 4.2**d), indicating an LSCO surface RMS roughness of ≈ 7.0 Å, which is in the range desired to obtain high-quality XRR data.[181]

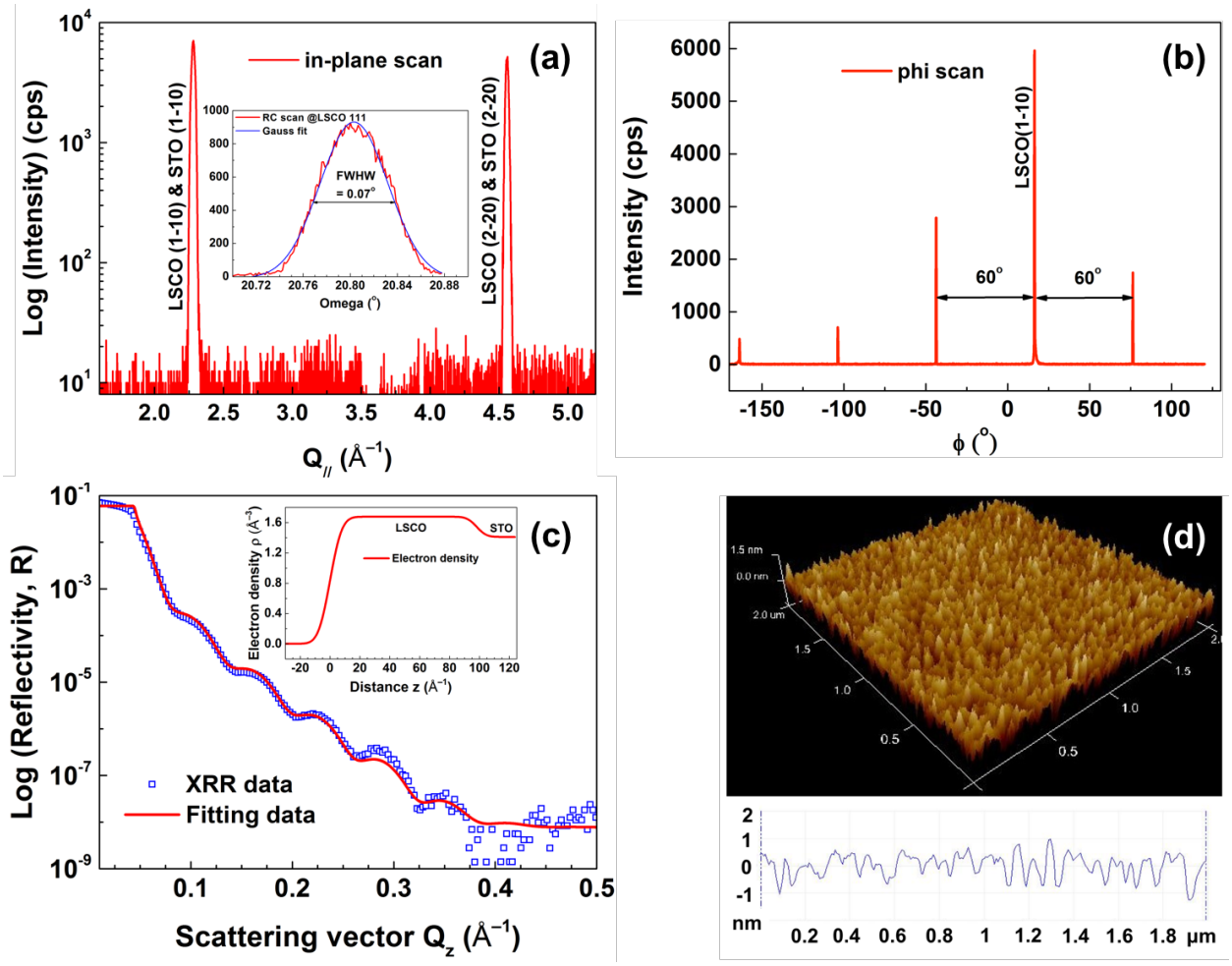

Figure 4.2 In-plane XRD (a) and phi-scan (b) patterns show the 10 nm LSCO/STO (111) thin film obtained in-plane epitaxy with [1$\bar{1}$0] preferred orientation and a sixfold symmetry. XRR spectrum with fitting curve and electron density profile (inset) for the LSCO film (c) and 3D AFM image with a line section profile (d) showing surface morphology of the LSCO film.

LMO on STO (111). LMO layers were grown on STO (111) by PLD to provide a comparison with LMO grown on LSCO-coated STO substrates. ICP-MS measurements show that the ratio of Li to Mn is about 0.68:2, indicating 32% Li was lost relative to the stoichiometric LMO target during the PLD process. Li loss is expected in LMO vapor deposition, especially given the present relatively large substrate-target separation (7.5 cm).[182] The loss of Li is not an issue for the use of these LMO films as a model system, because the Li content is still large enough to retain

the correct spinel structure as indicated by the XRD and HRTEM results. In prior work on LMO thin films with similar low Li content, cyclic voltammograms showed the expected spinel Mn^{3+}/Mn^{4+} redox characteristics.[182] XRD patterns were obtained by thin-film X-ray diffraction (ATX-G, Rigaku). **Figures 4.3**a-b exhibit the specular, in-plane and phi-scan XRD patterns of a typical single layer LMO film with a thickness of around 27 nm. $Q_{\perp}$ and $Q_{//}$ in x-axis are specular and in-plane momentum transfers, respectively. The specular scan (red line in **Figure 4.3**a) shows 111, 222, 333, and 444 specular diffraction lines. The in-plane scan (blue line in **Figure 4.3**a) shows that the $[1\bar{1}0]$-type LMO reflections are aligned with the $[1\bar{1}0]$-type STO substrate reflections. A sixfold symmetry is indicated by the phi scan pattern at LMO $(4\bar{4}0)$ with an interval of 60º shown in **Figure 4.3**b. A phi scan through the STO $(2\bar{2}0)$ reflections is also shown for comparison. These results clearly indicate that the LMO film was epitaxial on STO (111), with orientation relationship: LMO {111} // STO {111}, $[1\bar{1}0]$ LMO // $[1\bar{1}0]$ STO. The out-of-plane lattice constant of the LMO film determined from the (111) reflection is 8.230 Å, indicating expansion was induced due to a positive lattice misfit (4.9% shown in **Table 4.2**) between LMO and STO. The low angle XRR data and fitting result shown in **Figure 4.3**c indicate that the interface and surface roughnesses are 2.6 Å and 11.7 Å, respectively. The AFM image and linear section profile (**Figure 4.3**d) indicate an RMS roughness of ≈ 12.0 Å.

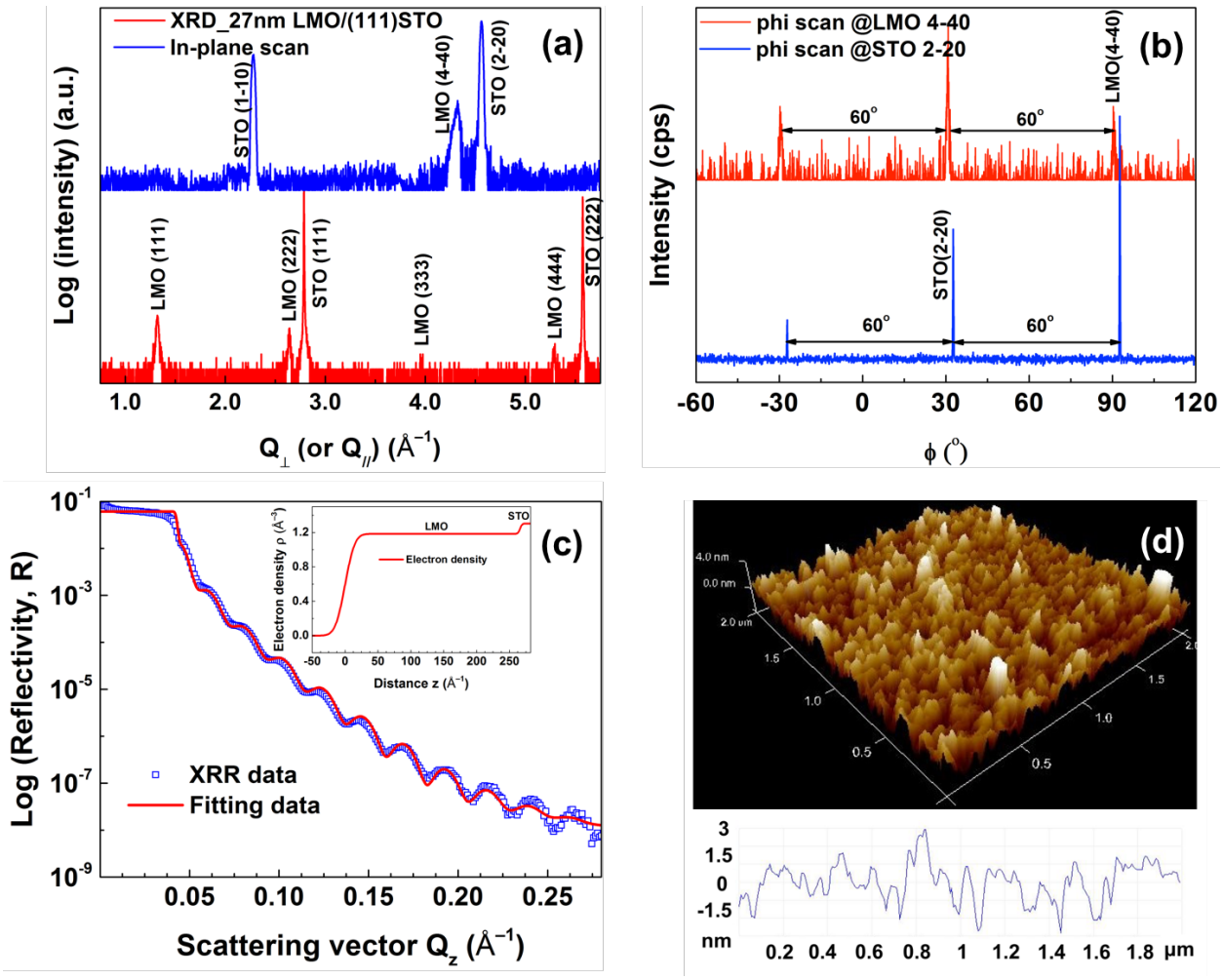

Figure 4.3 (a) Specular thin film XRD pattern (red line) from 27nm LMO thin film grown on STO (111) substrate. The pattern indicates [111] preferred specular orientation of the LMO film. In-plane XRD (blue line) shows that the LMO thin film exhibits in-plane epitaxy with $[1\bar{1}0]$ preferred orientation. (b) Phi scans of both LMO (red line) and STO (blue line) corresponding to the $(4\bar{4}0)$ and $(2\bar{2}0)$ reflections, respectively, indicate a sixfold symmetry of the LMO film. (c) XRR spectrum with fitting curve and electron density profile (inset) for the LMO thin film, and 3D surface AFM image along with a line section profile (d) showing surface morphology of the LMO single layer film.

LMO/LSCO Bi-Layers on STO (111). Two different as-deposited LMO/LSCO bilayers were studied; the nominal LSCO thicknesses were 5 or 10 nm, while in both cases the nominal LMO thickness was 10 nm. According to the specular synchrotron XRD patterns in Figure 4a,

both LMO and LSCO show (111) and (222) reflections, although the LSCO peaks are weaker and appear as a shoulder on the substrate peaks for the 5-nm-thick LSCO layer. This indicates [111] preferred specular orientation for both LMO and LSCO. In addition, the thin film XRD pattern of an in-plane scan is illustrated in **Figure 4.4**b, indicating a "cube-on-cube" epitaxial relationship was established: LMO {111} // LSCO {111} // STO {111}, $[1\bar{1}0]$ LMO // $[1\bar{1}0]$ LSCO // $[1\bar{1}0]$ STO, which is demonstrated by the inset in **Figure 4.4**a.

Bulk crystal structures and lattice constant values of LMO, LSCO and STO, along with XRD-measured lattice constant values and calculated lattice misfits for the 10 nm LMO/10 nm LSCO/STO bilayer are summarized in **Table 4.2**. To calculate lattice constant parameters from the obtained data, we convert data both from synchrotron XRD (λ = 0.6198 Å) and standard Cu Kα1 (λ = 1.54056Å) XRD into intensity vs. momentum transfer vector q. For Cu Kα1 x-ray source:

$$\mathrm{q} = \frac{4\pi \sin\theta}{\lambda}, \qquad d = \frac{\lambda}{2sin\theta} \tag{4.1}$$

For the synchrotron X-ray source from APS sector 33BM-C:

$$\mathrm{q} = \frac{2\pi L}{2.2546} \tag{4.2}$$

where L represents momentum transfers $Q_{\perp}$ and $Q_{//}$. Thus, we can get the interplanar d-spacing by substituting q in Eq 4.1 with Eq 4.2 : $d = \frac{2.2546}{L}$.

The out-of-plane lattice constant of LMO, obtained from the (111) reflection in **Figure 4.4**a, is $a_{\perp}$ = 8.239 Å, which is larger than the bulk $Li_{0.68}Mn_2O_{4-\delta}$ lattice constant (~ 8.189 Å).[183,

[184] For LSCO, $a_{\perp}$ = 3.799 Å is obtained from the LSCO (111) reflection, which is, on the contrary, smaller than the bulk lattice constant (3.837 Å). **Figure 4.4**b shows the in-plane XRD scan, from which the in-plane lattice constants are acquired (shown in **Table 4.2**). The in-plane residual lattice misfits are then calculated to be 4.9% for LMO/LSCO and –0.1% for LSCO/STO. The extremely small LSCO/STO in-plane residual lattice misfit indicates that the LSCO was coherently strained (expanded) to match the STO substrate lattice, whereas the out-of-plane lattice spacing contracted due to the Poisson effect. On the other hand, the LMO/STO lattice misfit is almost equal to the bulk lattice misfit, indicating that the LMO film was largely relaxed. This is consistent with the fact that the out-of-plane LMO lattice constant is only 0.6% larger than the bulk value.

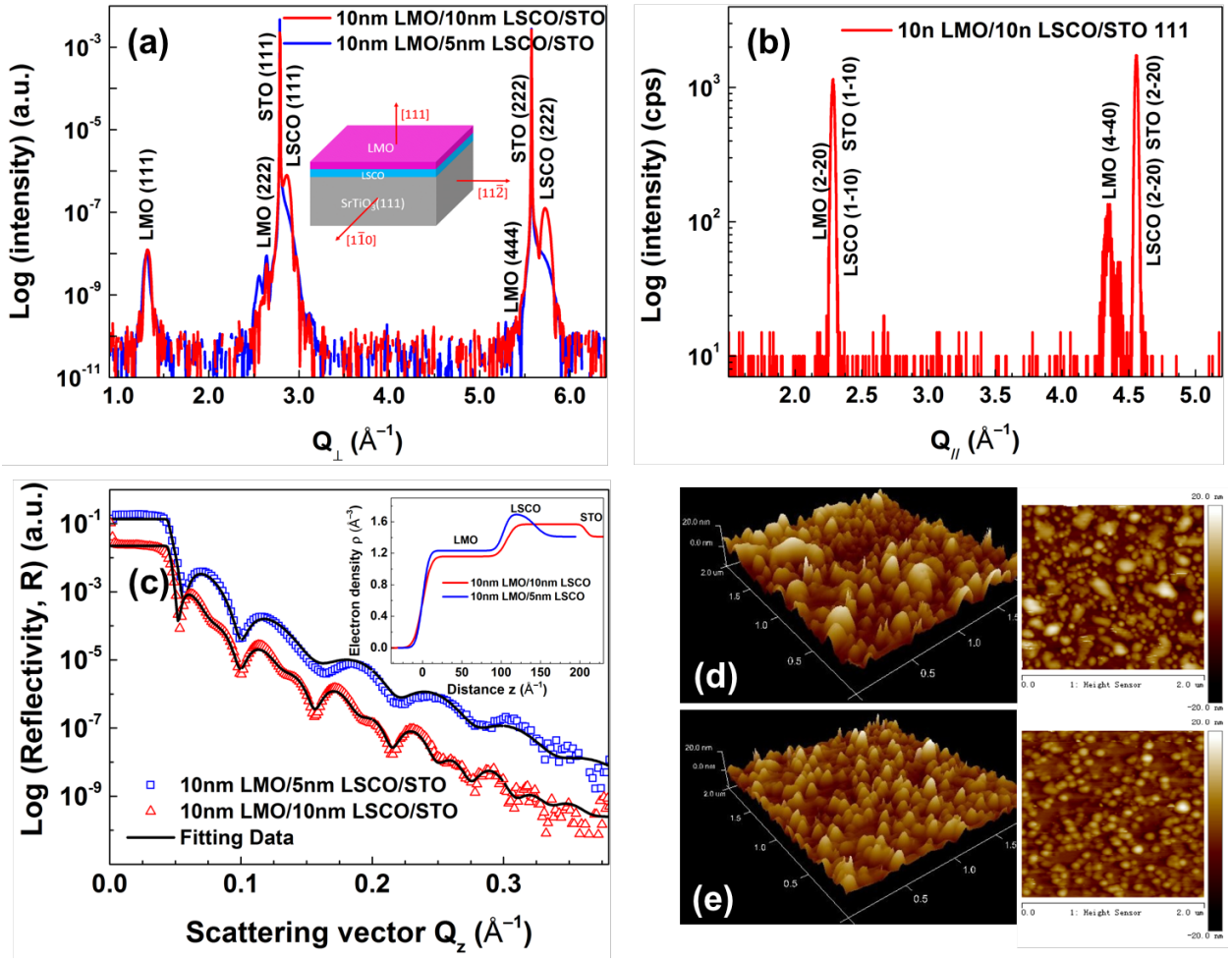

Figure 4.4 (a) Synchrotron XRD patterns from epitaxial LMO/LSCO bilayer thin films growing on STO (111). In-plane XRD (b) shows the LMO thin film obtained in-plane epitaxy with [1$\bar{1}$0] preferred orientation. (c) Ex situ XRR profiles for the hetero-epitaxial LMO/LSCO/STO (111) bilayer films. The fitting electron density profiles are shown in the inset. (d) and (e) Film morphology is exhibited by AFM images of the 10 nm LMO / 10 nm LSCO bilayer and 10 nm LMO / 5 nm LSCO bilayer, respectively.

Table 4.2 Crystal structures, lattice constant values, and lattice misfits for LiMn2O4, La0.5Sr0.5CoO3 and SrTiO3 of bulk and thin film.

Target	Crystal structure	Bulk lattice constants (Å)	Specular lattice constants (Å)	In-plane lattice constants (Å)	Bulk lattice misfits	In-plane residual lattice misfits
LMO	$Fd\bar{3}m$	8.248[1]	8.239	8.184	LMO/STO 4.9%	LMO/STO 4.8%
LSCO	$Pm\bar{3}m$	3.837[2]	3.799	3.901	LMO/LSCO 6.7%	LMO/LSCO 4.9%
STO	$Pm\bar{3}m$	3.905	3.905	3.905	LSCO/STO –1.7%	LSCO/STO –0.1%

[1]Bulk lattice constant parameter for LMO with 0.68 Li is 8.189 Å, which is used for subsequent calculations.

[2]Pseudocubic lattice constant parameter for bulk LSCO.

XRR profiles from the as-grown bilayers, shown in **Figure 4.4**c**,** exhibit periodic broad Kiessig fringes. The XRR spectrum from 10 nm LMO / 10 nm LSCO bilayer shows a doubling of the periodicity as expected given the equal layer thicknesses, whereas the 10 nm LMO / 5 nm LSCO bilayer shows single asymmetric peaks. The XRR fittings also shown in **Figure 4.4**c indicate that the LMO surface roughness was < 1 nm for both bilayers. The fitting results also reveal that the thinner LSCO buffer layer results in a smaller LMO surface roughness. AFM images of the as-prepared bilayer surfaces are shown in **Figure 4.4**d and e, indicating the height and width of LMO surface undulations are smaller for the thinner LSCO buffer layer, in agreement with the XRR results. Moreover, the calculated electron density profiles (inset in **Figure 4.4**c) indicates thinner LSCO buffer layer (5 nm) can result in a denser LMO film with slightly higher electron density.

Cross-sectional TEM images of the 10 nm LMO / 10 nm LSCO bilayer are shown in **Figure 4.5**. A lower-magnification image (**Figure 4.5**a) illustrates that the LMO surface has periodic depressions. The inset is a higher-magnification view of one such depression in the LMO layer surface. A higher magnification view (**Figure 4.5**b) depicts the bi-layer hetero-structure where the interfaces are clearly visible; the LSCO layer had a reasonably uniform thickness resulting in a flat LSCO/LMO interface, unlike the rough LMO surface. **Figure 4.5**c is a high resolution TEM image taken along the $[1\bar{1}0]$ LMO // $[1\bar{1}0]$ LSCO // $[1\bar{1}0]$ STO direction where the continuity of the lattice fringes from STO (110), LSCO (110) and LMO (220) planes (marked in yellow lines) clearly illustrates the hetero-epitaxial bilayer structure. The d-spacings of the LMO (111) and LSCO (111) lattice planes are calculated from the reduced FFT diffraction patterns, also shown in **Figure 4.5**c. For the LMO layer, d_{111} = 4.8 Å, which is larger than the d-spacing value 4.728 Å for bulk $Li_{0.68}Mn_2O_{4-\delta}$. Similarly, d_{111} of LSCO is calculated to be around 2.2 Å, slightly smaller than the theoretical value, i.e. 2.215 Å. Those interplanar spacing differences reveal specular lattice expansion and contraction occurred in the LMO and LSCO layers, respectively. That is in accordance with the results of the XRD measurements in **Table 4.2** above. An enlarged HRTEM image (**Figure 4.5**d) depicts the LMO/LSCO hetero-interface with an overlaid diamond-shaped structure model indicating atom columns positions. The inset presents a computed projection of the Mn diamond configuration from ideal $LiMn_2O_4$ spinel structure, viewed along $[1\bar{1}0]$ orientation as the TEM images. The $[1\bar{1}0]$ cross-sectional projection is a special direction along which Li, Mn and O reside on completely separated atom columns from each other. This enables direct visualization of the hetero-interfaces through HRTEM imaging.[32, 70] Moreover, the ratio of the shorter (m) and longer (n) diagonal lengths of the Mn diamond is a quick measurement of the

structural distortion of LMO due to oxygen and lithium deficiencies at the hetero-interface. The m/n ratio of LMO layer measured far beyond the LMO/LSCO interface shown in **Figure 4.5**d is around 0.71, which is close to the value for ideal cubic spinel LMO structure, i.e. 0.707.[70, 167] However, the ratio at the LMO/LSCO interface is found to be ~0.74, which approximates that for tetragonal oxygen-deficient $Li_{1-x}Mn_2O_{4-\delta}$, i.e. 0.732 (the pseudo-cubic lattice parameters for tetragonal LMO are: a = b = 8.111 Å, c = 8.646 Å)[185]. It results in that the in-plane lattice misfit between LMO and LSCO at the interface is reduced to 4.0% from 6.7% (**Table 4.2**). The phase transformation from spinel cubic to tetragonal allowed layer-by-layer epitaxial LMO thin layer growth to be favored up to several monolayers above the LSCO surface by compensating for the lattice misfit strain. Far above the interface, the LMO crystal symmetry became spinel cubic, relaxed through misfit dislocations and 3D islands formation.

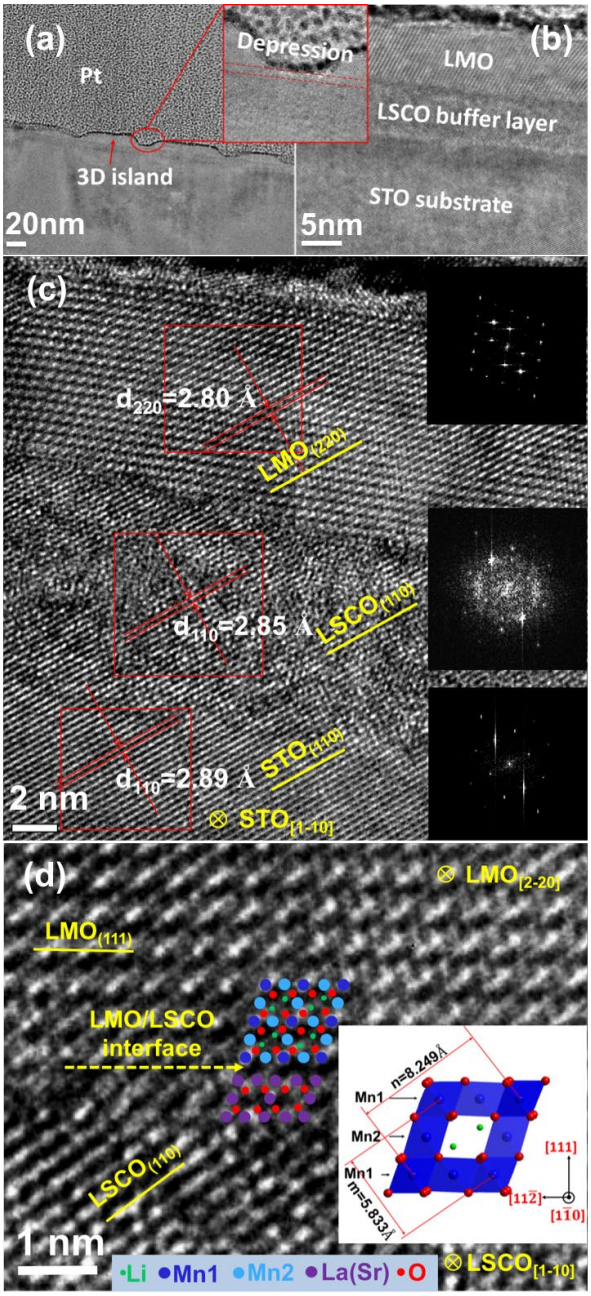

Figure 4.5 (a) and (b) TEM images showing hetero-structure of the 10 nm LMO / 10 nm LSCO / STO (111) bilayer film. 3D islands and depressions on LMO layer are illustrated in the enlarged inset. (c) Cross-sectional high resolution TEM image taken on the $(1\bar{1}0)$ plane along with reduced FFT diffraction patterns of LMO, LSCO and STO. (d) HRTEM image showing the LMO/LSCO hetero-interface. The overlaid diamond-shaped structure model indicates the atom columns positions. The inset is a projection of the diamond configuration of ideal spinel LMO along $[1\bar{1}0]$ direction, showing separate Li, O and Mn atom columns. Mn1 and Mn2 have different atom densities.

TEM-EDS elemental maps across the bilayer of the same TEM sample are shown in **Figure 4.6**a. Mn is detected only in LMO, whereas Co is present only in the LSCO layer. Sr distributes across both LSCO and STO substrate. La is mostly present in the LSCO layer; the La signal in the STO layer is an artifact due to peak overlap with Ti. The TEM results for LSCO grown on STO indicate that the layer remained coherently strained with a sub-nano flat surface. This suggests a layer-by-layer Frank–van der Merwe (FM) growth mode due to the relatively small LSCO/STO lattice misfit, i.e. –1.7%. The lack of strain relaxation is reasonably consistent with Matthews-Blakeslee theory for relaxation due to misfit dislocations, applied to oxide materials at these thickness and mismatch values.[186, 187] With rational and ideal assumptions (pure edge dislocations, Poisson ratio of LSCO ~ 0.3, burger's vector equals in-plane d-spacing), the critical thickness of strained LSCO film is about 2 nm according to Matthews-Blakeslee optimal relaxation theory.[165] The 10 nm LSCO film here continued to maintain epitaxy by forming misfit dislocations beyond the calculated critical thickness. On the other hand, for LMO grown on LSCO-coated STO, the layers were mostly relaxed and showed periodic depressions or undulations; such roughening is commonly observed due to the large mismatch between LMO and these substrates or the underlying layer[62, 71], suggesting Stranski-Krastanov (SK) mode growth.[188] In this mode, a thin flat film forms initially, followed by an instability in the growth front that leads to large surface roughness; the enlarged inset in **Figure 4.5**a appears to show that a thin initial layer of LMO (~2nm) is present on the LSCO layer beneath the depression. In this region, relaxation of the coherency strain probably occurs by a combination of misfit dislocations and depressions on the rough film surface.[188, 189] To further verify the different thin film growth mechanisms, **Figure 4.6**b shows an enlarged HRTEM image from **Figure 4.5**c, revealing a dislocation, labeled "T", at the LMO/LSCO (111) interface with the Burger's vector perpendicular to the LMO (220) planes. The

dislocation is more visible in the inverse FFT-filtered image shown in **Figure 4.6**c. In contrast, no dislocations are discerned at the LSCO/STO (111) interface (**Figure 4.6**d), indicating a coherently-strained LSCO layer as expected due to the small lattice misfit.

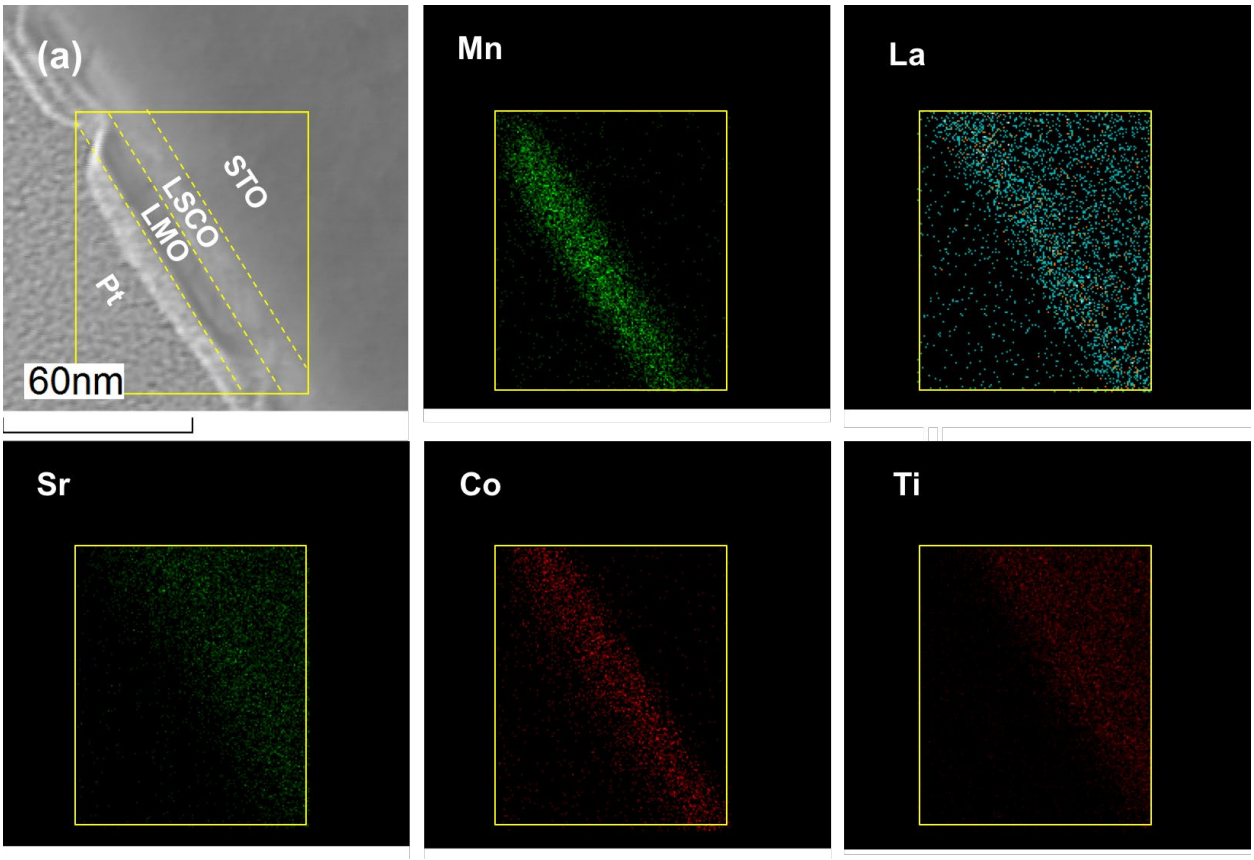

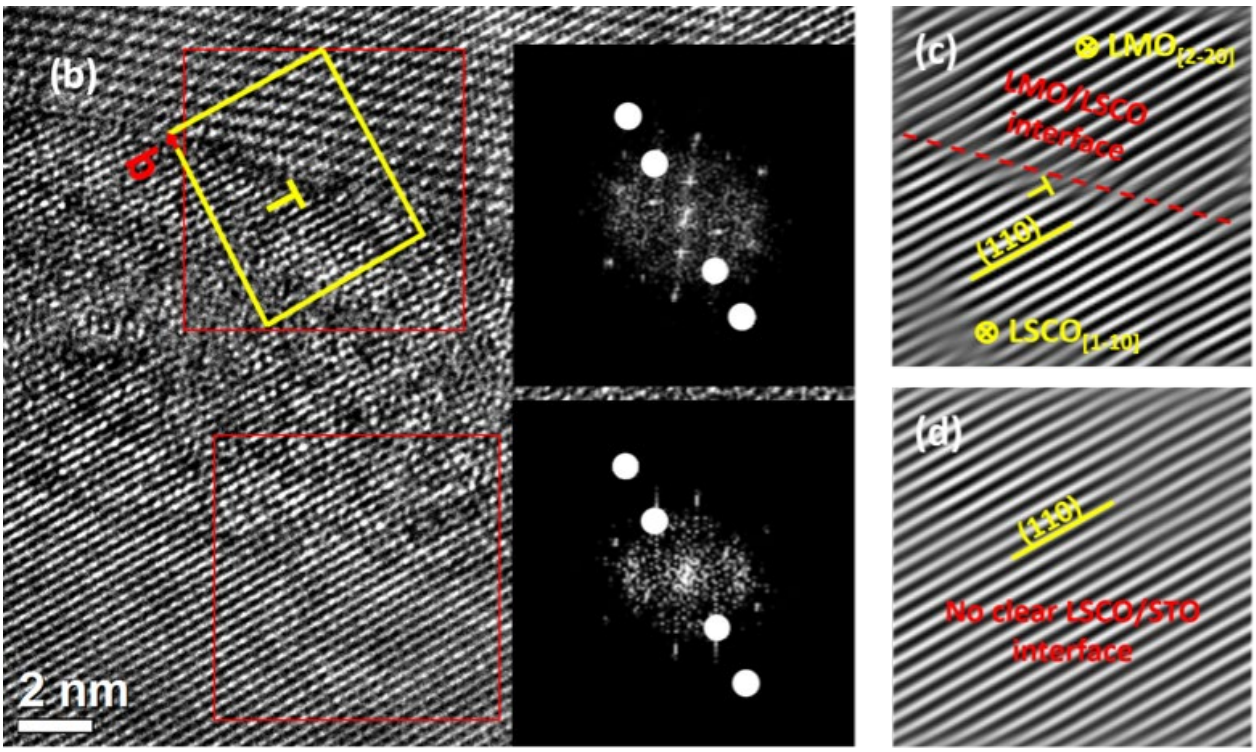

Figure 4.6 (a) Cross-sectional EDS elemental mapping on the TEM sample of LMO/LSCO/STO (111) bilayer thin film. (b) Cross-sectional HRTEM images taken along the [11$\bar{2}$] LMO // [11$\bar{2}$] LSCO // [11$\bar{2}$] STO direction showing hetero-interfaces of the 10 nm LMO / 10 nm LSCO/STO (111) bilayer. A dislocation labeled "T" was formed at the LMO/LSCO interface. Insets are reduced FFT diffraction patterns of the LMO/LSCO and LSCO/STO interfaces, respectively. (c) and (d) exhibit inverse reduced FFT images of the LMO (220) (440), LSCO and STO (110) (220) planes circled in the insets in (b), clearly showing a dislocation at the LMO/LSCO interface.

Synchrotron low angle XRR profiles for the 10 nm LMO / 10 nm LSCO bilayer before, during and after cycling are shown in **Figure 4.7**a. The dramatically different XRR curves after both the thin film was soaked in electrolyte and 1st cycle indicate notable interface structure and/or morphology changes between LMO and the liquid electrolyte. The similar XRR profiles after 1st and 3rd cycles indicate that the surface morphology of LMO did not evolve significantly beyond the first cycle. A four-layer model including STO, LSCO, LMO, and SEI (inset in **Figure 4.7**a) was applied to fit the XRR spectra using Motofit package in Igor Pro software. Part of the fitting results are shown in **Table 4.3**. Significant shape changes of the XRR spectra resulted from

thickness and surface morphology changes of the SEI layer between the LMO surface and the liquid electrolyte. An ~ 3.3 nm SEI layer, assumed to consist of low density lithium salts and various organic compounds, was formed after LMO contacted with the electrolyte solution, in agreement with prior reports for epitaxial LMO thin films.[21, 25, 59] The refined electron density of this SEI layer is 0.0413 $Å^{-3}$, similar to previously reported values.[59, 62] In addition, the fitting results indicate that the SEI layer became thicker and rougher after 3 cycles, while the LMO (111) surface morphology stayed relatively stable. The 2D intensity spectra from *in situ* Synchrotron XRD during the first 3 cycles is shown in **Figure 4.7**b for the LMO (111) Bragg peak. The LMO (111) peak position irreversibly shifts to lower Q value after the first cycle and then stays nearly constant, indicating that the LMO redox reaction almost stopped after the first cycle.

Table 4.3 Parameters obtained by fitting the in situ XRR data from the 10nm LMO/10nm LSCO/STO bilayer. (unit: Å)

Conditions	SEI layer		LMO		LSCO		STO	
	thickness	roughness	thickness	roughness	thickness	roughness	thickness	roughness
As-deposited	-	-	108.6	8.1	99.7	8.3	-	7.9
As-assembled	32.9	11.5	105.2	6.8	95.2	7.9	-	9.3
After 1st cycle	43	15.9	100.4	6	98.4	25.2	-	6.1
After 3rd cycle	50.9	20.3	91.1	6.5	93.4	27.9	-	6.2

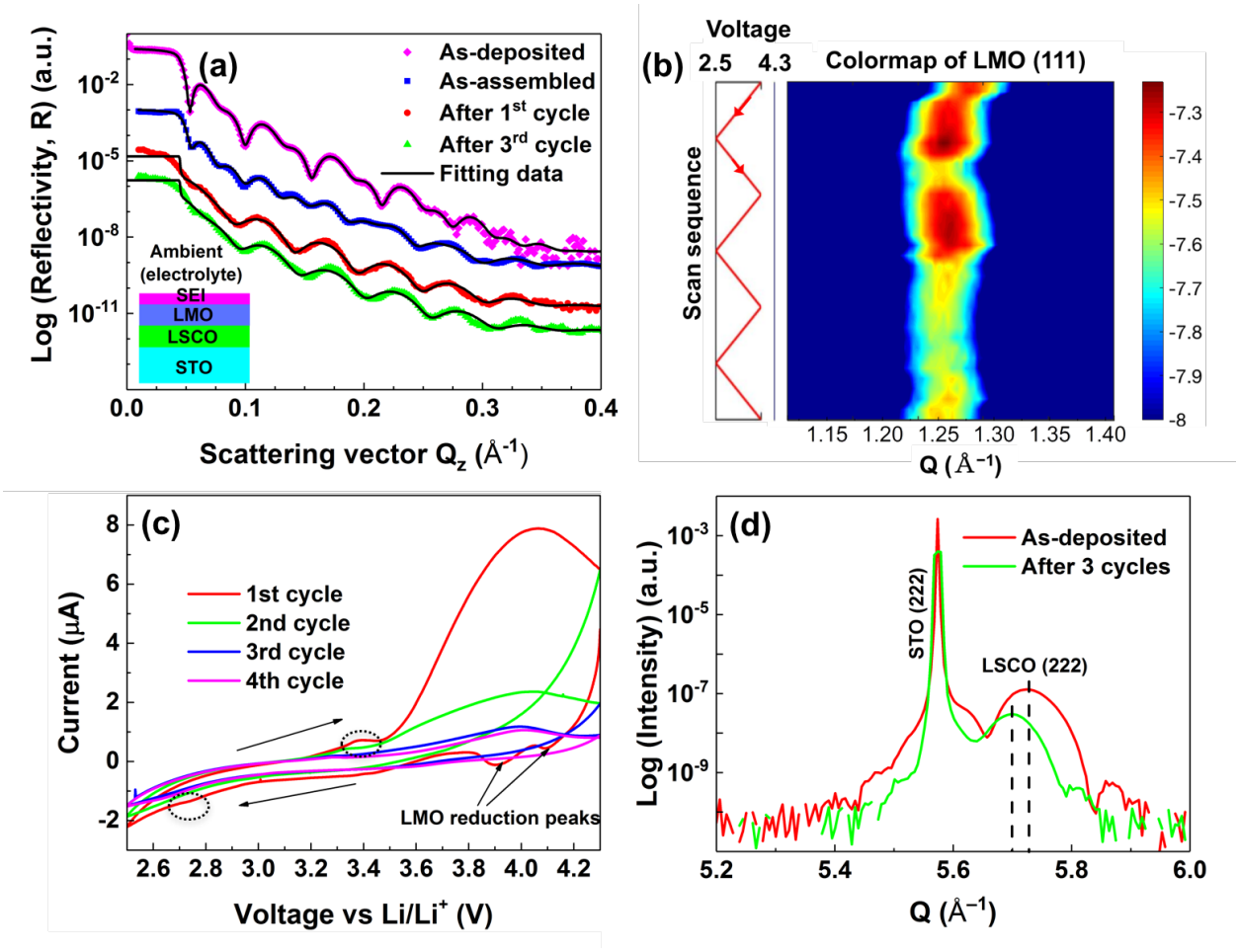

Figure 4.7 (a) XRR profiles by synchrotron X-ray scattering for the 10 nm LMO / 10 nm LSCO bilayer films of as-deposited, as-assembled, after 1st and 3rd cycles. The profiles are vertically offset in order to make clear comparison. The inset shows a four-layer model used to fit the XRR spectra. (b) 2D intensity spectra from in situ synchrotron XRD of LMO (111) peak during 3 voltammetric cycles between 2.5V to 4.3V at potential intervals of 0.5 mV/s. (c) Cyclic voltammetry of a 10 nm LMO / 10 nm LSCO/STO (111) bilayer thin film between 2.5V to 4.3V at potential intervals of 0.5 mV/s. The Mn^{3+}/Mn^{2+} redox peaks around the 3.0 V plateau are circled by two black dashed circles. (d) Synchrotron XRD of LSCO peak (222) from the 10 nm LMO/10 nm LSCO/STO (111) bilayer. The peak slightly shifted to lower Q after 3 voltammetry cycles.

Cyclic voltammetry profiles over the first four cycles of the 10nm LMO / 10nm LSCO bilayer are shown in **Figure 4.7**c where redox peaks are present for the first cycle. Data began to be obtained after charging the cell to 4.3V. The 0.5 mV/s potential sweep rate was slow enough to get good cyclic voltammetry resolution for very thin (10 nm) LMO layers, as indicated by the

LMO reduction peaks observed in the first cycle.[182] Two reduction peaks coming from LMO are clearly identified during the first discharge reaction at Mn^{3+}/Mn^{4+} cathodic plateaus. During the following charge process, a very broad redox peak resides at a voltage of around 4.1V, which is not typical for LMO and obscures the LMO Mn^{3+}/Mn^{4+} anodic peaks. The net charge obtained by integrating over this peak is much larger than the charge from complete delithiation of the LMO layer. The additional charge associated with this peak may originate from a change in oxygen content of the LSCO layer. Indeed, the observed excess charge can be explained by an ~ 50% change in the lattice oxygen content in the LSCO buffer layer. After the first cycle, little if any redox reactions are detected from either LMO or LSCO. This is in apparent agreement with the result in **Figure 4.7**b, where LMO X-ray peak shifts only in the first cycle. Subsequent electrical sheet resistance measurements show a significant decrease in LSCO electrical conductivity by around 10 times. These results suggest that the initial charging process caused irreversible changes in the LSCO, resulting in the decreased conductivity, which prevented further LMO redox reactions. In addition, the LMO Mn^{2+}/Mn^{3+} redox peaks can be identified around the 3.0 V plateau during the first cycle, marked by two black dashed circles. The redox peak positions are similar to those reported for LMO thin films in the literature,[51] but the peaks are weak and poorly resolved. The broad weak peak shape was probably caused by structural defects, similar to prior results for $LiNiVO_4$ thin films.[190]

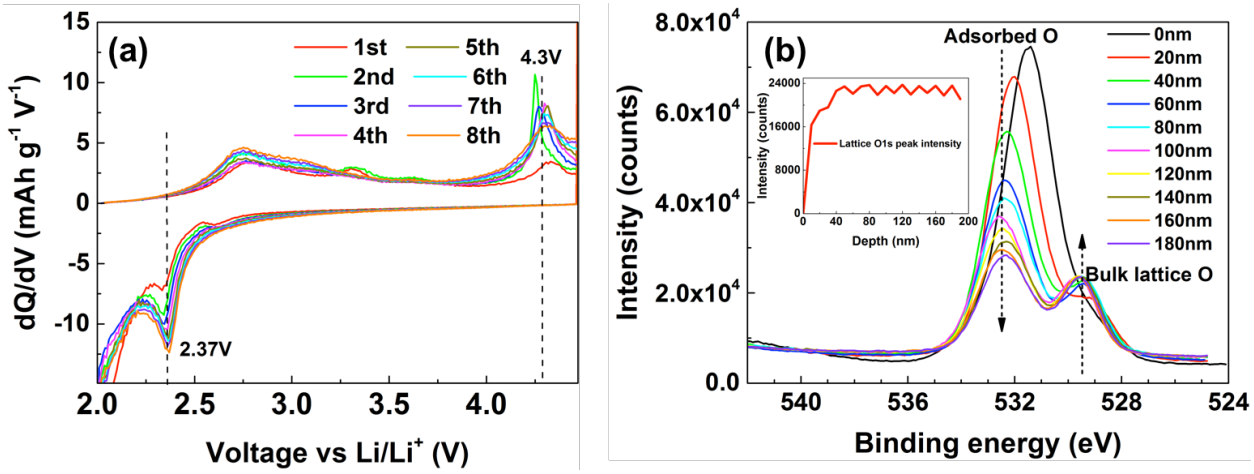

Figure 4.8 (a) Galvanostatic cycling test on LSCO powder as active cathode materials between 2.0V to 4.5V using a current density of 10 μA/g. (b) XPS depth profile of doublet O1s peak from LSCO powder after 100 galvanostatic cycles. The inset shows a depth profile of the bulk lattice O1s peak intensity.

To further examine the electrochemical characteristics of LSCO, synthesized LSCO powder was used as the active cathode material in a half-cell, and galvanostatically cycled between 2.0V to 4.5V at a current density of 10 μA/g; the results are shown in **Figure 4.8**a. One oxidation peak at 4.3V is found, which is similar to the anodic peak around 4.1V of the LSCO/LMO bilayer at the first charge process (**Figure 4.7**c). One reduction peak at 2.37V is also identified. It is inferred that those two redox peaks are in coincidence with oxygen reduction and evolution reactions in a lithium-air battery cathode with LSCO as catalysts (ORR: $O_2 + Li^+ + e^- = LiO_2$, $LiO_2 + Li^+ + e^- = Li_2O_2$).[132] Therefore, the oxygen evolution reaction during the first charge process of the LSCO/LMO bilayers resulted in LSCO lattice oxygen loss which cannot be restored due to low oxygen content in the glovebox (<1 ppm). In consequence, electrical conductivity of LSCO is dramatically reduced ascribed to increased oxygen vacancy concentration.[174] **Figure 4.7**d shows the LSCO 222 peak from the 10 nm LMO / 10 nm LSCO/STO bilayer irreversibly shifted to lower Q value after 3 cycles, also indicating oxygen loss in LSCO along with a lattice spacing increase.

To further verify the aforementioned LSCO lattice oxygen loss interpretation, XPS depth profiling was done on cycled LSCO powder. The evolution of the doublet O1s peak along a depth range of 190 nm is exhibited in **Figure 4.8**b. Two O1s peak positions with binding energy (BE) values of around 529.5 eV and 532.5 eV were identified. The peak with higher BE value is generally accepted as adsorbed oxygen while the peak with lower BE value is attributed to be the weak metal-oxygen bond (bulk lattice oxygen).[191] The inset shows the peak intensity of the bulk lattice O1s as a function of sputtering depth. It can be seen that the peak intensity keeps almost constant after a rapid increase over the first 40 nm of depth, indicating significant lattice oxygen loss at the outermost surface of the electrochemically cycled LSCO powder. These results, taken together, strongly suggest that oxygen loss during cycling led to a dramatic electrical conductivity loss of the LSCO powder, which is not desired for a conductive buffer layer material.

4.4 Conclusions

In summary, hetero-epitaxial LMO/LSCO bilayer thin films have been grown on STO (111) substrates using PLD. *Ex situ* XRD and XRR measurements verified successful synthesis of 10 nm epitaxial LMO thin films. LMO/LSCO bilayers had a "cube-on-cube" epitaxial relationship with the STO substrates. It was demonstrated that a thinner LSCO buffer layer favored lower LMO surface roughness. Cross-sectional high resolution TEM imaging of the bilayer thin films indicated a Stranski-Krastanov (SK) growth mode of LMO layers on which 3D islands and depressions were formed due to the large lattice mismatch between LMO and the underlying LSCO/STO. Misfit dislocations at the LMO/LSCO hetero-interface were discerned through HRTEM. A phase transformation from cubic spinel LMO to tetragonal oxygen-deficient LMO was observed at the LMO/LSCO interface, suggesting epitaxial LMO growth was facilitated by an interface structural

distortion to reduce lattice misfit strain. The overall crystal quality and surface flatness of the hetero-epitaxial LMO/LSCO bilayer thin films was generally comparable or better than observed for other back-contact materials. Significant changes of the bilayer XRR profiles after battery assembly indicates formation of a SEI layer (~3.3 nm by XRR refinement) which got thicker and rougher after cycling while the LMO (111) surface morphology stayed relatively stable.

In situ synchrotron XRD measurements showed clear characteristics of LMO redox reactions which, however, stopped after the first cycle, consistent with the cyclic voltammetry results showing no apparent redox peaks after first discharge step. A probable explanation is that the buffer layer LSCO lost electrical conductivity due to lattice oxygen loss during the first charge process, which is further verified by a severely reduced intensity of the bulk lattice XPS O1s peak at the outermost layer (40nm) of electrochemically cycled LSCO powder. Despite this issue, further studies of LSCO may still be warranted because of the general difficulty of finding a good epitaxial conducting back-contact layer. As discussed in the Introduction, various approaches have been reported including Nb:$SrTiO_3$ substrates and various conducting-layer / substrate systems. All of these, with the possible exception of $SrRuO_3$, have shown problems with conductivity loss or poor LMO epitaxy due to three-dimensional island formation or poor crystal quality. A possible avenue for future work can be seen by noting that LSCO layer retain ~ 10% of their original conductivity after electrochemical cycling. Thus, increasing the LSCO layer thickness may provide sufficient electrical connection to allow good cycling characteristics.

4.5 Acknowledgments

This work was supported as part of the Center for Electrochemical Energy Science, an Energy Frontier Research Center funded by the U.S. Department of Energy, Office of Science, Basic Energy Sciences (DE- AC02-06CH11357). Research at the Advanced Photon was supported by DOE, Office of Science, BES. This work made use of the EPIC, Keck-II, and/or SPID facility(ies) of Northwestern University's NUANCE Center, which has received support from the Soft and Hybrid Nanotechnology Experimental (SHyNE) Resource (NSF ECCS-1542205); the MRSEC program (NSF DMR-1121262) at the Materials Research Center; the International Institute for Nanotechnology (IIN); the Keck Foundation; and the State of Illinois, through the IIN. This work also made use of Pulsed Laser Deposition Shared Facility at the Materials Research Center at Northwestern University supported by the National Science Foundation's MRSEC program (DMR-1121262).

Chapter 5: Revisit Cathode Electrolyte Interphase on Thin-Film $LiMn_2O_4$ Cathodes

5.1 Introduction

It is well known in lithium battery community that the electrically nonconductive solid electrolyte interphase (SEI) on anode plays a critical role in preventing continuous liquid electrolyte reductive decomposition while resulting in direct loss of lithium and hence capacity by formation of lithium salts in gradually growing SEI layer on the anode surface.[23, 73-75] The electrolyte decomposition reactions occur during recharging due to higher reduction potential of the electrolyte than chemical potential of anode materials.[18] Similarly, a passivation interphase layer or so-called cathode electrolyte interphase (CEI) usually forms on cathode materials surface due to oxidative decomposition of the electrolyte solvent (such as ethylene carbonate (EC), dimethyl carbonate (DMC), ethyl methyl carbonate (EMC), etc.) and side reactions (nucleophilic attack) of electrolyte with cathode materials surface.[76, 77] However, there is much less known about the nature of CEI layer, such as chemical compositions, formation mechanisms, functionalities, etc. Moreover, properties of CEI vary with cathode surface crystalline structure, state of charge, temperature and electrolyte compositions (i.e. solvents, lithium salts and/or additives), etc..[77] It has been point out there are differences between SEI and CEI formation processes.[23, 78] Apart from electrolyte solvent decomposition on cathode surface similar to SEI formation, CEI formation processes also involve cathode materials reaction with electrolyte, such as transition metal dissolution and cathode surface interphase formation reactions.[60]

Lithium manganese oxide $LiMn_2O_4$ (LMO) has been extensively receiving studies as one of the most common cathode materials due to its superior merits such as high abundance, low cost, environmental friendliness, proper redox potential (i.e. 4 V vs. Li/Li^+), and relatively high

chemical stability and rate capability compared to conventional cathode materials $LiCoO_2$ and $LiFePO_4$.[1, 5, 19, 34, 43, 99] In spite of those advantages, one critical challenge of LMO cathode for mature application is severe capacity loss or poor cycalability upon extended cycling especailly at elevated temperature.[20, 21] Conventional widson being that electrode-electrolyte interfacial (electro)chemistry, including manganess dissluiton into the liquid electrolyte, accounts for degradation of LMO cathode.[60, 82] Since manganese dissolution reactions are directly associated with CEI layer formation on LMO cathode surface, it is enssential and necessary to develop deep understanding of CEI layer in order to illustrate LMO cathode capacity fading mechanisms. Although several researchers have reported that it is the increased interfacial resistances rather than mere manganese dissolution that are responsible for the majority of cell capacity loss, manganese dissolution is considered to be a detrimental chain-reaction factor leading to the capacity fading since increase of cell resistances at both anode and cathode interfaces, and growth of SEI and CEI layers are inevitably correlated with manganese ions dissolution, migration and re-deposition (DMD) processes.[21, 60, 127, 192] It's generally believed that dominant cause of manganese dissolution are Mn^{3+} disproportionation reaction due to attack of solvent-derived HF acid formed from fluorinated lithium salt (such as $LiPF_6$, $LiBF_4$ and $LiAsF_6$) dissociation in present of traces of moisture at the interface between LMO and electrolyte.[26, 61, 78, 79, 107]

For over two decades, the prevailing explanation of Mn^{3+} ions disproportionation in LMO (i.e. $2Mn^{3+} \rightarrow Mn^{2+} + Mn^{4+}$) followed by Mn^{2+} ions dissolution into organic electrolyte solvents in LIBs originates from report by Hunter who found soluble Mn^{2+} when he tried to obtain λ-MnO_2 by treating LMO in an aqueous acidic solution.[20, 107] However, this kind of concept transfer from aqueous solution to aprotic organic solvent lacks theoretical and experimental supports. Ever since that, nearly all publications touching upon Mn dissolution merely assume Mn^{2+} is the only readily

soluble species in the liquid electrolyte.[21, 60, 67, 126, 127, 193-196] Moreover, it has been believed and later experimentally verified those soluble Mn ions are prone to migrating and re-depositing on anode surface as components of SEI layer, although controversy being there around oxidation state of those precipitated manganese species on anode surface.[21, 127, 129, 195, 197, 198] To our best knowledge, there are little thorough investigations on dissolved Mn ions in the CEI layer attached LMO cathode surface.[128] Kim et al. reported re-deposition of manganese compounds (Mn_xY, Y = O, F, CO_3) on delithiated LMO cathode surface after storage at elevated temperatures.[192] However, further study is not available to determine whether manganese also exists in CEI layer of reversibly cycled LMO cathode and corresponding oxidation state of those residual Mn ions.

Therefore, the primary object of this work is to characterize and identify chemical compositions in CEI layer on cycled LMO cathode, especially addressing existence and oxidation state of dissolved Mn ions in CEI layer. Experimentally, UV-vis spectroscopy, electron paramagnetic resonance (EPR), inductively coupled plasma (ICP) spectroscopy, X-ray absorption near-edge spectroscopy (XANES), photoelectron spectroscopy (PES) with conventional or synchrotron X-ray radiation or neutron radiation sources coupled with depth profiling capability haven been widely used to examine and identify chemical species in CEI layer.[76, 78, 80, 81, 128, 199, 200] In this work, X-ray photoelectron spectroscopy (XPS) depth profiling combined with scanning transmission electron microscopy (STEM) – energy dispersive X-ray spectroscopy (EDS) were adopted to comprehensively study CEI layer on a well-constructed LMO thin film cathode which facilitated precise and easy aforementioned characterizations compared to LMO powder composite electrodes accompany with undesired effects from particle shape and size, pack macropores, solvents, binders, additives, etc.[26, 27]

5.2 Experimental Details

Sample Preparation: A stoichiometric $LiMn_2O_4$ target (2 inch in diameter, Kurt J. Lesker Company, 99.9% purity) was used as the sputtering material for LMO thin film deposition. Stainless steel (SS) substrates with a diameter of 15 mm and thickness of 0.5 mm were first mechanically polished on a rotating wheel (EcoMet 250 grinder/polisher) using an 8 μm polishing paper. Next, the SS substrates were further polished using a series of micro-cloth and diamond/Al_2O_3 suspensions with sizes from 6 μm down to 0.05 μm. The final prepared SS substrates obtained a mirror-like appearance (**Figure 5.1**a) with a surface roughness around 3 nm shown by AFM in **Figure 5.1**b. Prior to thin film deposition, the SS substrates were successively washed in acetone and ethanol ultrasonic bath. Depositions were done in a sputter apparatus (ATC-Orion 8 HV, AJA International Inc.) with a base vacuum of 10^{-6} Torr. The substrates were first coated with a 500 nm Au-Pd layer by DC sputtering. The Au-Pd layer serves as both current collector and barrier layer preventing Fe, Cr and Ni inter-diffusion from SS substrates to LMO layers. LMO thin film deposition was conducted at a radio frequency power of 150 W and under a mixed gas flow of 6 sccm O_2 and 20 sccm Ar at 5 mTorr and room temperature. Afterwards, the deposited LMO films with nominal thickness of 100 nm were annealed at 450 ºC and 550 ºC in air for 2 hours to get crystalline cubic spinel structure.

Electrochemical Measurement: All the electrochemical tests were performed using CR2036-type coin cells with the prepared LMO thin films as positive electrode and lithium metal discs as the counter and reference electrodes. Around 100 mL electrolyte, a mixture of 1 M $LiPF_6$ dissolved in ethylene carbonate (EC) and ethyl methyl carbonate (EMC) (v/v = 1:1), was used for each cell. All cells were assembled in a glovebox filled with high-purity argon (O_2 < 0.5 ppm)

followed by uniaxial pressing at a pressure of 1000 psi. Galvanostatic cycling was done on a galvanostat testing system (Arbin Instrument) at a voltage range of 3.5 to 4.4 V at a current rate of 4C (53 μA). Combined measurements of galvanostatic cycling and in situ electrochemical impedance spectroscopy (EIS) were performed with a bi-potentiostat / galvanostat (SP-300, Bio-Logic Science Instrument). The EIS data were recorded between 100 kHz and 10 mHz applying an AC voltage of 10 mV after the coin cell was fully discharged to 3.5 V and the OCV got stable by resting the cell for 30 minutes. EIS data were collected in every cycle for the first 10 cycles and once in every 10 cycles for the rest 190 cycles.

Characterization and Data Analysis: For post characterizations of the cycled LMO thin films, the cells were disassembled in the glovebox, and rinsed with DMC solution three times and stored for 3 days to completely remove the residual electrolyte salts. The surface morphologies of all pristine and cycled LMO thin films were observed by atomic force microscope (AFM, Bruker Dimension FastScan®) and scanning electron microscope (SEM, Hitachi SU8030). Grazing incidence X-ray diffraction was carried out using ATX-G (Rigaku) with Cu Kα (λ = 1.5406 Å) radiation. X-ray photoelectron spectroscopy (XPS) measurements including depth profiling were performed on a spectrometer equipped with a Mg Kα radiation (Thermo Scientific Co., ESCALAB 250Xi). TEM samples of cycled thin films were prepared by a dual-beam focused ion beam (FIB, FEI Helios Nanolab 600). High resolution cross-sectional observations of the LMO thin film cathodes were conducted on an aberration-corrected scanning transmission electron microscope (STEM, BioCryo Hitachi Co., HD2300) at an acceleration voltage of 200 kV. Energy dispersive X-ray spectroscopy (EDS) mapping scans were conducted on the same TEM microscope equipped with ultra-sensitive dual EDS detectors.

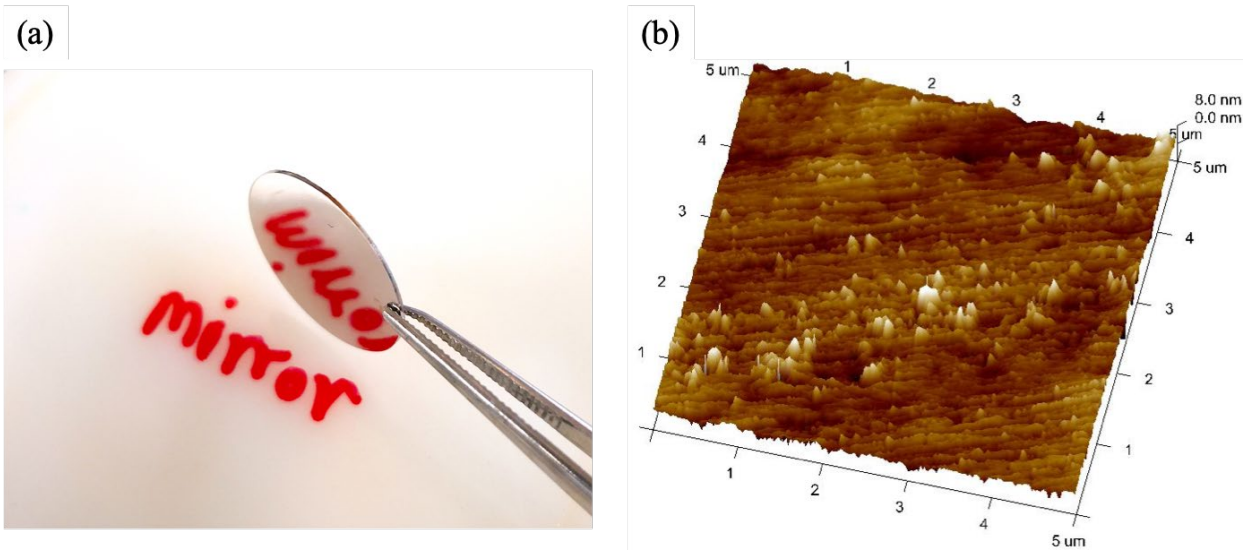

Figure 5.1 (a) Well prepared mirror-like SS substrates after polishing and ultrasonic bath cleaning. (b) 3D AFM image illustrating surface morphology of the prepared SS substrates with a root-mean-square (RMS) roughness of around 3 nm.

5.3 Results and Discussion

LMO thin films have been directly deposited on SS substrates by researchers using RF sputtering and pulsed laser deposition (PLD).[57, 105, 201-205] Although element contaminations due to inter-diffusion of Fe, Cr and Ni in SS at high substrate temperature was reported, there were actually little concerns in literature about purity of LMO thin film grown on SS substrates or efforts to mitigate this issue to get high quality LMO thin films.[203] Therefore, strategy in this work was first polish SS substrates to get mirror-like surface (roughness around 3 nm shown in **Figure 5.1**a) which facilitated subsequent growth of uniform and dense barrier layer. Next, a thick Au-Pd layer (500 nm) was deposited by DC sputtering on the prepared SS substrate working as a current collector and physical barrier layer as well. LMO thin films were deposited on top of Au-Pd layer at room temperature using RF sputtering followed by annealing in air at 450 ºC and 550 ºC. Relatively low annealing temperatures for LMO thin films were chosen to avoid enhanced inter-diffusion issues discussed above. Grazing incidence X-ray diffraction (GIXRD) patterns of LMO

thin films were displayed in **Figure 5.2**a from which it can be seen that diffraction pattern of LMO thin film annealed at 450 ºC matches well with that of cubic spinel LMO while LMO annealed at higher temperature, i.e. 550 ºC, was apparently contaminated by inter-diffused Fe and Cr from the SS substrate since there are notable peak shifts of the diffraction lines. This indicates Fe and Cr are still able to remarkably diffuse through the thick Au-Pd barrier layer once the annealing temperature higher than 450 ºC. XPS depth profiling was applied to examine elemental contents including Fe and Cr (**Figure 5.2**b). Sputtering depth was approximated according to the LMO thin film thickness and sputtering rate. It is clear that contents of both Fe and Cr at the interface between LMO and Au-Pd layer were less than 5% and there were nearly no any contaminations of alien elements within the body of LMO thin film layer. According to XRD and XPS results, all LMO thin film cathodes for the following study were annealed at 455 ºC which guaranteed high quality and purity LMO thin film cathodes.

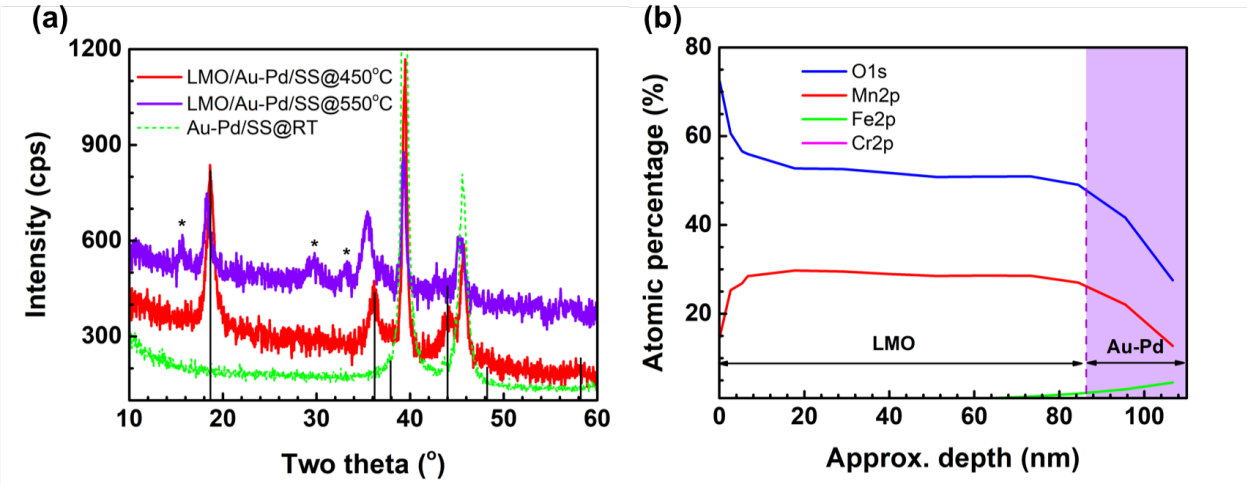

Figure 5.2 (a) Grazing incidence XRD patterns of LMO thin films annealed at 450 ºC (purple line) and 550 ºC (red line), and a Au-Pd coated SS substrate (green line). Diffraction lines from cubic spinel LMO are illustrated in black line. Peaks marked by asterisks are from SS substrate. (b) Element distributions (O, Mn, Fe and Cr) in LMO and Au-Pd layer obtained from XPS depth profiling.

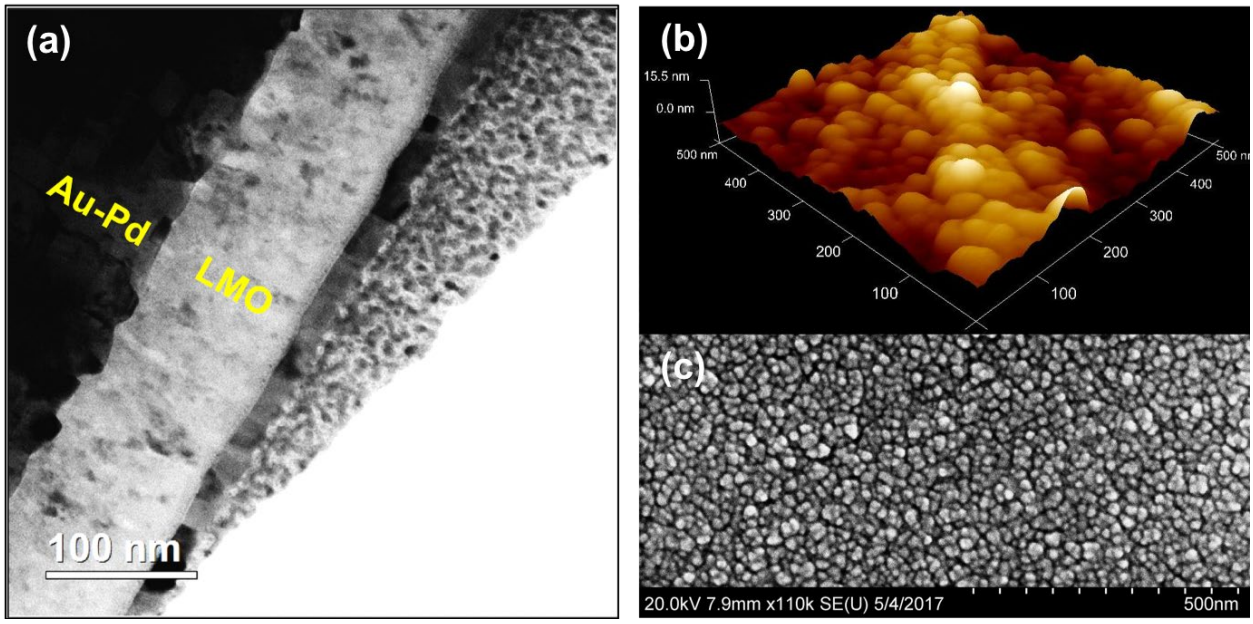

Figure 5.3 (a) STEM image showing cross section of 100 nm LMO/500nm Au-Pd/SS thin film cathode. Surface morphology of the LMO thin film cathode is illustrated by images from AFM (b) and SEM (c).

The cross-sectional structure of LMO thin film is revealed by STEM in **Figure 5.3**a which indicates a dense LMO layer of around 100 nm on top of Au-Pd barrier layer with a smooth surface. The surface morphology is further illustrated by AFM and SEM images in **Figure 5.3**b and c, respectively and it is estimated the LMO thin film surface RMS roughness is 3.8 nm and surface round-shaped grain size is about 30 nm. Nano-sized grains increase contact areas between LMO cathode and liquid electrolyte, which will accelerate Mn dissolution and growth of CEI layer. Therefore, it is supposed to observe well-formed CEI layer at LMO thin film cathode interface, fostering easy subsequent characterizations using XPS and STEM.

The 100 nm LMO thin film cathode was tested by galvanostatic cycling between 3.5 – 4.4 V under a current rate of 30 $\mu A/cm^2$ (or 4C) for 200 cycles. According to the cycling results plotted in **Figure 5.4**a, the prepared LMO thin film cathode obtained an initial specific capacity of 58

mAh/g which is much smaller than the theoretical value of LMO (148 mAh/g). It was primarily caused by low crystallinity of the LMO thin film which was annealed only at 450 ºC to avoid elemental contaminations from SS substrates. Moreover, 11% of the initial capacity was lost after 200 cycles. Two redox plateaus at around 4.0 V and 4.2 V can be faintly discerned on the charge/discharge capacity curves. They are more clearly revealed from the differential capacity plots shown in **Figure 5.4**b where the first redox plateau resides at 4.01 V and second redox reaction occurs at 4.17 V. It has been found the two redox peaks are characteristic of one Li^+ extraction-insertion from/into the cubic spinel framework of $LiMn_2O_4$/λ-Mn_2O_4 which is a two-step process represented by the following two redox reactions[47, 48]:

$$\lambda\text{–}\,Mn_2O_4 + 0.5Li^+ + 0.5e^- \leftrightarrow Li_{0.5}Mn_2O_4 \quad (5.1)$$

$$Li_{0.5}Mn_2O_4 + 0.5Li^+ + 0.5e^- \leftrightarrow LiMn_2O_4 \quad (5.2)$$

Splitting of the intercalation-deintercalation process is believed to be caused by rearrangement of lithium ions once a stoichiometry of around $Li_{0.5}Mn_2O_4$ is reached upon lithiation from λ-Mn_2O_4.[206] Eq 5.1 represents the redox reaction at higher potential plateau (4.17 V) with flat slope where two phases coexist while Eq 5.2 stands for redox reaction at lower potential plateau (4.01 V) with steep slope where only one phase exist.[48, 49] In addition, a tiny overpotential of around 10 mV is observed from dQ/dV plots in **Figure 5.4**b which is much smaller than what's reported for LMO particle composite cathodes[207], indicating this LMO thin film cathode demonstrated higher rate capability due to shortened Li^+ diffusion pathway.

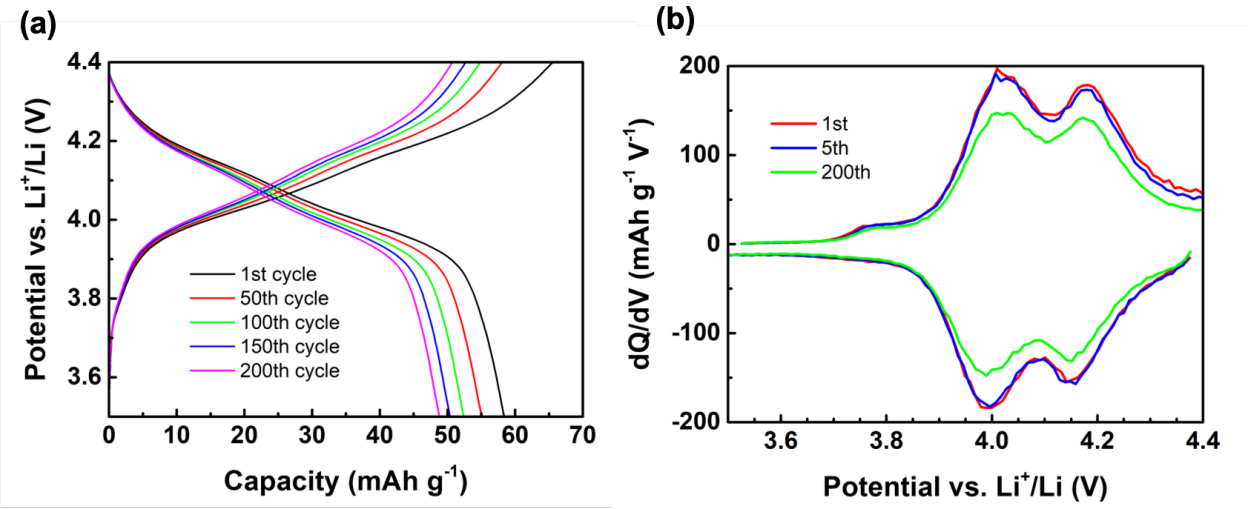

Figure 5.4 (a) Charge and discharge curves for 100 nm LMO / 500nm Au-Pd / SS thin film cathode cycled at 4C in the voltage range of 3.5 – 4.4 V vs Li^+/Li. (b) Differential capacity (dQ/dV) plots derived from data in (a) at 1st, 5th and 200th cycles.

The coin cells were disassembled after cycling and LMO thin film cathodes were carefully cleaned for further characterizations. The surface morphology of cycled LMO thin film cathode at fully discharged state is illustrated by SEM in **Figure 5.5**b indicating a CEI layer formed on the surface by comparison with surface morphology of pristine LMO depicted in **Figure 5.5**a. The CEI layer with large cracks (indicated by red arrow in **Figure 5.5**b) consisted of much smaller particles than LMO thin film. It is found that the CEI layer was actually thick and relatively dense as displayed by a STEM image in **Figure 5.6**a. Since nominal thickness of pristine LMO thin film is 100 nm, the top portion on LMO surface in the STEM image must be CEI layer which was around 100 nm thick. In addition, similar contrasts between CEI and LMO layer indicate CEI layer was in fact dense and probably contained heavy element such as Mn, which is verified by STEM-EDS mapping of Mn shown in **Figure 5.6**b. It can be found that considerable account of Mn resided in CEI layer. In contrast to what's believed in literature that Mn ions lost from LMO are completely dissolved into the liquid electrolyte and further migrate to anode side[21, 126], we suggest

Mn ions also exist in the thick CEI layer. To our knowledge, this is the first time to report Mn ions in CEI layer on a cycled LMO cathode and evaluate oxidation state of those newly discovered Mn ions to be discussed next.

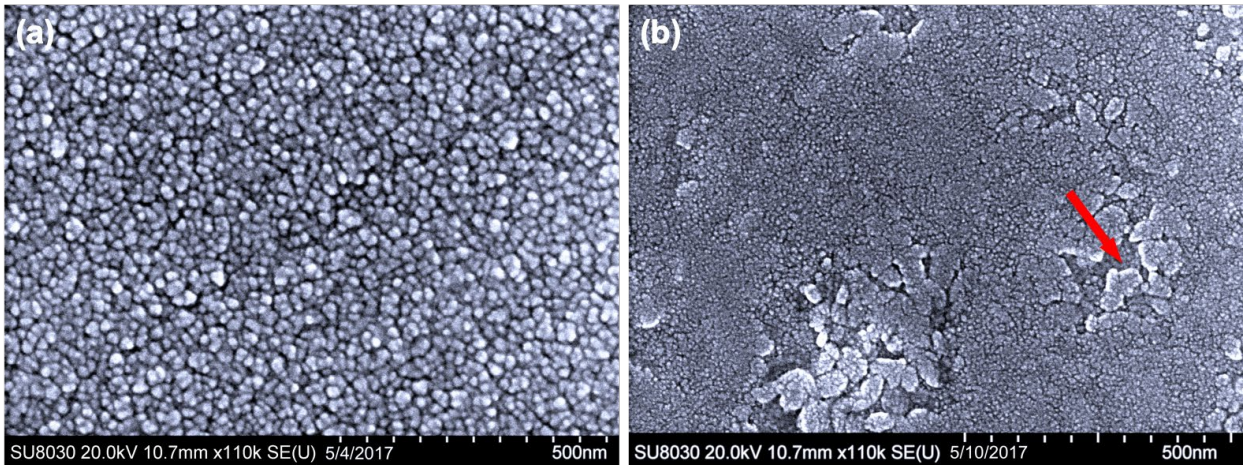

Figure 5.5 Surface morphology of LMO thin film cathode before (a) and after (b) 200 cycles at 4C. Red arrow in (b) indicates cracks of CEI layer on surface of the cycled LMO thin film cathode.

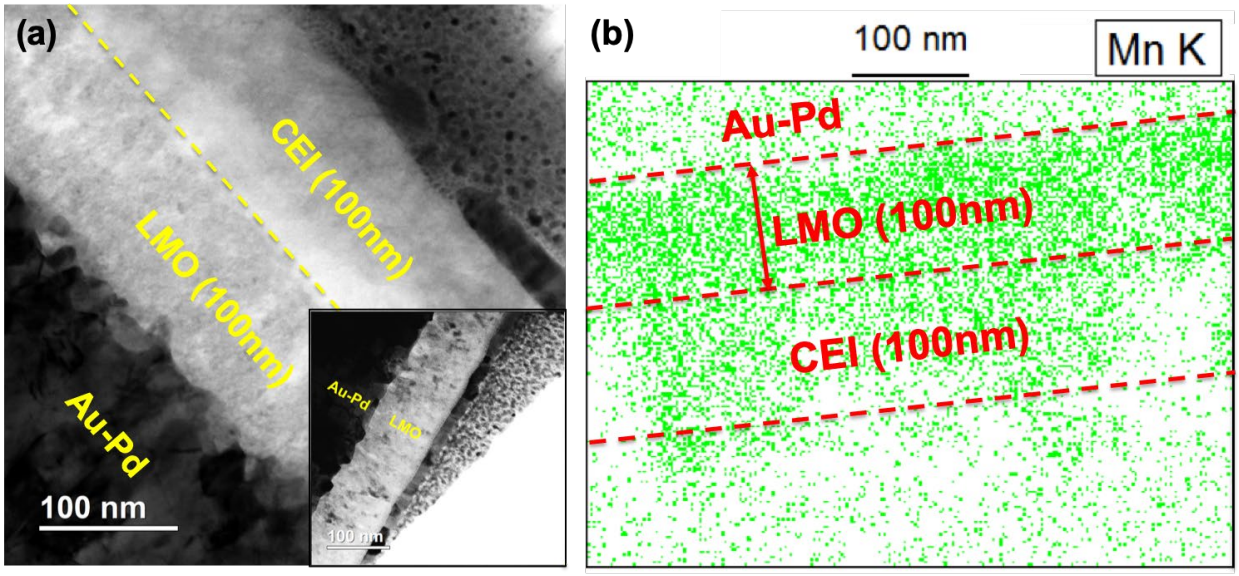

Figure 5.6 (a) STEM image illustrating cross-sectional structure of cycled LMO thin film cathode. A yellow dash line schematically separates LMO and CEI layer. Inset is a STEM image from pristine LMO thin film for comparison. (b) STEM-EDS map of Mn where Au-Pd, LMO and CEI layer are segregated by red dash lines based on geometry information in (a).

XPS depth profiling was carried out on the cycled LMO thin film cathode and the results were shown in **Figure 5.7**. Elemental distributions as a function of depth were determined and plotted by the integral intensities of collected photoelectrons (**Figure 5.7**a). It must be mentioned that the integral intensity on the ordinate axis does not directly give atomic density but it is proportional to element content. Therefore, plots here provide straightforward information about the elemental distributions in the whole LMO thin film cathode. Comparing distributions of Mn from pristine and cycled LMO thin film cathodes, one can realize a thick CEI layer of around 100 nm formed on 100 nm LMO thin film surface. LMO layer is marked by region III while Au-Pd barrier layer is assigned to region IV and beyond. According to profiles of C1s, O1s, Li1s and F1s, the thick CEI layer can be divided into two sublayers marked by region I and region II. C, Li and O apparently existed in the outermost CEI layer (region I) while F and Mn were contained in the interior CEI layer (region II). That verifies previous findings from STEM that the CEI layer was thick (around 100 nm) and contained Mn ions. Chemical compositions of CEI layer were identified according to XPS spectra of C1s, O1s and Mn2p at various depths shown in **Figure 5.7**b, c and d, respectively. The peak at higher binding energy (BE) of C1s spectrum (**Figure 5.7**b) is usually assigned to emission from lithium carbonate (Li_2CO_3) and/or lithium alkyl carbonates ($ROCO_2Li$) formed due to electrolyte solvent oxidation, while the peak at lower BE is mainly contributed by hydrocarbons.[77, 208, 20971] Electrolyte solvent oxidation has been proposed to be lithium ion insertion process and/or lattice oxygen loss from LMO spinel structure at high cathode potential[210, 211]:

$$\lambda\text{–}\,Mn_2O_4(s) + xLi^+(sol.) + xEl(sol.) \longrightarrow Li_xMn_2O_4(s) + xEl^+(s) \qquad (5.3)$$

or

$$Li_yMn_2O_4(s) + 2xEl(sol.) \longrightarrow Li_yMn_2O_{4-x}(s) + x(\text{oxidized El})_2O(s) \qquad (5.4)$$

In the XPS spectrum of O1s shown by **Figure 5.7**c, peak at higher BE is ascribed to species such as lithium carbonate (Li_2CO_3), lithium hydrate (LiOH) and phosphorous oxides ($Li_xPF_yO_z$) resulting from electrolyte lithium salts decomposition, while the photoelectron emission at lower BE is assigned to lattice oxygen, Li_2O and MnO_x species.[2375, 76] Li_2CO_3 has been reported to be formed from reaction between Li_2O and CO_2 or due to attacking carbonate solvents by superoxide from lattice oxygen release.[212] Li_2O can be produced according to Hunter's proposal of Mn^{3+} disproportionation reaction[107]:

$$2LiMn_2O_4(s) \longrightarrow 3\lambda\text{–}MnO_2(s) + MnO(s) + Li_2O(s) \quad (5.5)$$

With present of traces of H_2O, Aurbach et al. suggested a pathway of $LiPF_6$ salts decomposition generating HF and LiF[213, 214]:

$$LiPF_6(sol.) \longrightarrow LiF(s) + PF_5(g) \quad (5.6)$$

$$PF_5(g) + H_2O(l) \longrightarrow 2HF(sol.) + POF_3(g) \quad (5.7)$$

Li_2O and MnO can react with HF producing LiF and MnF_2.

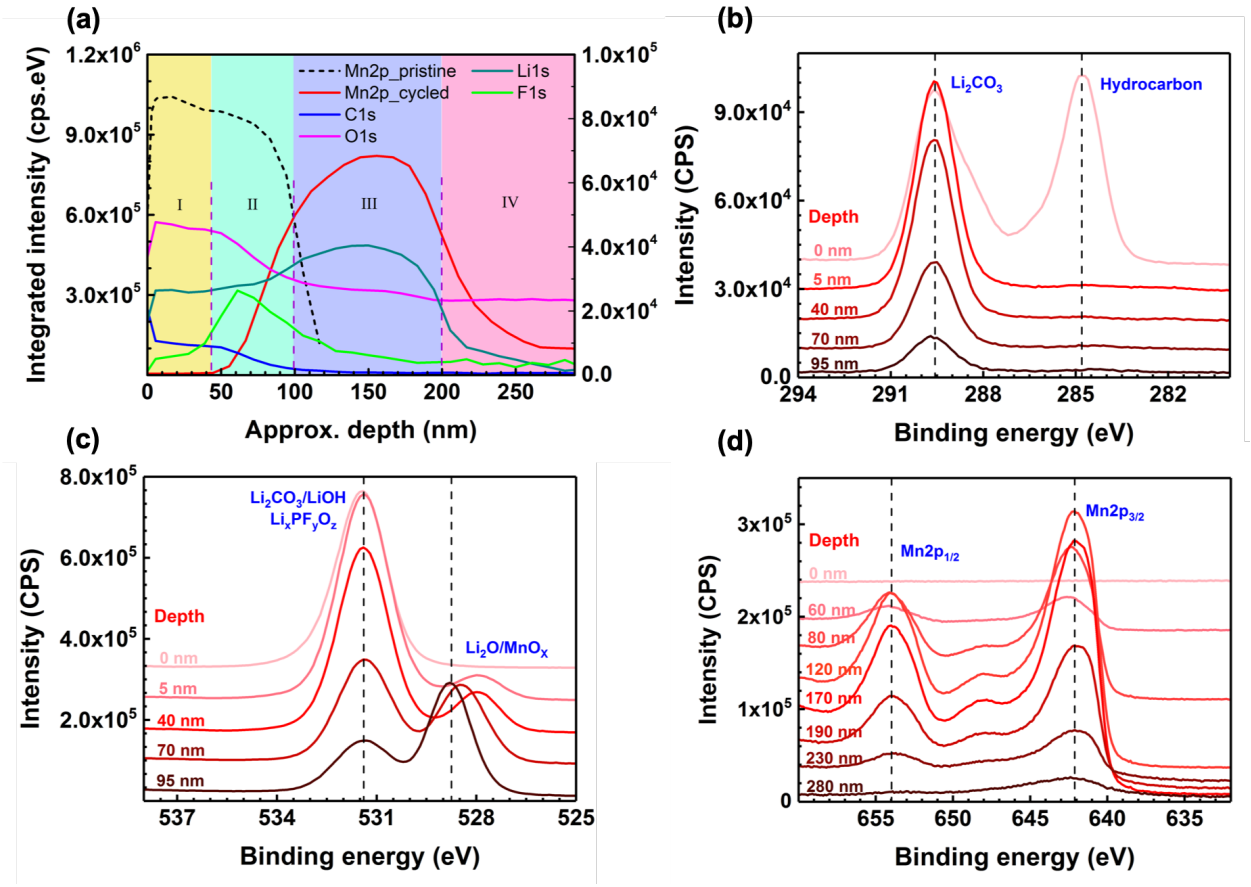

Figure 5.7 (a) XPS depth profiles of cycled LMO thin film cathode. The black dash curve is Mn2p profile from pristine (as-deposited) LMO thin film for comparison. Plotted are integral intensities (in the unit of cps·eV) of photoelectrons from chosen elements Mn2p, C1s, O1s, Li1s and F1s. XPS spectra of C1s (b) and O1s (c) are displayed at selected depths in CEI layer. Mn2p XPS spectra at depths from top surface to Au-Pd barrier layer are exhibited in (d).

A controversy about oxidation state of dissolved Mn ions arises recently although it has been widely accepted that it is Mn^{2+} ions from disproportionation reaction completely dissolve into liquid electrolyte.[107, 128] We report finding of Mn-containing species in the thick CEI layer on cycled LMO thin film cathode surface via STEM and XPS depth profiling. **Figure 5.7**d exhibits photoelectron spectra from Mn 2p at depths throughout both CEI and LMO layer. Two typical peaks corresponding to spin-orbit splitting components Mn $2p_{1/2}$ (~ 654 eV) and Mn $2p_{3/2}$ (~ 642 eV) are observed on all spectra which are corrected to adventitious C 1s at 284.8 eV and

normalized to Mn $2p_{3/2}$ for comparison and peak fitting.[215] Since separation between the two peaks is large enough (> 11 eV), it is only required to consider the more intense Mn $2p_{2/3}$ peak for analysis of electronic structure and assignment of Mn oxidation states.[215] In addition, a small satellite peak arising from shake-up phenomenon of divalent manganese Mn^{2+} appears between BE of 645 eV and 650 eV in some of the XPS spectra.[216] Full width at half-maximum (FWHM) is over 3.5 eV in all Mn $2p_{3/2}$ peaks, indicating the coexistence of mixed Mn^{3+} and Mn^{4+} ions.[217] Therefore, a simplified fitting only considering four single multiplet splitting components (shake-up from Mn^{2+}, Mn^{2+}, Mn^{3+} and Mn^{4+}) was conducted to obtain manganese oxidation states.[118] An example of assigning those multiplet peaks to deconvolute Mn $2p_{3/2}$ is demonstrated in **Figure 5.8**b. In detail, the Mn $2p_{3/2}$ spectra were curve fitted in CasaXPS applying Voigt profiles composed of 70% Gaussian and 30% Lorentzian line shapes and using a Shirley-type background. The FWHM of all multiplet peaks were allowed to be adjusted accordingly.[68] Positions of the four multiplet peaks followed a fixed sequence by decreasing binding energy: Mn^{2+} shake-up > Mn^{4+} > Mn^{3+} > Mn^{2+}.[215]

Curve fittings for XPS spectra collected from pristine and cycled LMO thin film cathodes at both LMO surface (or inner CEI, region II) and middle positions are presented in **Figure 5.8** and quantitative results are summarized in **Table 5.1**. One unexpected finding is that considerable Mn^{2+} ions contributed to both pristine and cycled LMO thin film cathodes at middle depth (**Figure 5.8**b and d), clearly revealed by appearance of shake-up peak. This indicates manganese oxidation state at core of LMO was actually less than 3.5 presented in stoichiometric spinel $LiMn_2O_4$. When determining Mn oxidation state using XPS, most reports in literature only examined surface XPS of LMO particle composite cathode as shown in **Figure 5.8**a where nearly no Mn^{2+} or shake-up presented.[68, 118, 217] LMO thin film cathode provided a much better platform for accurate XPS depth profiling comparing to LMO particle cathode with complications of binders, additives and pores.

Every XPS depth profile is indeed an average of photoelectron emission from each slicing cross section (2mm x 2mm) produced by Ar-ion sputtering (XPS ESCALAB 250Xi). Therefore, there is no notable difference between XPS spectra of particle pack surface and core, making it impossible to precisely probe Mn oxidation state at LMO particle core. That plight is totally overcome by using a dense and uniform LMO thin film cathode with smooth surface. There were barely Mn^{2+} ions on pristine LMO thin film surface indicating higher Mn oxidation state (3.36) than that at LMO thin film cathode core (3.21) shown in **Table 5.1**. The Mn $2p_{3/2}$ spectrum collected in the inner CEI layer (region II in **Figure 5.7**a) and corresponding curved fitted peaks are presented in **Figure 5.8**c which indicates nearly no Mn^{2+} existed in the interior CEI layer. It can be interpreted that Mn^{2+}-containing species dissolved into electrolyte while other Mn-containing species (Mn^{3+} and Mn^{4+} ions) still resided in the compact CEI layer (region II).

Calculated manganese oxidation state by fitting Mn $2p_{3/2}$ spectra collected from **Figure 5.7**a are plotted in **Figure 5.8**e. It can be seen that the average oxidation state of manganese in pristine and cycled LMO thin film cathodes are about 3.20 and 3.15, respectively, which are smaller than 3.5 in spinel $LiMn_2O_4$ probably due to existence of Mn^{2+} at inner LMO. These quantitative results provide useful information about relative change of Mn oxidation state along depth despite of evitable errors of the simplified XPS curve fitting method. A maximum value of Mn oxidation state was found at the interface between cycled LMO and inner compact CEI layer (region II), indicating an interphase consisting of manganese with higher oxidation state was formed at the LMO thin film cathode surface after electrochemical cycling. It was reported inactive and defect $Mn^{4+}O_2$ formation on LMO surface at high charging potential (Eq. 5.5).[107] Recent high resolution STEM studies found a defect tetragonal Mn_3O_4-like phase on LMO particle surface or subsurface due to lattice oxygen loss and manganese migration within the spinel framework.[68, 217,

[218] Those migrated manganese reduced to Mn^{2+} ions were readily dissolved into electrolyte resulting in irreversible interphase with increased Mn oxidation state. Those observations are coincident with the XPS depth profiling results demonstrating existence of manganese with higher oxidation state at LMO thin film cathode surface and inner CEI layer.

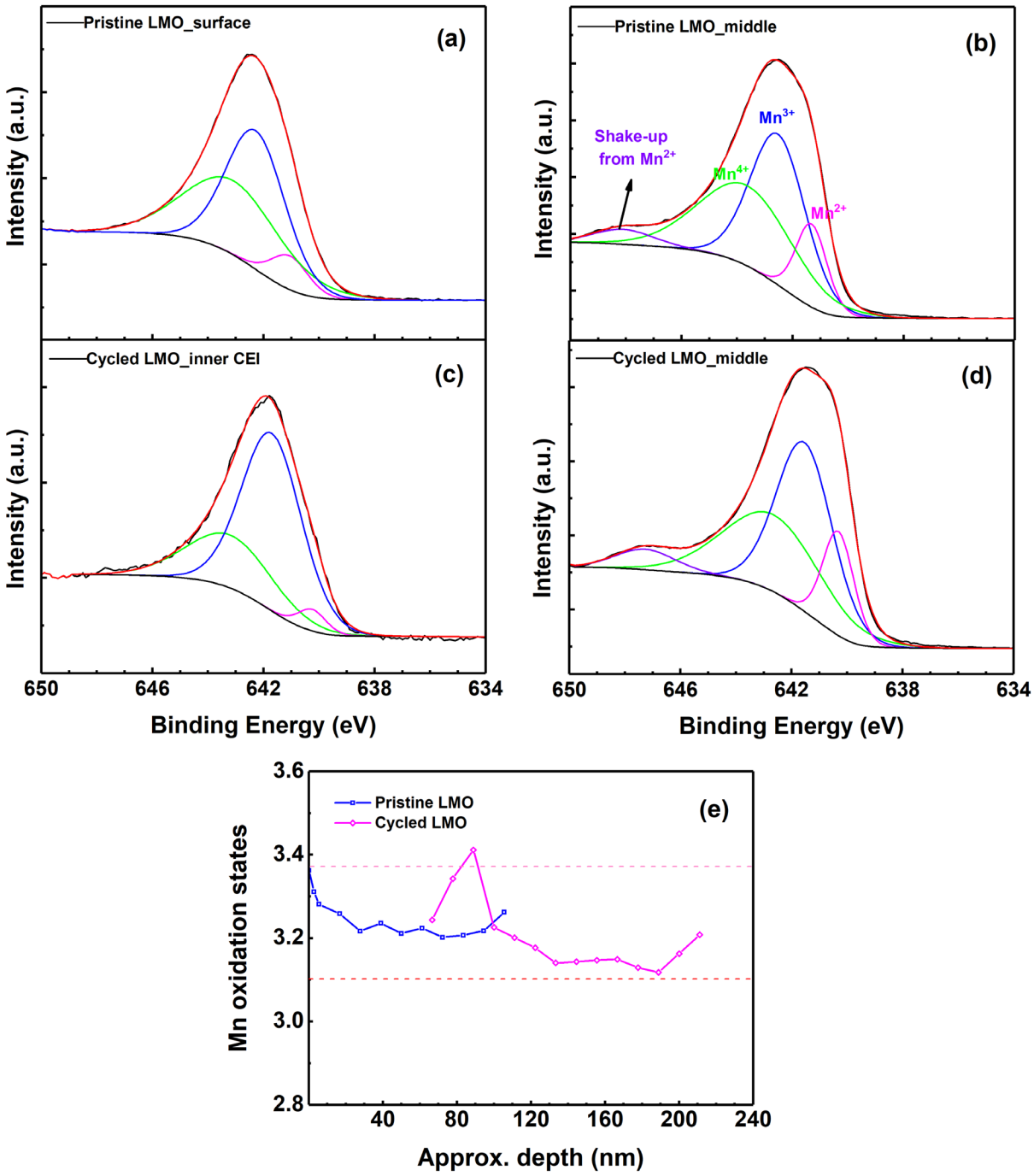

Figure 5.8 Mn $2p_{3/2}$ spectra and curve fitted multiplet peak spectra. (a) and (b) are from pristine LMO thin film cathode surface and middle depths while (c) and (d) are from inner CEI and middle depths of galvanostatically cycled LMO thin film cathode. (e) Calculated oxidation states of manganese in pristine (blue) and cycled (magenta) LMO thin film cathodes from XPS curve fitting.

Table 5.1 Quantitative curve fitting results: atomic percentages of multiplet components of Mn $2p_{3/2}$ spectra from pristine and cycled LMO thin film cathodes.

Percentage (%)	Near surface					Middle				
	Mn^{4+}	Mn^{3+}	Mn^{2+}	Shake-up	Oxidation state	Mn^{4+}	Mn^{3+}	Mn^{2+}	Shake-up	Oxidation state
Pristine LMO	43.39	48.99	7.61	0	3.36	39.15	42.93	13.32	4.60	3.21
Cycled LMO	26.04	71.79	2.17	0	3.24	34.96	44.44	15.18	5.42	3.14

In situ EIS analysis was conducted for the LMO thin film cathode/Li metal anode coin cell between 100 kHz and 10 mHz applying an AC voltage of 10 mV in the fully discharged state (3.5 V vs. Li/Li^+). The cell was rested for 30 minutes to get stable open circuit voltage (OCV) before each AC impedance spectrum was collected. An equivalent circuit model (ECM) shown in **Figure 5.9**a was applied for EIS fitting and Nyquist plots along with fitting curves are displayed in **Figure 5.9**b. In general, the impedance spectra exhibit three semicircles, a 45°-sloped straight line region (black dash line in **Figure 5.9**b) related to "Warburg" Li-ion solid state diffusion at low frequency, and a steeper line region corresponding to onset of finite length diffusion at even lower frequency[219, 220]. Corresponding to EIS spectra, the applied ECM consists of a resistor R_{el} describing the electrolyte resistance (intercept with the x-axes), a $R_{cc}Q_{cc}$ element, a $R_{Li}Q_{Li}$ element and a circuit proposed by Meyers et al.[221]. $R_{cc}Q_{cc}$ is composed of a parallel connection between a constant phase element Q_{cc} and a resistor R_{cc} associated with the polarization resistance at the current collector (Au-Pd/SS) /electrode interface.[222-224] Since R_{cc} is usually tiny, a small semicircle at extremely high frequency is exhibited by $R_{cc}Q_{cc}$ circuit. The large semicircle at high frequency is fitted by R_{Li} and Q_{Li}, representing impedance from SEI layer on Li metal anode surface.[225, 226] The Meyers element models the mid- and low-frequency part of the spectra and it is composed of the $R_{CEI}Q_{CEI}$ element and a Randles circuit. The depressed semicircle at middle frequency is

attributed to $R_{CEI}Q_{CEI}$ element which is associated with the resistance furnished by the CEI layer, spontaneously formed after electrolyte decomposition on the LMO thin film cathode surface. The Randles circuit is composed of a parallel connection between the charge transfer resistance at the LMO thin film surface R_{ct} and the constant phase element Q_{dl}, associated with the double layer capacitance. $R_{ct}Q_{dl}$ element produces another depressed semicircle at low frequency. The resistor R_{ct} is connected in series with a general finite space Warburg element $W_{GSF,3D}$ associated with the Li diffusion process along a three-dimensional diffusion path within LMO spinel framework, terminated by an impermeable boundary.[227] Lithium diffusion is linked to the sloped linear region of the EIS spectra.[112, 226] The impedance associated with $W_{GSF,3D}$ is calculated as:

$$Z_{GFSW,3D}(\omega) = R_w \cdot \frac{\tanh[(j\omega\tau_w)^{n_w}]}{\tanh[(j\omega\tau_w)^{n_w}] - (j\omega\tau_w)^{n_w}} \tag{5.8}$$

with the time constant:

$$\tau_w = \frac{L^2}{D} \tag{5.9}$$

R_w is polarization resistance, n_w is an exponent ($0 < n_w < 0.5$) reflecting the degree of non-uniform diffusion[228, 229], L is the electrode thickness and D is the diffusion coefficient of lithium in LMO.

As seen from the **Figure 5.9**b, there was a significant impedance increase once the cell is cycled (after 1st cycle) and the impedance quickly got stable after 5 cycles and even slightly decreased after 50 cycles. That indicates prompt formation of CEI and SEI layers upon charging/discharging of the coin cell. That is even more clearly revealed from fitting results plotted in **Figure 5.9**c showing total film resistance ($R_{cc} + R_{Li} + R_{CEI}$) and charge transfer resistance (R_{ct}) in regard to cycle numbers. Both resistances were found to drastically increased of during the first 10 cycles, followed by gradually stable states. Under finite space diffusion conditions, the

chemical diffusion coefficient of Li-ion can be derived from Warburg impedance analysis over the 45° sloped linear region of the Nyquist plots. The real part of Warburg impedance is expressed as[28, 219, 230]:

$$Z_{w,real} = \sigma\omega^{-1/2} = \frac{V_m}{AFn\sqrt{2\widetilde{D}_{Li}}}\frac{dE}{dx}\omega^{-1/2} \quad (5.9)$$

where σ is termed the Warburg factor, ω the angular frequency (rad), V_m the molar volume of the LMO (cm^3/mol), A the surface area of the LMO thin film (cm^2), F the Faraday constant (C/mol), n the charge transfer number, $\widetilde{D}_{Li}$ the Li-ion chemical diffusion coefficient (cm^2/s), E the potential at which the EIS data were recorded (V), and x the lithium content at potential E. According to Eq. 5.9, $\widetilde{D}_{Li} = V_m^2(dE/dx)^2/\ 2A^2F^2n^2\sigma^2$. dE/dx can be derived from the Potential vs. Specific capacity profiles in **Figure 5.4**a. The Warburg factor σ is obtained from the slop of Z_real vs. $\omega^{-1/2}$ as shown in **Figure 5.9**d. It should be noted that EIS data extracted for linear fitting were within the frequency range associated with Warburg diffusion region marked by a 45° sloped line illustrated in **Figure 5.9**b. The calculation result of $\widetilde{D}_{Li}$ is plotted in **Figure 5.9**e which indicates a gradual increase of Li-ion chemical diffusivity during the first 20 cycles. The average value of $\widetilde{D}_{Li}$ is around 2.3×10^{-11} cm^2/s which is in good agreement with values reported in literature for discharged LMO at 3.5 V.[201, 206, 220]

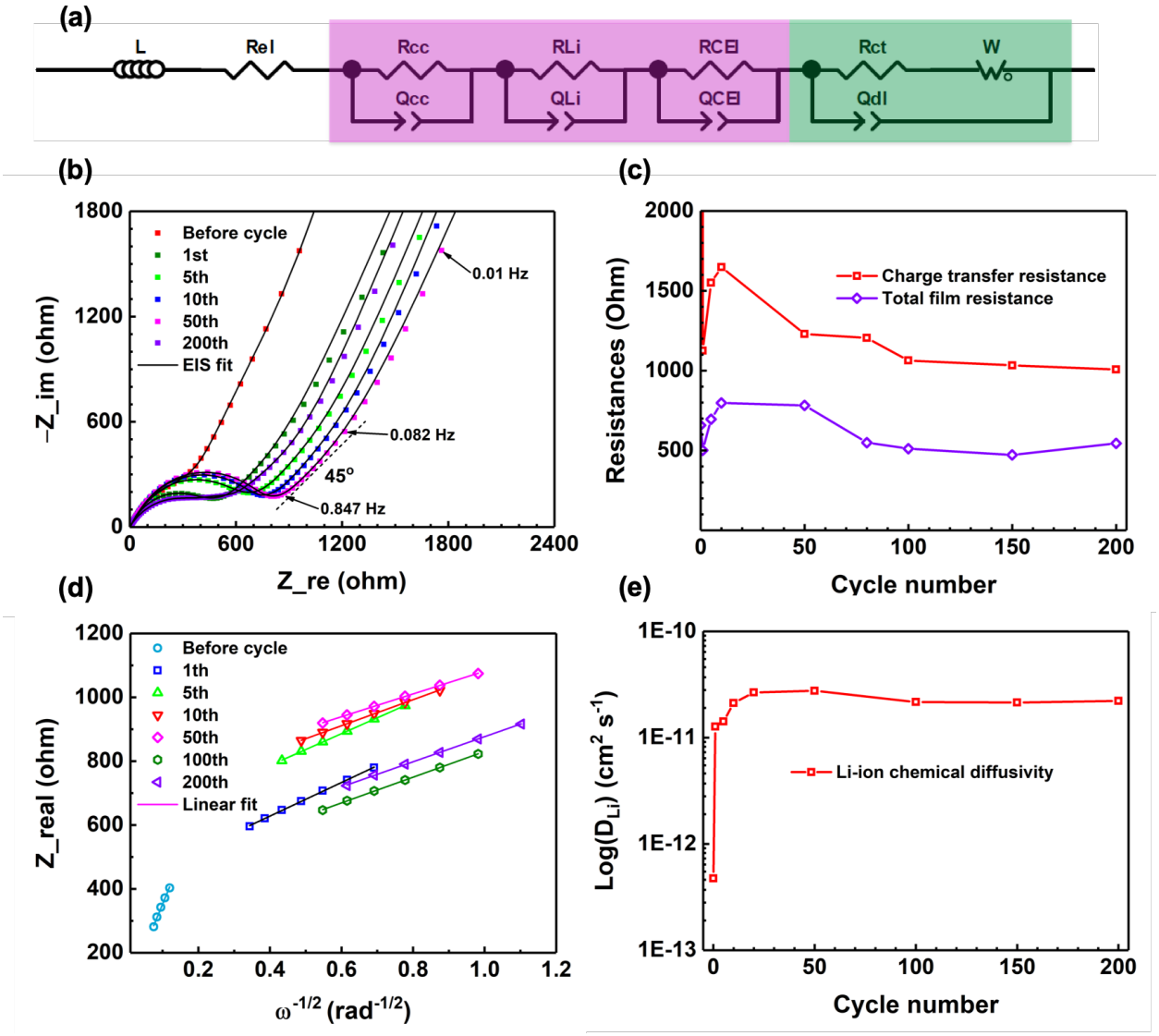

Figure 5.9 (a) Equivalent circuit model for EIS fitting of LMO thin film based coin-type cell with lithium metal as anode. (b) Nyquist plots and fitting curves from EIS measurements on the LMO thin film based half coin cell. (c) Total film resistance (red) resulting from SEI, CEI and current collector, and LMO thin film cathode charge transfer resistance (purple). (d) EIS data along with linear fitting lines in Warburg region associated with Li-ion diffusion process within LMO thin film. (e) Calculated Li-ion chemical diffusion coefficient from Warburg impedance analysis based on fitting results in (d).

5.4 Conclusions

In summary, a 100 nm LMO/Au-Pd/SS thin film cathode fabricated by sputtering deposition demonstrated a relatively small specific capacity of 58 mAh/g due to low annealing temperature to alleviate element contaminations from the stainless steel substrate. Around 10% capacity was lost due to manganese dissolution and formations of SEI and CEI layer increasing interfacial resistances. Chemical compositions were characterized using XPS depth profile. It was found the thick CEI layer (100 nm) consisted of two sub-regions containing Li_2CO_3, LiOH, Li_2O, $Li_xPF_yO_z$, MnF_x, MnO_x, etc. Mn-containing species were first found to exist in the inner compact CEI layer (region II), which was verified by STEM-EDS mapping of Mn distribution in both LMO and interior CEI layer. Curve fitting of Mn $2p_{3/2}$ spectra indicates Mn^{2+} existed in core of both pristine and cycled LMO thin film cathodes leading to higher manganese oxidation state at LMO surface. A maximum value of Mn oxidation state was found at the interface between cycled LMO and interior compact CEI layer (region II), indicating an interphase consisting of manganese with higher oxidation state was formed at the LMO thin film cathode surface after electrochemical cycling. EIS fitting results show rapid rise of interfacial film resistances during the first 5 cycles, indicating prompt formation of CEI layer. Li-ion chemical diffusivity derived from Warburg impedance analysis was found to be averagely 2.3×10^{-11} $cm^2 \cdot s^{-1}$ which was in good agreement with values reported in literature.

5.5 Acknowledgments

This work was supported as part of the Center for Electrochemical Energy Science, an Energy Frontier Research Center funded by the U.S. Department of Energy, Office of Science, Basic Energy Sciences (DE- AC02-06CH11357). Research at the Advanced Photon was supported

by DOE, Office of Science, BES. This work made use of the EPIC, Keck-II, and/or SPID facility(ies) of Northwestern University's NUANCE Center, which has received support from the Soft and Hybrid Nanotechnology Experimental (SHyNE) Resource (NSF ECCS-1542205); the MRSEC program (NSF DMR-1121262) at the Materials Research Center; the International Institute for Nanotechnology (IIN); the Keck Foundation; and the State of Illinois, through the IIN. This work made use of Pulsed Laser Deposition Shared Facility at the Materials Research Center at Northwestern University supported by the National Science Foundation's MRSEC program (DMR-1121262). This work utilized Northwestern University Micro/Nano Fabrication Facility (NUFAB), which is partially supported by Soft and Hybrid Nanotechnology Experimental (SHyNE) Resource (NSF ECCS-1542205), the Materials Research Science and Engineering Center (DMR-1720139), the State of Illinois, and Northwestern University. This work made use of the MatCI Facility which receives support from the MRSEC Program (NSF DMR- 1720139) of the Materials Research Center at Northwestern University.

Chapter 6: Ultrahigh Power Density Enabled by Novel Thin-Film $LiMn_2O_4$ Cathodes for Lithium Ion Batteries

6.1 Introduction

Nowadays, there has been a rapidly increasing trend to pursuit the future of Internet of Things (IoT) which extents conventional internet connectivity into smart physical microdevices, such as sensors, wearable electronics, remote monitors, and microelectromechanical systems (MEMSs).[6] However, crucial challenges especially developing high power density sources at millimeter scale lay ahead of fabricating next generation embedded microelectronics of IoT.[83, 84] Lithium ion battery (LIB) is maturely developed power storage technology and has been applied in some microelectronics. However, microstructures of conventional bulk electrode materials impose restrictions on high rate capability.[85, 86] Downscaling the electrode materials has been intensively studied by synthesis of nanostructured particles with a variety of shapes, morphologies, crystallinities and porosities in efforts to shorten Li^+ and electron migration channels and hence improve high rate capability.[85, 87-93]

Thin films share similar characteristic length scale to nano particles and hence nanoscale effects are supposed to reveal.[85, 94] Therefore, all solid state thin-film batteries are believed to be promising candidates with readily higher power density than bulk lithium ion batteries (LIBs) due to much shortened Li^+ diffusion distance.[28, 29, 89, 95] Choice of cathode materials largely determines achievable power density of a LIB. Typical cathode materials for LIBs, such as $LiFePO_4$, $LiCoO_2$, $LiNi_xMn_yCo_{1-x-y}O_2$ and $LiMn_2O_4$, are categorized to be classical intercalation-type materials which suffer from kinetic issues of constrained solid-state diffusion of lithium ions during intercalation reactions.[96-98] As a result, most of current LIBs allow only up to moderate charging/discharging

current rates. Still and all, lithium manganese oxide $LiMn_2O_4$ (LMO) has been received wide-spread interests due to its intrinsic characteristic obtaining relatively higher rate capability than the others.[1, 5, 19, 26] Within LMO cubic spinel lattice (space group $Fd\bar{3}m$), a cubic close-packed array of oxygen (32e) accommodates Li and Mn cations at one eighth of tetrahedral (8a) and half of octahedral (16d) sites, respectively.[1, 46] Unlike olive-type or layered materials, the interstitial space in $[Mn_2]O_4$ framework which can be treated as a three-dimensional (3D) network of face-sharing tetrahedral (8a) and empty octahedral (16c) sites offers a facile 3D pathway for lithium ions reversibly transport within the host structure.[49, 50] Due to that exclusive 3D Li^+ conducting framework, LMO is theoretically and potentially supposed to delivery higher power density.[1, 5]

Since conventional bulk LMO cathodes consisting of microsized particles are unlikely to be charged/discharged at high rate due to poor electron conduction and long lithium ion diffusion pathways within both single microsized LMO particle and the cathode composite bulk pack, considerable efforts have been made to develop high rate LMO thin film cathodes which inherently obtain short Li-ion diffusion length making them ideal for high power applications.[27, 29, 85, 89] For example, Put et al. explored high rate stability of LMO thin films cycled at various current rates within extended voltage window of 2 – 4.3 V.[89] Fehse et al. applied LMO thin film electrodes into pseudocapactive microbatteries achieving ultrafast dischargeable capability.[29] In addition, LMO thin films have been widely applied to study critical interfacial (electro)chemical issues in LMO-based LIBs, such as surface coating effects[57], manganese dissolution reactions and cathode electrolyte interphase (CEI) formation[57, 82], due to superior merits of LMO electrodes with thin-film geometry which obtain well-controlled reaction area, surface morpholgy and crystalline structure, and avoid complexities presented in bulk-type composite electrode such as additives,

binders and solvents.[26, 27, 82, 100] Experimentally, both polycrystalline and epitaxial LMO thin films have been successfully fabricated using a variety of deposition techniques including pulsed laser deposition (PLD), radio-frequency (r.f.) magnetron sputtering, atomic layer deposition (ALD) and chemical solution deposition (CSD).[62, 69, 70, 101-104] Among those techniques, magnetron sputtering is widely adopted for multilayer depositions of metal and oxide thin films.[29, 100] To ensure high rate cycling of LMO electrodes, a well constructued current collecting back contact system is required. It is common to direct use electrically conductive substrates such as stainless steel (SS), Al and Pt foils as current collectors while another choice is to engineer a stack of successive thin film layers including barrier layer (Al_2O_3, SiO_2), adhesion layer (Ti, TiN) and conductive buffer layer (Pt, Au, ITO) on top of insulating substrates (Si, Al_2O_3, YSZ).[29, 100, 10557, 64]

In this work, we report on fabrication of well-architected LMO thin-film-based cathode consisting of a multilayer stack LMO||Pt||Ti||Al_2O_3 substrate back screen printed with Au paste using magnetron sputtering. The prepared LMO thin film cathodes with various thickness were electrochemically cycled at a series of current rates to explore their cycling stability and high rate capability. Chemical kinetics of those thin film cathodes are reported using both galvanostatic intermittent titration technique (GITT) and electrochemical impedance spectroscopy (EIS). Phase separation and stabilities of redox reactions at two potential plateaus of LMO cathodes were explored. At last, analysis of cell impedances during cycling was conducted via EIS measurement and fitting.

6.2 Experimental Details

Sample Preparation: A stoichiometric $LiMn_2O_4$ target (2 inch in diameter, Kurt J. Lesker Company, 99.9% purity) was used as the sputtering material. Sapphire (Al_2O_3) substrates were

pre-annealed at 1000 ºC for 8 hours in air, followed by screen printing with Au paste on the back, side and partial front surfaces working as back contact current collector. Prior to LMO deposition, the substrates were successively washed in acetone and ethanol ultrasonic bath. Depositions were done in a sputter apparatus (ATC-Orion 8 HV, AJA International Inc.) with a base vacuum of 10^{-6} Torr. The substrates were first coated with a stack of 100 nm Pt || 20 nm Ti by DC sputtering. LMO thin film deposition was conducted at a radio frequency power of 150 W and under a mixed gas flow of 6 sccm O_2 and 20 sccm Ar at 5 mTorr and room temperature. Afterwards, the deposited LMO films with nominal thickness of 100 nm or 25 nm were annealed at 750 ºC in air for 2 hours to get highly crystalline phase.

Electrochemical Measurement: All the electrochemical tests were performed using CR2036-type coin cells with the prepared LMO thin films as positive electrode and lithium metal foils as the counter and reference electrodes. Around 40 mL electrolyte, a mixture of 1 M $LiPF_6$ dissolved in ethylene carbonate (EC) and ethyl methyl carbonate (EMC) (v/v = 1:1), was used for each cell. All cells were assembled in a glovebox filled with high-purity argon (O_2 <0.5 ppm) followed by uniaxial pressing at a pressure of 500 psi. Galvanostatic cycling was done on a galvanostat testing system (Arbin Instrument) at a voltage range of 3.3 – 4.5 V or 3.5 – 4.3 V with various current rates. Combined measurements of galvanostatic cycling and *in situ* electrochemical impedance spectroscopy (EIS) were performed with a bi-potentiostat / galvanostat (SP-300, Bio-Logic Science Instrument). The EIS data were recorded between 100 kHz and 10 mHz applying an AC voltage of 10 mV. The cycling cells were stopped at 4.07 V and rested for 30 minutes to get stable open circuit voltage (OCV) before each AC impedance spectrum was recorded in every cycle for the first 10 cycles and once in every 10 cycles for the rest 190 cycles.

Characterization and Data Analysis: The surface morphologies of LMO thin films were observed by atomic force microscope (AFM, Bruker Dimension FastScan®) and scanning electron microscope (SEM, Hitachi SU8030). Grazing incidence X-ray diffraction was carried out using ATX-G (Rigaku) with Cu Kα (λ = 1.5406 Å) radiation. For characterizations of the cycled LMO thin films, the cells were disassembled in the glovebox, and rinsed with DMC solution three times in 3 days for removing the residual electrolyte salts. Cross-sectional TEM samples of cycled thin films were prepared by a dual-beam focused ion beam (FIB, FEI Helios Nanolab 600). High resolution atomic structure observations were conducted on an aberration-corrected scanning transmission electron microscope (STEM, JEOL Co., ARM-200CF) at an acceleration voltage of 200 kV. Electron energy-loss spectroscopy (EELS) data were collected on the same TEM microscope.

6.3 Results and Discussion

Grazing incidence X-ray diffraction shown in **Figure 6.1** was conducted for the deposited 100 nm LMO || Pt || Ti || Al_2O_3 thin films schematic of which is illustrated in **Figure 6.2**a. It can be seen the LMO thin film obtained a high crystallinity and the diffraction pattern matches well with that from cubic spinel LMO. The full width at half maximum (FWHM) at peak LMO 111 is 0.39° (gauss fit in the inset) indicating a domain size of 21 nm according to Scherrer equation $d = \frac{0.9\lambda}{\beta cos\theta}$.[231] The cross sectional structure of the LMO || Pt || Ti || Al_2O_3 thin film illustrated by a STEM image in Figure 6.2a shows 25 nm dense LMO thin film and a compact cathode electrolyte interphase (CEI) layer formed on it. Porous region above the yellow dash line is carbon deposited before preparing FIB TEM sample to protect LMO thin film from high energy Ga ion damage. Surface morphology of the as-deposited 25 nm LMO thin film was displayed by both SEM and

AFM in **Figure 6.2**c and d which indicate an averge surface grain size of 83 nm and RMS (root-mean-square) roughness of 12 nm.

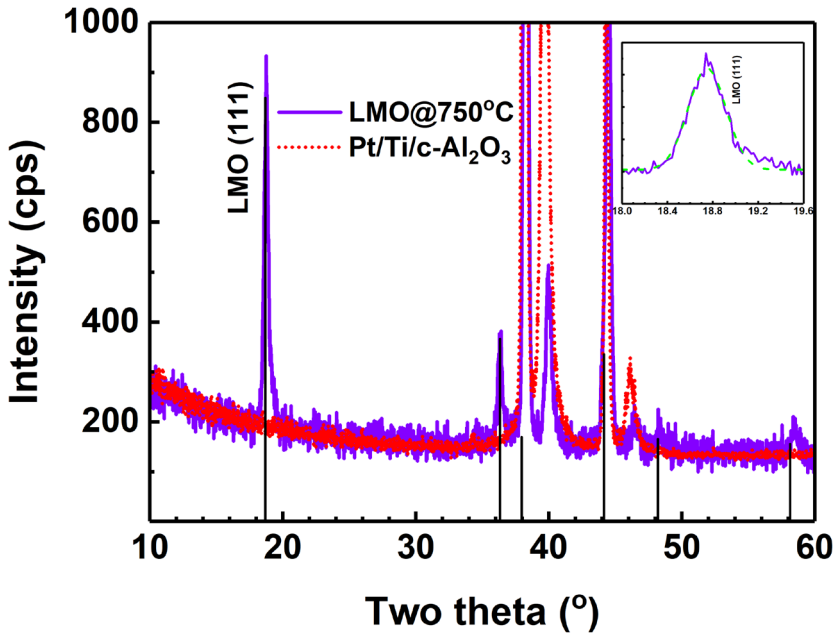

Figure 6.1 Grazing incidence XRD patterns of as-deposited 100 nm LMO || Pt || Ti || Al2O3 (purple curve) and Pt || Ti || Al2O3 substrate (red dash curve). Diffraction lines from cubic spinel LMO are presented by black lines. Inset shows LMO peak 111 and Gauss fit (green dash curve)

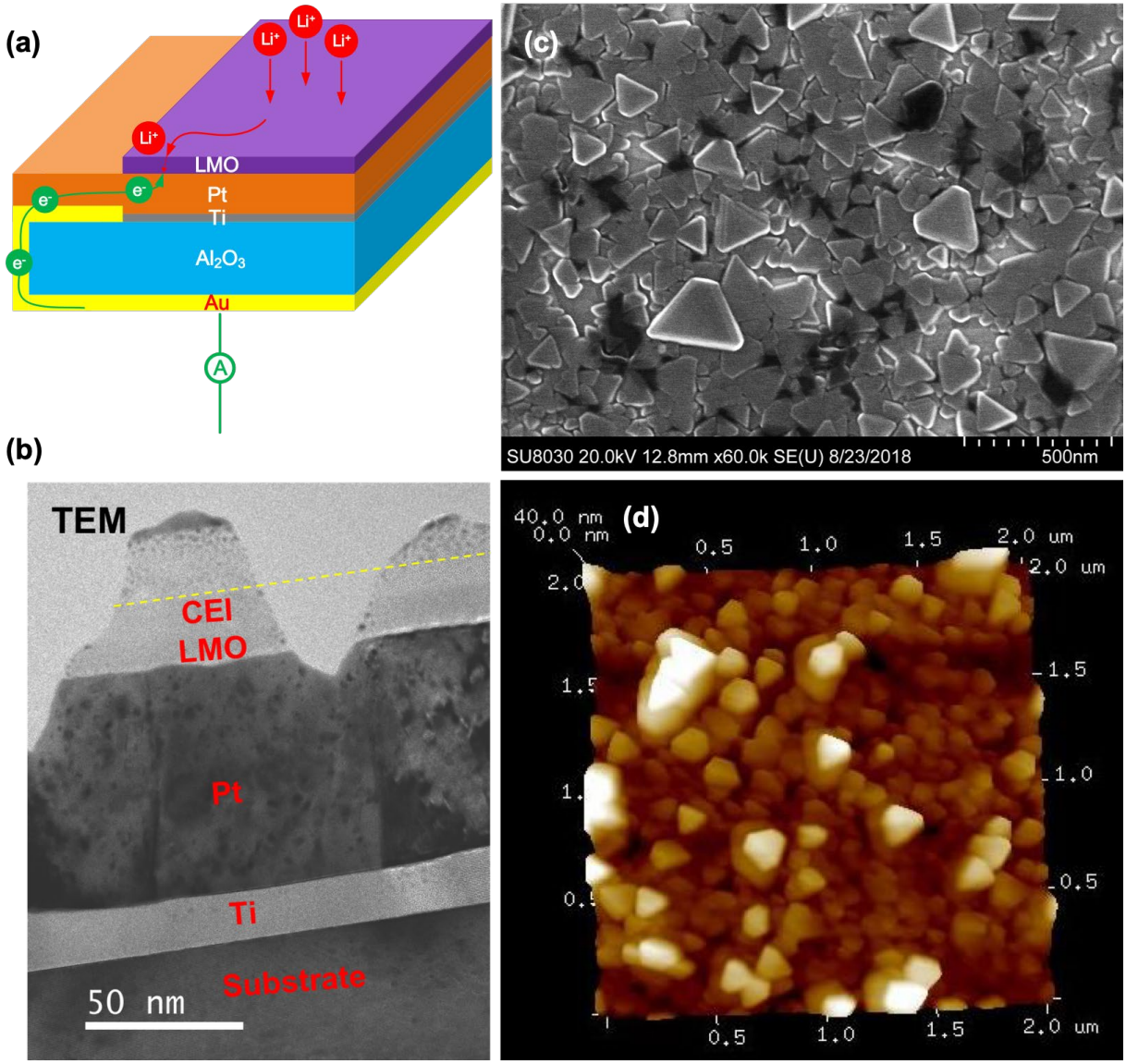

Figure 6.2 (a) Schematic illustration of the multilayer stack of a LMO || Pt || Ti || Al_2O_3 thin film. (b) STEM image showing the cross-sectional structure of 25 nm LMO thin film cathode after 100 cycles. A CEI layer is formed on LMO surface. Surface morphology of 25 nm LMO thin film is shown by both SEM (c) and AFM (d).

100 nm LMO thin film cathodes without post annealing and annealed at 700 ºC, 750 ºC and 800 ºC were cycled between 3.5 – 4.3 V at a current rate of 1C (6.33 µA). According to the discharge specific capacity profiles shown in **Figure 6.3**a, LMO thin film annealed at 750 ºC demonstrated a highest specific capacity of 128 mAh/g and little capacity loss (around 2%) after

100 cycles. All subsequent LMO thin films were annealed at 750 ºC. Without post annealing to get crystalline cubic spinel structure, the LMO thin film cathode obtained significantly declined initial capacity and quickly suffered from drastic fade upon charging/discharging. LMO thin films of various thickness all annealed at 750 ºC were discharged/discharged within an extended voltage window 3.3 – 4.5 V at a higher current rate of 4C to accelerate capacity degradation. 25 nm LMO thin film cathode exhibited best capacity retention (**Figure 6.3**b) mainly due to enhanced effects of nano scaling.[85, 90, 91, 95] Prolonged cycling on the 25 nm LMO thin film cathode was conducted and the charging/discharging voltage in regard with cycling time was plotted in **Figure 6.3**c which demonstrates high reversibly and stability. A relatively low coulombic efficiency of 98% was achieved, ascribed to pronounced current leak through the polymer separator comparing to a so small cycling current (around 25 μA) applied on such a thin film of LMO cathode (25 nm). Reduced coulombic efficiency at early cycling stage could be primarily attributed to formation of irreversible and/or inactive surface phases, and parasitic reactions of the liquid electrolyte.[29] Potential vs. specific capacity profiles obtained from cycling data in **Figure 6.3**d clearly show two potential plateaus corresponding to two redox reactions of LMO cathode during Li insertion/extraction which are marked by peak A1/A2 and B1/B2 presented in **Figure 6.3**e. A "transition" voltage at 4.07 V marked in **Figure 6.3**e divides the electrochemical reaction of LMO cathode into two voltage regions in **Figure 6.3**d tinted by magenta and yellow, respectively. It can be seen only 23% capacity was lost after 900 cycles (inset in **Figure 6.3**d), which is much better performance than most reports in literature for LMO cathodes.[111] The discharge capacity retention curve plotted in the inset indicates drastic capacity drop primarily occurred during the first 50 cycles. In addition, it was found there was nearly no overpotential (3 mV) between the two redox

peaks (**Figure 6.3**e), indicating the Li-ion intercalation/extraction process was not limited by lithium ion diffusion through the 25 nm LMO thin film cathode.

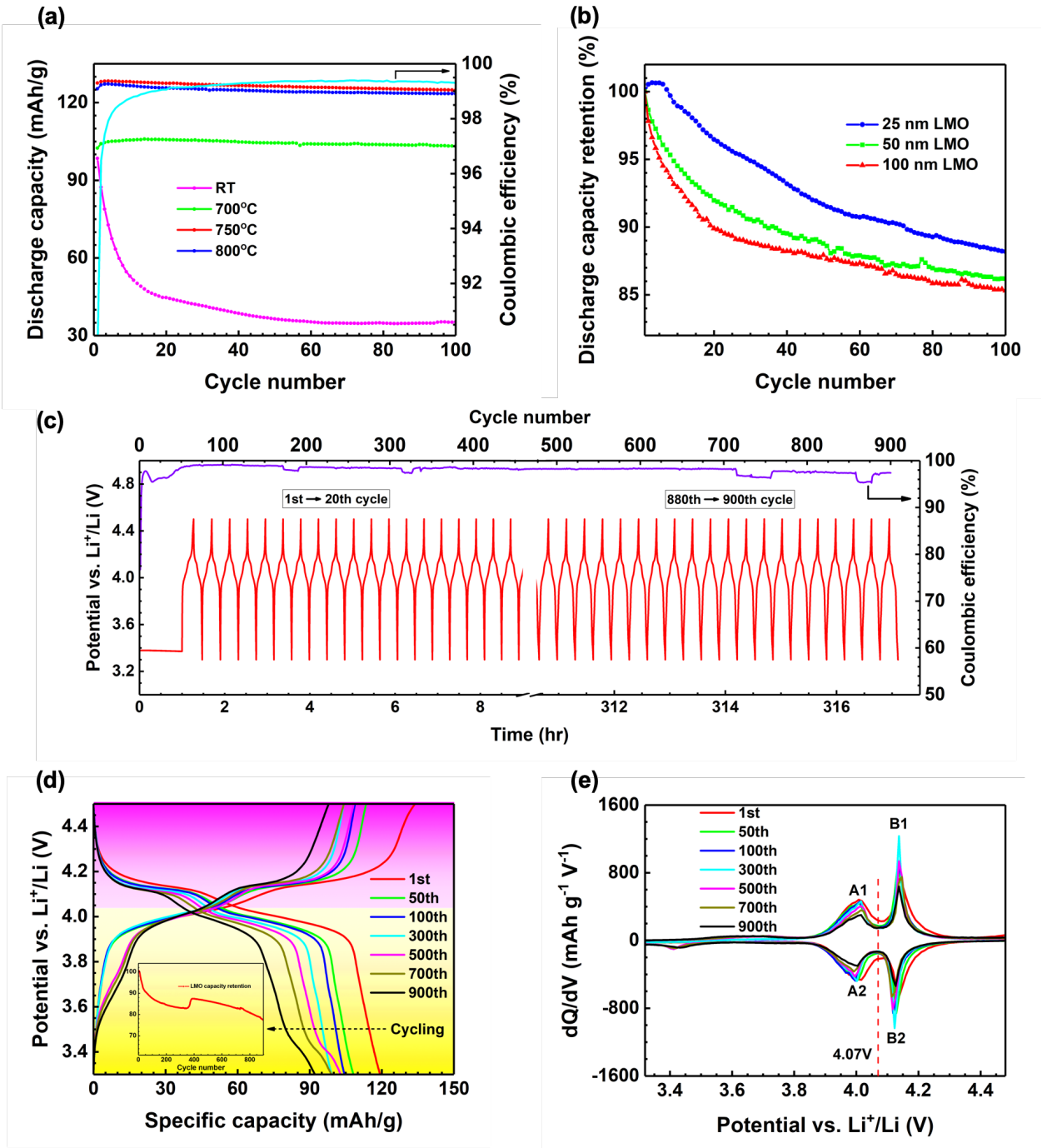

Figure 6.3 (a) Specific discharge capacity from 100 nm LMO thin film cathodes without post annealing or annealed at 700 °C, 750 °C or 800 °C, which were galvanostatically cycled in a voltage

range of 3.5 – 4.3 V at a current rate of 1C (6.33 μA). (b) Discharge capacity retention of LMO thin film cathodes with thickness of 25 nm, 50 nm and 100 nm cycled between 3.3 – 4.5 V at a current rate of 4C (25.3 μA). (c) Charge/discharge potential vs. time from a 25 nm LMO thin film cathode annealed at 750 ºC. The cathode was cycled 900 times between 3.3 – 4.5 V at a current rate of 4C (25.3 μA). Coulombic efficiency is plotted in purple curve. (d) Potential vs. specific capacity profiles obtained from cycling results in (c). Discharge capacity retention curve is plotted in the inset. Two regions of high voltage (4.07 – 4.5 V) and low voltage (3.3 – 4.07 V) are marked by two colors. (e) Differential capacity (dQ/dV) profiles derived from data in (d). A "transition" voltage is marked by the red dash line at 4.07 V.

To explore high rate capability, the well-prepared 25 nm LMO thin film cathode was cycled between 3.3 – 4.5 V at 1C, 10C, 20C, 40C, 80C, 160C and 1C again. Discharge profiles at each current rate were plotted in **Figure 6.4**a where two potential plateaus are apparently discerned on profiles from cycling at low current rates. It has been found the two plateaus are characteristic of one Li^+ extraction-insertion from/into the cubic spinel framework of $LiMn_2O_4$/λ-Mn_2O_4 which is a two-step process represented by two redox reactions.[47-49] As illustrated in **Figure 6.4**a, the flat plateau at 4.13 V (on 1C curve) in higher voltage range (4.07 – 4.5 V) is ascribed to a two-phase redox reaction of LMO, while the steep plateau at 3.99 V within lower voltage range (3.3 – 4.07 V) represents a solid-solution reaction where lattice parameter of the cubic phase linearly related with lithium content.[38] It is worth to be noted that the flat potential plateau of two-phase reaction gets narrower and narrower with increasing cycling current rate as schematically presented by the black dash lines (**Figure 6.4**a). The first plateau gradually disappears beyond 40C. That indicates the phase separation process of LMO was suppressed at high charging/discharging current where solid-solution reaction dominated the whole Li-ion insertion/extraction process. It was reported LMO particles with an average grain size of 14 – 20 nm were observed to reveal a solid-solution-like behavior which was expected to attain higher rate capability.[85] The continuously sloped potential profiles over 40C reported in this work indicate similar Li-ion migration behavior in

LMO framework, contributing to the outstanding high power characteristic of the 25 nm LMO thin film cathode. Phase separation has been considered to be critical rate-limiting step for various electrode materials for LIBs.[232, 233] Zhou et al. reported transition from phase separation to solid-solution of layer-structured cathode NMC induced by high-rate charging using *in situ* synchrotron X-ray diffraction.[234] Bai et al. predicted moving phase boundaries with applied current between phase separation and quasi-solid solution/solid solution of $LiFePO_4$ using a novel electrochemical phase-field model.[235] They claimed one key to the high rate capability of nano-$LiFePO_4$ is that phase separation is dynamically suppressed since the surface overpotential easily exceeding the solid-solution voltage barrier removes the thermodynamic driving force for phase separation.[235]

Although phase separation of LMO at low charging/discharging rate has been well known[38], we first report observation of phase separation suppression of LMO thin film cathodes driven by high current rates. The moving from two-phase reaction to solid-solution reaction is more clearly revealed from differential capacity (dQ/dV) profiles in **Figure 6.4**b where redox peak of two-phase reaction gradually gets similar to the one of solid-solution reaction when current rate increases. The ratios of the two redox peak heights plotted in **Figure 6.4**c (bottom-left axes) suggest slops of the potential plateaus get to be the same beyond 40C. The two redox peaks are barely visible at extremely high rate (160C). Lesel, et al. who cycled LMO thin films up to 1000C believed that the sloping voltage profile at such an extremely high current rate originated from pseudocapacitive behavior which was dominated by nonsolid solution diffusion-controlled Li storage mode, i.e. surface adsorption/desorption.[236] Therefore, ultrafast cycling capability of LMO thin film cathodes was achieved by sacrifice of capacity or energy density, typical shortcomings of supercapacitors. Another factor leading to the remarkable rate performance of LMO thin film cathodes was solid

and intimate contact between LMO thin film and the Pt current collecto layer whereas conduction pathways are established by adding carbon black and binders in a LMO powder composition cathode pack where complete contact is not guaranteed.[89]

Overpotentials between the two redox peaks linearly increase with current rates from 3 mV at 1C to nearly 0.4 V at 160C (**Figure 6.4**c top-right axes). The increased overpotential due to kinetic hindrance of Li-ion transfer hence caused obvious capacity loss shown in **Figure 6.4**d consisting of capacity retention profiles for both 25 nm and 100 nm LMO thin film cathodes under high rate tests. It can be seen 25 nm LMO demonstrated much better high rate capability, obtaining as high as 85% capacity retention even at 80C while a 92% capacity retention was retained for 100 nm LMO thin film cathode cycled at 12C. The better rate performance of 25 nm LMO thin film could be mainly ascribed to less constraints of Li-ion kinetics due to shorter diffusion length. In addition, the curves of capacity retentions in regard to current rates plotted in the inset show linear decline of capacity at high current rates.

To study the cycling stability or cyclability, 25 nm LMO thin film cathodes were partially cycled at 4C and in two voltage windows, i.e. a high voltage range of 4.07 – 4.5 V (magenta region in **Figure 6.3**d) and a low voltage range of 3.3 – 4.07 V (yellow region in **Figure 6.3**d), respectively. Capacity retention profiles in **Figure 6.4**e indicate the solid-solution reaction in lower voltage range was more stable than two-phase reaction in high voltage range. Therefore, suppression of phase separation of LMO charged/discharged at high voltage is desired in order to get higher cycling stability. In this regard, efforts have been made through surface modification to enhance LMO reversibility and details are to be discussed in Chapter 7. Moreover, **Figure 6.4**f presents two redox peaks corresponding to one low voltage cycle (3.3 – 4.07 V) and one high

voltage cycle (4.07 – 4.5 V) shown by the inset. Comparing with redox peaks from one full cycle between 3.3 – 4.5 V, there is nearly no overpotential for the solid-solution redox reaction at low voltage while a visible overpotential was observed from the two-phase redox reaction at high voltage. That further indicates reduced cyclability of LMO due to phase separation at high voltage.

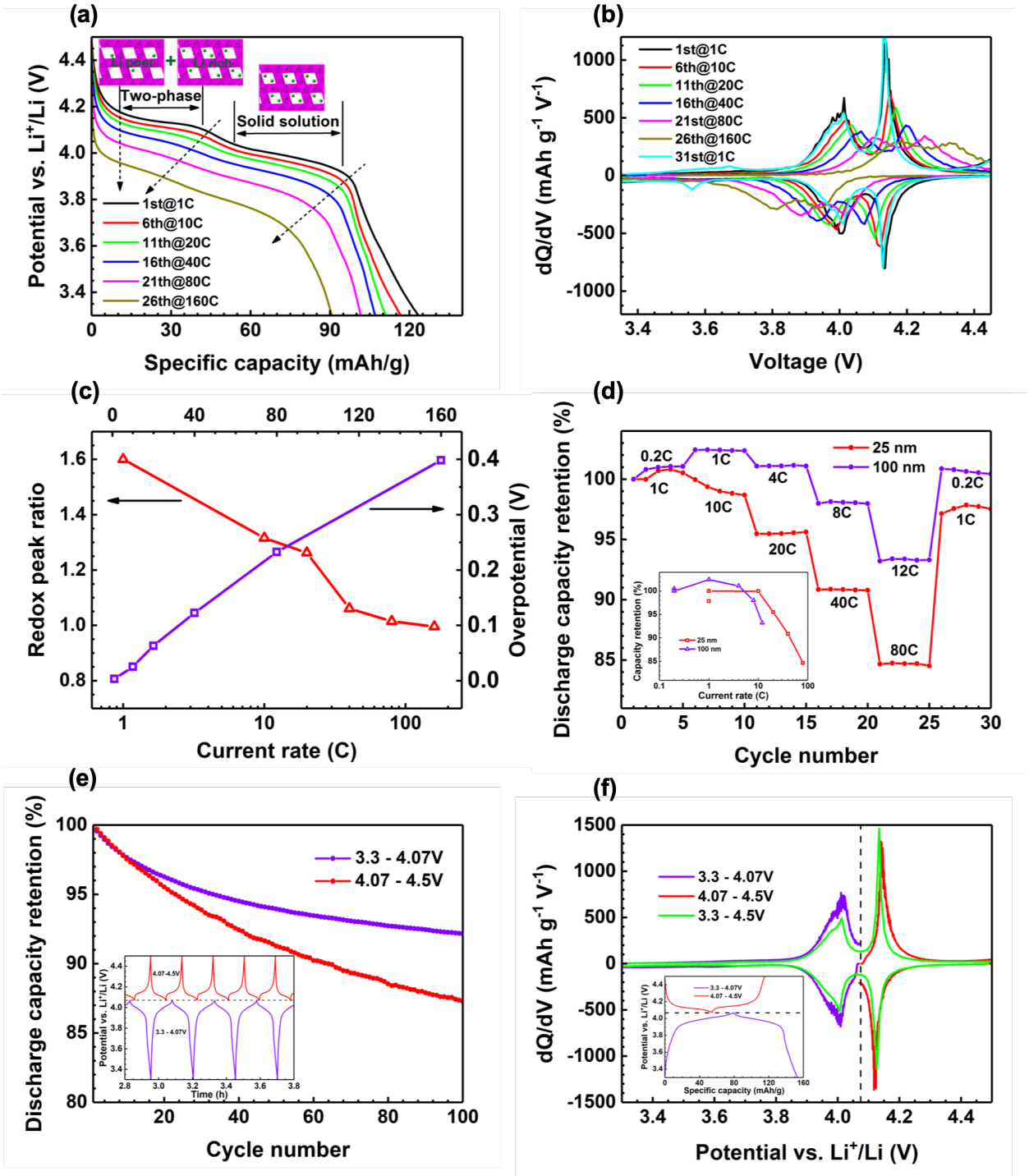

Figure 6.4 (a) Discharge profiles from 25 nm LMO thin film cathode cycled at various current rates. The first potential plateau at higher voltage represents two-phase redox reaction of LMO. A solid-solution reaction is assigned to the second potential plateau at lower voltage. (b) Two redox peaks revealed from differential capacity dQ/dV profiles at various current rates. (c) Ratios of the two redox peak heights (bottom-left axes) and overpotentials (top-right axes) at various current

rates. (d) Rate cycling results from 25 nm and 100 nm LMO thin film cathodes. Capacity retentions vs. current rates are plotted in the inset. (e) Discharge capacity retention curves from two 25 nm LMO thin film cathodes partially cycled in a low voltage range of 3.3 – 4.07 V and a high voltage range of 4.07 – 4.5 V, respectively. Inset shows charge/discharge voltage curves. (f) Redox peaks in dQ/dV curves from partial cycling and full cycling of 25 nm LMO thin film cathodes. The potential vs. capacity profiles from one low voltage and one high voltage cycles are shown in the inset.

In situ EIS measurement was conducted for a 25 LMO thin film cathode/Li metal anode coin cell between 100 kHz and 10 mHz applying an AC voltage of 10 mV at the "transition" voltage (4.07 V vs. Li/Li^+). The cycling cell was stopped and rested for 30 minutes to get stable open circuit voltage (OCV) before each AC impedance spectrum was recorded. An equivalent circuit model (ECM) shown in **Figure 6.5**a was applied for EIS fitting. Details about the ECM and fitting process are discussed in the results section of Chapter 6. The discharge capacity retention profile plotted in **Figure 6.5**b shows significant capacity drop during the first 50 cycles. Nyquist plots over 200 cycles were exhibited in **Figure 6.5**c from which selected Nyquist plots along with fitted curves are presented in **Figure 6.5**d. It can be seen that the AC impedance considerably increased until 10 cycles and started to slightly decline until 50 cycles after which the impedance got stabilized. EIS fitting parameters including impedances from SEI and CEI layers and Li-ion chemical diffusion coefficient are presented in **Figure 6.5**e. Remarkable increases of both impedances are consistent with observations from the Nyquist plots. The interfacial impedances slightly reduced while LMO discharge capacity suffered from apparent degradation (**Figure 6.5**b) during 10 – 50 cycles, suggesting there were other factors dominating LMO capacity fading at later cycling stage, such as Manganese dissolution and gradual surface structure reconstruction due to new interphase formation[57, 67, 68, 82].

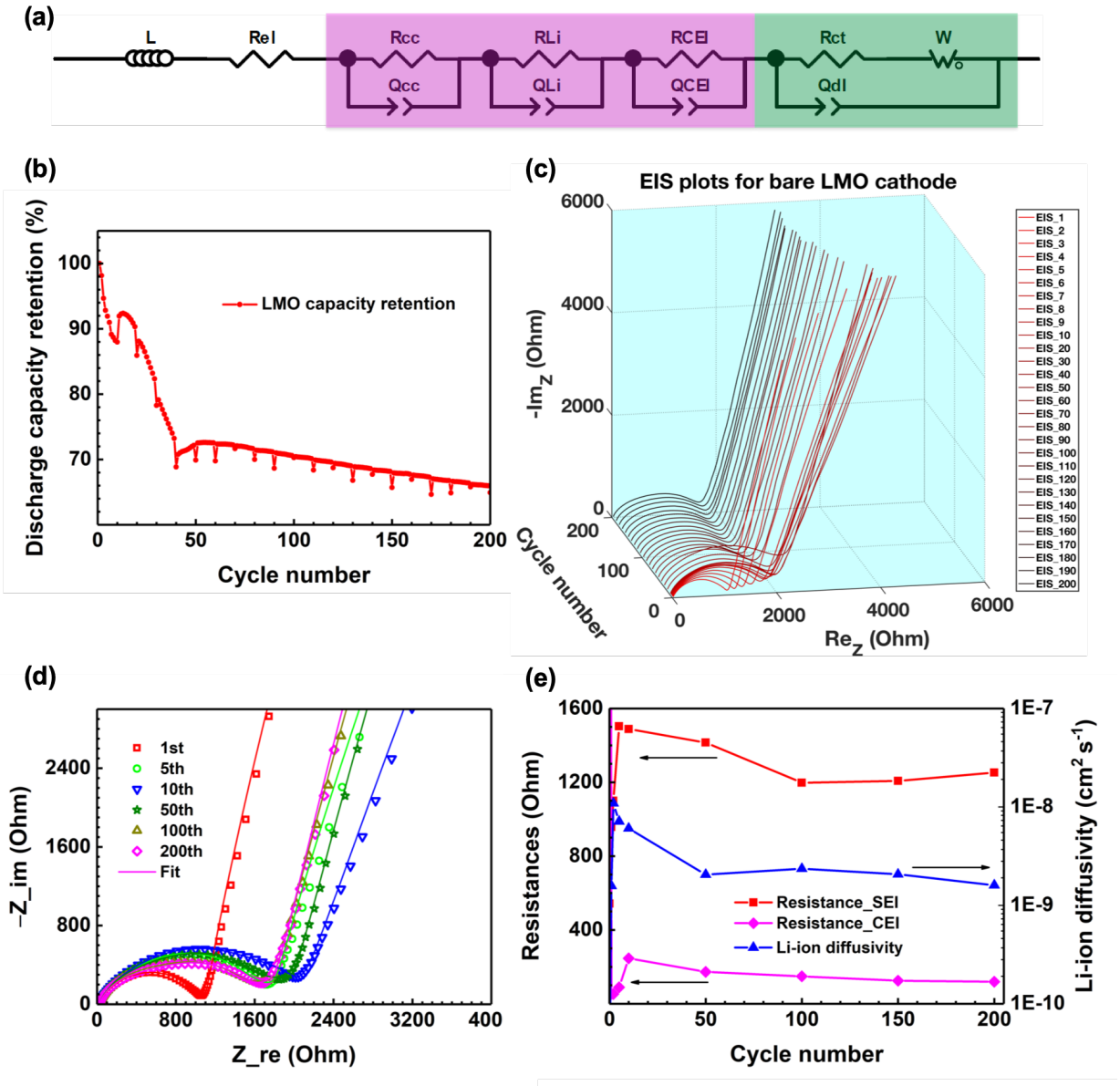

Figure 6.5 (a) A equivalent circuit model applied for EIS curve fitting for half coin-type cell with LMO thin film as cathode and Li metal as anode. (b) Discharge capacity retention during EIS measurement. (c) Nyquist plots recorded at 4.07 V over 200 cycles. (d) Selected Nyquist plots and corresponding EIS fitting curves. (e) Resistances of SEI and CEI, Li-ion chemical diffusivity obtained from EIS fitting.

6.4 Conclusion

LMO thin film cathodes sputtering deposited on well-prepared 100 nm Pt || 20 nm Ti || Al_2O_3 substrates demonstrated excellent cycling stability and superior ultrahigh rate capability. A 25 nm LMO thin film attained a high capacity retention of 77% after 900 cycles at 4C between an extended voltage range of 3.3 – 4.5 V. The LMO thin film cathodes were cycled up to 160C with a retention of 85% observed for 25 nm LMO and 92% retention for 100 nm LMO. The outstanding rate performance was attributed to absence of phase separation at high voltage range which was considered to be a rate-limiting step for various electrode materials including LMO. In addition, it was also found solid-solution redox reaction of LMO at lower voltage was more stable than the two-phase reaction at higher voltage. Therefore, it is suggested to suppress phase separation to enhance cyclability of LMO cathode through elemental doping or surface modification. Another key factor contributing to high rate capability of LMO thin film was good contact between the cathode material and Pt current collector layer. It is worth to be noted that extremely high power density of the LMO thin film cathodes was attained by sacrifice of total capacity due to characteristically transition of Li-ion storage modes from solid-solution diffusion in LIBs to pseudocapacitive behavior of surface absorption/desorption.

6.5 Acknowledgements

This work was supported as part of the Center for Electrochemical Energy Science, an Energy Frontier Research Center funded by the U.S. Department of Energy, Office of Science, Basic Energy Sciences (DE- AC02-06CH11357). Research at the Advanced Photon was supported by DOE, Office of Science, BES. This work made use of the EPIC, Keck-II, and/or SPID facility(ies) of Northwestern University's NUANCE Center, which has received support from the Soft and Hybrid Nanotechnology Experimental (SHyNE) Resource (NSF ECCS-1542205); the

MRSEC program (NSF DMR-1121262) at the Materials Research Center; the International Institute for Nanotechnology (IIN); the Keck Foundation; and the State of Illinois, through the IIN. This work made use of Pulsed Laser Deposition Shared Facility at the Materials Research Center at Northwestern University supported by the National Science Foundation's MRSEC program (DMR-1121262). This work utilized Northwestern University Micro/Nano Fabrication Facility (NUFAB), which is partially supported by Soft and Hybrid Nanotechnology Experimental (SHyNE) Resource (NSF ECCS-1542205), the Materials Research Science and Engineering Center (DMR-1720139), the State of Illinois, and Northwestern University.

Chapter 7: Unraveling Effects of Protective Coatings on Thin-Film $LiMn_2O_4$ Cathodes for Lithium Ion Batteries

7.1 Introduction

Spinel intercalation-type $LiMn_2O_4$ (LMO) has been accepted as one of the most attractive and proper cathode materials for lithium ion batteries (LIBs), and thus has been extensively studied since it was first introduced by J. B. Goodenough in 1983.[1, 3, 5, 18-21, 35, 47] This is due to its superior characteristics of high abundance, low cost, environment friendliness, good structural and chemical stability, a good Mn^{3+}/Mn^{4+} redox potential (4 V vs. Li/Li+), and fast charging rates compared with conventional layered materials $LiCoO_2$, $LiNi_{1-x-y}Mn_xCo_yO_2$ and olivine-type $LiFePO_4$.[1, 5, 18-20, 35] Rapid insertion/extraction reactions within the host spinel structure of a 3D $[Mn_2]O_4$ interstitial framework give LMO the edge for high power applications, such as full electric vehicles (EVs) and hybrid electric vehicles (HEVs).[48, 50] Despite these advantages, LMO-based LIBs suffer from severe loss of capacity (poor cyclability) upon repeated electrochemical cycling, especially at elevated temperature.[2,8] In literatures, the LMO capacity fading phenomenon has been attributed to several mechanisms including cooperative Jahn−Teller distortion of $Mn^{3+}O_6$ octahedra (high spin $3d^4$, $t_{2g}^3e_g^1$) at a deep state of discharge[23, 59], electrochemical reactions with the liquid electrolyte[56, 110], loss of crystallinity during cycling[58], manganese dissolution into the liquid electrolyte[57, 82], and etc. Although several researchers have reported that it is the increased interfacial resistances rather than simple manganese dissolution that are responsible for the majority of cell capacity loss, manganese dissolution is considered to be a crucial chain-reaction factor leading to the capacity fade since increase of cell resistances on both electrodes and formations of SEI and CEI layers are inevitably associated with manganese ions dissolution, migration and re-deposition (DMD) processes.[21, 26, 60, 61] It's generally believed

that principal causes of manganese dissolution are Mn^{3+} disproportionation reaction due to attack of HF acid at the interface between LMO and electrolyte[26, 61, 106, 107], irreversible loss of MnO to form more stable surface single-phase structures due to instability of the spinel LMO two-phase structure at high voltage[60, 61, 67, 106], and ready existence of Mn^{2+} prone to be dissolved at certain truncated LMO surfaces.[60, 63-65, 108-110] It has been always difficult to determine which single mechanism above remarkably dominants manganese dissolution reactions over the whole cycling life of LMO cathodes.[60]

Successful prevention strategies such as cationic and anionic doping[106, 113-116], surface coating[21, 57, 117-119], morphology tailoring[65, 108], and use of electrolyte additives treatments[120-122], have been applied to mitigate Mn dissolution. Among them, surface coating is treated as one of the most effective and economical approach without large sacrifice of LMO initial capacity, an inferior drawback of metal element doping.[57, 60] A variety of metal oxides such as Al_2O_3, ZnO, ZrO_2, TiO_2, Y_2O_3, $LiAlO_2$, $LiCoO_2$ have been coated on LMO particles to suppress Mn dissolution.[21, 118, 119, 123-125] Although LMO cathode capacity retention has been improved, there is yet not much detail on the fundamental mechanisms of manganese dissolution and how coating layers inhibit those aforementioned Mn ion-involved (electro)chemical reactions. For instance, there has been a controversy surrounded oxidation state of the dissolved manganese ions and those in the deposited manganese species on anode and cathode SEI (CEI) layers.[126-129] Besides, the suppression effects of coating layers can vary significantly with coating materials choice, coating layer thickness and coating routes.[21, 57, 118, 119] It is becoming great challenge to architect and further examine effective candidate coatings due to the complicated interfacial reactions among the coating layer, LMO electrode and electrolyte.[117, 130] Literature also reported additive of binder in

LMO particle composite cathode can form a surface layer which affects manganese dissolution as well.[237] With an aim to develop basic understanding of the manganese dissolution and address the crucial issues above, following criteria of a promising LMO coating layer should be stressed: 1) thin and uniform to cover entire LMO surface; 2) electrochemically stable on cycling and not react with LMO; 3) retain enough Li-ion conductivity; 4) rapid route to fabricate LMO cathode covered with various coatings.[118]

So far, LMO particles have been mostly used for coating study in literature.[21, 57, 117-119, 130] However, precise characterization is constrained due to complexity of LMO particle-based composite cathode. Particle shape, size, composite pack density and electrode components (solvent, binder and conductive additive) can significantly affect cell performance apart from coating layer.[26, 27] Unlike LMO particles, LMO thin films can serve as a more appropriate model cathode to comprehensively study manganese dissolution and coating effects in LIBs, attributed to the following merits. First, the coating materials can be easily deposited on LMO thin film with full and uniform coverage, so that direct contact with electrolyte is prohibited to avoid any possible attach from HF acid.[118] Second, it is probable to accurately control thickness of coating layer which is critical to optimize cell performance promoted by coating.[57, 119, 238] Third, thin film techniques such as sputtering and pulsed laser deposition provide rapid and effective routes to fabricate coated LMO thin films for fundamental study.[28, 29] Beside, LMO thin films grown on conductive substrates such as Pt require no solvents, binders or additives for electrochemical tests, which helps avoid unknown effects from those components in cathode. At last, advanced characterization at the molecular level is highly desired for precisely examining the interfacial reaction processes in LIBs.[30] Unlike particle-based electrodes, the LMO thin film geometry is ideally suited for interface

study by a range of advanced *in situ* and *ex situ* characterization tools such as X-ray photoelectron spectroscopy (XPS), synchrotron X-ray scattering and absorption spectroscopy, atomic force microscopy (AFM), and high-resolution scanning transmission electron microscopy (STEM).[30-33]

The perovskite oxide LSCO was chosen as a coating material due to its high electrical conductivity at room temperature and good electrochemical stability.[131, 132] In this paper, taking into consideration thickness and crystallinity of coatings, the promoted surface modification effects of LSCO on LMO thin film cathodes with a specific address of suppressing manganese dissolution processes were comprehensively examined via a series of electrochemical tests and various advanced characterization methods such as high-resolution STEM, EELS, EIS, etc.

7.2 Results and Discussion

Samples preparation. Nine types of LMO thin film cathodes were prepared and coated with ultra-thin LSCO layers via multiple-step sputtering deposition. **Figure 1** shows a schematic representation of the all-thin-film cathode geometry. For an accurate description of the LMO || Pt || Ti || Al_2O_3 cathodes fabrication, including coating layers via multiple-step sputtering deposition, please read the Experimental Section. **Table 1** reports a list of all the thin-film cathode types fabricated and characterized in this research. The sample sets are labeled with respect to the LMO and LSCO layer thicknesses, and the annealing temperature of the coating layer: e.g. "L2-LMO25_750" refers to a 25nm thick LMO cathode, covered with a 2 nm sputtered LSCO layer which was annealed at a temperature of 750 °C. If the temperature is not specified in the label, the coating layer was annealed at 450 °C. All the LMO cathodes were prior annealed at 750°C in air for two hours before the coating deposition.

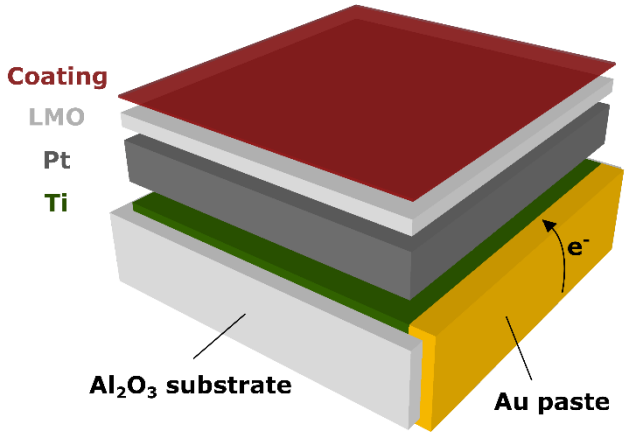

Figure 7.1 Schematic representation of the all-thin-film cathode geometry.

Table 7.1 Overview of the thin-film cathode sets.

Sample type	LMO thickness [nm]	LSCO thickness [nm]	Annealing Temperature [°C]	Test
LMO25	25	-	-	GCPL, STEM, SEM
LMO100	100	-	-	GCPL, STEM, XRD
L1-LMO25	25	1	450	GCPL, STEM, SEM
L2-LMO25	25	2	450	GCPL, STEM, SEM
L3-LMO25	25	3	450	GCPL, STEM, SEM
L2-LMO100	100	2	450	EIS
L6-LMO100	100	6	450	EIS, XRD
L2-LMO25_RT	25	2	RT	GCPL
L2-LMO25_750	25	2	750	GCPL

The 25 nm LMO thin film cathode geometry is illustrated in **Figure 7.2**a including a schematic of corresponding layers and an enlarged inset clearly showing the LMO layer. The surface morphology of a 25 nm LMO thin film shown by a SEM image in **Figure 7.2**b indicates truncated octahedral crystallites are formed and well-aligned along [111] crystalline orientation. Recent study suggests Mn dissolution is largely dependent on the lattice orientation of the LMO surface attached to the electrolyte and {110} surface aligned to Li diffusion channels are most vulnerable to Mn dissolution.[62, 65] Besides, it was reported that LMO (111) surface with Li-rich layer is more resistant to Mn dissolution by DFT calculations.[63, 64] Truncated octahedron-shaped

LMO particles synthesized under controlled conditions that favor stability of LMO demonstrated excellent cyclability and high rate capability.[60] Therefore, the prepared 25 nm LMO thin film in this work was supposed to attain good cycling performance. That special surface morphology characteristic is further verified by XRD patterns in **Figure 7.3** which indicates crystallites with specular LMO (111) planes dominate for 25 nm LMO film while 100 nm LMO film is polycrystalline with apparent (111) and (311) main refection lines shown in **Figure 7.3**a. In fact, it has been reported that epitaxial LMO thin films were synthesized on Pt and Au coated oxide substrates as long as the films were thin enough.[169, 239] In addition, it can be seen in **Figure 7.3**a that the diffraction lines from 100 nm LMO films match well with the lines from cubic spinel $LiMn_2O_4$ (space group $Fd\bar{3}m$, a = 8.248 Å, ICSD 99367) with a slight angle shift which is caused by Li deficiency in the LMO films. The LMO thin film with 6-nm-thick LSCO coated on the surface still kept cubic spinel crystal structure.

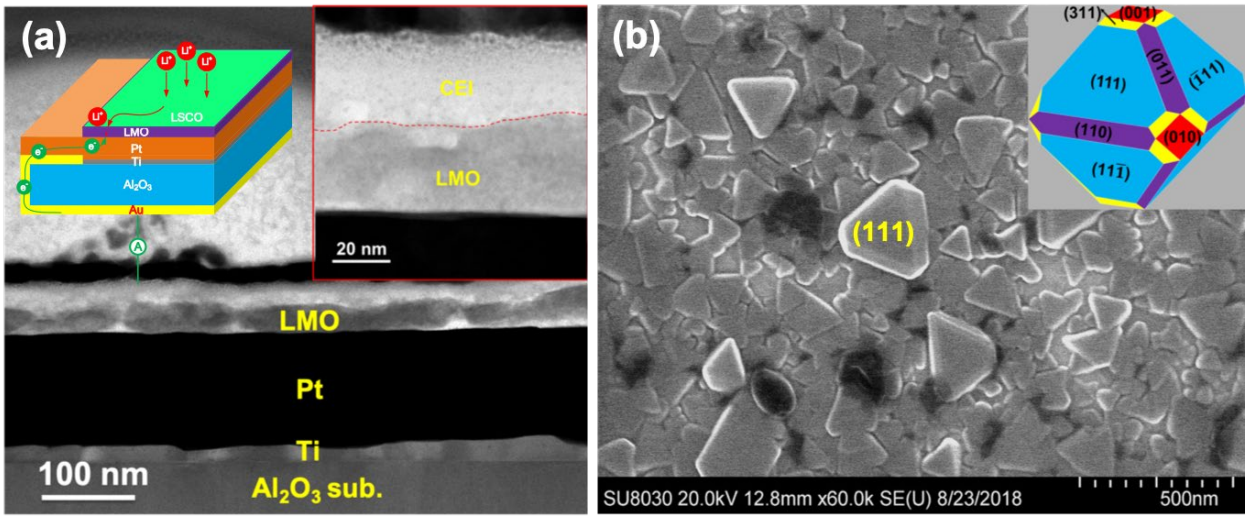

Figure 7.2 (a) STEM image showing cross-sectional geometry of a 25 nm LMO thin film on Pt/Ti/Al_2O_3 substrate, which is schematically illustrated in the upper left inset. A zoom-in image clearly showing LMO individual layer is embedded at the upper right corner. (b) SEM image shows the surface morphology of the LMO thin film, revealing truncated octahedral gains with well-aligned (111) out-of-plane facets (demonstrated by the inset).

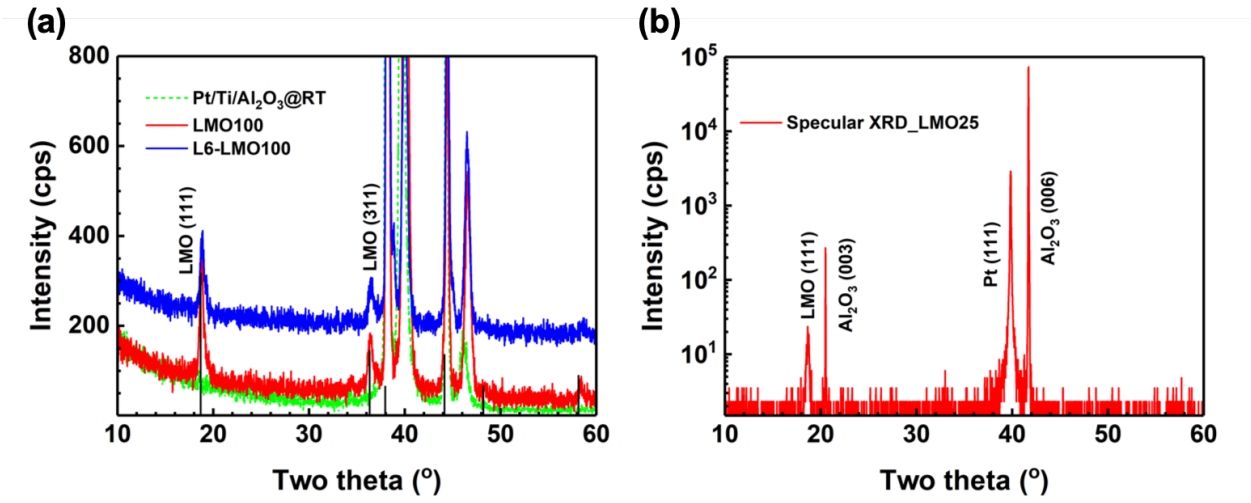

Figure 7.3 (a) Grazing incidence XRD patterns of 100-nm-thick LMO thin film annealed at 750 °C in air (red line), LMO thin film coated with 6nm LSCO layer which was annealed at 450 °C in air (blue line) and Pt-coated Al_2O_3 substrate at room temperature (dash green line). The reflection lines in black are from cubic spinel $LiMn_2O_4$. The patterns are vertically offset to make clear comparison. (b) Specular XRD for a 25-nm-thick LMO thin film.

Electrochemical testing and characterization. It is well known that manganese dissolution gets significant once at deep states of charge/discharge, i.e. relatively high/low electrode voltages.[60] Therefore, choosing a proper cycling voltage window is required to clearly observe manganese dissolution effects. Electrochemical performance of the thin-film LMO cathodes were evaluated by galvanostatic cycling with potential limitation (GCPL)in a half coin-type cell geometry. **Figure 7.4**a shows the discharge capacity retention profiles of different LMO100 cathodes cycled at 1C within various voltage windows. The cathode cycled between 3.5 – 4.3 V exhibited the best performance achieving an initial specific capacity of 128 mAh/g and showing a capacity retention of about 2.2% after 100 cycles. The electrodes cycled to either a higher or lower cutoff voltage displayed instead a smaller capacity retention, with the lowest cyclability when discharged to 2.5V which severely damaged LMO spinel structure. The extended voltage range of 3.3 – 4.5 V was chosen for to accelerate capacity fading while avoiding LMO structural damage.

The thickness effects of coating layer were studied by applying four different LMO thin film cathodes: bare LMO25, L1-, L2- and L3-LMO25. Besides, all received LMO thin films modified with surface coatings were annealed at 450 ºC in air to get the coating layers crystallized. The discharge specific capacities of those thin film cathodes cycled between 3.3 – 4.5 V are plotted in **Figure 7.4**b, indicating 2 nm LSCO coating demonstrated best performance with an initial capacity of 113 mAh/g and smallest capacity loss of about 3.1% after 300 cycles. Differences of initial specific capacities were primarily due to variations of estimated thickness and area among tested LMO thin films. It was particularly noted that thicker coating (3 nm LSCO) drastically sacrificed initial capacity of LMO cathode which gradually recovered with cycling. It could be ascribed to increased Li-ion transfer resistance through thick LSCO coating layer at early stage. The poor performance of thick LSCO coating highlighted the essentiality of accurately controlling thickness and uniformity of the coating layer.

To further optimize the coating effect in terms of crystallinity, 2 nm LSCO-coated LMO cathodes post annealed at various temperatures were tested. It is evident that L2-LMO25 annealed at 450 ºC exhibited best cycling stability with merely 3% capacity loss over 300 cycles shown in **Figure 7.4**c. It has been found crystallinity of the coating materials can work as an important property concerning capacity retention improvement of the protected cathodes. For instance, Al_2O_3 coatings prepared by ALD were demonstrated to function better with amorphous phase (or without annealing)[225] while higher cycling stability and promoted charge transfer ability were ascribed to TiO_2 coatings annealed at high temperature[240]. It was attributed to higher electron and Li-ion conductivities of amorphous Al_2O_3 and crystallized TiO_2. LSCO obtains high electrical conductivity at high crystallinity. Grazing incidence XRD patterns in **Figure 7.5** indicate the

synthesized LSCO thin films by DC sputtering without annealing or annealed at 450 ºC had very poor crystallinity and became crystallized only above 750 ºC. Therefore, the enhanced coating effects from 2 nm LSCO@450 ºC must have resulted from additional bonus which are to be discussed latter in this section.

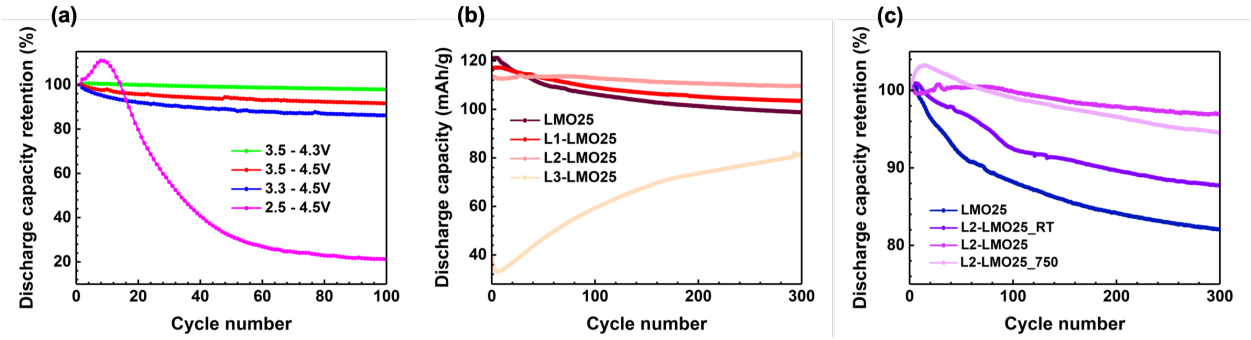

Figure 7.4 (a) Discharge capacity retention profiles of 100 nm LMO thin film cathodes cycled within various voltage windows at a current rate of 1C. (b) Discharge specific capacity profiles of 25 nm LMO thin film cathodes coated with annealed (at 450 ºC) LSCO layer of various thicknesses. (c) Discharge capacity retention profiles of 25 nm LMO thin film cathodes coated with 2 nm LSCO layer annealed at various temperatures.

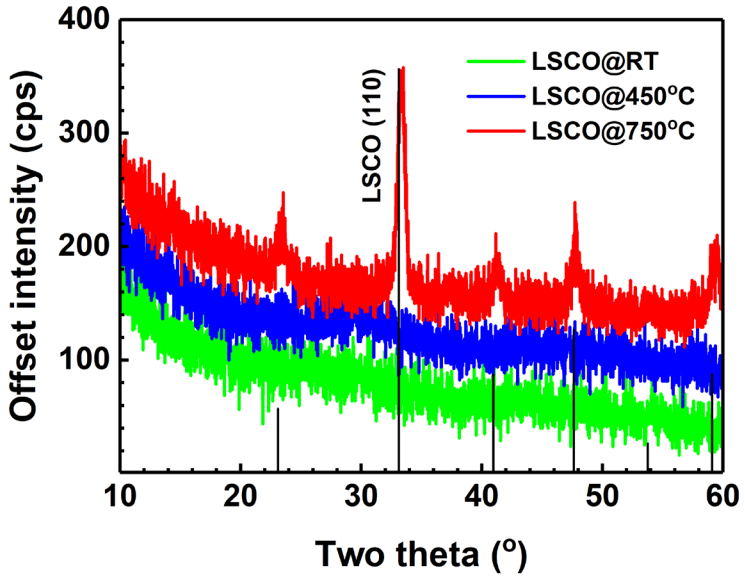

Figure 7.5 Grazing incidence XRD patterns of 20 nm LSCO || Al_2O_3 thin films prepared by DC sputtering deposition with various post annealing temperatures. The patterns are vertically offset to make clear comparison.

Once determined that L2-LMO25 is the electrode of choice, longer term tests (up to 500 cycles) were run and the charge/discharge curves, along with the relative incremental (IC) capacity analysis, are compared with the bare LMO electrode. **Figure 7.6**a-c show the charge/discharge profiles for LMO25, L2-LMO25_RT and L2-LMO25. All the electrodes cycled between 3.3-4.5V at a constant C-rate of 4C exhibit a specific discharge capacity close to 120 mAh/g, with the only exception of the coated L2-LMO25 (~110 mAh/g). Although the coated and annealed sample shows a slightly lower initial capacity, it is characterized by the smallest degradation after 500 cycles, as shown by the capacity retention profiles presented in **Figure 7.6**d. It can be seen that LSCO coatings serving as an effective surface modification strategy demonstrated remarkable improvement of LMO cathode cycling stability. The 2nm-coated and annealed sample shows a capacity retention as high as 94.8% after 500 cycles, in contrast with the 84.0% observed for LMO25.

Two redox potential plateaus were revealed obviously at 4.13V and 4.01V in the discharge voltage-capacity curve (**Figure 7.6**a) or IC curve (**Figure 7.6**e) from bare LMO thin film cathode. This distinctive behavior of cubic spinel LMO is consistent with what was reported in literature.[47, 48, 50, 241] $Li_xMn_2O_4$ showed two distinct regions in the shape of discharge curve during lithiation from x = 0 to x = 1 at low current rate. In region I, Li-ion started to intercalate into the $[Mn_2]O_4$ framework occupying empty 8a tetrahedral sites upon discharging. Two different cubic phases coexisted due to ordering of Li^+ in the lattice matrix accompanied by formation of Li-poor and Li-rich phases within a flat potential plateau. With more incoming Li^+, the two-phase redox reaction proceeded to a homogeneous solid solution reaction in region II where the potential curve continuously decreased.[206] However, this inhomogeneity of various LMO crystal structures got indistinct with surface modification by a coating layer of LSCO. The two regions in **Figure 7.6**b

began to merge once LMO thin film cathode was coated with non-annealed LSCO, which became even more obvious after the coating layer was annealed at 450 ºC shown in **Figure 7.6**c where region I transitioned into region II. It is interesting that LMO cycling stability was significantly improved with disappearing of the two-phase redox reaction in region I, which is indicated by the drastic reduction of redox peak height at ca. 4.13V marked with arrows in **Figure 7.6**f. By comparison, it can be concluded that the homogeneous solid solution phase of LMO at low potential was more electrochemically stable, dominance of which due to surface coating of annealed LSCO thus promoted LMO cathode capacity retention. It is inferred that coating of annealed LSCO may have reacted with and stabilized LMO surface structure and hence suppressed phase separation at high voltage in region I, though the exact underlying mechanism is still ambiguous. More detailed discussion is presented along with the analysis of STEM characterization results. Furthermore, the overpotential of LMO redox reactions were calculated to be around as small as 10 mV (**Figure 7.6**e), indicating Li^+ bulk diffusion within 25 nm LMO thin film cathode was neglectable as a limiting step. Therefore, high power density superiority which will be further discussed in **Figure 7.8** is expected.

It is also interesting to notice an extra redox potential plateau at ca. 3.6V which became apparent after 390 cycles shown in **Figure 7.6**a and more clearly revealed by the IC curves in the inset of **Figure 7.7**. Since the redox potential plateau for lithiation/delithiation between $LiMn_2O_4$ and $Li_2Mn_2O_4$ is at around 3.0V, the extra redox peak must result from a newly formed phase which added an extra reversible capacity of LMO by about 8% indicated in **Figure 7.6**d. In addition, the plateau was mildly observed for the coated and annealed sample (**Figure 7.6**c,f). This interesting discovery of bare LMO redox chemistry is first reported here and no further explanation so far can be provided concerning composition and crystal structure of this new phase.

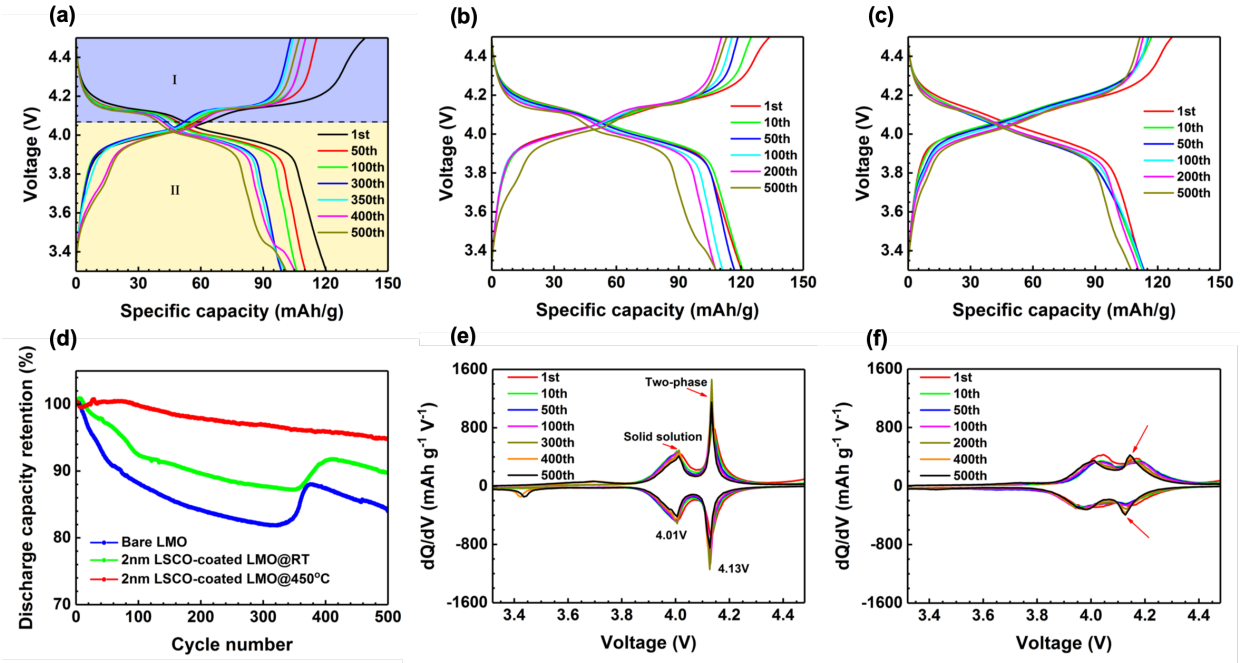

Figure 7.6 (a-c) Charge/discharge profiles from (a) LMO25, (b) L2-LMO25_RT, and (c) L2-LMO25 cycled between 3.3 – 4.5 V at 4C. (d) Discharge capacity retention profiles of those three cells from a-c over 500 cycles. (e-f) IC profiles derived from data in a and c.

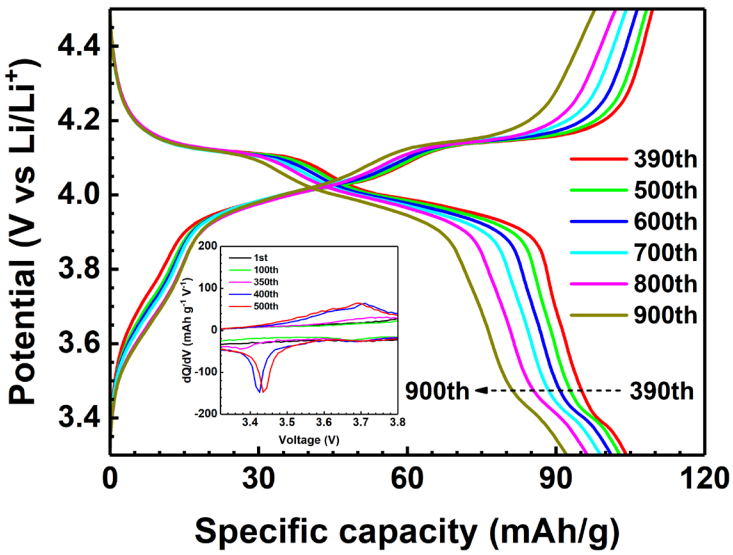

Figure 7.7 Charge/discharge curves of bare LMO25 cathode cycled between 3.3 – 4.5 V at 4C for 900 times. The inset shows IC (dQ/dV) curves illustrating a gradually evident extra unknown redox peak at around 3.6V after 390 cycles.

High rate cyclability of the LMO thin film cathode was explored as well. Both LMO25 and L2-LMO25 were cycled at increasing current rates, up to 160C and back to 1C, and the results are displayed in **Figure 7.8**. It is remarkable how both the bare and coated electrodes show very little capacity fade up to extreme C-rates, as observed in **Figure 7.8**a. The comparison of the capacity retentions for the 2 electrodes is shown in **Figure 7.8**b where L2-LMO25 exhibited higher capacities than the bare electrode when cycled up to 80C. However, limited electron and Li-ion mobilities of the LSCO coating layer constrained LMO thin film cathode performance at extremely high rate, i.e. 160C, where the situation was inverted. When the electrodes were finally cycled at 1C, L2-LMO25 was able to reach the initial discharge capacity, while LMO25 loses 20% of its initial capacity. This further verified coatings of annealed LSCO could remarkably promoted LMO thin film cathode cycling stability.

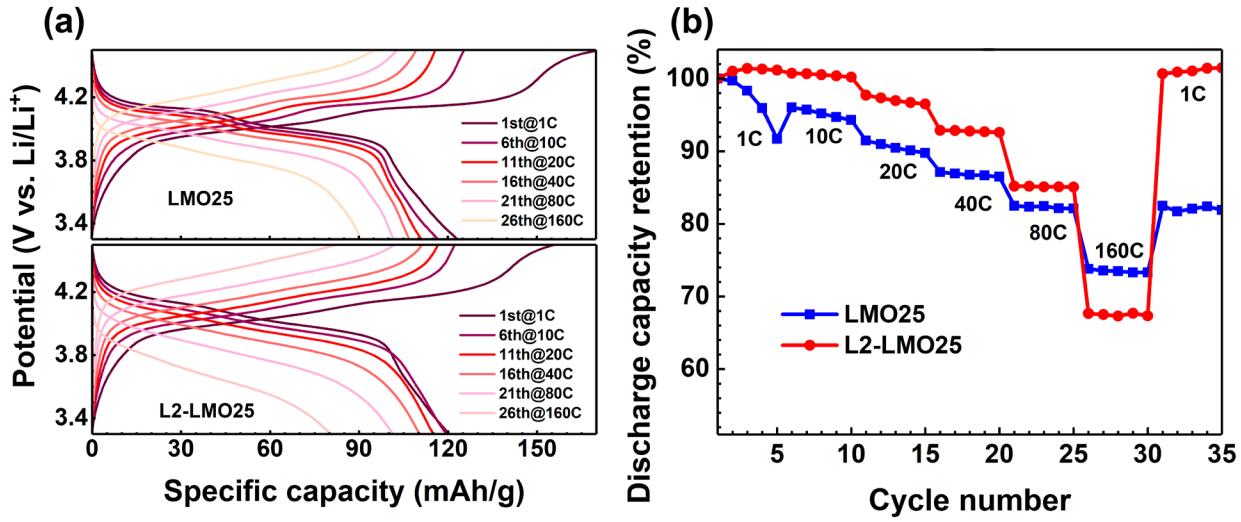

Figure 7.8 (a) Charge/discharge curves at increasing C-rates up to 160C of LMO25 (top) and L2-LMO25 (bottom). (b) Discharge capacity retentions at increasing current rates for the 2 electrodes, as a function of the cycle number.

Fracture and loss of crystallinity, widely observed in both andoe and cathode materials after progressively electrochemical cycles, have been considered as vital causes of LMO cathode

capacity fade as well.[242-244] 25 nm bare LMO and LSCO-coated LMO thin film cathodes were galvanostatically cycled betweeen 3.3 – 4.5V at 1C. Surface morphorlogies of the pristime and degradated samples are presented by SEM images in **Figure 7.9**. A notable amount of secondary grains were formed on the primary particles in bare LMO thin film cathode after 5 cycles (**Figure 7.9**a and b), while most of the pristine particles on the surfae modified LMO cathode still preserved original sizes and shapes (**Figure 7.9**c and d). Grain fracturing and intergranular cracking at boundaries of the primary particles have been ascribled to anisotropic lattice spacings and crystal structure inhomogeneity.[244, 245] Those cracks formed and propagated progressively along cycling, leading to less electrical connections and increase of exposed interface between LMO and electrolyte where Mn dissolution through disproportionation reaction ($Mn^{3+} \rightarrow Mn^{2+} + Mn^{4+}$) was accelerated.[244] It is disccussed accompany the electrocehmcial results that the coatings of annealed LSCO suppressed phase seperation at high voltage in region I, resulting in enduring lattice strucuture homogeneity and much less microstrain formation over cycling. As a consequence, the surface modified LMO thin film cathode maintained pristine surface morphoglogy with undisrupted primary particles (**Figrue 7.9**d). Moreover, grazing incidence X-ray diffraction patterns on **Figure 7.10** suggest the LMO thin film cathode coated with annealed LSCO layer kept much better crystal structure integrity and much higher crystallinity than bare LMO after cycling. Therefore, it can be concluded here that apart from inhibition of untable two-phase redox reaction disscussed previously, annealed LSCO as a coating material also effectively prolonged cycling stability of LMO thin film cathodes by inhibiting fracturing and cracking of LMO grains and keeping high crystallinity through extended cycling.

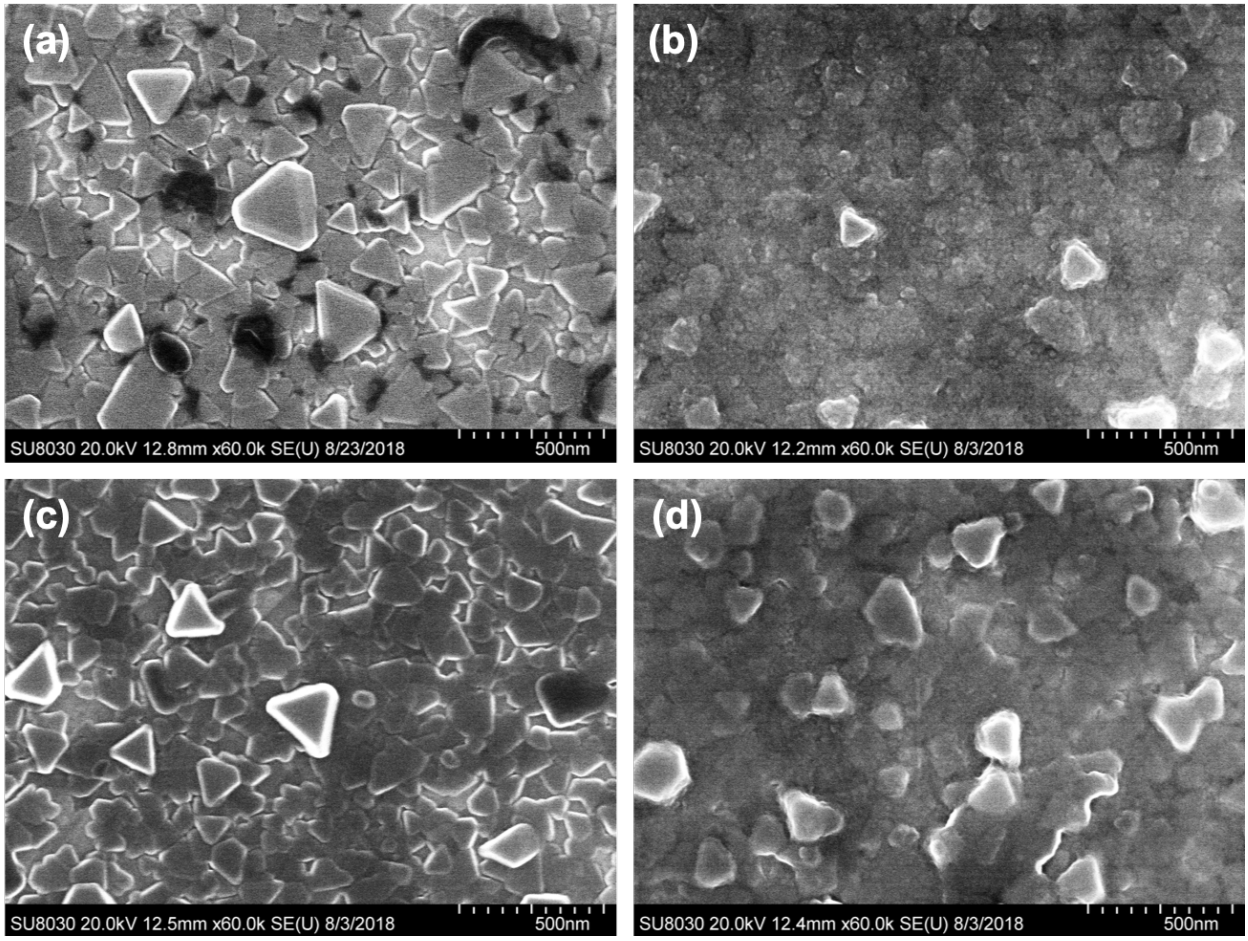

Figure 7.9 (a-b) SEM images from bare LMO25 before and after 5 cycles at 1C. (c-d) SEM images from L2-LMO25 before and after 5 cycles at 1C.

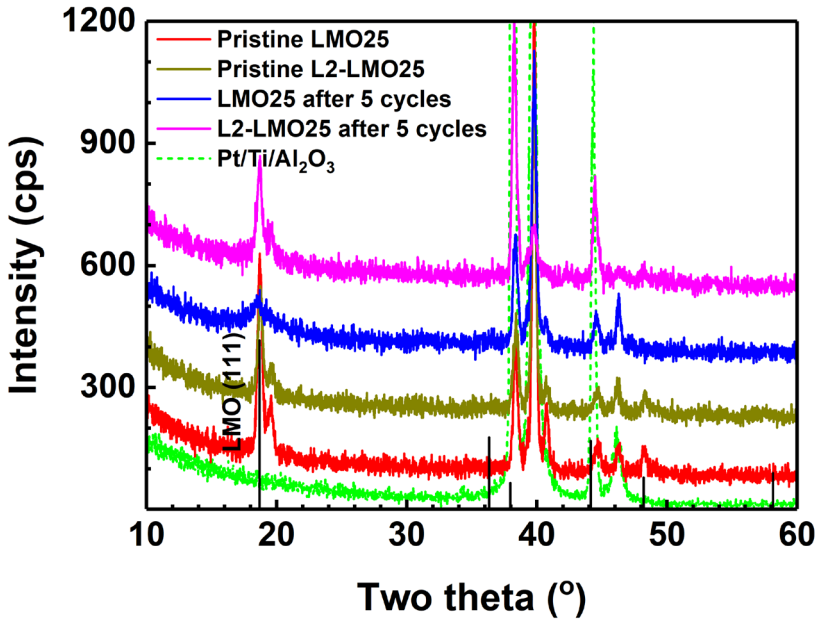

Figure 7.10 Grazing incidence XRD patterns of $Pt/Ti/Al_2O_3$ substrate (dash green curve), pristine and cycled bare LMO25 (red and blue curves), pristine and cycled L2-LMO25 (dark yellow and magenta curves). The black lines represent reflections from cubic spinel $LiMn_2O_4$. The patterns are vertically offset to make clear comparison.

The LSCO coating effects on local atomic structure of aged LMO thin film cathode were investigated by aberration corrected high-resoluiton scanning transmission electron microscopy (STEM). It has been reported new distorted phases formed in surface and subsurface regions of cycled LMO material, especailly at high cycling voltage (>4.3 V).[67, 68, 217, 218] Oxygen release and Mn ion displacement were believed to cause LMO material lattice structure distortion and surface phase transformation forming interphases such as rocksalt $LiMnO_2$, layered Li_2MnO_3, and defect spinel $LiMn_3O_4$.[217, 218] Those phase transformation resulted in excess Mn^{3+} at the interface betweeen electrode and liquid electrolyte. It boosted Mn^{2+} dissolution due to the disporportionation reaction ($Mn^{3+} \rightarrow Mn^{2+} + Mn^{4+}$). As inferred in the disscussion of electrochemical cycling results above, annealed LSCO coating layer was explained to account for stabalizing LMO surface crystalline structure at high voltage. i.e. region I (**Figrue 7.6**a) where unstable two-phase redox

reaction was inhibbited. This deduction was further verified by atomic structure observations illustrated by two STEM-ABF images viewed at $(11\overline{2})$ lattice plane from bare LMO25 and L2-LMO25 after 500 cycles at 4C in **Figure 7.11**. It is apparent that LSCO coating prevented drastic loss of LMO crystallinity during long term cycling by comparison of atomic resolution between two STEM-ABF images. Actually, this coating effect was also observed by GIXRD results in **Figure 7.10**. Therefore, precise lattice structure analysis was only conducted on the L2-LMO25 sample which obtained high crystallinity even after 500 cycles.

Reduced FFT inserted in **Figure 7.11**b clearly displays diffraction patterns from spinel LMO. Calculation from d-spacings of those marked lattice planes results in $d_{111} = 4.632$ Å and $d_{\overline{2}02} = 2.915$ Å. For spinel cubic $LiMn_2O_4$, lattice constant value is $a = 8.2476$ Å with $d_{LMO111} = 4.762$ Å and $d_{LMO\overline{2}02} = 2.916$ Å (ICSD 99367). Thus, the lattice structure of cycled L2-LMO25 was tetragonally distorted with calculated pseudo-cubic lattice parameters as $a = b = 7.588$ Å, $c = 9.109$ Å and c/a = 1.2. Similar calculation became challenge for cycled bare LMO25 sample reduced FFT image (inset in Figure **7.11**a) of which retained much lower resolution due to drastic crystallinity loss. The c/a ratio was approximately calculated to be 1.4, which indicated larger lattice structure distortion than the coated L2-LMO25 sample. By comparing theoretical lattice model with the enlarged atomic structure pattern in **Figure 7.11**b inset, it is found the contrast of each Mn2 ion column spatially spreads along [111] direction, which is clearly exhibited by simulated STEM-ABF image for tetragonal defect spinel Mn_3O_4 (or $Mn^{2+}[Mn_2^{3+}]O_4$) in **Figure 7.12**b. That indicates some Mn ions also reside in Li ion column occupying Li 8b tetrahedral sites which are connected with Mn ion column. Actually, it was reported in literature that DTF

calculation indicated the delithiated metastable state $\lambda\text{-}Mn_2O_4$ can decompose into more stable phase by the following reaction[68]:

$$\lambda\text{-}Mn_2O_4 \longrightarrow (2/3)Mn_3O_4 + (2/3)O_2 \quad (7.1)$$

The negative formation Gibbs free energy of above reaction indicates thermodynamically favorable phase transition which involves oxygen loss and Mn ion migration. By stimulating LMO phase transitions using focused electron beam from aberration corrected STEM, Mn^{4+} ion migration from octahedral sites to corner-shared empty tetrahedral sites was observed.[218] The $Mn_{oct} \longrightarrow Mn_{tet}$ process resulted in formation of a new interphase which held a tetragonally-distorted defect spinel structure ($LiMn_3O_4$-like $LiMn_x[MnMn_{1-x}]O_{4-\delta}$). The interphase with small x value was stable and highly reversible according to the cycling results for L2-LMO25 thin film cathode in **Figure 7.6**, which is in accordance with reports in literature.[217] For bare LMO25 cathode, reaction (7.1) became more notable and much more Mn ion migrated through $Mn_{oct} \longrightarrow Mn_{tet}$, leading to dramatic lattice structure distrotion and significant level of oxygen loss. As a result, more low valence Mn ions (Mn^{2+} and Mn^{3+} in Mn_3O_4-like new interphase) were produced. Tetrahedrally coordinated Mn^{2+} was readily prone to dissolving in liquid electrolye while octaherally site Mn^{3+} underwent disproportionation reaction ($Mn^{3+} \rightarrow Mn^{2+} + Mn^{4+}$) forming more disssolvable Mn^{2+}.

Direct loss of active materials, crystallinity and violent lattice structure distortion caused large capacity decline of bare LMO25 cathode. So far, one can conclude that LSCO coating supppressed the new defect spinel interphase formation reaction (7.1) which was though thermodynamically favoriable and hence allevated LMO structure distortion and Mn dissolution to some degree. Moreover, STEM resutls here also indicate the new phase formation not merely

occur at LMO material (sub)surface (several nanometers deep as literature reported[68, 217, 218]), the phase transition can reach as far as at least 25 nm deep, i.e. the entire 25 nm LMO thin film cathode in our experiments. It may suggest nano sized cathode materials do not necessarily optimize their performance without any surfae modification. Most reported results of LMO surface coating researches in literature were based on limited cycled (<200). It is essential for coating layers to keep stable and intact over long-term cycling. Therefore, condition of LSCO coating layer after 500 cycles was examined by STEM-EELS mapping in **Figure 7.13**. It can be seen a continuous layer of 2 nm La coming from LSCO coating uniformly covered LMO thin film surface, indicating the coating layer still kept integrity even after extended cycling (500 cycles).

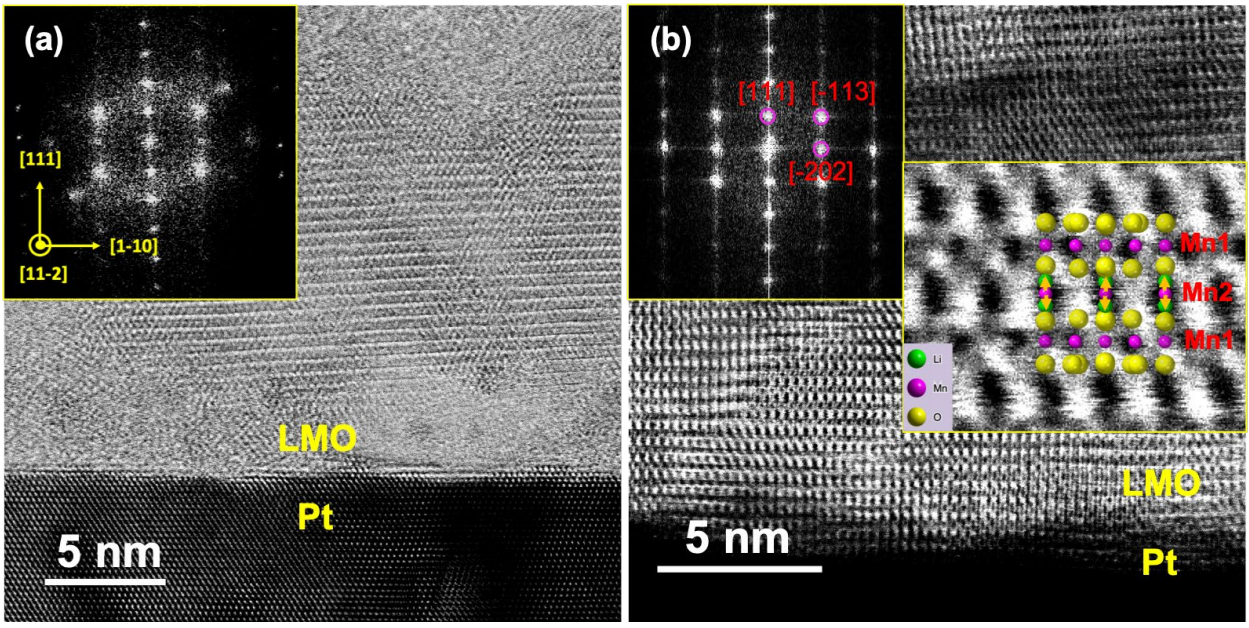

Figure 7.11 STEM-ABF images taken along [11-2] direction illustrated by the crystallographic coordination in the panel (a) inset. (a) from bare LMO25 after 500 cycles at 4C. Inset at top left is reduced FFT. (b) from L2- LMO25 after 500 cycles at 4C. Top left inset is reduced FFT marked with lattice planes from spinel crystalline structure. An enlarged atomic structure image is inserted at the middle right, overlaid with a schematic lattice structure produced by CrystalMaker.

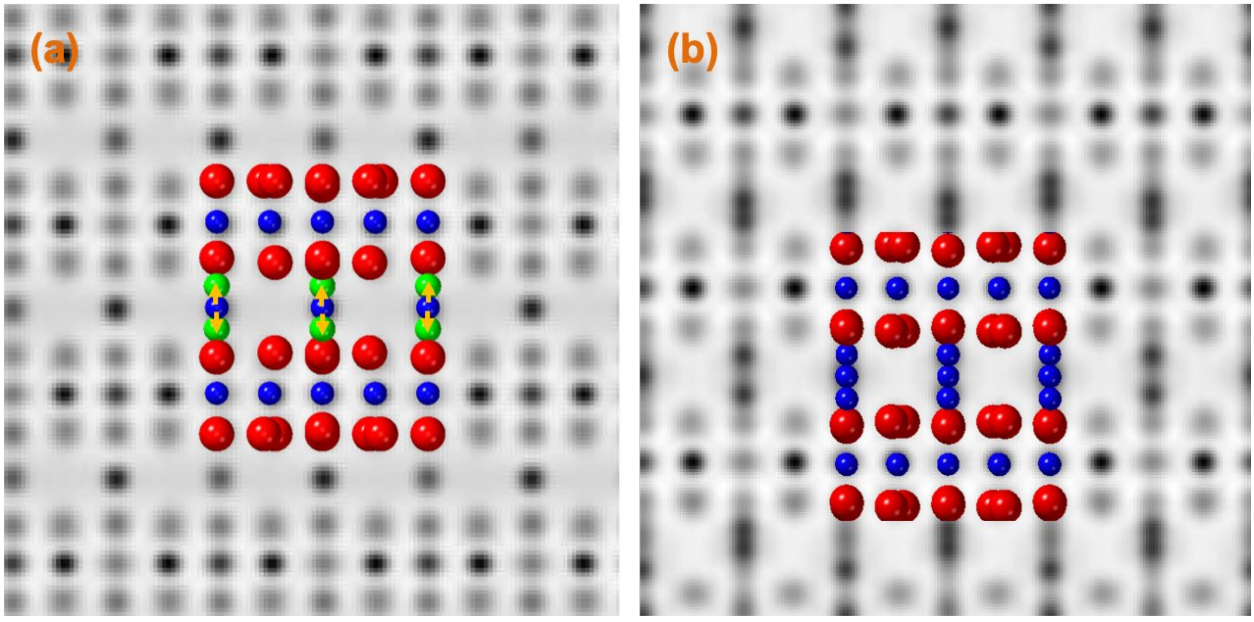

Figure 7.12 Simulated STEM-ABF images of (a) spinel cubic $LiMn_2O_4$ and (b) defect spinel Mn_3O_4 (output from Dr. Probe[246]). Theoretical atomic models produce by CrystalMaker are overlaid on corresponding images.

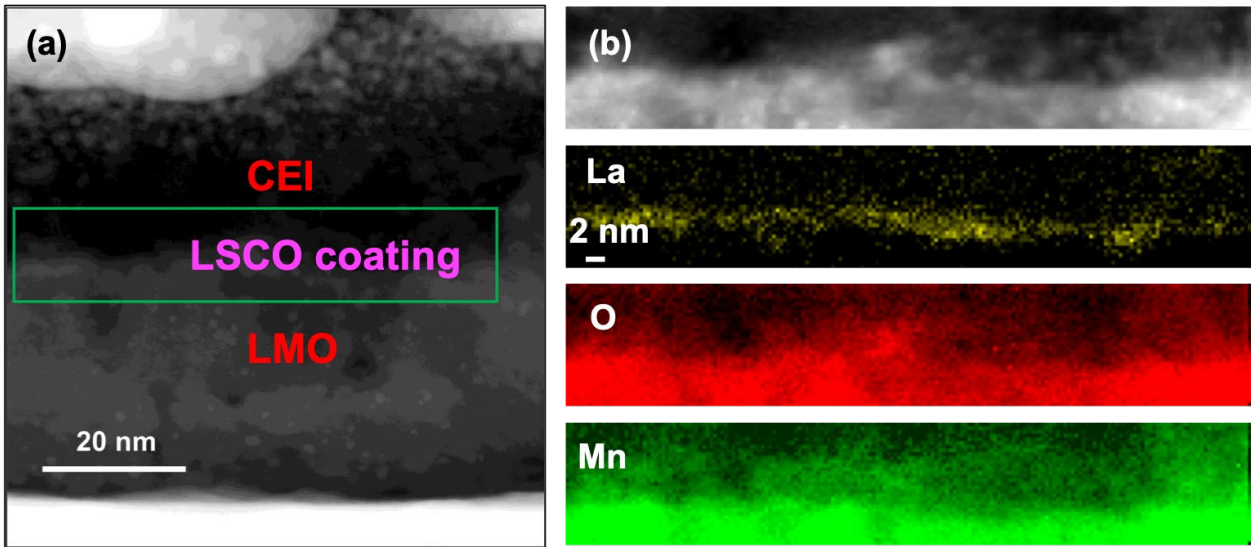

Figure 7.13 EELS mapping of La, O and Mn at the interface between L2-LMO25 (after 500 cycles) and CEI.

The proposed interpretation of LMO surface crystalline structure reconstruction upon cycling by formation of a tetragonal defect spinel Mn_3O_4-like phase from cubic spinel was further

examined by EELS characterizing manganese oxidation state in the degraded L2-LMO25 thin film cathode. An EEL spectrum map of Mn-$L_{2,3}$ edge measured in a sliced area (inset in **Figure 7.14**a) across the cycled LMO and CEI layer is presented in **Figure 7.14**a. The Mn L_3 edge of higher peak intensity exhibited a clear peak position shift with respect to depth from LMO surface to bottom, while peak position of Mn L_2 edge barely changed. The white-line energy difference of Mn-$L_{2,3}$ edge was reported to be proportional to nominal Mn oxidation state.[247, 248] Therefore, it was expected to observe various Mn oxidation states in LMO and CEI layer.

The most common method widely applied to relate EELS spectra to the nominal oxidation state of a transition metal such as Mn is to quantitatively calculate the anomalous L_3/L_2 white-line ratio. This work used the same method reported by Schmid, et al. to obtain Mn L_3/L_2 ratio.[247] First, the background intensity underneath the Mn-$L_{2,3}$ spectra was subtracted by an inverse power-law function in the pre-edge region (590 – 630 eV). A Hartree-Slater cross-section step function scaled and normalized to the experimental Mn-$L_{2,3}$ spectra 2 eV window positioned at the relative minimum between L_2 edge and the first EXELFS oscillation was removed in order to isolate the while-line intensities (**Figure7.14**b). the remaining signals (red line) under the corrected L3 and L2 edges are integrated over 4 eV windows positioned at the peak maxima. The resulting integrated intensities were used to calculate Mn L_3/L_2 ratios.

Dependence of the Mn-$L_{2,3}$ white-line ratio with the nominal oxidation state for a series of Mn compounds is plotted in **Figure 7.14**c (Reproduced from **Ref.** [247]). The red dashed line represents a calibration curve fitted by a power-law function to the reported data[247]. Mn oxidation states calculated by applying the fitting function (**Figure 7.14**c) and Mn L_3/L_2 ratio values extracted using aforementioned method (**Figure 7.14**b) are presented in **Figure 7.14**d. A gradual decrease of Mn oxidation state from bottom to surface was observed with an average value of 2.4

within the cycled L2-LMO25 thin film cathode. The average Mn oxidation state was close to the value in $LiMn_3O_4$, verifying formation of Mn_3O_4-like tetragonal defect spinel interphase from the electrochemically cycled LMO thin film cathode. It is also worth noting that manganese species with much lower oxidation state value (< 2) were observed within the CEI layer. Those Mn ions in CEI layer caused extra capacity loss of LMO thin film cathodes.

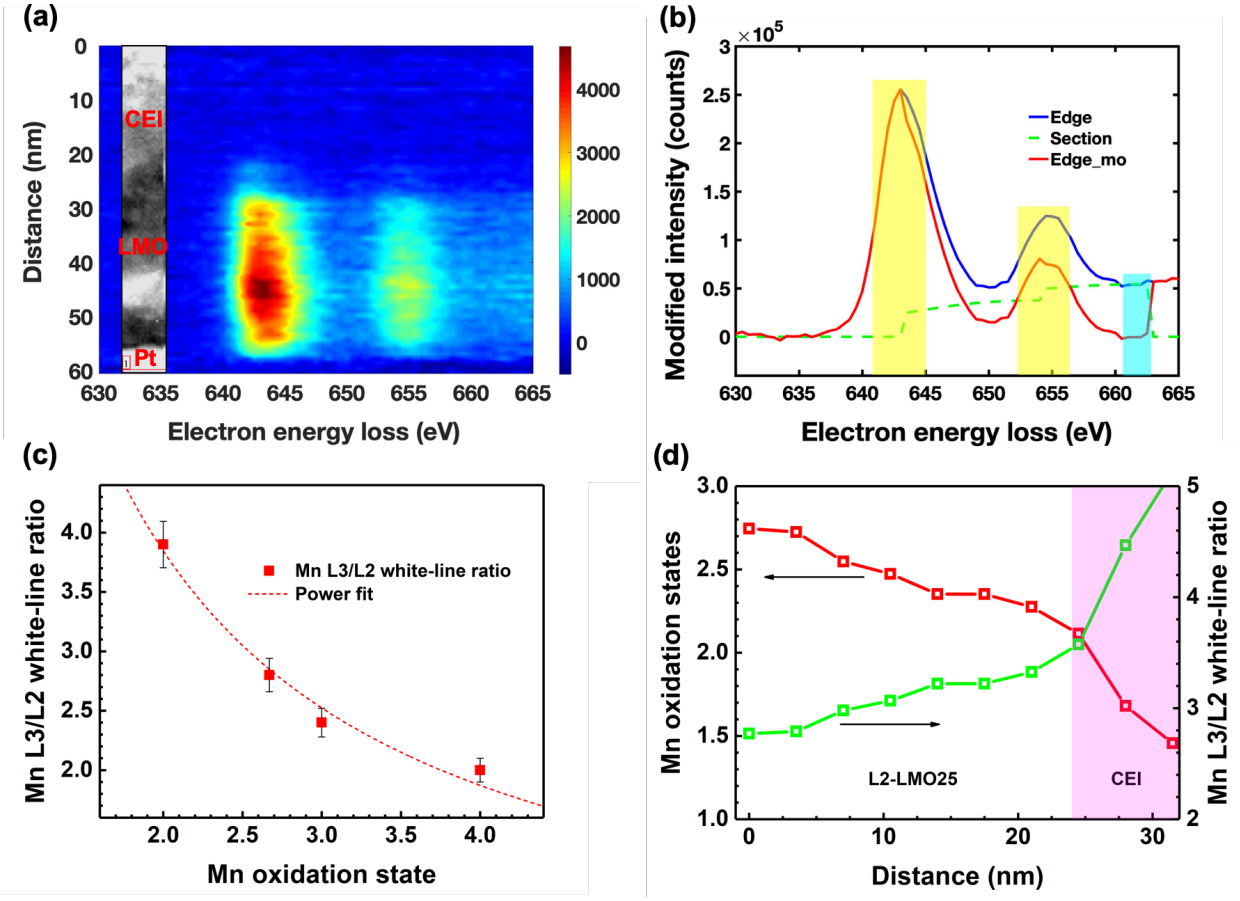

Figure 7.14 (a) EEL spectrum map of Mn-$L_{2,3}$ edge measured in a sliced area across CEI and L2-LMO25 thin film layer (after 500 cycles) depicted by the inset. (b) A sketch showing a obtained Mn-$L_{2,3}$ edge (blue line) after subtraction of background intensity fitted by an inverse power-law function in the pre-edge region (590 – 630 eV), two 4 eV windows (yellow boxes) used for integration of the Mn-L_3 and Mn-L_2 white line intensities, and one 2 eV window positioned at the relative minimum between L_2 edge and the first EXELFS oscillation (cyan box) used to scale the Hartree-Slater cross-section step function (green line). After scaling and subtraction of this function, the remaining signals (red line) under the corrected L_3 and L_2 edges are integrated, and their ratio is calculated. (c) Dependence of the Mn-$L_{2,3}$ white-line ratio with the nominal oxidation

state for a series of Mn compounds. (Reproduced from **Ref.** [247]) The red dashed line represents a calibration curve fitted by a power-law function to the data. (d) Calculated Mn-L_3/L_2 white-line ratios and corresponding Mn oxidation states at various depths from the L2-LMO25 sample after 500 cycles.

Apart from manganese dissolution, accumulated interfacial resistances are another key factor that have been recognized to cause LMO capacity depleting.[60, 61] Electrochemical impedance spectroscopy (EIS) has been a widely applied technique to characterize AC impedances in electrochemical devices.[206] EIS in a 3-electrode (3-el) setup was performed on bare and LSCO-coated 100 nm thick LMO electrodes. **Figure 15**a shows a schematic representation of the lab-made device used for the 3-electrode test. The electrodes and a glass fiber separator, soaked with the electrolytic solution, were placed and compressed between a copper disk and an aluminum piston. A lithium metal pin, in contact with the electrolytic solution, was used as a reference electrode. **Figure 15**b shows the resolved EIS spectra for the working (W.E.) and counter (C.E.) electrodes in an LMO100/Li cell (green dotted line). The thin film LMO100 electrode (blue dotted line) was characterized by a relatively small impedance, compared to the large contribution from the lithium metal anode (red dotted line), making the 3-el test crucial for the study of the cathode polarization processes. The resolution of the single electrode impedance was found to be extremely accurate, as the arithmetic sum of the W.E. and C.E. contributions (black solid line) perfectly resembled the full cell impedance (**Figure 15**b). The relative residuals between the 2 curves were observed to be within ±0.04% (**Figure 15**c).

Figure 15d displays the Nyquist plot of the EIS spectra recorded on bare (LMO100) and coated (L2- and L6-LMO100) thin film cathodes. All the impedance spectra were characterized by a very small semicircle in the high frequency region, as shown in the zoomed view in **Figure**

15e, and a second semicircle in the mid-frequency range, whose size was observed to increase with thicker coatings. The low frequency region of the spectra was instead characterized by a mixed diffusive and capacitive vertical tail.

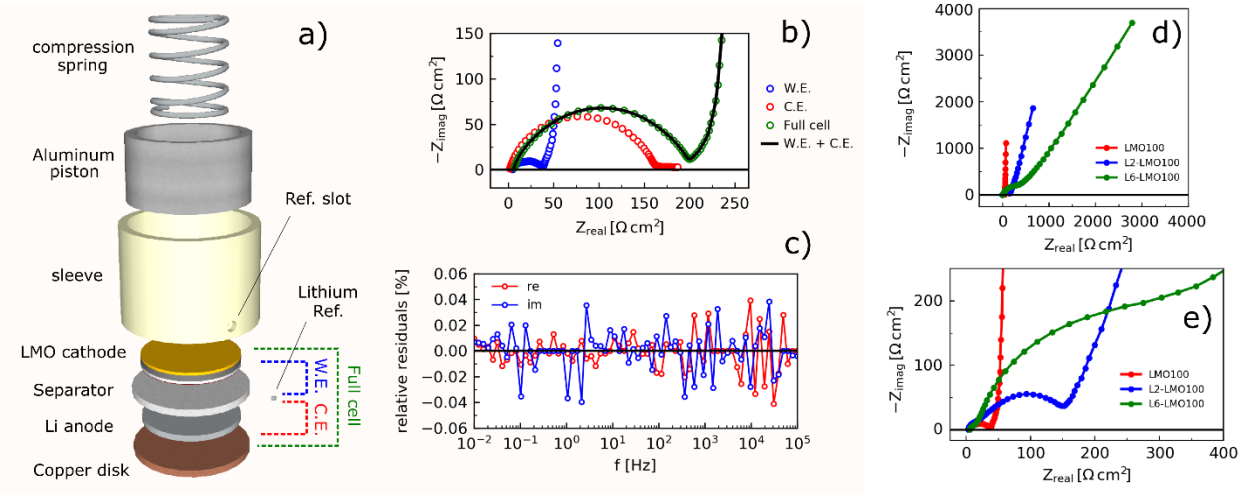

Figure 7.15 (a) Schematic representation of the 3-electrode setup and (b) Nyquist plot of the resolved EIS spectra for working (LMO100) and counter electrodes. (c) relative residuals between measured full cell EIS and calculated EIS as sum of W.E. and C.E. contributions. (d) Nyquist plot of the resolved EIS spectra for the thin film cathodes and (e) zoomed view of the high frequency region.

The equivalent circuit model (ECM) used to fit the thin film cathode spectra is schematically shown in **Figure 16**a. It consists of a resistor R_{ohm} describing the electrolyte resistance (intercept with the x-axes), an RQ_{CC} element and the circuit proposed by Meyers et al.[221]. RQ_{CC} is composed of a parallel connection between a constant phase element Q_{CC} and a resistor R_{CC} associated with the polarization resistance at the current collector/electrode interface.[222-224] The Meyers element models the mid- and low-frequency part of the spectra and it is composed of the RQ_{layers} element and a Randles circuit. RQ_{layers} is associated with the resistance furnished by the LSCO coating layer and the cathode electrolyte interface (CEI) layer, spontaneously formed after electrolyte decomposition on the cathode surface. The Randles circuit

is composed of a parallel connection between the charge transfer resistance at the LMO/LSCO interface R_{ct} (assuming Li ion diffusion through the coating) and the constant phase element Q_{dl}, associated with the double layer capacitance. The resistor R_{ct} is then connected in series with a general finite space Warburg element $W_{GSF,3D}$ associated with the Li diffusion process along a three-dimensional diffusion path, terminated by an impermeable boundary.[227] The impedance associated with $W_{GSF,3D}$ is calculated as:

$$Z_{GFSW,3D}(\omega) = R_w \cdot \frac{\tanh[(j\omega\tau_w)^{n_w}]}{\tanh[(j\omega\tau_w)^{n_w}] - (j\omega\tau_w)^{n_w}}$$

with the time constant:

$$\tau_w = \frac{L^2}{D}$$

R_w is polarization resistance, n_w is an exponent ($0<n_w<0.5$) reflecting the degree of non-uniform diffusion[228, 229], L is the electrode thickness and D is the diffusion coefficient of lithium in LMO.

Figure 16b-d shows Nyquist and Bode plots of the impedance spectrum measured for L2-LMO100 at 50% SOC. The solid black line represents the best fit to the measured data (gray dots) using the ECM described in **Figure 16**a, while the colored lines illustrate the deconvoluted single elements of the ECM. **Figure 16**e shows the relative residuals between the model fit and measured data. The relative residuals for the real and imaginary part are observed to be within ±2%, supporting the goodness of fit.

The high frequency semicircle (red line) observed in the zoomed Nyquist plot in **Figure 16**c describes the polarization at the current collector/electrode interface, and it is observed to be much smaller than the RQ element (yellow line) associated with the coating layers. The low frequency branch (dotted blue line) represents the Randles element used to model the interfacial

charge transfer resistance and lithium ion diffusion within the LMO electrode. Several impedance spectra were measured for LMO100, L2- and L6-LMO100 at different SOCs and the fitted value for the most meaningful parameters were calculated and plotted in **Figure 17**.

The current collector resistance R_{CC} was found to be in the range 5-20 Ωcm^2, and independent on the SOC. R_{layers} and R_{ct} are instead observed to be higher when the battery is fully discharged (**Figure 17**a,b), as described in literature[224], and to increase with thicker coating layers. R_{layers} for the bare LMO electrode is calculated equal to 18±6 Ωcm^2. The resistance in the coated samples is instead measured to be 143±11 Ωcm^2 with a 2nm coating, and 361±29 Ωcm^2 with a 6nm coating at all SOCs, with exception of the lowest one (inset in **Figure 17**a). This means that each additional 1nm-thick layer increases the ohmic resistance of 60±3 Ωcm^2. Finally, **Figure 17**c shows the lithium diffusion coefficient D_{Li} calculated for all the thin film LMO cells as a function of the SOC. As reported in literature[201, 206, 220], it is found to be in the 10^{-8}-10^{-10} cm^2s^{-1} range. The highest diffusivity values for LMO100 (red line) are observed when the battery is fully charged or discharged, and at 50% SOC when the transition between the solid solution and two-phase structure occurs. The "W' shape observed for the D_{Li} curve at different SOCs is less pronounced when the LMO electrode is coated with LSCO (blue and green line).

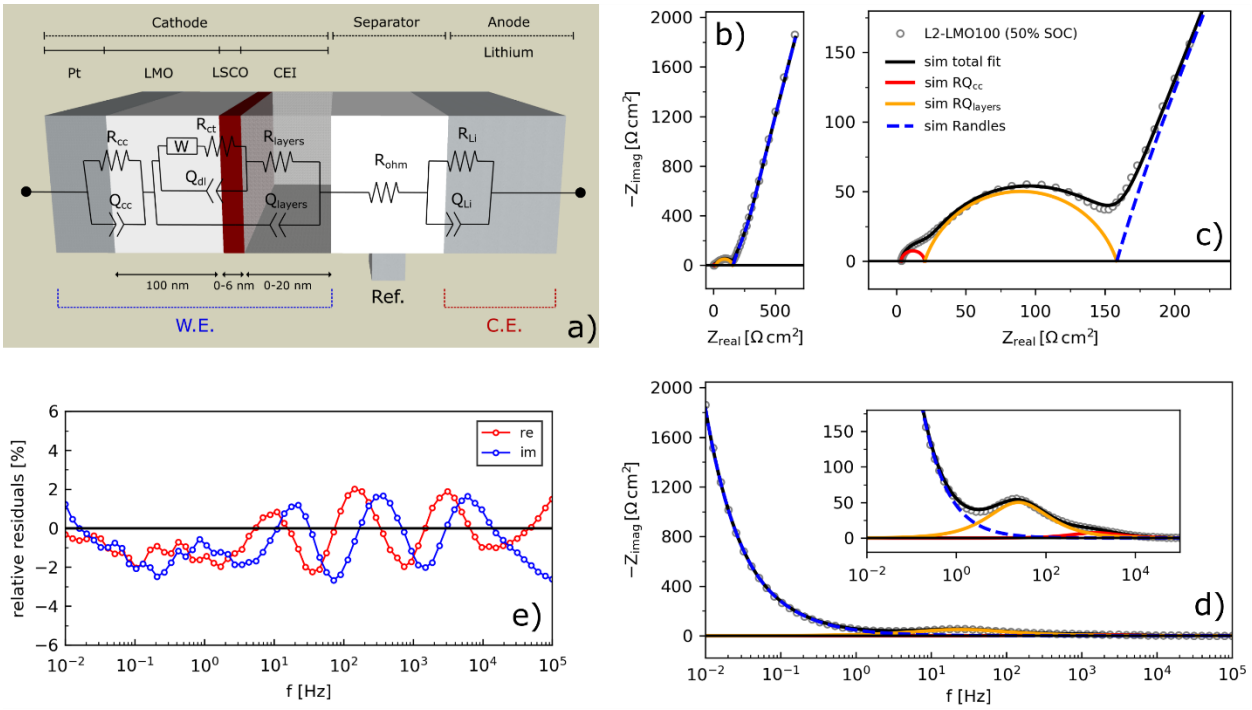

Figure 7.16 (a) Schematic representation of the equivalent circuit model used to fit the W.E. and C.E. impedance. (b) Nyquist plot of the EIS spectrum for L2-LMO100 at 50% state-of-charge and (c) zoomed view of the high frequency region. (d) Bode plot of the EIS spectrum for L2-LMO100 at 50% state-of-charge and zoomed view in the inset. (e) relative residuals between model fit and relative data.

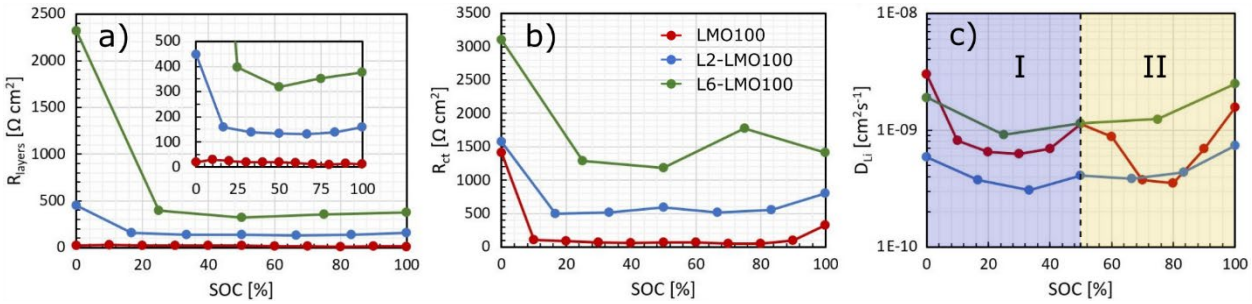

Figure 7.17 Fitted values for (a) Rlayers, (b) Rct and (c) DLi as a function of state-of-charge.

Apart from LSCO, two other coatings of WO_3 and ZnO were also fabricated on the LMO thin film cathodes to explore their coating performances. Aykol, et al. predicted WO_3 and ZnO as promising coating materials for LMO cathode using DFT high-throughput computational design methodology.[117] In addition, both these two materials have also been experimentally demonstrated

to enhance capacity retention of LMO powder cathodes to certain degree.[123, 249, 250] However, those reported work were from results of limited cycles (100 times). Coating effects and stability of coatings during long-term cycling were seldom covered in literature. Therefore, similar to work on LSCO coating discussed above, coating effects of WO_3 and ZnO were studied in terms of coating layer thickness and crystallinity over extended cycling (500 times). According to discharge capacity retention profiles plotted in **Figure 7.18**a, 2 nm unannealed WO_3 notably improved LMO capacity for the first 250 cycles in a voltage range of 3.3 – 4.5 V at 4C. However, drastic capacity loss was observed afterwards, phenomenon of which instantly occurred on the coated LMO sample with annealed WO_3 upon cycling. Unlike the case of LSCO coating, it was obvious that post annealing of WO_3 coatings had deteriorated effect on LMO performance (**Figure 7.18**c) while unannealed WO_3 coating remarkably promoted LMO capacity at early cycling stage (**Figure 7.18**b). Actually, it was found Li^+ diffusivity in amorphous (unannealed) WO_3 was higher than that in crystalline (annealed) WO_3.[117] That could be an interpretation that the unannealed WO_3 coating worked better due to smaller Li^+ transfer resistance within the coating layer. The rapid capacity degradation of the sample represented by green profile in Figure 7.18a was probably caused by dissolution and dissipation of WO_3 coating layer after 250 cycles.

The same work was repeated for ZnO coating. It was surprising that ZnO coatings barely had any improvement on LMO capacity in terms of both thickness and post annealing according to the discharge capacity retention curves in displayed in **Figure 7.19**a. A drastic loss and quick recovering behavior of discharge capacity retention was observed on the ZnO-coated LMO thin film cathodes during the first 50 cycles. A possible explanation was that ZnO coatings could dissolve into the electrolyte or be damaged during early cycling process. As a result, coating effect of ZnO quickly disappeared once the LMO cathodes were reversibly cycled. This deduction was

verified by comparing the charge/discharge profiles at early and late stages illustrated in **Figure 7.19**b. An apparent overpotential between the two potential plateaus of LMO cathode can be observed at the very beginning, indicating existence of ZnO coating layer which caused large Li^+ diffusion resistance. However, the charge/discharge profile shape at the 100th cycle resembled the one from bare LMO demonstrated in **Figure 7.6**a, indicating disappearance of ZnO coating layer. Therefore, it is concluded here that neither WO_3 nor ZnO demonstrated promoted long-term coating effects probably due to poor stability during reversible cycling.

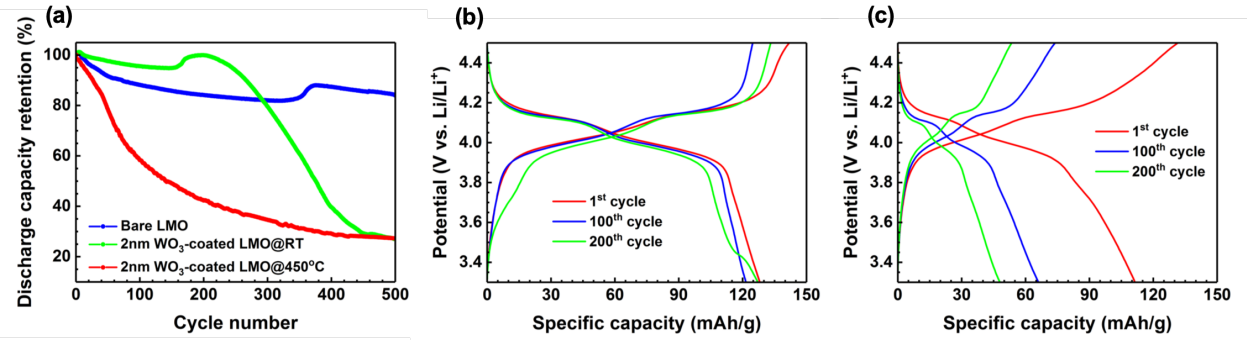

Figure 7.18 (a) Discharge capacity retentions of bare LMO25 and coated LMO25 with 2 nm WO_3 layers which were either not annealed or annealed at 450 °C. All samples were cycled between 3.3 – 4.5 V at 4C. Specific charge/discharge profiles of LMO25 with (b) unannealed 2 nm WO_3 and (c) annealed 2 nm WO_3 at 450 °C.

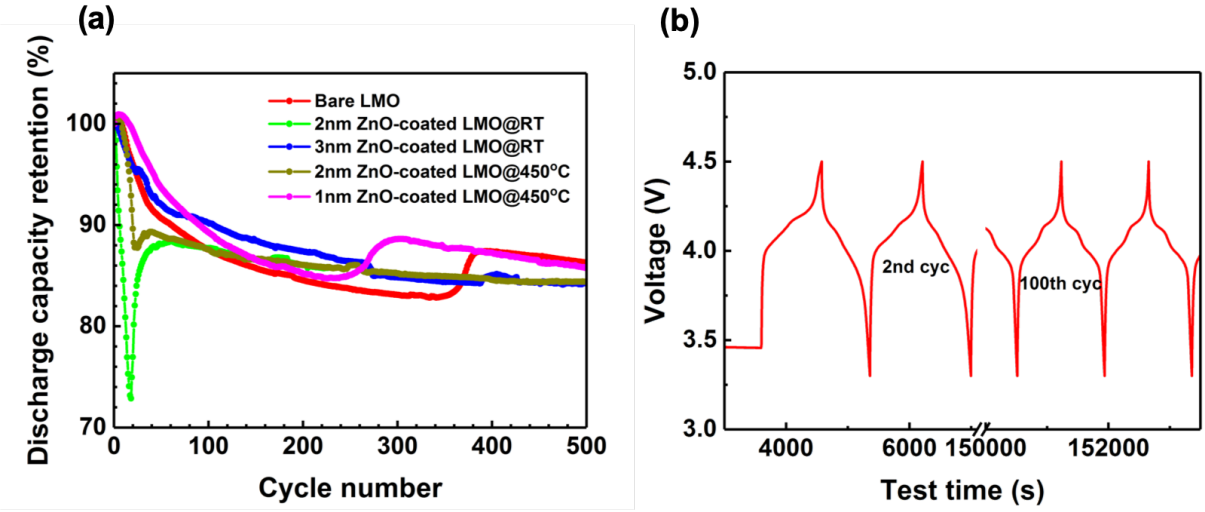

Figure 7.19 (a) Discharge capacity retention profiles of both bare LMO25 and surface coated

LMO25 with annealed/unannealed ZnO of various thickness. All samples were cycled between 3.3 – 4.5 V at 4C. (b) Voltage evolution profile of coated LMO25 by 2 nm unannealed ZnO layer.

7.3 Conclusion

The capacity fade of spinel LMO cathodes, which is primarily associated with Mn^{2+} dissolution into the liquid electrolyte, is a serious drawback of this otherwise promising lithium ion battery material. Apply an ultrathin conformal coating on LMO electrode was explored to help mitigate the capacity fading issue. Thin-film LMO cathodes were studied to unravel LSCO coating effects on mitigating LMO capacity loss. A 25 nm LMO || Pt || Ti || Al_2O_3 thin film cathode attained an initial specific capacity of 120 mAh/g when cycled in an extended voltage range of 3.3 – 4.5 V at 4C. An ultrathin coating layer of 2 nm LSCO annealed at 450 ºC was demonstrated to significantly improve LMO thin film capacity retention from 84% for bare LMO to 95% for coated LMO cathode, especially at early cycling stage. It was found the LSCO coatings suppressed phase separation process of LMO at high voltage range, resulting in better cycling stability attributed to a more stable solid-solution redox reaction during charging/discharging. In addition, SEM images illustrated much more stable surface grain size and morphology of coated LMO sample, suggesting LSCO coating inhibited grain cracking due to long term cycling and hence improved LMO capacity retention. A Mn_3O_4-like defect tetragonal spinel was revealed by STEM-ABF in cycled LMO thin film cathodes. The LSCO surface coating was believed to help restrain the thermodynamically favorable phase transition reaction which caused LMO structure distortion due to Mn migration and lattice oxygen loss. Formation of the Mn_3O_4-like new phase was further verified by EELS analysis of manganese oxidation states. Quantification of the Mn L_3/L_2 white-line ratios showed the oxidation state of cycled LMO thin film cathode was averagely 2.4 which was consistent with oxidation state in the newly formed Mn_3O_4-like defect tetragonal spinel. It was

also interesting to find manganese existed within the CEI layer formed on LMO surface, resulting in extra irreversible capacity loss.

7.4 Experimental Section

Sample Preparation: A stoichiometric $LiMn_2O_4$ target (2 inch in diameter, Kurt J. Lesker Company, 99.9% purity) was used as the sputtering material. Lab made $La_{0.5}Sr_{0.5}CoO_3$ pellet was used as the target of coating material. Synthesis of LSCO powder and fabrication the corresponding target were discussed in detail in our previous publication.[82] Sapphire substrates were pre-annealed at 1000 ºC for 8 hours in air, followed by screen printing with Au paste on the back, side and partial front surfaces working as back contact current collector. Prior to LMO deposition, the substrates were successively washed in acetone and ethanol ultrasonic bath. Depositions were done in a sputter apparatus (ATC-Orion 8 HV, AJA International Inc.) with a base vacuum of 10^{-6} Torr. The substrates were first coated with a stack of 200 nm Pt || 15 nm Ti by DC sputtering. A cohesion layer of Ti (~15 nm) was coated on Al_2O_3 substrate prior to Pt layer deposition to obtain uniform and smooth surface for subsequent LMO thin film growth. LMO thin film deposition was conducted at a radio frequency power of 150 W and under a mixed gas flow of 6 sccm O_2 and 20 sccm Ar at 5 mTorr and room temperature. Afterwards, the deposited LMO films with nominal thickness of 100 nm or 25 nm were annealed at 750 ºC in air for 2 hours followed by LSCO coating layers deposition using the same sputter instrument at room temperature. Apart from LSCO, two other coating materials, i.e. WO_3 and ZnO, were also deposited on LMO thin film cathodes to explore their coating effects. DC sputtering was applied to fabricated WO_3 coating by using a tungsten metal target and O_2 as reactive background gas, while ZnO coating was deposited through RF sputtering of a ZnO target at room temperature.

Some of the coated LMO thin film cathodes were annealed at 450 ºC or 750 ºC in air for 2 hours to crystallize the coatings.

Electrochemical Measurement: All the electrochemical tests were performed using CR2036-type coin cells with the prepared LMO thin films as positive electrode and lithium metal discs as the counter and reference electrodes. Around 40 mL electrolyte, a mixture of 1 M $LiPF_6$ dissolved in ethylene carbonate (EC) and ethyl methyl carbonate (EMC) (v/v = 1:1), was used for each cell. All cells were assembled in a glovebox filled with high-purity argon (O_2 <0.5 ppm) followed by uniaxial pressing at a pressure of 500 psi. Galvanostatic cycling was done on a galvanostat testing system (Arbin Instrument) at a voltage range of 3.3 to 4.5 V with various current rates. Combined measurements of galvanostatic cycling and in situ electrochemical impedance spectroscopy (EIS) were performed with a bi-potentiostat / galvanostat (SP-300, Bio-Logic Science Instrument). The EIS data were recorded between 100 kHz and 10 mHz applying an AC voltage of 10 mV.

Characterization and Data Analysis: For characterizations of the cycled LMO thin films, the cells were disassembled in the glovebox, and rinsed with DMC solution three times in 3 days for removing the residual electrolyte salts. The surface morphologies of all pristine and cycled LMO thin films were observed by scanning electron microscope (SEM, Hitachi SU8030). Grazing incidence X-ray diffraction was carried out using ATX-G (Rigaku) with Cu Kα (λ = 1.5406 Å) radiation. Cross-sectional TEM samples of cycled thin films were prepared by a dual-beam focused ion beam (FIB, FEI Helios Nanolab 600). High resolution atomic structure observations were conducted on an aberration-corrected scanning transmission electron microscope (STEM, JEOL Co., ARM-200CF) at an acceleration voltage of 200 kV. Electron energy-loss spectroscopy

(EELS) data were collected on the same TEM microscope. X-ray photoelectron spectroscopy (XPS) measurements were performed on a spectrometer equipped with a Mg Kα radiation (Thermo Scientific Co., ESCALAB 250Xi).

7.5 Acknowledgements

This work was supported as part of the Center for Electrochemical Energy Science, an Energy Frontier Research Center funded by the U.S. Department of Energy, Office of Science, Basic Energy Sciences (DE- AC02-06CH11357). Research at the Advanced Photon was supported by DOE, Office of Science, BES. This work made use of the EPIC, Keck-II, and/or SPID facility(ies) of Northwestern University's NUANCE Center, which has received support from the Soft and Hybrid Nanotechnology Experimental (SHyNE) Resource (NSF ECCS-1542205); the MRSEC program (NSF DMR-1121262) at the Materials Research Center; the International Institute for Nanotechnology (IIN); the Keck Foundation; and the State of Illinois, through the IIN. This work utilized Northwestern University Micro/Nano Fabrication Facility (NUFAB), which is partially supported by Soft and Hybrid Nanotechnology Experimental (SHyNE) Resource (NSF ECCS-1542205), the Materials Research Science and Engineering Center (DMR-1720139), the State of Illinois, and Northwestern University.

Chapter 8: Summary and Outlook

In this thesis work, $LiMn_2O_4$ as one of the promising cathode material for LIBs has been comprehensively explored in the aim to establish fundamental understanding of relationship between interfacial (electro)chemistry and its detrimental drawback, i.e. fast capacity fade over cycling, and then develop effective mitigation methods. With aid of a variety of advanced materials characterization techniques including *in situ* synchrotron X-ray scattering, high resolution STEM, EELS, XPS depth profile, four distinct research topics were cover here including characterization of surface chemistry of hetero-epitaxial LMO thin film in chapter 4, revisiting cathode electrolyte interphase in terms of chemical composition and manganese distribution in chapter 5, exploring ultrahigh power density LMO thin film cathodes in chapter 6, and raveling enhanced surface coating effects on LMO cycling stability in chapter 7.

In chapter 4, efforts have been made to fabricate and characterize a high quality and atomically flat hetero-epitaxial 10 nm LMO/10 nm LSCO/STO (111) thin film as model cathode by pulsed laser deposition. The LMO thin film demonstrated a "cube-on-cube" epitaxial relationship between LSCO electrically conductive buffer layer and STO substrate: LSCO {111} // STO {111}, $[1\bar{1}0]$ LSCO // $[1\bar{1}0]$ STO. Apparent dislocations were discerned by high resolution STEM at the interface between LMO and LSCO due to relatively large lattice mismatch which resulted in formation of 3D islands of LMO. Poor cyclability was observed due to damage of the LSCO buffer layer which was suspected to lose electrical conductivity when cycled at high voltage. *In situ* low angle synchrotron X-ray scattering indicated CEI layer was rapidly formed upon fist cycle and got stabilized afterwards. It has been a challenge to fabricate epitaxial LMO thin film with a good and stable conduction buffer layer. LSCO worked as a poor buffer layer

material though it obtained small lattice mismatches with both STO and LMO favoring epitaxial growth. A possible avenue for future work can be seen by noting that LSCO layer retain ~ 10% of their original conductivity after electrochemical cycling. Thus, increasing the LSCO layer thickness may provide sufficient electrical connection to allow good cycling characteristics.

Cathode electrolyte interphase on a polycrystalline 100 nm LMO || 500 nm Au-Pd || SS thin film cathode grown by magnetron RF sputtering was studied in chapter 5. The LMO thin film cathode attained a moderate capacity of 58 mAh/g primarily due to poor crystallinity of LMO annealed at a low temperature of 450 ^{o}C to avoid element contaminations inter-diffusing from the SS substrates. A thick CEI layer (about 100 nm) observed by both XPS depth profile and STEM was found to consist of two distinct sub-regions: a porous outermost layer containing organic species of decomposed electrolyte and various lithium salts, and a compact interior layer containing lithium salts, Li_2O and Mn species. It is worth noting that Mn ions were first reported to exist in the CEI layer observed by both XPS depth profile and TEM-EDS mapping, not like what's believed in literature that Mn lost from LMO cathode is totally dissolved into the liquid electrolyte as Mn^{2+} ions. Existence of those Mn ions in CEI layer caused extra loss of LMO cathode capacity. For perspective work, it is suggested to analyze oxidation state of those Mn ions in the CEI layer in order to determine possible mechanism of manganese dissolution. In addition, formation, growth and morphology evolution of CEI layer are desired to be studied by *in situ* low angle synchrotron X-ray scattering during electrochemical cycling of LMO thin film cathodes. That work should shed light onto the correlation between LMO capacity fading and manganese dissolution and CEI layer growth.

LIBs with high rate capability are becoming highly demand nowadays especially in the EV and HEV fields. In chapter 6, a novel fabrication method based on multilayer thin film sputtering deposition was applied to construct an ultrahigh power density LMO thin film cathode on Pt || Ti || Al_2O_3. The well-engineered high-quality LMO thin film cathode of 25 nm attained an initial specific capacity of 128 mAh/g and demonstrated an excellent cyclability with only 23% capacity loss over 900 cycles at 4C. Extremely high rate performance was achieved for 25 nm LMO thin film which exhibited a capacity retention of 85% at 80C (equivalent 45 s to full charge or discharge the cell). This remarkable characteristic was primarily attributed to much shortened Li-ion diffusion length in the 25 nm LMO thin film and well-engineered conduction contact between LMO and Pt layer. In addition, it was observed that the unstable phase separation process which was considered to be critical rate-limiting step of LMO at high electrode potential was suppressed at high cycling current rates, resulting in higher cycling stability and high rate capability. The LMO thin film cathode retrained a low specific capacity when cycled at extreme rate, i.e. 160C. Such a superior rate capability was achieved by sacrifice of total capacity since in such scenario Li-ion storage mode transitioned from solid-solution diffusion in a LIB to surface adsorption/desorption behavior of a pseudocapacitor. It would be interesting to observe phase separation and its transition to solid solution phase by using operando synchrotron X-ray scattering. Moreover, other promising cathode materials such as $LiFePO_4$ and NMC are also worth construction of thin film cathodes to explore viability of high-power density. Besides, all-solid-state thin film batteries with potential application in modern smart microdevices could also be fabricated to study various solid state electrolytes and solid-solid interfacial (electro)chemistry.

Surface modification of LMO || Pt || Ti || Al_2O_3 thin film cathodes by ultrathin LSCO coating was applied to effectively promote LMO cycling stability in chapter 7. A 25 nm LMO thin film cathode attained an initial specific capacity of 120 mAh/g when cycled in an extended voltage range of 3.3 – 4.5 V at 4C. 3-electrode EIS analysis observed increased CEI ohmic resistance and LMO surface charge transfer resistance with thicker LSCO coating applied, indicating the significance of accurately controlling and determining optimized coating thickness. A coating of 2 nm LSCO annealed at 450 ^oC was demonstrated to significantly improve LMO thin film capacity retention from 84% for bare LMO to 95% for coated LMO cathode. It was found the LSCO coatings suppressed phase separation process of LMO at high voltage range, resulting in better cycling stability attributed to a more stable solid-solution phase. In addition, it was observed LSCO coating inhibited grain cracking and crystallinity loss, which hence improved LMO capacity retention. A Mn_3O_4-like defect tetragonal spinel was revealed by STEM-ABF in cycled LMO thin film cathodes. The LSCO surface coating was believed to inhibit that phase transition reaction which caused LMO structure distortion due to Mn migration and lattice oxygen loss. Formation of the Mn_3O_4-like new phase was further verified by EELS analysis of manganese oxidation states. Quantification of the Mn L_3/L_2 white-line ratios showed the oxidation state of cycled LMO thin film cathode was averagely +2.4 which was consistent with oxidation state in the newly formed Mn_3O_4-like defect tetragonal spinel. A worthwhile perspective is to explore other promising coating materials reported in literature on LMO and other cathode materials including $LiFePO_4$ and NMC. Moreover, a hybrid surface modification strategy combining surface coating and doping could be applied using similar thin film fabrication technique and characterization methods demonstrated in this work to optimize performance of LIB electrode materials by both stabilizing crystalline structure and preventing transition metal dissolution.

Reference

1. Goodenough, J. B.; Park, K. S., The Li-Ion Rechargeable Battery: A Perspective. *J Am Chem Soc* **2013,** *135* (4), 1167-1176.
2. Yang, Z. G.; Zhang, J. L.; Kintner-Meyer, M. C. W.; Lu, X. C.; Choi, D. W.; Lemmon, J. P.; Liu, J., Electrochemical Energy Storage for Green Grid. *Chem Rev* **2011,** *111* (5), 3577-3613.
3. Andre, D.; Kim, S. J.; Lamp, P.; Lux, S. F.; Maglia, F.; Paschos, O.; Stiaszny, B., Future generations of cathode materials: an automotive industry perspective. *J Mater Chem A* **2015,** *3* (13), 6709-6732.
4. Berg, E. J.; Villevieille, C.; Streich, D.; Trabesinger, S.; Novak, P., Rechargeable Batteries: Grasping for the Limits of Chemistry. *J Electrochem Soc* **2015,** *162* (14), A2468-A2475.
5. Scrosati, B.; Garche, J., Lithium batteries: Status, prospects and future. *J Power Sources* **2010,** *195* (9), 2419-2430.
6. Gardner, D. S.; Holzwarth, C. W.; Liu, Y.; Clendenning, S. B.; Jin, W.; Moon, B. K.; Pint, C.; Chen, Z. H.; Hannah, E. C.; Chen, C. H.; Wang, C. L.; Makila, E.; Chen, R.; Aldridge, T.; Gustafson, J. L., Integrated on-chip energy storage using passivated nanoporous-silicon electrochemical capacitors. *Nano Energy* **2016,** *25*, 68-79.
7. *Lithium Ion Battery Market to 2025 - Global Analysis and Forecasts Type, by Power Capacity, by Application*; 4669197; Research and Markets, 2018.
8. Luntz, A. C.; Voss, J.; Reuter, K., Interfacial Challenges in Solid-State Li Ion Batteries. *J Phys Chem Lett* **2015,** *6* (22), 4599-4604.
9. Dunn, B.; Kamath, H.; Tarascon, J. M., Electrical Energy Storage for the Grid: A Battery of Choices. *Science* **2011,** *334* (6058), 928-935.
10. Park, C. R., *Next generation lithium ion batteries for electrical vehicles*. In-Teh: India, 2010.
11. Oudenhoven, J. F. M.; Baggetto, L.; Notten, P. H. L., All-Solid-State Lithium-Ion Microbatteries: A Review of Various Three-Dimensional Concepts. *Adv Energy Mater* **2011,** *1* (1), 10-33.
12. Luntz, A., Beyond Lithium Ion Batteries. *J Phys Chem Lett* **2015,** *6* (2), 300-301.
13. Scrosati, B.; Hassoun, J.; Sun, Y. K., Lithium-ion batteries. A look into the future. *Energ Environ Sci* **2011,** *4* (9), 3287-3295.
14. Armand, M.; Tarascon, J. M., Building better batteries. *Nature* **2008,** *451* (7179), 652-657.
15. Luntz, A. C.; McCloskey, B. D., Nonaqueous Li-Air Batteries: A Status Report. *Chem Rev* **2014,** *114* (23), 11721-11750.
16. Muldoon, J.; Bucur, C. B.; Gregory, T., Quest for Nonaqueous Multivalent Secondary Batteries: Magnesium and Beyond. *Chem Rev* **2014,** *114* (23), 11683-11720.
17. Xu, B.; Qian, D. N.; Wang, Z. Y.; Meng, Y. S. L., Recent progress in cathode materials research for advanced lithium ion batteries. *Mat Sci Eng R* **2012,** *73* (5-6), 51-65.
18. Manthiram, A., Materials Challenges and Opportunities of Lithium Ion Batteries. *J Phys Chem Lett* **2011,** *2* (3), 176-184.

19. Fergus, J. W., Recent developments in cathode materials for lithium ion batteries. *J Power Sources* **2010,** *195* (4), 939-954.
20. Gummow, R. J.; Dekock, A.; Thackeray, M. M., Improved Capacity Retention in Rechargeable 4v Lithium Lithium Manganese Oxide (Spinel) Cells. *Solid State Ionics* **1994,** *69* (1), 59-67.
21. Lu, J.; Zhan, C.; Wu, T. P.; Wen, J. G.; Lei, Y.; Kropf, A. J.; Wu, H. M.; Miller, D. J.; Elam, J. W.; Sun, Y. K.; Qiu, X. P.; Amine, K., Effectively suppressing dissolution of manganese from spinel lithium manganate via a nanoscale surface-doping approach. *Nat Commun* **2014,** *5*.
22. Yi, X.; Wang, X. Y.; Ju, B. W.; Shu, H. B.; Wen, W. C.; Yu, R. Z.; Wang, D.; Yang, X. K., Effective enhancement of electrochemical performance for spherical spinel LiMn2O4 via Li ion conductive Li2ZrO3 coating. *Electrochim Acta* **2014,** *134*, 143-149.
23. Gauthier, M.; Carney, T. J.; Grimaud, A.; Giordano, L.; Pour, N.; Chang, H. H.; Fenning, D. P.; Lux, S. F.; Paschos, O.; Bauer, C.; Magia, F.; Lupart, S.; Lamp, P.; Shao-Horn, Y., Electrode-Electrolyte Interface in Li-Ion Batteries: Current Understanding and New Insights. *J Phys Chem Lett* **2015,** *6* (22), 4653-4672.
24. Haruta, M.; Shiraki, S.; Ohsawa, T.; Suzuki, T.; Kumatani, A.; Takagi, Y.; Shimizu, R.; Hitosugi, T., Preparation and in-situ characterization of well-defined solid electrolyte/electrode interfaces in thin-film lithium batteries. *Solid State Ionics* **2016,** *285*, 118-121.
25. Takada, K., Progress and prospective of solid-state lithium batteries. *Acta Mater* **2013,** *61* (3), 759-770.
26. Jang, D. H.; Shin, Y. J.; Oh, S. M., Dissolution of spinel oxides and capacity losses in 4V Li/LixMn2O4 coils. *J Electrochem Soc* **1996,** *143* (7), 2204-2211.
27. Marks, T.; Trussler, S.; Smith, A. J.; Xiong, D. J.; Dahn, J. R., A Guide to Li-Ion Coin-Cell Electrode Making for Academic Researchers. *J Electrochem Soc* **2011,** *158* (1), A51-A57.
28. Letiche, M.; Hallot, M.; Huve, M.; Brousse, T.; Roussel, P.; Lethien, C., Tuning the Cation Ordering with the Deposition Pressure in Sputtered LiMn1.5Ni0.5O4 Thin Film Deposited on Functional Current Collectors for Li-Ion Microbattery Applications. *Chem Mater* **2017,** *29* (14), 6044-6057.
29. Fehse, M.; Trocoli, R.; Ventosa, E.; Hernandez, E.; Sepulveda, A.; Morata, A.; Tarancon, A., Ultrafast Dischargeable LiMn2O4 Thin-Film Electrodes with Pseudocapacitive Properties for Microbatteries. *Acs Appl Mater Inter* **2017,** *9* (6), 5295-5301.
30. Harks, P. P. R. M. L.; Mulder, F. M.; Notten, P. H. L., In situ methods for Li-ion battery research: A review of recent developments. *J Power Sources* **2015,** *288*, 92-105.
31. Lee, S.; Oshima, Y.; Hosono, E.; Zhou, H. S.; Kim, K.; Chang, H. M.; Kanno, R.; Takayanagi, K., In Situ TEM Observation of Local Phase Transformation in a Rechargeable LiMn2O4 Nanowire Battery. *J Phys Chem C* **2013,** *117* (46), 24236-24241.
32. Gao, X.; Ikuhara, Y. H.; Fisher, C. A. J.; Moriwake, H.; Kuwabara, A.; Oki, H.; Kohama, K.; Yoshida, R.; Huang, R.; Ikuhara, Y., Structural Distortion and Compositional Gradients Adjacent to Epitaxial LiMn2O4 Thin Film Interfaces. *Adv Mater Interfaces* **2014,** *1* (8).

33. Zeng, Z. Y.; Liang, W. I.; Liao, H. G.; Xin, H. L. L.; Chu, Y. H.; Zheng, H. M., Visualization of Electrode-Electrolyte Interfaces in LiPF6/EC/DEC Electrolyte for Lithium Ion Batteries via in Situ TEM. *Nano Lett* **2014,** *14* (4), 1745-1750.
34. Etacheri, V.; Marom, R.; Elazari, R.; Salitra, G.; Aurbach, D., Challenges in the development of advanced Li-ion batteries: a review. *Energ Environ Sci* **2011,** *4* (9), 3243-3262.
35. Tarascon, J. M.; Armand, M., Issues and challenges facing rechargeable lithium batteries. *Nature* **2001,** *414* (6861), 359-367.
36. Tan, G. Q.; Wu, F.; Zhan, C.; Wang, J.; Mu, D. B.; Lu, J.; Amine, K., Solid-State Li-Ion Batteries Using Fast, Stable, Glassy Nanocomposite Electrolytes for Good Safety and Long Cycle-Life. *Nano Lett* **2016,** *16* (3), 1960-1968.
37. Nazri, G. A.; Pistoia, G., *Lithium Batteries: Science and Technology*. Springer US: 2009.
38. Choi, N. S.; Chen, Z. H.; Freunberger, S. A.; Ji, X. L.; Sun, Y. K.; Amine, K.; Yushin, G.; Nazar, L. F.; Cho, J.; Bruce, P. G., Challenges Facing Lithium Batteries and Electrical Double-Layer Capacitors. *Angew Chem Int Edit* **2012,** *51* (40), 9994-10024.
39. Li, Q.; Chen, J.; Fan, L.; Kong, X.; Lu, Y., Progress in electrolytes for rechargeable Li-based batteries and beyond. *Green Energy & Environment* **2016,** *1* (1), 18-42.
40. Goriparti, S.; Miele, E.; De Angelis, F.; Di Fabrizio, E.; Zaccaria, R. P.; Capiglia, C., Review on recent progress of nanostructured anode materials for Li-ion batteries. *J Power Sources* **2014,** *257*, 421-443.
41. Chen, Z. H.; Belharouak, I.; Sun, Y. K.; Amine, K., Titanium-Based Anode Materials for Safe Lithium-Ion Batteries. *Adv Funct Mater* **2013,** *23* (8), 959-969.
42. Shinova, E.; Mandzhukova, T.; Grigorova, E.; Hristov, M.; Stoyanova, R.; Nihtianova, D.; Zhecheva, E., On the incorporation of extra Li in lithium cobaltate Li1+xCo1-xO2. *Solid State Ionics* **2011,** *187* (1), 43-49.
43. Whittingham, M. S., Lithium batteries and cathode materials. *Chem Rev* **2004,** *104* (10), 4271-4301.
44. Goodenough, J. B.; Kim, Y., Challenges for Rechargeable Li Batteries. *Chem Mater* **2010,** *22* (3), 587-603.
45. Wakihara, M., Recent developments in lithium ion batteries. *Mat Sci Eng R* **2001,** *33* (4), 109-134.
46. Akimoto, J.; Takahashi, Y.; Gotoh, Y.; Mizuta, S., Single crystal X-ray diffraction study of the spinel-type LiMn2O4. *Chem Mater* **2000,** *12* (11), 3246-+.
47. Thackeray, M. M.; David, W. I. F.; Bruce, P. G.; Goodenough, J. B., Lithium Insertion into Manganese Spinels. *Mater Res Bull* **1983,** *18* (4), 461-472.
48. Ohzuku, T.; Kitagawa, M.; Hirai, T., Electrochemistry of Manganese-Dioxide in Lithium Nonaqueous Cell .3. X-Ray Diffractional Study on the Reduction of Spinel-Related Manganese-Dioxide. *J Electrochem Soc* **1990,** *137* (3), 769-775.
49. Thackeray, M. M.; Johnson, P. J.; Depicciotto, L. A.; Bruce, P. G.; Goodenough, J. B., Electrochemical Extraction of Lithium from Limn2o4. *Mater Res Bull* **1984,** *19* (2), 179-187.
50. Bruce, P. G., Solid-state chemistry of lithium power sources. *Chem Commun* **1997,** (19), 1817-1824.
51. Lee, K. T.; Jeong, S.; Cho, J., Roles of Surface Chemistry on Safety and Electrochemistry in Lithium Ion Batteries. *Accounts Chem Res* **2013,** *46* (5), 1161-1170.

52. Abe, T.; Fukuda, H.; Iriyama, Y.; Ogumi, Z., Solvated Li-ion transfer at interface between graphite and electrolyte. *J Electrochem Soc* **2004,** *151* (8), A1120-A1123.
53. Wu, B. B.; Wang, S. Y.; Evans, W. J.; Deng, D. Z.; Yang, J. H.; Xiao, J., Interfacial behaviours between lithium ion conductors and electrode materials in various battery systems. *J Mater Chem A* **2016,** *4* (40), 15266-15280.
54. Aurbach, D.; Gamolsky, K.; Markovsky, B.; Salitra, G.; Gofer, Y.; Heider, U.; Oesten, R.; Schmidt, M., The study of surface phenomena related to electrochemical lithium intercalation into LixMOy host materials (M = Ni, Mn). *J Electrochem Soc* **2000,** *147* (4), 1322-1331.
55. Ma, C.; Chen, K.; Liang, C. D.; Nan, C. W.; Ishikawa, R.; More, K.; Chi, M. F., Atomic-scale origin of the large grain-boundary resistance in perovskite Li-ion-conducting solid electrolytes. *Energ Environ Sci* **2014,** *7* (5), 1638-1642.
56. Antonini, A.; Bellitto, C.; Pasquali, M.; Pistoia, G., Factors affecting the stabilization of Mn spinel capacity upon staring and cycling at high temperatures. *J Electrochem Soc* **1998,** *145* (8), 2726-2732.
57. Jaber-Ansari, L.; Puntambekar, K. P.; Kim, S.; Aykol, M.; Luo, L. L.; Wu, J. S.; Myers, B. D.; Iddir, H.; Russell, J. T.; Saldana, S. J.; Kumar, R.; Thackeray, M. M.; Curtiss, L. A.; Dravid, V. P.; Wolverton, C.; Hersam, M. C., Suppressing Manganese Dissolution from Lithium Manganese Oxide Spinel Cathodes with Single-Layer Graphene. *Adv Energy Mater* **2015,** *5* (17).
58. Aurbach, D.; Levi, M. D.; Gamulski, K.; Markovsky, B.; Salitra, G.; Levi, E.; Heider, U.; Heider, L.; Oesten, R., Capacity fading of Li(x)Mn(2)O(4) spinel electrodes studied by XRD and electroanalytical techniques. *J Power Sources* **1999,** *81*, 472-479.
59. Hirayama, M.; Sonoyama, N.; Ito, M.; Minoura, M.; Mori, D.; Yamada, A.; Tamura, K.; Mizuki, J.; Kanno, R., Characterization of electrode/electrolyte interface with X-ray reflectometry and epitaxial-film LiMn2O4 electrode. *J Electrochem Soc* **2007,** *154* (11), A1065-A1072.
60. Bhandari, A.; Bhattacharya, J., Review-Manganese Dissolution from Spinel Cathode: Few Unanswered Questions. *J Electrochem Soc* **2017,** *164* (2), A106-A127.
61. Xia, Y. Y.; Zhou, Y. H.; Yoshio, M., Capacity fading on cycling of 4 V Li/LiMn2O4 cells. *J Electrochem Soc* **1997,** *144* (8), 2593-2600.
62. Hirayama, M.; Ido, H.; Kim, K.; Cho, W.; Tamura, K.; Mizuki, J.; Kanno, R., Dynamic Structural Changes at LiMn2O4/Electrolyte Interface during Lithium Battery Reaction. *J Am Chem Soc* **2010,** *132* (43), 15268-15276.
63. Benedek, R.; Thackeray, M. M.; Low, J.; Bucko, T., Simulation of Aqueous Dissolution of Lithium Manganate Spinel from First Principles. *J Phys Chem C* **2012,** *116* (6), 4050-4059.
64. Kim, S.; Aykol, M.; Wolverton, C., Surface phase diagram and stability of (001) and (111) LiMn2O4 spinel oxides. *Physical Review B* **2015,** *92* (11).
65. Kim, J. S.; Kim, K.; Cho, W.; Shin, W. H.; Kanno, R.; Choi, J. W., A Truncated Manganese Spinel Cathode for Excellent Power and Lifetime in Lithium-Ion Batteries. *Nano Lett* **2012,** *12* (12), 6358-6365.
66. Yang, C. X.; Deng, Y. F.; Gao, M.; Yang, X. F.; Qin, X. S.; Chen, G. H., High-rate and long-life performance of a truncated spinel cathode material with off-stoichiometric composition at elevated temperature. *Electrochim Acta* **2017,** *225*, 198-206.

67. Amos, C. D.; Roldan, M. A.; Varela, M.; Goodenough, J. B.; Ferreira, P. J., Revealing the Reconstructed Surface of Li[Mn-2]O-4. *Nano Lett* **2016,** *16* (5), 2899-+.
68. Tang, D. C.; Sun, Y.; Yang, Z. Z.; Ben, L. B.; Gu, L.; Huang, X. J., Surface Structure Evolution of LiMn2O4 Cathode Material upon Charge/Discharge. *Chem Mater* **2014,** *26* (11), 3535-3543.
69. Sonoyama, N.; Iwase, K.; Takatsuka, H.; Matsumura, T.; Imanishi, N.; Takeda, Y.; Kanno, R., Electrochemistry of LiMn2O4 epitaxial films deposited on various single crystal substrates. *J Power Sources* **2009,** *189* (1), 561-565.
70. Ikuhara, Y. H.; Gao, X.; Huang, R.; Fisher, C. A. J.; Kuwabara, A.; Moriwake, H.; Kohama, K., Epitaxial Growth of LiMn2O4 Thin Films by Chemical Solution Deposition for Multilayer Lithium-Ion Batteries. *J Phys Chem C* **2014,** *118* (34), 19540-19547.
71. Suzuki, K.; Kim, K.; Taminato, S.; Hirayama, M.; Kanno, R., Fabrication and electrochemical properties of LiMn2O4/SrRuO3 multi-layer epitaxial thin film electrodes. *J Power Sources* **2013,** *226*, 340-345.
72. Kim, S.; Hirayama, M.; Suzuki, K.; Kanno, R., Hetero-epitaxial growth of Li0.17La0.6TiO3 solid electrolyte on LiMn2O4 electrode for all solid-state batteries. *Solid State Ionics* **2014,** *262*, 578-581.
73. Edstrom, K.; Herstedt, M.; Abraham, D. P., A new look at the solid electrolyte interphase on graphite anodes in Li-ion batteries. *J Power Sources* **2006,** *153* (2), 380-384.
74. Yan, J.; Zhang, J.; Su, Y. C.; Zhang, X. G.; Xia, B. J., A novel perspective on the formation of the solid electrolyte interphase on the graphite electrode for lithium-ion batteries. *Electrochim Acta* **2010,** *55* (5), 1785-1794.
75. Peled, E.; Menkin, S., Review-SEI: Past, Present and Future. *J Electrochem Soc* **2017,** *164* (7), A1703-A1719.
76. Malmgren, S.; Ciosek, K.; Hahlin, M.; Gustafsson, T.; Gorgoi, M.; Rensmo, H.; Edstrom, K., Comparing anode and cathode electrode/electrolyte interface composition and morphology using soft and hard X-ray photoelectron spectroscopy. *Electrochim Acta* **2013,** *97*, 23-32.
77. Baggetto, L.; Dudney, N. J.; Veith, G. M., Surface chemistry of metal oxide coated lithium manganese nickel oxide thin film cathodes studied by XPS. *Electrochim Acta* **2013,** *90*, 135-147.
78. Edstrom, K.; Gustafsson, T.; Thomas, J. O., The cathode-electrolyte interface in the Li-ion battery. *Electrochim Acta* **2004,** *50* (2-3), 397-403.
79. Jang, D. H.; Oh, S. M., Electrolyte effects on spinel dissolution and cathodic capacity losses in 4 v Li/LixMn2O4 rechargeable cells. *J Electrochem Soc* **1997,** *144* (10), 3342-3348.
80. Park, Y.; Shin, S. H.; Hwang, H.; Lee, S. M.; Kim, S. P.; Choi, H. C.; Jung, Y. M., Investigation of solid electrolyte interface (SEI) film on LiCoO2 cathode in fluoroethylene carbonate (FEC)-containing electrolyte by 2D correlation X-ray photoelectron spectroscopy (XPS). *J Mol Struct* **2014,** *1069*, 157-163.
81. Nordh, T.; Younesi, R.; Brandell, D.; Edström, K., Depth profiling the solid electrolyte interphase on lithium titanate (Li4Ti5O12) using synchrotron-based photoelectron spectroscopy. *J Power Sources* **2015,** *294*, 173-179.
82. Yu, X. K.; Chen, X.; Buchholz, D. B.; Li, Q. Q.; Wu, J. S.; Fenter, P. A.; Bedzyk, M. J.; Dravid, V. P.; Barnett, S. A., Pulsed Laser Deposition and Characterization of Heteroepitaxial

LiMn2O4/La0.5Sr0.5CoO3 Bilayer Thin Films as Model Lithium Ion Battery Cathodes. *Acs Appl Nano Mater* **2018,** *1* (2), 642-653.
83. Sun, C. W.; Liu, J.; Gong, Y. D.; Wilkinson, D. P.; Zhang, J. J., Recent advances in all-solid-state rechargeable lithium batteries. *Nano Energy* **2017,** *33*, 363-386.
84. Kim, J.; Kumar, R.; Bandodkar, A. J.; Wang, J., Advanced Materials for Printed Wearable Electrochemical Devices: A Review. *Adv Electron Mater* **2017,** *3* (1).
85. Okubo, M.; Mizuno, Y.; Yamada, H.; Kim, J.; Hosono, E.; Zhou, H. S.; Kudo, T.; Honma, I., Fast Li-Ion Insertion into Nanosized LiMn2O4 without Domain Boundaries. *Acs Nano* **2010,** *4* (2), 741-752.
86. Tan, X. H.; Liu, H. Q.; Jiang, Y.; Liu, G. Y.; Guo, Y. J.; Wang, H. F.; Sun, L. F.; Chu, W. G., Graphite assisted synthesis of nanoparticles interconnected porous two-dimensional LiMn2O4 nanoplates with superior performance. *J Power Sources* **2016,** *328*, 345-354.
87. Lee, H. W.; Muralidharan, P.; Ruffo, R.; Mari, C. M.; Cui, Y.; Kim, D. K., Ultrathin Spinel LiMn2O4 Nanowires as High Power Cathode Materials for Li-Ion Batteries. *Nano Lett* **2010,** *10* (10), 3852-3856.
88. Hua, W. B.; Wang, S. N.; Guo, X. D.; Chou, S. L.; Yin, K.; Zhong, B. H.; Dou, S. X., Vacuum induced self-assembling nanoporous LiMn2O4 for lithium ion batteries with superior high rate capability. *Electrochim Acta* **2015,** *186*, 253-261.
89. Put, B.; Vereecken, P. M.; Labyedh, N.; Sepulveda, A.; Huyghebaert, C.; Radu, I. P.; Stesmans, A., High Cycling Stability and Extreme Rate Performance in Nanoscaled LiMn2O4 Thin Films. *Acs Appl Mater Inter* **2015,** *7* (40), 22413-22420.
90. Chen, L. N.; Zhai, W.; Chen, L.; Li, D. P.; Ma, X. X.; Ai, Q.; Xu, X. Y.; Hou, G. M.; Zhang, L.; Feng, J. K.; Si, P. C.; Ci, L. J., Nanostructured LiMn2O4 composite as high-rate cathode for high performance aqueous Li-ion hybrid supercapacitors. *J Power Sources* **2018,** *392*, 116-122.
91. Zhang, H.; Xu, Y. L.; Liu, D., Novel nanostructured LiMn2O4 microspheres for high power Li-ion batteries. *Rsc Adv* **2015,** *5* (15), 11091-11095.
92. Hosono, E.; Kudo, T.; Honma, I.; Matsuda, H.; Zhou, H. S., Synthesis of Single Crystalline Spinel LiMn2O4 Nanowires for a Lithium Ion Battery with High Power Density. *Nano Lett* **2009,** *9* (3), 1045-1051.
93. Luo, J. Y.; Cheng, L.; Xia, Y. Y., LiMn2O4 hollow nanosphere electrode material with excellent cycling reversibility and rate capability. *Electrochem Commun* **2007,** *9* (6), 1404-1409.
94. Maier, J., Pushing Nanoionics to the Limits: Charge Carrier Chemistry in Extremely Small Systems. *Chem Mater* **2014,** *26* (1), 348-360.
95. Zhou, Y. N.; Xue, M. Z.; Fu, Z. W., Nanostructured thin film electrodes for lithium storage and all-solid-state thin-film lithium batteries. *J Power Sources* **2013,** *234*, 310-332.
96. Kang, K. S.; Meng, Y. S.; Breger, J.; Grey, C. P.; Ceder, G., Electrodes with high power and high capacity for rechargeable lithium batteries. *Science* **2006,** *311* (5763), 977-980.
97. Taberna, L.; Mitra, S.; Poizot, P.; Simon, P.; Tarascon, J. M., High rate capabilities Fe3O4-based Cu nano-architectured electrodes for lithium-ion battery applications. *Nat Mater* **2006,** *5* (7), 567-573.
98. Wang, G.; Zhang, L.; Zhang, J., A review of electrode materials for electrochemical supercapacitors. *Chem Soc Rev* **2012,** *41* (2), 797-828.

99. Chen, S. M.; Wen, K. H.; Fan, J. T.; Bando, Y. S.; Golberg, D., Progress and future prospects of high-voltage and high-safety electrolytes in advanced lithium batteries: from liquid to solid electrolytes. *J Mater Chem A* **2018,** *6* (25), 11631-11663.
100. Wang, Y.; Peng, Q.; Yang, G.; Yang, Z.; Zhang, L. C.; Long, H.; Huang, Y. H.; Lu, P. X., High-stability 5 V spinel LiNi0.5Mn1.5O4 sputtered thin film electrodes by modifying with aluminium oxide. *Electrochim Acta* **2014,** *136*, 450-456.
101. Kim, S.; Hirayama, M.; Taminato, S.; Kanno, R., Epitaxial growth and lithium ion conductivity of lithium-oxide garnet for an all solid-state battery electrolyte. *Dalton T* **2013,** *42* (36), 13112-13117.
102. Kumatani, A.; Shiraki, S.; Takagi, Y.; Suzuki, T.; Ohsawa, T.; Gao, X.; Ikuhara, Y.; Hitosugi, T., Epitaxial growth of Li4Ti5O12 thin films using RF magnetron sputtering. *Jpn J Appl Phys* **2014,** *53* (5).
103. Wei, J.; Ogawa, D.; Fukumura, T.; Hirose, Y.; Hasegawa, T., Epitaxial Strain-Controlled Ionic Conductivity in Li-Ion Solid Electrolyte Li0.33La0.56TiO3 Thin Films. *Cryst Growth Des* **2015,** *15* (5), 2187-2191.
104. Shiraki, S.; Takagi, Y.; Shimizu, R.; Suzuki, T.; Haruta, M.; Sato, Y.; Ikuhara, Y.; Hitosugi, T., Orientation control of LiCoO2 epitaxial thin films on metal substrates. *Thin Solid Films* **2016,** *600*, 175-178.
105. Kim, J. H.; Park, J.; Cheong, J. Y.; Song, A.; Chung, K. B.; Park, Y. C.; Kim, I. D.; Kim, Y. J.; Park, K.; Kim, H. S., Suppressed ionic contamination of LiNi0.5Mn1.5O4 with a Pt/ITO/stainless steel multilayer current collector. *Ceram Int* **2018,** *44* (16), 20093-20104.
106. Lee, J. H.; Hong, J. K.; Jang, D. H.; Sun, Y. K.; Oh, S. M., Degradation mechanisms in doped spinels of LiM0.05Mn1.95O4 (M = Li, B, Al, Co, and Ni) for Li secondary batteries. *J Power Sources* **2000,** *89* (1), 7-14.
107. Hunter, J. C., Preparation of a New Crystal Form of Manganese-Dioxide - Lambda-Mno2. *J Solid State Chem* **1981,** *39* (2), 142-147.
108. Ragavendran, K.; Chou, H. L.; Lu, L.; Lai, M. O.; Hwang, B. J.; Kumar, R. R.; Gopukumar, S.; Emmanuel, B.; Vasudevan, D.; Sherwood, D., Crystal habits of LiMn2O4 and their influence on the electrochemical performance. *Mater Sci Eng B-Adv* **2011,** *176* (16), 1257-1263.
109. Lee, Y. K.; Park, J.; Lu, W., Electronic and Bonding Properties of LiMn2O4 Spinel with Different Surface Orientations and Doping Elements and Their Effects on Manganese Dissolution. *J Electrochem Soc* **2016,** *163* (7), A1359-A1368.
110. Benedek, R.; Thackeray, M. M., Simulation of the surface structure of lithium manganese oxide spinel. *Physical Review B* **2011,** *83* (19).
111. Li, J. L.; Zhu, Y. Q.; Wang, L.; Cao, C. B., Lithium Titanate Epitaxial Coating on Spinel Lithium Manganese Oxide Surface for Improving the Performance of Lithium Storage Capability. *Acs Appl Mater Inter* **2014,** *6* (21), 18742-18750.
112. Kim, W. K.; Han, D. W.; Ryu, W. H.; Lim, S. J.; Kwon, H. S., Al2O3 coating on LiMn2O4 by electrostatic attraction forces and its effects on the high temperature cyclic performance. *Electrochim Acta* **2012,** *71*, 17-21.
113. Choi, W.; Manthiram, A., Comparison of metal ion dissolutions from lithium ion battery cathodes. *J Electrochem Soc* **2006,** *153* (9), A1760-A1764.

114. Choi, W.; Manthiram, A., Superior capacity retention spinel oxyfluoride cathodes for lithium-ion batteries. *Electrochem Solid St* **2006,** *9* (5), A245-A248.
115. Ragavendran, K. R.; Lu, L.; Hwang, B. J.; Barner, K.; Veluchamy, A., Trap State Spectroscopy of LiMyMn2-yO4 (M = Mn, Ni, Co): Guiding Principles for Electrochemical Performance. *J Phys Chem C* **2013,** *117* (8), 3812-3817.
116. Shin, Y.; Manthiram, A., High Rate, Superior Capacity Retention LiMn2− 2y Li y Ni y O 4 Spinel Cathodes for Lithium-Ion Batteries. *Electrochemical and solid-state letters* **2003,** *6* (2), A34-A36.
117. Aykol, M.; Kim, S.; Hegde, V. I.; Snydacker, D.; Lu, Z.; Hao, S. Q.; Kirklin, S.; Morgan, D.; Wolverton, C., High-throughput computational design of cathode coatings for Li-ion batteries. *Nat Commun* **2016,** *7*.
118. Jeong, M.; Lee, M. J.; Cho, J.; Lee, S., Surface Mn Oxidation State Controlled Spinel LiMn2O4 as a Cathode Material for High-Energy Li-Ion Batteries. *Adv Energy Mater* **2015,** *5* (13).
119. Park, J. S.; Meng, X. B.; Elam, J. W.; Hao, S. Q.; Wolverton, C.; Kim, C.; Cabana, J., Ultrathin Lithium-Ion Conducting Coatings for Increased Interfacial Stability in High Voltage Lithium-Ion Batteries. *Chem Mater* **2014,** *26* (10), 3128-3134.
120. Huang, T.; Zheng, X. Z.; Wu, M. X.; Wang, W. G.; Pan, Y.; Fang, G. H., Ethyl 3,3,3-trifluoropropanoate as an additive to improve the cycling performance of LiMn2O4 cathode on lithium-ion batteries at elevated temperature. *J Power Sources* **2016,** *318*, 264-269.
121. Chung, K. Y.; Lee, H. S.; Yoon, W. S.; McBreen, J.; Yang, X. Q., Studies of LiMn2O4 capacity fading at elevated temperature using in situ synchrotron X-ray diffraction. *J Electrochem Soc* **2006,** *153* (4), A774-A780.
122. Seo, H.; Na, S.; Lee, B.; Yim, T.; Oh, S. H., Enhancement of surface stability of lithium manganese oxide spinel by silyl-group functionalized fluoride-responsive ionic liquid additives. *J Ind Eng Chem* **2018,** *64*, 311-317.
123. Liu, H. W.; Cheng, C. X.; Zongqiuhu; Zhang, K. L., The effect of ZnO coating on LiMn2O4 cycle life in high temperature for lithium secondary batteries. *Mater Chem Phys* **2007,** *101* (2-3), 276-279.
124. Walz, K. A.; Johnson, C. S.; Genthe, J.; Stoiber, L. C.; Zeltner, W. A.; Anderson, M. A.; Thackeray, M. M., Elevated temperature cycling stability and electrochemical impedance of LiMn2O4 cathodes with nanoporous ZrO2 and TiO2 coatings. *J Power Sources* **2010,** *195* (15), 4943-4951.
125. Sun, Y. C.; Wang, Z. X.; Chen, L. Q.; Huang, X. J., Improved electrochemical performances of surface-modified spinel LiMn2O4 for long cycle life lithium-ion batteries. *J Electrochem Soc* **2003,** *150* (10), A1294-A1298.
126. Nordh, T.; Younesi, R.; Hahlin, M.; Duarte, R. F.; Tengstedt, C.; Brandell, D.; Edstrom, K., Manganese in the SEI Layer of Li4Ti5O12 Studied by Combined NEXAFS and HAXPES Techniques. *J Phys Chem C* **2016,** *120* (6), 3206-3213.
127. Zhan, C.; Lu, J.; Kropf, A. J.; Wu, T. P.; Jansen, A. N.; Sun, Y. K.; Qiu, X. P.; Amine, K., Mn(II) deposition on anodes and its effects on capacity fade in spinel lithium manganate-carbon systems. *Nat Commun* **2013,** *4*.

128. Banerjee, A.; Shilina, Y.; Ziv, B.; Ziegelbauer, J. M.; Luski, S.; Aurbach, D.; Halalay, I. C., On the Oxidation State of Manganese Ions in Li-Ion Battery Electrolyte Solutions. *J Am Chem Soc* **2017,** *139* (5), 1738-1741.
129. Gowda, S. R.; Gallagher, K. G.; Croy, J. R.; Bettge, M.; Thackeray, M. M.; Balasubramanian, M., Oxidation state of cross-over manganese species on the graphite electrode of lithium-ion cells. *Phys Chem Chem Phys* **2014,** *16* (15), 6898-6902.
130. Aykol, M.; Kirklin, S.; Wolverton, C., Thermodynamic Aspects of Cathode Coatings for Lithium-Ion Batteries. *Adv Energy Mater* **2014,** *4* (17).
131. Shi, T.; Dong, Y.; Wang, C. M.; Tao, F.; Chen, L., Enhanced cycle stability at high rate and excellent high rate capability of La0.7Sr0.3Mn0.7Co0.3O3-coated LiMn2O4. *J Power Sources* **2015,** *273*, 959-965.
132. Oh, M. Y.; Lee, J. J.; Zahoor, A.; Kumar, G. G.; Nahm, K. S., Enhanced electrocatalytic activity of three-dimensionally-ordered macroporous La0.6Sr0.4CoO3-delta perovskite oxide for Li-O-2 battery application. *Rsc Adv* **2016,** *6* (38), 32212-32219.
133. Chrisey, D. B.; Hubler, G. K., *Pulsed Laser Deposition of Thin Films*. Wiley: 1994.
134. Andor, http://www.andor.com/learning-academy/pulsed-laser-deposition-an-introduction-to-pulsed-laser-deposition.
135. Wikipedia, https://en.wikipedia.org/wiki/Pulsed_laser_deposition#cite_note-Perry-1.
136. IST, http://groups.ist.utl.pt/rschwarz/rschwarzgroup_files/PLD_files/PLD2.htm.
137. Wikipedia, https://en.wikipedia.org/wiki/Sputter_deposition.
138. Sciences, A., https://www.angstromsciences.com/magnetron-sputtering-deposition.
139. Vacuum, D., https://www.dentonvacuum.com/products-technologies/magnetron-sputtering/.
140. Komaba, S.; Kumagai, N.; Baba, M.; Miura, F.; Fujita, N.; Groult, H.; Devilliers, D.; Kaplan, B., Preparation of Li–Mn–O thin films by rf-sputtering method and its application to rechargeable batteries. *J Appl Electrochem* **2000,** *30* (10), 1179-1182.
141. Dumont, T.; Lippert, T.; Döbeli, M.; Grimmer, H.; Ufheil, J.; Novák, P.; Würsig, A.; Vogt, U.; Wokaun, A., Influence of experimental parameter on the Li-content of LiMn2O4 electrodes produced by pulsed laser deposition. *Applied surface science* **2006,** *252* (13), 4902-4906.
142. Chen, C.; Chiu, K.; Lin, K.; Lin, H.; Yang, C.; Wang, F., Improved electrochemical performances of oxygen plasma treated LiMn2O4 thin films. *Physica Scripta* **2007,** *2007* (T129), 74.
143. ISAI, M.; NAKAMURA, M., Investigation of deposition condition of LiMn2O4 films prepared by RF magnetron sputtering. *Transactions of the Materials Research Society of Japan* **2012,** *37* (1), 99-101.
144. Doi, T.; Inaba, M.; Tsuchiya, H.; Jeong, S.-K.; Iriyama, Y.; Abe, T.; Ogumi, Z., Electrochemical AFM study of LiMn2O4 thin film electrodes exposed to elevated temperatures. *J Power Sources* **2008,** *180* (1), 539-545.
145. Babu, K. J.; Kumar, P. J.; Hussain, O., Microstructural and electrochemical properties of rf-sputtered LiMn 2 O 4 thin film cathodes. *Applied Nanoscience* **2012,** *2* (4), 401-407.
146. Shin, D. W.; Yoon, S.-J.; Choi, J.-W., Sn-substituted LiMn2O4 thin films prepared by RF magnetron sputtering. *Solid State Sciences* **2013,** *16*, 13-15.

147. Fister, T. T.; Esbenshade, J.; Chen, X.; Long, B. R.; Shi, B.; Schleputz, C. M.; Gewirth, A. A.; Bedzyk, M. J.; Fenter, P., Lithium Intercalation Behavior in Multilayer Silicon Electrodes. *Adv Energy Mater* **2014,** *4* (7).
148. Fister, T. T.; Long, B. R.; Gewirth, A. A.; Shi, B.; Assoufid, L.; Lee, S. S.; Fenter, P., Real-Time Observations of Interfacial Lithiation in a Metal Silicide Thin Film. *J Phys Chem C* **2012,** *116* (42), 22341-22345.
149. Daillant, J.; Gibaud, A., *X-ray and neutron reflectivity: principles and applications*. Springer: 2008; Vol. 770.
150. You, H.; Melendres, C.; Nagy, Z.; Maroni, V.; Yun, W.; Yonco, R., X-ray-reflectivity study of the copper-water interface in a transmission geometry under in situ electrochemical control. *Physical Review B* **1992,** *45* (19), 11288.
151. Rigaku, Advanced Thin film X-ray system-Grazing incidence in-plane diffractometer. *The Rigaku Journal* **1999,** *16* (1), 53-58.
152. Nelson, A., Co-refinement of multiple-contrast neutron/X-ray reflectivity data using MOTOFIT. *J Appl Crystallogr* **2006,** *39*, 273-276.
153. Heavens, O. S., *Optical Properties of Thin Solid Films*. Dover Publications: 1991.
154. Wikipedia, https://en.wikipedia.org/wiki/Atomic-force_microscopy.
155. Wikipedia, https://en.wikipedia.org/wiki/Scanning_electron_microscope.
156. Wikipedia, https://en.wikipedia.org/wiki/Energy-dispersive_X-ray_spectroscopy.
157. Huang, R.; Ikuhara, Y., STEM characterization for lithium-ion battery cathode materials. *Curr Opin Solid St M* **2012,** *16* (1), 31-38.
158. Huang, R.; Hitosugi, T.; Findlay, S. D.; Fisher, C. A. J.; Ikuhara, Y. H.; Moriwake, H.; Oki, H.; Ikuhara, Y., Real-time direct observation of Li in LiCoO2 cathode material. *Appl Phys Lett* **2011,** *98* (5).
159. Wikipedia, https://en.wikipedia.org/wiki/X-ray_photoelectron_spectroscopy.
160. Inagaki, M.; Kang, F., *Materials Science and Engineering of Carbon: Fundamentals*. Elsevier Science: 2014.
161. Wikipedia, https://en.wikipedia.org/wiki/Cyclic_voltammetry.
162. Qu, D. Y.; Wang, G. W.; Kafle, J.; Harris, J.; Crain, L.; Jin, Z. H.; Zheng, D., Electrochemical Impedance and its Applications in Energy-Storage Systems. *Small Methods* **2018,** *2* (8).
163. Miikkulainen, V.; Ruud, A.; Ostreng, E.; Nilsen, O.; Laitinen, M.; Sajavaara, T.; Fjellvag, H., Atomic Layer Deposition of Spinel Lithium Manganese Oxide by Film-Body-Controlled Lithium Incorporation for Thin-Film Lithium-Ion Batteries. *J Phys Chem C* **2014,** *118* (2), 1258-1268.
164. Liu, J.; Sun, X. L., Elegant design of electrode and electrode/electrolyte interface in lithium-ion batteries by atomic layer deposition. *Nanotechnology* **2015,** *26* (2).
165. Ohring, M., *Materials Science of Thin Films*. Elsevier Science: 2001.
166. Shiraki, S.; Oki, H.; Takagi, Y.; Suzuki, T.; Kumatani, A.; Shimizu, R.; Haruta, M.; Ohsawa, T.; Sato, Y.; Ikuhara, Y.; Hitosugi, T., Fabrication of all-solid-state battery using epitaxial Li CoO2 thin films. *J Power Sources* **2014,** *267*, 881-887.
167. Huang, R.; Ikuhara, Y. H.; Mizoguchi, T.; Findlay, S. D.; Kuwabara, A.; Fisher, C. A. J.; Moriwake, H.; Oki, H.; Hirayama, T.; Ikuhara, Y., Oxygen-Vacancy Ordering at Surfaces of

Lithium Manganese(III,IV) Oxide Spinel Nanoparticles. *Angew Chem Int Edit* **2011,** *50* (13), 3053-3057.
168. Francis, A. J.; Cao, Y.; Salvador, P. A., Epitaxial growth of Cu(100) and Pt(100) thin films on perovskite substrates. *Thin Solid Films* **2006,** *496* (2), 317-325.
169. Ikuhara, Y. H.; Ma, X. L.; Iwamoto, Y.; Ikuhara, Y.; Kikuta, K.; Hirano, S., Interfaces between solution-derived LiMn2O4 thin films and MgO and Au/MgO substrates. *J Mater Res* **2002,** *17* (2), 358-366.
170. Reddy, M. V.; Raju, M. J. S.; Sharma, N.; Quan, P. Y.; Nowshad, S. H.; Emmanuel, H. E. C.; Peterson, V. K.; Chowdari, B. V. R., Preparation of Li1.03Mn1.97O4 and Li1.06Mn1.94O4 by the Polymer Precursor Method and X-ray, Neutron Diffraction and Electrochemical Studies. *J Electrochem Soc* **2011,** *158* (11), A1231-A1236.
171. Reddy, M. V.; Sakunthala, A.; SelvashekaraPandian, S.; Chowdari, B. V. R., Preparation, Comparative Energy Storage Properties, and Impedance Spectroscopy Studies of Environmentally Friendly Cathode, Li(MMn11/6)O-4 (M = Mn-1/6, Co-1/6, (Co1/12Cr1/12)). *J Phys Chem C* **2013,** *117* (18), 9056-9064.
172. Reddy, M. V.; Manoharan, S. S.; John, J.; Singh, B.; Rao, G. V. S.; Chowdari, B. V. R., Synthesis, Characterization, and Electrochemical Cycling Behavior of the Ru-Doped Spinel, Li[Mn2-xRux]O-4 (x=0, 0.1, and 0.25). *J Electrochem Soc* **2009,** *156* (8), A652-A660.
173. Li, M. Y.; Wang, Z. L.; Fan, S. S.; Zhao, Q. T.; Xiong, G. C., Influences of substrates and substrate temperatures on characteristics of epitaxial La0.5Sr0.5CoO3 thin films. *Thin Solid Films* **1998,** *323* (1-2), 304-308.
174. Mitberg, E. B.; Patrakeev, M. V.; Leonidov, I. A.; Kozhevnikov, V. L.; Poeppelmeier, K. R., High-temperature electrical conductivity and thermopower in nonstoichiometric La1-xSrxCoO3-delta (x=0.6). *Solid State Ionics* **2000,** *130* (3-4), 325-330.
175. Xie, Q. Y.; Wu, Z. P.; Wu, X. S.; Tan, W. S., Sr content on the structure and magnetic properties of La1-xSrxCoO3. *J Alloy Compd* **2009,** *474* (1-2), 81-85.
176. Bychkov, S. F.; Sokolov, A. G.; Popov, M. P.; Nemudry, A. P., Relation between oxygen stoichiometry and thermodynamic properties and the electronic structure of nonstoichiometric perovskite La0.6Sr0.4CoO3-delta. *Phys Chem Chem Phys* **2016,** *18* (42), 29543-29548.
177. Gunasekaran, R. A.; Pedarnig, J. D.; Dinescu, M., Structural, electrical, and surface characteristics of La0.5Sr0.5CoO3 thin films prepared by pulsed-laser deposition. *Appl Phys a-Mater* **1999,** *69* (6), 621-624.
178. Luo, G. P.; Wang, Y. S.; Chen, S. Y.; Heilman, A. K.; Chen, C. L.; Chu, C. W.; Liou, Y.; Ming, N. B., Electrical and magnetic properties of La0.5Sr0.5CoO3 thin films. *Appl Phys Lett* **2000,** *76* (14), 1908-1910.
179. Chan, P. W.; Wu, W. B.; Wong, K. H.; Tong, K. Y.; Cheung, J. T., Preparation and characterization of epitaxial La0.5Sr0.5CoO3 films and of an all a-axis oriented YBa2Cu3O7-y/La0.5Sr0.5CoO3/YBa2Cu3O7-y heterostructure on (001) LaAlO3 by pulsed laser deposition. *J Phys D Appl Phys* **1997,** *30* (6), 957-961.
180. Wu, W. B.; Lu, F.; Wong, K. H.; Pang, G.; Choy, C. L.; Zhang, Y. H., Epitaxial and highly electrical conductive La0.5Sr0.5TiO3 films grown by pulsed laser deposition in vacuum. *J Appl Phys* **2000,** *88* (2), 700-704.

181. Filies, O.; Boling, O.; Grewer, K.; Lekki, J.; Lekka, M.; Stachura, Z.; Cleff, B., Surface roughness of thin layers - a comparison of XRR and SFM measurements. *Applied Surface Science* **1999,** *141* (3-4), 357-365.
182. Rougier, A.; Striebel, K. A.; Wen, S. J.; Cairns, E. J., Cyclic voltammetry of pulsed laser deposited LixMn2O4 thin films. *J Electrochem Soc* **1998,** *145* (9), 2975-2980.
183. Mukai, K.; Sugiyama, J.; Kamazawa, K.; Ikedo, Y.; Andreica, D.; Amato, A., Magnetic properties of the chemically delithiated LixMn2O4 with 0.07 <= x <= 1. *J Solid State Chem* **2011,** *184* (5), 1096-1104.
184. Piszora, P.; Nowicki, W.; Darul, J.; Wolska, E., Synthesis and characterization of the lithium-deficient Fe-substituted Li-Mn oxide spinel phases. *Mater Lett* **2004,** *58* (7-8), 1321-1326.
185. Kanno, R.; Kondo, A.; Yonemura, M.; Gover, R.; Kawamoto, Y.; Tabuchi, M.; Kamiyama, T.; Izumi, F.; Masquelier, C.; Rousse, G., The relationships between phases and structures of lithium manganese spinels. *J Power Sources* **1999,** *81*, 542-546.
186. Matthews, J. W.; Blakeslee, A. E., Defects in Epitaxial Multilayers .2. Dislocation Pile-Ups, Threading Dislocations, Slip Lines and Cracks. *J Cryst Growth* **1975,** *29* (3), 273-280.
187. Whall, T. E.; Parker, E. H. C., SiGe heterostructures for FET applications (vol 31, pg 1397, 1998). *J Phys D Appl Phys* **1999,** *32* (10), 1187-1187.
188. Baskaran, A.; Smereka, P., Mechanisms of Stranski-Krastanov growth. *J Appl Phys* **2012,** *111* (4).
189. Hull, R.; Gray, J.; Wu, C. C.; Atha, S.; Floro, J. A., Interaction between surface morphology and misfit dislocations as strain relaxation modes in lattice-mismatched heteroepitaxy. *J Phys-Condens Mat* **2002,** *14* (48), 12829-12841.
190. Reddy, M. V.; Pecquenard, B.; Vinatier, P.; Levasseur, A., Cyclic voltammetry and galvanostatic cycling characteristics of LiNiVO4 thin films during lithium insertion and re/de-insertion. *Electrochem Commun* **2007,** *9* (3), 409-415.
191. Gunasekaran, N.; Rajadurai, S.; Carberry, J. J.; Bakshi, N.; Alcock, C. B., Surface Characterization and Catalytic Properties of La(1-X)a(X)Mo(3) Perovskite Oxides .2. Studies on La1-Xbaxmno3 (0-Less-Than-or-Equal-to-X-Less-Than-or-Equal-to-0.2) Oxides. *Solid State Ionics* **1995,** *81* (3-4), 243-249.
192. Kim, D.; Park, S.; Chae, O. B.; Ryu, J. H.; Kim, Y. U.; Yin, R. Z.; Oh, S. M., Re-Deposition of Manganese Species on Spinel LiMn2O4 Electrode after Mn Dissolution. *J Electrochem Soc* **2012,** *159* (3), A193-A197.
193. Terada, Y.; Nishiwaki, Y.; Nakai, I.; Nishikawa, F., Study of Mn dissolution from LiMn2O4 spinel electrodes using in situ total reflection X-ray fluorescence analysis and fluorescence XAFS technique. *J Power Sources* **2001,** *97-8*, 420-422.
194. Blyr, A.; Sigala, C.; Amatucci, G.; Guyomard, D.; Chabre, Y.; Tarascon, J. M., Self-discharge of LiMn2O4/C Li-ion cells in their discharged state - Understanding by means of three-electrode measurements. *J Electrochem Soc* **1998,** *145* (1), 194-209.
195. Ochida, M.; Doi, T.; Domi, Y.; Tsubouchi, S.; Nakagawa, H.; Yamanaka, T.; Abe, T.; Ogumi, Z., Effects of Electrolyte Additives on the Suppression of Mn Deposition on Edge Plane Graphite for Lithium-Ion Batteries. *J Electrochem Soc* **2013,** *160* (2), A410-A413.
196. Saulnier, M.; Auclair, A.; Liang, G.; Schougaard, S. B., Manganese dissolution in lithium-ion positive electrode materials. *Solid State Ionics* **2016,** *294*, 1-5.

197. Shkrob, I. A.; Kropf, A. J.; Marin, T. W.; Li, Y.; Poluektov, O. G.; Niklas, J.; Abraham, D. P., Manganese in Graphite Anode and Capacity Fade in Li Ion Batteries. *J Phys Chem C* **2014,** *118* (42), 24335-24348.
198. Borner, M.; Klamor, S.; Hoffmann, B.; Schroeder, M.; Nowak, S.; Wursing, A.; Winter, M.; Schappacher, F. M., Investigations on the C-Rate and Temperature Dependence of Manganese Dissolution/Deposition in LiMn2O4/Li4Ti5O12 Lithium Ion Batteries. *J Electrochem Soc* **2016,** *163* (6), A831-A837.
199. Shilina, Y.; Ziv, B.; Meir, A.; Banerjee, A.; Ruthstein, S.; Luski, S.; Aurbach, D.; Halalay, I. C., Combined Electron Paramagnetic Resonance and Atomic Absorption Spectroscopy/Inductively Coupled Plasma Analysis As Diagnostics for Soluble Manganese Species from Mn-Based Positive Electrode Materials in Li-ion Cells. *Anal Chem* **2016,** *88* (8), 4440-4447.
200. Zhao, L.; Chenard, E.; Capraz, O. O.; Sottos, N. R.; White, S. R., Direct Detection of Manganese Ions in Organic Electrolyte by UV-vis Spectroscopy. *J Electrochem Soc* **2018,** *165* (2), A345-A348.
201. Tang, S. B.; Lai, M. O.; Lu, L., Study on Li+-ion diffusion in nano-crystalline LiMn2O4 thin film cathode grown by pulsed laser deposition using CV, EIS and PITT techniques. *Mater Chem Phys* **2008,** *111* (1), 149-153.
202. Tang, S. B.; Lai, M. O.; Lu, L., Characterization of crystallized LiMn2O4 thin films grown by pulsed laser deposition. *Philos Mag* **2007,** *87* (22), 3249-3258.
203. Moon, H. S.; Park, J. W., Characteristics of in-situ annealed LiMn2O4 thin films for a MEMS power system. *J Korean Phys Soc* **2002,** *41* (6), 872-875.
204. Fischer, J.; Adelhelm, C.; Bergfeldt, T.; Chang, K.; Ziebert, C.; Leiste, H.; Stüber, M.; Ulrich, S.; Music, D.; Hallstedt, B., Development of thin film cathodes for lithium-ion batteries in the material system Li–Mn–O by rf magnetron sputtering. *Thin Solid Films* **2013,** *528*, 217-223.
205. Albrecht, D.; Wulfmeier, H.; Fritze, H., Preparation and Characterization of c‐LiMn2O4 Thin Films prepared by Pulsed Laser Deposition for Lithium‐Ion Batteries. *Energy Technol-Ger* **2016,** *4* (12), 1558-1564.
206. Lu, D. S.; Li, W. S.; Zuo, X. X.; Yuan, Z. Z.; Huang, Q., Study on Electrode Kinetics of Li+ Insertion in LixMn2O4 (0 <= x <= 1) by Electrochemical Impedance Spectroscopy. *J Phys Chem C* **2007,** *111* (32), 12067-12074.
207. Wan, C. Y.; Nuli, Y.; Zhuang, J. H.; Jiang, Z. Y., Synthesis of spinel LiMn2O4 using direct solid state reaction. *Mater Lett* **2002,** *56* (3), 357-363.
208. Bi, Y. J.; Wang, T.; Liu, M.; Du, R.; Yang, W. C.; Liu, Z. X.; Peng, Z.; Liu, Y.; Wang, D. Y.; Sun, X. L., Stability of Li2CO3 in cathode of lithium ion battery and its influence on electrochemical performance. *Rsc Adv* **2016,** *6* (23), 19233-19237.
209. Ismail, I.; Noda, A.; Nishimoto, A.; Watanabe, M., XPS study of lithium surface after contact with lithium-salt doped polymer electrolytes. *Electrochim Acta* **2001,** *46* (10-11), 1595-1603.
210. Tarascon, J.; Guyomard, D., New electrolyte compositions stable over the 0 to 5 V voltage range and compatible with the Li1+ xMn2O4/carbon Li-ion cells. *Solid State Ionics* **1994,** *69* (3-4), 293-305.

211. Gao, Y.; Dahn, J., Correlation between the growth of the 3.3 V discharge plateau and capacity fading in Li1+ xMn2− xO4 materials. *Solid State Ionics* **1996,** *84* (1-2), 33-40.
212. Yabuuchi, N.; Yoshii, K.; Myung, S. T.; Nakai, I.; Komaba, S., Detailed Studies of a High-Capacity Electrode Material for Rechargeable Batteries, Li2MnO3-LiCo1/3Ni1/3Mn1/3O2. *J Am Chem Soc* **2011,** *133* (12), 4404-4419.
213. Aurbach, D.; Markovsky, B.; Shechter, A.; Ein‐Eli, Y.; Cohen, H., A comparative study of synthetic graphite and Li electrodes in electrolyte solutions based on ethylene carbonate‐dimethyl carbonate mixtures. *J Electrochem Soc* **1996,** *143* (12), 3809-3820.
214. Eriksson, T.; Andersson, A. M.; Gejke, C.; Gustafsson, T.; Thomas, J. O., Influence of temperature on the interface chemistry of LixMn2O4 electrodes. *Langmuir* **2002,** *18* (9), 3609-3619.
215. Biesinger, M. C.; Payne, B. P.; Grosvenor, A. P.; Lau, L. W. M.; Gerson, A. R.; Smart, R. S., Resolving surface chemical states in XPS analysis of first row transition metals, oxides and hydroxides: Cr, Mn, Fe, Co and Ni. *Applied Surface Science* **2011,** *257* (7), 2717-2730.
216. Nesbitt, H. W.; Banerjee, D., Interpretation of XPS Mn(2p) spectra of Mn oxyhydroxides and constraints on the mechanism of MnO2 precipitation. *Am Mineral* **1998,** *83* (3-4), 305-315.
217. Ben, L. B.; Yu, H. L.; Chen, B.; Chen, Y. Y.; Gong, Y.; Yang, X. N.; Gu, L.; Huang, X. J., Unusual Spinel-to-Layered Transformation in LiMn2O4 Cathode Explained by Electrochemical and Thermal Stability Investigation. *Acs Appl Mater Inter* **2017,** *9* (40), 35463-35475.
218. Gao, P.; Ishikawa, R.; Tochigi, E.; Kumamoto, A.; Shibata, N.; Ikuhara, Y., Atomic-Scale Tracking of a Phase Transition from Spinel to Rocksalt in Lithium Manganese Oxide. *Chem Mater* **2017,** *29* (3), 1006-1013.
219. Ho, C.; Raistrick, I. D.; Huggins, R. A., Application of Ac Techniques to the Study of Lithium Diffusion in Tungsten Trioxide Thin-Films. *J Electrochem Soc* **1980,** *127* (2), 343-350.
220. Xie, J.; Tanaka, T.; Imanishi, N.; Matsumura, T.; Hirano, A.; Takeda, Y.; Yamamoto, O., Li-ion transport kinetics in LiMn2O4 thin films prepared by radio frequency magnetron sputtering. *J Power Sources* **2008,** *180* (1), 576-581.
221. Meyers, J. P.; Doyle, M.; Darling, R. M.; Newman, J., The impedance response of a porous electrode composed of intercalation particles. *J Electrochem Soc* **2000,** *147* (8), 2930-2940.
222. Illig, J.; Ender, M.; Chrobak, T.; Schmidt, J. P.; Klotz, D.; Ivers-Tiffee, E., Separation of Charge Transfer and Contact Resistance in LiFePO4-Cathodes by Impedance Modeling. *J Electrochem Soc* **2012,** *159* (7), A952-A960.
223. Gaberscek, M.; Moskon, J.; Erjavec, B.; Dominko, R.; Jamnik, J., The importance of interphase contacts in Li ion electrodes: The meaning of the high-frequency impedance arc. *Electrochem Solid St* **2008,** *11* (10), A170-A174.
224. Scipioni, R.; Jorgensen, P. S.; Graves, C.; Hjelm, J.; Jensen, S. H., A Physically-Based Equivalent Circuit Model for the Impedance of a LiFePO4/Graphite 26650 Cylindrical Cell. *J Electrochem Soc* **2017,** *164* (9), A2017-A2030.

225. Waller, G. H.; Brooke, P. D.; Rainwater, B. H.; Lai, S. Y.; Hu, R.; Ding, Y.; Alamgir, F. M.; Sandhage, K. H.; Liu, M. L., Structure and surface chemistry of Al2O3 coated LiMn2O4 nanostructured electrodes with improved lifetime. *J Power Sources* **2016,** *306*, 162-170.
226. Lai, F. Y.; Zhang, X. H.; Wang, H. Q.; Hu, S. J.; Wu, X. M.; Wu, Q.; Huang, Y. G.; He, Z. Q.; Li, Q. Y., Three-Dimension Hierarchical Al2O3 Nanosheets Wrapped LiMn2O4 with Enhanced Cycling Stability as Cathode Material for Lithium Ion Batteries. *Acs Appl Mater Inter* **2016,** *8* (33), 21656-21665.
227. Song, J. H.; Bazant, M. Z., Effects of Nanoparticle Geometry and Size Distribution on Diffusion Impedance of Battery Electrodes. *J Electrochem Soc* **2013,** *160* (1), A15-A24.
228. Macdonald, J. R., Frequency-Response of Unified Dielectric and Conductive Systems Involving an Exponential-Distribution of Activation-Energies. *J Appl Phys* **1985,** *58* (5), 1955-1970.
229. Barsoukov, E.; Macdonald, J. R., *Impedance Spectroscopy: Theory, Experiment, and Applications*. Wiley: 2005.
230. Narayanan, S. R.; Shen, D. H.; Surampudi, S.; Attia, A. I.; Halpert, G., Electrochemical Impedance Spectroscopy of Lithium-Titanium Disulfide Rechargeable Cells. *J Electrochem Soc* **1993,** *140* (7), 1854-1861.
231. Patterson, A., The Scherrer formula for X-ray particle size determination. *Physical review* **1939,** *56* (10), 978.
232. Wagemaker, M.; Borghols, W. J. H.; Mulder, F. M., Large impact of particle size on insertion reactions. A case for anatase LixTiO2. *J Am Chem Soc* **2007,** *129* (14), 4323-4327.
233. Okubo, M.; Hosono, E.; Kim, J.; Enomoto, M.; Kojima, N.; Kudo, T.; Zhou, H. S.; Honma, I., Nanosize effect on high-rate Li-ion intercalation in LiCoO2 electrode. *J Am Chem Soc* **2007,** *129* (23), 7444-7452.
234. Zhou, Y. N.; Yue, J. L.; Hu, E. Y.; Li, H.; Gu, L.; Nam, K. W.; Bak, S. M.; Yu, X. Q.; Liu, J.; Bai, J. M.; Dooryhee, E.; Fu, Z. W.; Yang, X. Q., High-Rate Charging Induced Intermediate Phases and Structural Changes of Layer-Structured Cathode for Lithium-Ion Batteries. *Adv Energy Mater* **2016,** *6* (21).
235. Bai, P.; Cogswell, D. A.; Bazant, M. Z., Suppression of Phase Separation in LiFePO4 Nanoparticles During Battery Discharge. *Nano Lett* **2011,** *11* (11), 4890-4896.
236. Lesel, B. K.; Ko, J. S.; Dunn, B.; Tolbert, S. H., Mesoporous LixMn2O4 Thin Film Cathodes for Lithium-Ion Pseudocapacitors. *Acs Nano* **2016,** *10* (8), 7572-7581.
237. Kim, E. Y.; Lee, B. R.; Yun, G.; Oh, E. S.; Lee, H., Effects of binder content on manganese dissolution and electrochemical performances of spinel lithium manganese oxide cathodes for lithium ion batteries. *Curr Appl Phys* **2015,** *15* (4), 429-434.
238. Chae, Y.; Lee, J. K.; Choi, W., Surface coating of spinel LiMn2O4 cathode electrode with lithium-nickel-manganese-oxide by RF sputtering method for lithium-ion batteries. *J Electroanal Chem* **2014,** *730*, 20-25.
239. Xie, J.; Kohno, K.; Matsumura, T.; Imanishi, N.; Hirano, A.; Takeda, Y.; Yamamoto, O., Li-ion diffusion kinetics in LiMn2O4 thin films prepared by pulsed laser deposition. *Electrochim Acta* **2008,** *54* (2), 376-381.
240. Yu, L. H.; Qiu, X. P.; Xi, J. Y.; Zhu, W. T.; Chen, L. Q., Enhanced high-potential and elevated-temperature cycling stability of LiMn2O4 cathode by TiO2 modification for Li-ion battery. *Electrochim Acta* **2006,** *51* (28), 6406-6411.

241. Yang, X. Q.; Sun, X.; Lee, S. J.; McBreen, J.; Mukerjee, S.; Daroux, M. L.; Xing, X. K., In situ synchrotron X-ray diffraction studies of the phase transitions in LixMn2O4 cathode materials. *Electrochem Solid St* **1999,** *2* (4), 157-160.
242. Huang, H.; Vincent, C. A.; Bruce, P. G., Correlating capacity loss of stoichiometric and nonstoichiometric lithium manganese oxide spinel electrodes with their structural integrity. *J Electrochem Soc* **1999,** *146* (10), 3649-3654.
243. McGrogan, F. P.; Raja, S. N.; Chiang, Y. M.; Van Vliet, K. J., Electrochemomechanical Fatigue: Decoupling Mechanisms of Fracture- Induced Performance Degradation in LiXMn2O4. *J Electrochem Soc* **2018,** *165* (11), A2458-A2466.
244. Liu, H.; Wolf, M.; Karki, K.; Yu, Y. S.; Stach, E. A.; Cabana, J.; Chapman, K. W.; Chupas, P. J., Intergranular Cracking as a Major Cause of Long-Term Capacity Fading of Layered Cathodes. *Nano Lett* **2017,** *17* (6), 3452-3457.
245. Shin, Y. J.; Manthiram, A., Microstrain and capacity fade in spinel manganese oxides. *Electrochem Solid St* **2002,** *5* (3), A55-A58.
246. Barthel, J., Dr. Probe: A software for high-resolution STEM image simulation. *Ultramicroscopy* **2018,** *193*, 1-11.
247. Schmid, H. K.; Mader, W., Oxidation states of Mn and Fe in various compound oxide systems. *Micron* **2006,** *37* (5), 426-432.
248. Varela, M.; Oxley, M. P.; Luo, W.; Tao, J.; Watanabe, M.; Lupini, A. R.; Pantelides, S. T.; Pennycook, S. J., Atomic-resolution imaging of oxidation states in manganites. *Physical Review B* **2009,** *79* (8).
249. Tu, J.; Zhao, X. B.; Xie, J.; Cao, G. S.; Zhuang, D. G.; Zhu, T. J.; Tu, J. P., Enhanced low voltage cycling stability of LiMn2O4 cathode by ZnO coating for lithium ion batteries. *J Alloy Compd* **2007,** *432* (1-2), 313-317.
250. Feng, X. Y.; Zhang, J. X.; Yin, L. W., Enhanced Cyclic Stability of Spinel LiMn2O4 for Lithium-Ion Batteries by Surface Coating with WO3. *Energy Technol-Ger* **2016,** *4* (4), 490-495.